P R O C E E D I N G S MPA/P10

June 1998

P R O C E E D I N G S

of the 9th Workshop on

"Nuclear Astrophysics"

Ringberg Castle, Tegernsee, Germany

March 23 - 27, 1998

Wolfgang Hillebrandt and Ewald Müller (eds.)
Max-Planck-Institut für Astrophysik
Karl-Schwarzschild-Strasse 1
85740 Garching b. München

Preface

From March 23 through 27, 1998, again one of the traditional Workshops on Nuclear Astrophysics was held at the Ringberg Castle near Munich and, as on all previuos occasions, nuclear physicists, astrophysicists, and astronomers met for one week at this spectacular place to discuss problems and projects of common interest. Also, as usual, many of the participants had attended previous workshops but, in addition, several students had an opportunity to present, for the fist time, their work to an internatinal audience.

48 scientists from 10 countries attended this year's workshop, and had productive days in the relaxed atmosphere of the Castle. In contrast to earlier meetings, the topics discussed in the talks were less diverse but were concentrated on supernova physics and the r-process, although other aspects of nuclear astrophysics were also presented. Extended abstracts of most of the contributions are collected in these Proceedings.

The success of the workshop, of course, also depended on financial support by the Max-Planck-Gesellschaft and, needless to say, on the enormous efficiency and friendliness of Mr. Hörmann and his crew.

Garching, June 1998

Wolfgang Hillebrandt Ewald Müller

	List of Participants
Lars Bildsten	Univ. of California, Berkely, USA
Guennadi Bisnovatyi-Kogan	Space Research Inst., Moscow, RUS
Adam Burrows	Univ. Arizona, Tucson, USA
Ramon Canal	Univ. Barcelona, E
Alessandro Chieffi	Instituto di Astrofisica Spaziale, I
Donald Clayton	Clemson Univ., USA
Gertrud Contardo	ESO, Garching, D
Pavel Denissenkov	Univ. of St. Petersburg, RUS
Roland Diehl	MPI für Extraterrestrische Physik, Garching, D
Thomas Faestermann	Techn. Univ., München, D
Stephane Goriely	Univ. Libre de Bruxelles, B
Uwe Greife	Ruhr-Univ. Bochum, D
Alexander Heger	MPI für Astrophysik, Garching, D
Gerhard Hensler	Univ. Kiel, D
Margarita Hernanz	IEEV-CSIC, Barcelona, E
Wolfgang Hillebrandt	MPI für Astrophysik, Garching, D
Peter Höflich	Univ. of Texas, Austin, USA
Jordi Isern	Inst. d'Estudis Espacials de Catalunya, E
Koichi Iwamoto	Univ. Tokyo, Japan
Thomas Janka	MPI für Astrophysik, Garching, D
Andreas Kercek	MPI für Astrophysik, Garching, D
Paul Kienle	Techn. Univ., München, D
Konstantinos Kifonidis	MPI für Astrophysik, Garching, D
Klaus Knie	Techn. Univ., München, D
Gunther Korschinek	Techn. Univ., München, D
Norbert Langer	Univ. Potsdam, D
Mark Leising	MPI für Extraterrestrische Physik,
Matthias Liebendoerfer	Inst.f. Physik, Univ. Basel, CH
Marco Limongi	Osservatorio Astronomico di Roma, I
Martin Lisewski	MPI für Astrophysik, Garching, D
Ewald Müller	MPI für Astrophysik, Garching, D
Dimitrij Nadyozhin	ITEP Moscow, RUS
Jens Niemeyer	Univ. of Chicago, USA
Birgitta Nordström	Niels Bohr Institute, Kopenhagen, DK
Bernd Pfeiffer	Univ. Mainz, D
Nikos Prantzos	Institut d'Astrophysique, Paris, F
Thomas Rauscher	Univ. Basel, CH
Marc Rayet	Univ. Libre de Bruxelles, B
Felix Rembges	Univ. Basel, CH
Stephan Rosswog	Univ. Basel, CH
Oscar Straniero	Osservatorio Astronomico di Teramo, I
Kohji Takahashi	MPI für Astrophysik, Garching, D
Friedel Thielemann	Univ. Basel, CH
Amedeo Tornambe	Osservatorio Astronomico, Teramo, I
Jim Truran	Univ. of Chicago, USA
Takuji Tsujimoto	Univ. Tokyo, Japan
Victor Utrobin	ITEP Moscow, RUS
Shoichi Yamada	Univ. Tokyo, Japan

Contents

Presupernova evolution of massive stars: the models

M. Limongi[1], *O. Straniero*[2], *A. Chieffi*[3]

[1] *Osservatorio Astronomico di Roma, Monteporzio Catone (Roma), Italy*
e-mail: marco@nemo.mporzio.astro.it
[2] *Osservatorio Astronomico di Collurania, Teramo, Italy*
e-mail: straniero@astrte.te.astro.it
[3] *Istituto di Astrofisica Spaziale CNR, Frascati, Italy*
e-mail: alessandro@altachiara.ias.rm.cnr.it

Abstract

We present the evolution of six massive star models (13, 15, 18, 20, 22 and 25 $M_\odot$) from the main sequence phase up to the onset of the iron core collapse. All these models have initial solar chemical composition, i.e. $Z = 0.02$ and $Y = 0.285$. These evolutions have been computed by means of the latest version of the FRANEC (release 4.2) which has been already described in detail by Chieffi, Limongi and Straniero (1998) [11] (Paper I). A 179 isotope network, extending from neutron up to ^{68}Zn, fully coupled to the stellar evolutionary code without any kind of quasi (or full) equilibrium approximation up to $4 \cdot 10^9$ K has been adopted. We discuss the main evolutionary properties of the models and compare them with similar data available in literature whenever possible.

1.1 Introduction

In the first paper of this series (Paper I) we presented in great detail the main properties of the latest version (4.0) of the Frascati RAphson Netwon Evolutionary Code (FRANEC) and discussed the results of a first test evolution of a 25 $M_\odot$ model from the main sequence phase up to the precollapse stage. This evolution has been computed by adopting a 149 isotope network for the advance burnings and a reduced networks for both hydrogen (12 isotopes) and helium (25 isotopes) burnings.

In this paper we present a more extended set of evolutionary models extending in mass between 13 and 25 $M_\odot$ (13, 15, 18, 20, 22, and 25 $M_\odot$) having solar chemical composition ($Y = 0.285$ and $Z = 0.02$). All these models have been computed by adopting a rather extended network for three different regimes: 41 isotopes for H burning, 88 isotopes for He burning and 179 isotopes for all the more advanced nuclear burning phases. A detailed analysis of these models will be presented in a forthcoming paper. Here we want to show just the main evolutionary properties of the six computed models.

1.2 The Code

Since the FRANEC evolutionary code (release 4.0) has already been described in Paper I, here we summarize just its main properties. It is an hydrostatic evolutionary code in which the four equations describing the physical structure of the star (by assuming spherical symmetry) and the N equations describing the chemical evolution of the matter due to the nuclear reactions (N is equal to the total number of isotopes included into the network) are fully coupled together and integrated simultaneously by means of a classical, but properly modified (speeded up), Newton-Raphson method. We adopt a rather extended nuclear networks for three different regimes (41 isotopes for H burning, 88 isotopes for He burning and 179 isotopes for the more advanced burnings) each of one includes, for each nuclear species, all the strong, weak, and electromagnetic interactions whose reaction rates are available in literature. The matter is evolved without any kind of quasi equilibrium approximation up to $4 \cdot 10^9$ K; only above this temperature (and if the ^{28}Si mass fraction is less than 10^{-8}) we shift to a full NSE network including the same nuclear species of the "standard" network. The extension of the convective reagions are fixed by means of the Schwarzschild criterion and no mechanical overshoot is allowed. On the contrary, the semiconvection and the induced overshooting, due to the transformation of He into C and O during central He burning, are properly taken into account [2]. A time dependent mixing is taken into account by following the scheme firstly introduced by Sparks and Endal (1980) [3] and properly modified. The interaction between the convective mixing and the nuclear burning is taken into account in this way: once the star model is evolved for an evolutionary timestep, the convective regions are mixed and then the model is further evolved for a timestep equal to the mixing turnover time. In this way the natural behavior of the matter is fulfilled in the sense that the nuclear species are completely or partially mixed or settle to their local equilibirum abundance depending on the comparison between the mixing turnover time and their nuclear burning timescale. All the adopted input physics are described in detail in Paper I.

1.3 Evolutionary results

The main evolutionary properties of the six computed models are summarized in Figure 1.

By looking at these figure a general trend can be recognized: the lower is the initial mass of the star, the lower is the final mass of the iron core, the more compact and degenerate is its structure, and the more expanded is the envelope. This property may have important consequences on the behavior of the following collapsing core.

As the temporal evolution of the convective zones is concerned (Figure 2) the situation is more complex: in particular the general trend is that the lower is the initial mass of the star the more complex is the evolution of the convective regions.

As the carbon burning is concerned, the 13 and 15 $M_{\odot}$ stars behave differently from all the other models. In fact, they are the only models to form a convective core during central carbon burning. This is due to the higher central carbon oxygen ratio left by the central helium burning. Even the number of convective shells is larger than in the more

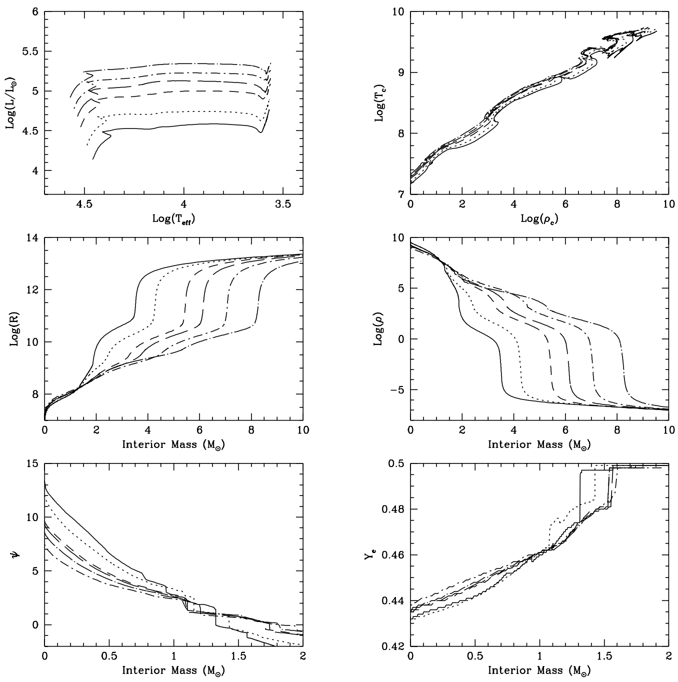

Figure 1: Main evolutionary properties of the six computed models: the path followed by the stars in the HR diagram (*upper left panel*) and in the central $\rho - \mathrm{T}$ diagram (*upper right panel*) all along their evolution; the radius (*middle left panel*), density (*middle right panel*), electron degeneracy (*lower left panel*) and electron mole number (*lower right panel*) profiles just prior to the onset of the iron core collapse. The various lines refer to the 13 (*solid*), 15 (*dot*), 18 (*short dash*), 20 (*long dash*), 22 (*dot - short dash*) and 25 (*dot - long dash*) $M_\odot$ models.

massive stars: five and four convective episodes respectively for the 13 and the 15 $M_\odot$ stars towards only two obtained in all the other models.

On the contrary each model forms a convective core during central neon, oxygen and silicon burning, three oxygen and three silicon convective shells. Actually, the extension and the time duration of all these convective regions differ significantly from one model to the other. This occurence influences not only the final physical structure, but also the final internal profiles of the various nuclear species (Figure 3)

1.4 Discussion

A comparison among the present evolutions and similar computations available in literature is a very difficult task since most of the work devoted to the evolution of massive stars contain very few data on the presupernova models. The comparison among the results obtained by different authors is almost always limited to the final, explosive, yields [4]. On the contrary, we think that only a comparison among all the evolutionary properties during the various nuclear burning phases may increase our confidence in modelling the hydrostatic evolution of massive stars and hence, in turn, in the predicted ejecta.

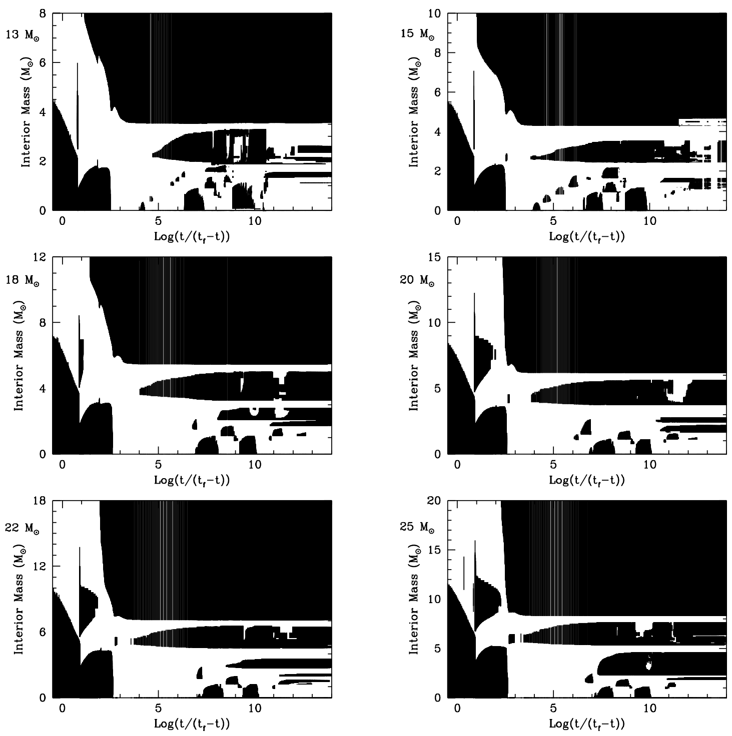

Figure 2: Temporal evolution of the convective zones for the five computed models: 13 (*upper left panel*), 15 (*upper right panel*), 18 (*middle left panel*), 20 (*middle right panel*), 22 (*lower left panel*) and 25 M$_\odot$ (*lower right panel*).

By looking at the literature of the last decade we were able to collect few data on the presupernova models of massive stars; they refer essentially to the works by the Nomoto and Hashimoto [5] (thereinafter NH88) and by Woosley and Weaver [6] (thereinafter WW95).

Figure 4 shows the comparison of the final location in mass of the various nuclear burning shells for the 13, 15, 20 and 25 M$_\odot$.

The location in mass of the H burning shell (or equivalently the He core) is a crucial quantity since all the evolution of the star, following the central H exhaustion, depends crucially on it and not on the total initial mass. Hence in order to have a meaningful comparison among the evolutionary properties of different models it would be desirable to have He cores as close as possible. In general the final size of the He core mainly depends on the maximum size of the H convective core and on the total amount of matter accreted by the advancing H burning shell. Since WW95 include some overshooting in their computations it is clear that they obtain larger He cores; this effect is much more evident for the 25 M$_\odot$. From this point of view a comparison with NH88 is less meaningful because they start their computations from pure fixed He cores and hence they do not follow the H burning phase.

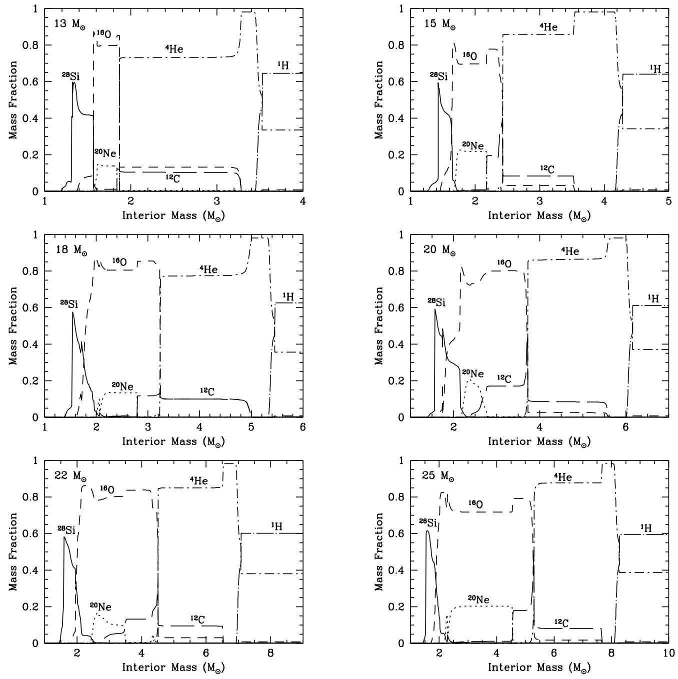

Figure 3: Internal profile of the most abundant nuclear species for the six computed models just prior to the onset of the iron core collapse.

Similarly to the He core, the CO core, or equivalently the location in mass of the He burning shell, is of great importance too since the evolution of the star following the central He exhaustion depends also on this quantity. NH88 found similar CO cores for the 13, 15 and 20 $M_\odot$ models, while for the 25 $M_\odot$ star they obtain a significantly larger CO core in spite of the fact that both of us have similar He cores, for this model, and none of us include the mechanical overshooting. On the contrary WW95 obtain larger CO cores as a result of the larger He core masses and of the higher He convective cores due to the mechanical overshooting during central He burning.

The final location in mass of the C burning shell, which actually coincides with the mass coordinate of the outer edge of the carbon convective shell, seems to follow the same trend shown for the He burning shell.

The behavior of the carbon convective shell directly influences the temporal evolution of the Ne burning shell since it acts as a barrier for the advancing Ne shell. The large difference between the WW95 25 $M_\odot$ star and our corresponding model seems to indicate that in the WW95 model the carbon convective shell vanishes at a certain point of the evolution and allows the neon burning shell to advance in mass. On the contrary in our 25 $M_\odot$ the carbon convective shell is active up to the end of the evolution keeping the Ne shell more internal. Obviously, we do not have any prompt explanation for such occurence. NH88 give no data on the location in mass of the Ne shell, however by comparing the final location of the O burning shell it is possible to guess that NH88 obtain a temporal evolution of the carbon convective shell similar to the one we found.

A last important quantity we can compare is the final size of the iron core, which is

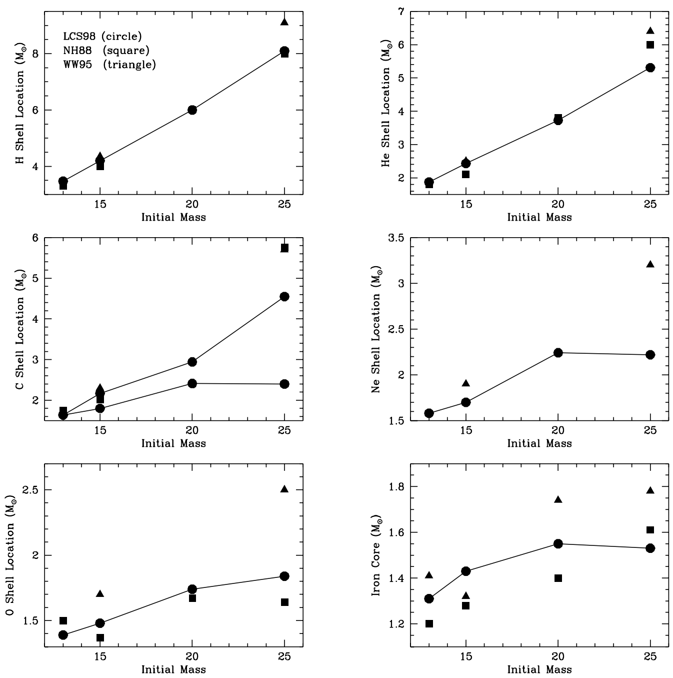

Figure 4: Comparison of the final location in mass of the various nuclear burning shells: H shell (*upper left panel*), He shell (*upper right panel*), C shell (*middle left panel*), Ne shell (*middle right panel*), O shell (*lower left panel*) and Si shell (*lower right panel*). The various symbols refer to NH88 (*squares*), WW95 (*triangles*) and the present computations (*circles*). No symbols indicate no available data.

directly connected to the extension in mass of the last silicon convective shell (Paper I). For the 25 $M_\odot$ NH88 found a silicon convective shell more extended, compared with our findings, and hence, in spite of a smaller oxygen exhausted core, they obtain a larger final iron core mass. A completely opposite behavior occurs for the 13 $M_\odot$, while for the 15 and 20 $M_\odot$ the final iron core size follows the behavior of the oxygen exhausted core. WW95 obtain iron core masses in general larger than the ones we found, except for the 15 $M_\odot$. This is probably due to the fact that they found in general all the core masses to be larger than the ones we obtain. We do not have any explanation for the anomalous behavior of the 15 $M_\odot$ model.

1.5 Conclusion

Our conclusion is that the comparison among our present results and other similar computations available in literature tell us that, at least from a theoretical point of view, the presupernova evolution of massive stars is not yet well established. In our opinion it would be extremely important that people involved in the computation of this kind of models would make some effort in order to try to find out the origin of the existing differences among models computed by different groups. We think this to be a crucial and necessary step in order to increase our confidence in the hydrostatic models and, in turn, in the explosive (more or less simulated) outcome.

References

[1] A. Chieffi, M. Limongi and O. Straniero, ApJ in press

[2] V. Castellani, A. Chieffi, L. Pulone and A. Tornambè, ApJ **296** (1985) 204

[3] W.M. Sparks and A.S. Endal, ApJ **237** (1980) 130

[4] W.D. Arnett, A&A Rev. **33** (1995) 115

[5] K. Nomoto and M. Hashimoto, Phys. Rep. **163** (1988) 13 (NH88)

[6] S.E. Woosley and T.A. Weaver, ApJS **101** (1995) 181 (WW95)

Evolution and Nucleosynthesis in rotating massive stars

A. Heger[1], *N. Langer*[2], *S.E. Woosley*[3]

[1] *Max-Planck-Institut für Astrophysik, Karl-Schwarzschild-Str. 1, D-85740 Garching, Germany*
[2] *Institut für Physik, Universität Potsdam, D-14415 Potsdam, Germany*
[3] *Board of Studies in Astronomy and Astrophysics, University of California, Santa Cruz, CA 95064, U.S.A.*

We investigate the evolution of rotating stars with initial masses above $\sim 8\,\mathrm{M}_\odot$. The evidences for rotation being important in the evolution of massive stars are manifold. First, massive main sequence stars show average equatorial rotation rates of $200\,\mathrm{km\,s^{-1}}$ or more [4], i.e. they rotate, on average, at about half of their break-up velocity. Second, the surface-abundance patterns show signs of nuclear processing [5]. This cannot be explained by mere mass loss, as it would require loss rates in excess of what is expected from both observations and stellar evolution calculations. Also, the observed surface abundance patterns themselves are not compatible with this picture [3]. Thus rotationally induced mixing processes must be employed. Finally, the axisymmetric shapes of circumstellar shells and rings around many stars can be understood when rotation is the cause for breaking the spherical symmetry in the stellar mass loss. A famous example of this is the progenitor of supernova SN 1987A [11, 15].

For our calculations we use hydrodynamic stellar evolution codes [9, 14], which are modified to include specific angular momentum as a local variable. Centrifugal terms are also included in the force equation [1, 7]. The transport of angular momentum and mixing of chemical species are both modeled as diffusive processes [2, 13]. In addition to convection and semi-convection, rotationally induced instabilities are also taken into account, especially the dynamical and secular shear instabilities, the Goldreich-Schubert-Fricke instability, the Eddington-Sweet circulation and the Solberg-Høiland instability [2, 13]. Uncertain efficiency parameters are adjusted for each so that the observed surface abundance patterns for theses stars [5] are reproduced. Obviously there is some ambiguity in the choice of these parameters.

In Fig. 1, the evolutionary tracks of rotating and non-rotating stars of solar composition are compared in the Hertzsprung-Russell diagram [6]. The slightly lower luminosities and surface temperatures of the rotating models at the onset of central hydrogen burning are caused by the reduction of the effective gravity due to centrifugal forces. However, during the main sequence evolution, the rotating stars become more luminous than non-rotating stars of the same mass because the rotationally induced instabilities lead to the mixing of helium into layers above the core. Some even rises to the surface. This leads to an increase of the average mean molecular weight of the star and therefore to a higher luminosity [8]. Thus rotation broadens the main-sequence.

The mixing of helium on the main sequence is responsible for an increase in the mass of the helium core. Moreover, the layers above the core are depleted in hydrogen, causing the

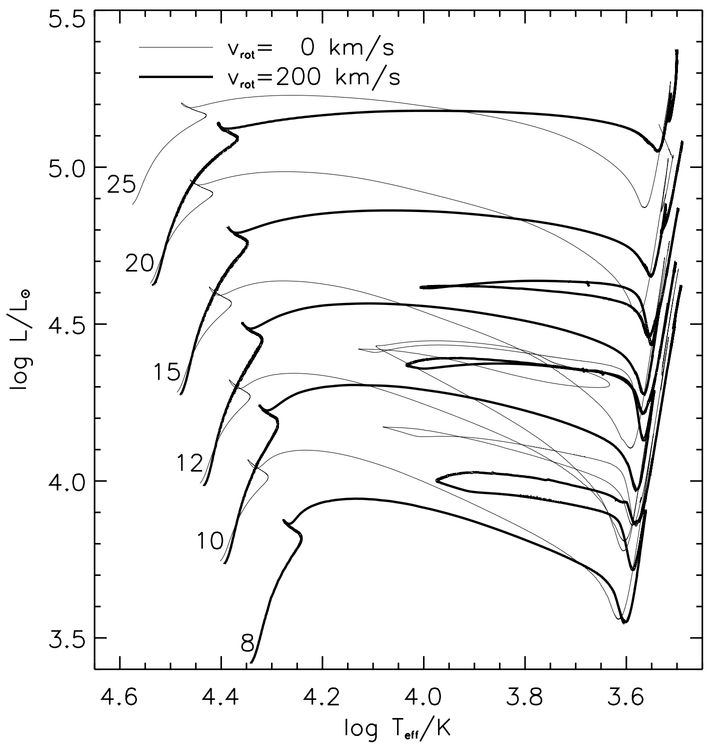

Figure 1: Evolutionary tracks for rotating (thick lines) and non-rotating (thin lines) stars in the mass range 8...25 $M_\odot$ from the ignition of central hydrogen burning to the pre-supernova stage (from [6]). The tracks are labeled with the initial masses (in $M_\odot$). The rotating models have an initial equatorial rotation rate at the surface of 200 km s^{-1}
.

helium core to grow faster during central helium burning, so the stars also have a larger helium core at the time of core collapse. E.g., our rotating 12 $M_\odot$ stars ends up with a helium core of about the same mass as our non-rotating star of 15 $M_\odot$. This strongly affects the nucleosynthetic yields of the stars as a function of their initial mass.

From central helium burning onwards, the evolutionary time-scales of the stars become shorter than those for rotationally induced mixing processes. This inhibits the transport of angular momentum or mixing of chemical species over large distances. That is, the products of central helium burning are *not* transported up to the hydrogen burning shell, nor is there any important loss of angular momentum from the helium core to the stellar envelope (neglecting magnetic fields). Therefore after central helium burning the central regions of rotating stars evolve similar to the cores of more massive non-rotating stars.

However, in some models we find that after the hydrogen shell source has become extinct, protons can be mixed down into the helium burning shell source (i.e. after termination of central helium burning) and this opens new channels of nucleosynthesis [10].

Because of the inefficiency of angular momentum transport by rotationally induced instabilities from central helium burning onwards, only convection is able to transport angular momentum on scales large enough to be important for the redistribution of angular momentum in the late evolutionary stages. The subsequent convective regions of central

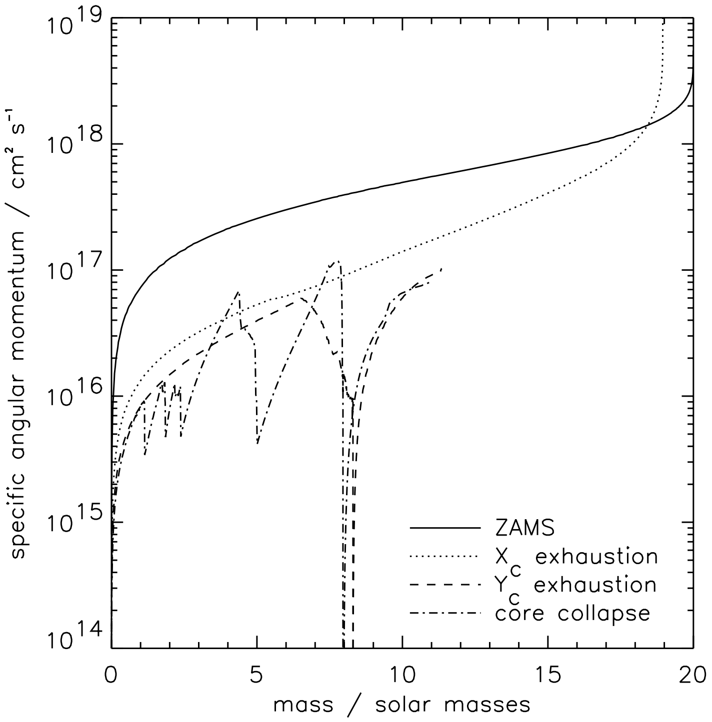

Figure 2: Specific angular momentum as a function of interior mass for the $20\,M_{\odot}$ star. The solid line gives the distribution at the onset of central hydrogen burning, the dotted line at the termination of central hydrogen burning, the dashed line at the termination of central helium burning and the dash-dotted line at the onset of core-collapse.

and shell burning of carbon, neon, oxygen, and silicon thus leave their fingerprints in the angular momentum profile and lead to the spiky structures that can be seen in Fig. 2. However, the total angular momentum remaining in the cores of our models is large: It would be sufficient to bring the neutron stars, formed from the collape of the stellar iron core, close to critical rotation. That is, our models might result in pulsars with initial rotation periods around 1 ms. On the other hand, the fastest known young neutron star, PSR J0537-6910, has a rotation period of 16 ms [12]. The cause of this discrepancy might be either an important angular momentum transport mechanism that is missing in our models, e.g., magnetic fields, or an indication that angular momentum has to be lost during the core collapse or the early evolution of the young neutron star.

Acknowledgments

This work has been supported by a “DAAD-Doktorandenstipendium aus den Mitteln des 2. Hochschulprogramms”, the Deutsche Forschungsgemeinschaft through grant No. La 587/15-1, by the National Science Foundation (AST-94-17161) and NASA (NAG5-3434).

References

[1] A.S. Endal and S. Sofia, ApJ **210** (1976) 184.

[2] A.S. Endal and S. Sofia, ApJ **220** (1978) 279.

[3] J. Fliegner, N. Langer, K. Venn, A&A **308** (1996) L13.

[4] I. Fukuda, PASP **94** (1982) 271.

[5] D.R. Gies and D.L. Lambert, ApJ **387** (1992) 673.

[6] A. Heger, S.E. Woosley, and N. Langer, ApJ (1998) in preparation.

[7] R. Kippenhahn and H.-C. Thomas, in *Stellar rotation*, ed. A. Slettebak, Reidel, Dortrecht, (1970) 20.

[8] R. Kippenhahn, and A. Weigert, *Stellar Structure and Evolution*, Springer-Verlag, Berlin (1991).

[9] N. Langer, M. Kiriakidis, M.F. El Eid, K.J. Fricke, A. Weiss, A&A **192** (1988) 177.

[10] N. Langer, J. Fliegner, A. Heger, S.E. Woosley, Nuc. Phys. A **621** (1997) 457c.

[11] F. Meyer, MNRAS **285** (1997) L11.

[12] F.E. Marshall, E.V. Gotthelf, W. Zhang, J. Middleditch, Q.D. Wang, ApJL (1998) submitted.

[13] H.M. Pinsonneault, S.D. Kawaler, S. Sophia, P. Demarque, ApJ **338** (1989) 424.

[14] T.A. Weaver, G.B. Zimmerman, S.E. Woosley, ApJ **225** (1978) 1021.

[15] A. Weiss, W. Hillebrandt, J.W. Truran, A&A **197** (1988) L11.

Massive Close Binaries as Source of Galactic ^{26}Al

N. Langer†[1], *H. Braun‡*, *S. Wellstein†*

†*Institut für Physik, Universität Potsdam, D–14415 Potsdam, Germany*
‡*Max-Planck-Institut für Astrophysik, D–85740 Garching, Germany*

Abstract

We propose a new site for the synthesis of the radionuclide ^{26}Aluminum which is observed in the Galactic interstellar medium: massive close binary systems. We present the results of an examplary calculation and conclude that — depending on the still somewhat uncertain ^{26}Al production efficiency in supernovae — massive close binaries may even be the dominant source of ^{26}Al in the Galaxy.

1 Introduction

Most stars appear to be members of binary or multiple systems. The fraction of massive stars being members of *close* binaries — i.e. such in which mass overflow is expected to occur — is estimated to be of the order of 20...40% (cf. Garmany et al. 1989, Podsiadlowski 1997, Mason et al. 1998). Thus, it appears necessary to investigate the effect of binary mass transfer on the overall massive star nucleosynthesis yields: if the mass transfer would increase the yield of an isotope only by a factor of ~ 3, then massive close binaries might be the dominant source of this isotope.

Braun & Langer (1998) have studied the nucleosynthesis processes in typical massive close binaries. Fig. 1 gives an example of the evolution of a close $20+18\,M_\odot$ pair of Case A — i.e. mass transfer occurs during the core hydrogen burning phase of the primary (the initially more massive star) — in the HR diagram. Due to the transfer of most of the hydrogen-rich envelope of the primary to the secondary component, the primary becomes a helium star (cf. point D in Fig. 1) while the secondary evolves into a luminous blue supergiant. In both cases, the core masses evolve differently compared to single stars of the same initial mass (i.e., 20 or $18\,M_\odot$ in our example); the primaries' core masses are smaller, that of the secondaries larger.

Then, the primary may, as a helium star, develop strong Wolf-Rayet type winds mass loss (cf. Langer 1989ab, Woosley et al. 1995), further reducing its helium core mass. This can affect the chemical yields of primary isotopes substantially, e.g. the carbon yield is enhanced at the expense of oxygen (cf. Langer & Henkel 1995). As long as the primary's helium core mass remains above $\sim 2\,M_\odot$ it will develop a collapsing iron core and become a supernova of Type Ib or Ic (Woosley et al. 1995).

As for the secondary star, which accretes the envelope of the primary during its core hydrogen burning evolution, it is a common assumption that it evolves after accretion exactly like a single star of the corresponding new mass ($\sim 32\,M_\odot$ in our example). However,

[1] E-mail: ntl@astro.physik.uni-potsdam.de

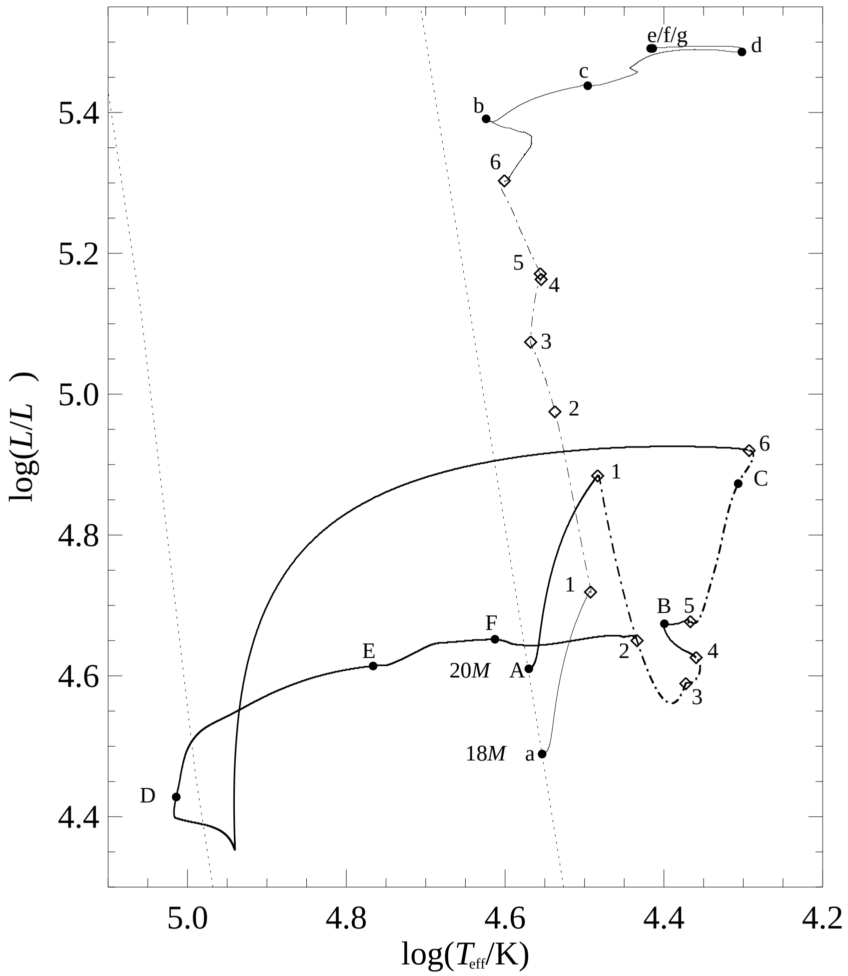

Figure 1: Evolutionary tracks in the HR diagram of the components of a 20+18 $M_{\odot}$ case A close binary system with a metallicity of $Z_{\odot}/4$ and an initial period of 2.5 days. The path of the primary component (initial mass 20 $M_{\odot}$) is marked by the thick line and upper case letters, that of the secondary by the thin line and lower case letters. Mass transfer stages correspond to the dot-dashed parts of the lines. The thin dotted lines designate the zero age main sequence and the location of pure helium stars (helium main sequence). The letters designate beginning and end of nuclear burning stages, i.e. core hydrogen burning (a/A – b/B), core helium burning (c/C – d/D), core carbon burning (e/E – f/F). g/G marks the beginning of core neon burning. Numbers designate mass transfer events for both stars. 1: beginning of Case A mass transfer, 2: maximum of mass transfer rate, 3: start of slow phase of Case A mass transfer, 4: end of Case A mass transfer, 5: start of Case AB mass transfer, 6: end of Case AB mass transfer. The final masses of the primary and secondary are 3 and 32 $M_{\odot}$, respectively.

Braun & Langer (1995) found that secondaries may retain significant structural differences compared to single stars, e.g. with the consequence that the supernova explosion occurs in the blue supergiant stage (cf. Fig. 1) — as in the case of the progenitor of SN 1987A — rather than in the red supergiant stage.

However, independent of this phenomenon, Braun & Langer (1998) found that substantial differences in the synthesis of secondary CNO isotopes do occur in the secondary components of massive close binaries, due to the interplay between CNO burning and so called thermohaline mixing. This mixing process does occur in the whole hydrogen-rich envelope of the secondary from the surface down to the convective H-burning shell since the star accretes helium enriched matter from the primary component (i.e. matter with a higher mean molecular weight is lying above matter with lower mean molecular weight). As the time scale for thermohaline mixing — which is for the first time treated as a time dependent process by Braun & Langer (1998) — and CNO processing at the bottom of the mixed zone are comparable, the production particularly of ^{13}C and ^{14}N is boosted in the whole H-rich envelope, increasing the yield of these isotopes by factors of the order of 2...3.

2 Production of ^{26}Aluminum in close binaries

The synthesis of ^{26}Al in secondary components of close binaries was found to deserve special attention. The reason is that for ^{26}Al, as it is β-unstable with a mean life time of $1.03\,10^6$ yr ($\tau_{1/2} = 7.2\,10^5$ yr), not only the amount which is synthesized matters, but also the time of the synthesis if one wants to explain the observed γ-ray line emission from the decay of ^{26}Al in the Galaxy. We can only see the decay of ^{26}Al nuclei in the interstellar medium; the decay inside stars is unobservable. Therefore, the ^{26}Al which is observed should either be produced during supernova explosions or shortly before. From the spatial distribution of the γ-ray line emission (Prantzos & Diehl 1996) we know that it originates from massive stars. Supernovae are in fact the currently favored production site, although the corresponding yields are very uncertain (Weaver & Woosley 1993, Woosley & Weaver 1995, Timmes & Woosley 1997).

However, ^{26}Al is also produced during hydrostatic hydrogen burning, by proton capture on ^{25}Mg. Although very massive stars, through extremely strong stellar winds, can eject ^{26}Al generated during H-burning and contribute to the Galactic ^{26}Al (Langer et al. 1995, Meynet et al. 1997), the hydrogen burning contribution of less massive stars (say 10...30 $M_\odot$) is not considered as important (though see Langer et al. 1997) since the major fraction of the ^{26}Al decays inside the star before it is released in the course of the supernova explosion.

Braun & Langer (1998) found this to be different in massive close binary secondaries. Fig. 2 shows the time dependence of the amount of ^{26}Al generated by hydrogen burning in the interior of the secondary component of the 20+18 $M_\odot$ system shown in Fig. 1. Obviously, the ^{26}Al mass, although $10^{-5}\,M_\odot$ initially, would be of the order of $10^{-8}\,M_\odot$ at the end of the evolution if no mass accretion would occur. However, since fresh fuel — i.e. also fresh ^{25}Mg — is mixed into the core due to the mass accretion process (cf. Braun & Langer 1995) the amount of ^{26}Al is increased by orders of magnitude at that time.

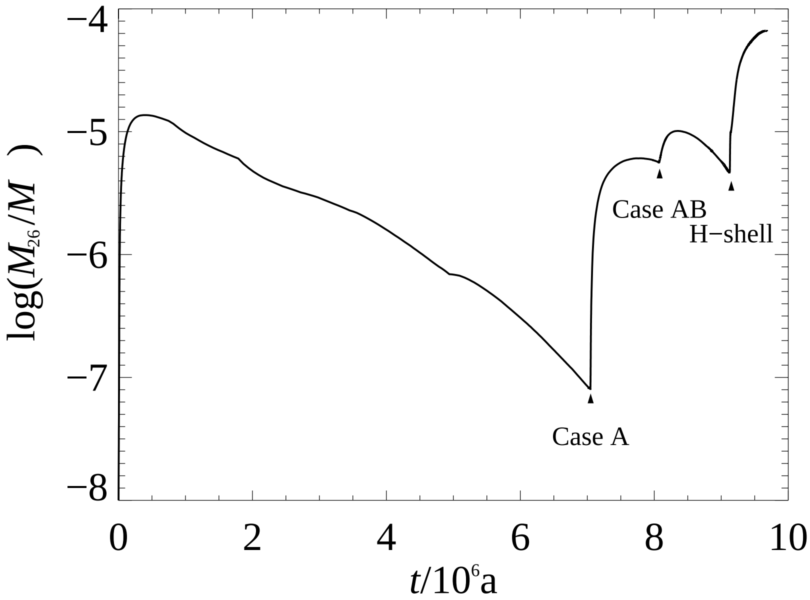

Figure 2: Evolution of the total mass of ^{26}Al inside the secondary component of a 20+18 $M_\odot$ case A close binary system (cf. Fig. 1) as a function of time (in 10^6 yr). The beginning of the Case A and Case AB mass transfer phase is indicated, as well as the beginning of hydrogen shell burning which marks the end of the core helium burning evolutionary phase. When the star explodes as a supernova of Type SN 1987A ($t = 9.68\,10^6$ yr) it contains almost $10^{-4}\,M_\odot$ of 26Al. Note that the initial metallicity of the stars is $Z_\odot/4$.

This would already be sufficient to produce as much as $\sim 10^{-6}\,M_\odot$ ^{26}Al from this star of initially 18 $M_\odot$ — two orders of magnitude more than expected from single star calculations at $Z_\odot/4$ (cf. Langer et al. 1995). However, we find the H-burning shell source in the secondary component to be much more efficient than in corresponding single stars. This leads to the coupling of an extended convection zone to the hydrogen burning shell, and consequently to the enrichment of the whole convection zone with ^{26}Al. In the end, our secondary star contains almost $10^{-4}\,M_\odot$ of ^{26}Al which will be liberated during the supernova explosion. As the chosen example appears to be a rather typical case, the Galactic ^{26}Al production may in fact be dominated by massive close binary systems.

Acknowledgements

This work has been supported by the Deutsche Forschungsgemeinschaft through grant No. La 587/15-1.

References

[1] Braun H and Langer N 1995 A&A **297** 483

[2] Braun H and Langer N 1998 in preparation for A&A

[3] Garmany C D, Conti P S and Massey P 1980 ApJ **242** 1063

[4] Langer N 1989a A&A **210** 93

[5] Langer N 1989b A&A **220** 135

[6] Langer N and Henkel C 1995 *Space Sci. Rev.* **74** 343

[7] Langer N, Braun H and Fliegner J 1995 *Astrophys. Space Sci.* **224** 275

[8] Langer N, Fliegner J, Heger A and Woosley S E 1997 *Nucl. Phys.* **A621** 457c

[9] Mason B D, Gies D R, Hartkopf W I, Bagnuolo W G Jr, Brummelaar T T and McAlister H A 1998 ApJ **115** 821

[10] Meynet G, Arnould M, Prantzos N and Paulus G 1997 A&A **320** 460

[11] Podsiadlowski Ph 1997 in: *Evolutionary Processes in Binary Stars* eds. R A M J Wijers et al. NATO ASI Ser. C Vol. **477** (Dordrecht: Reidel) p 181

[12] Prantzos N and Diehl R 1996 *Phys. Rep.* **267** 1

[13] Timmes F X and Woosley S E 1997 ApJ **489** 160

[14] Weaver T A and Woosley S E 1993 *Phys. Rep.* **227** 65

[15] Woosley S E and Weaver T A 1995 ApJS **101** 181

[16] Woosley S E, Langer N and Weaver T A 1995 ApJ **448** 315

S-Process in Massive Stars: Efficiency vs. Metallicity

Marc Rayet[1] *and Masaaki Hashimoto*[2]

[1]*Institut d'Astronomie et d'Astrophysique, Université Libre de Bruxelles CP 226, Bd. du Triomphe, B-1050 Brussels – Belgium*
[2]*Faculty of Science, Kyushu University, Fukuoka 810 – Japan*

The purpose of this work is to investigate the effect of neutron captures on ^{16}O on the production of s-nuclei during the core He burning phase of massive stars, in the light of a recent measurement of the capture reaction σ_{16} [1] and for a large range of metallicities. Following the work of Prantzos et al. [2], we use the evolutionary models of Nomoto and Hashimoto [3] for a helium star of mass $M_\alpha = 8M_\odot$. We follow the nucleosynthesis with an updated reaction network which is fully described in [4].

The amount of s-nuclei produced during the helium burning phase depends on the relative abundances of the *seed* (iron-peak) nuclei, of nuclei entering neutron producing reactions (neutron *sources*) and of neutron capturing light nuclei which act as neutron *poisons* by limiting the neutron irradiation of the seed nuclei. The initial abundance of ^{14}N, the progenitor of the neutron source ^{22}Ne, is assumed to be the sum of the CNO nuclei present in the H burning phase and scales therefore with metallicity. The latter is also true for the abundances of the seed nuclei.

Since the recent measurement of a large neutron capture cross section on ^{16}O ($\sigma_{16} = 34\,\mu$b [1]), this nucleus, one of the main product of He burning, has been considered as a potentially effective neutron poison. Although most of the neutrons captured by ^{16}O are recycled by the reaction $^{17}\mathrm{O}\,(\alpha\,,\mathrm{n})\,^{20}\mathrm{Ne}$, this recycling is never complete, some neutrons being lost in the competing $^{17}\mathrm{O}\,(\alpha\,,\gamma)\,^{21}\mathrm{Ne}$ channel. At solar metallicity, this neutron loss is small enough not to affect significantly the synthesis of s-nuclei [5], but the situation can be quite different at lower metallicities as the abundance of ^{16}O increases with respect to the abundances of seed and source nuclei.

We calculate the s-process efficiency, defined as the abundance of a synthesized s-nucleus normalized to its initial abundance (X_{seed}), for different values of the metallicity. In order to vary also the relative importance of *source* and *seed* nuclei we consider a scenario where the abundance of iron with respect to oxygen decreases continuously when going back in the galactic time (this scenario corresponds to case B of [2], where $X\,(\mathrm{Fe})/X_\odot(\mathrm{Fe}) = (z/z_\odot)^{1.42}$, $z/z_\odot$ being the oxygen abundance relative to solar). The implementation of those prescriptions in our calculations is obtained by using different scalings for the initial abundances of ^{14}N (scaling like O) and of the $A \geq 20$ nuclei (scaling like Fe).

The s-process efficiency, (X/X_{seed}), is shown in Fig. 1 for metallicities ranging between $z/z_\odot = 1$ and $z/z_\odot = 10^{-3}$, for the s-only isotopes with $70 \leq A < 90$ which are mainly produced in the central He burning of massive stars. Two values of σ_{16} are considered for comparison, the old value $\sigma_{16} = 0.2\,\mu$b of Bao and Käppeler [6] and the presently accepted large value $\sigma_{16} = 34\,\mu$b[1]. With the small one, the efficiency first increases by one order of magnitude with increasing *source/seed* ratio, the poisoning effect of ^{16}O showing up only

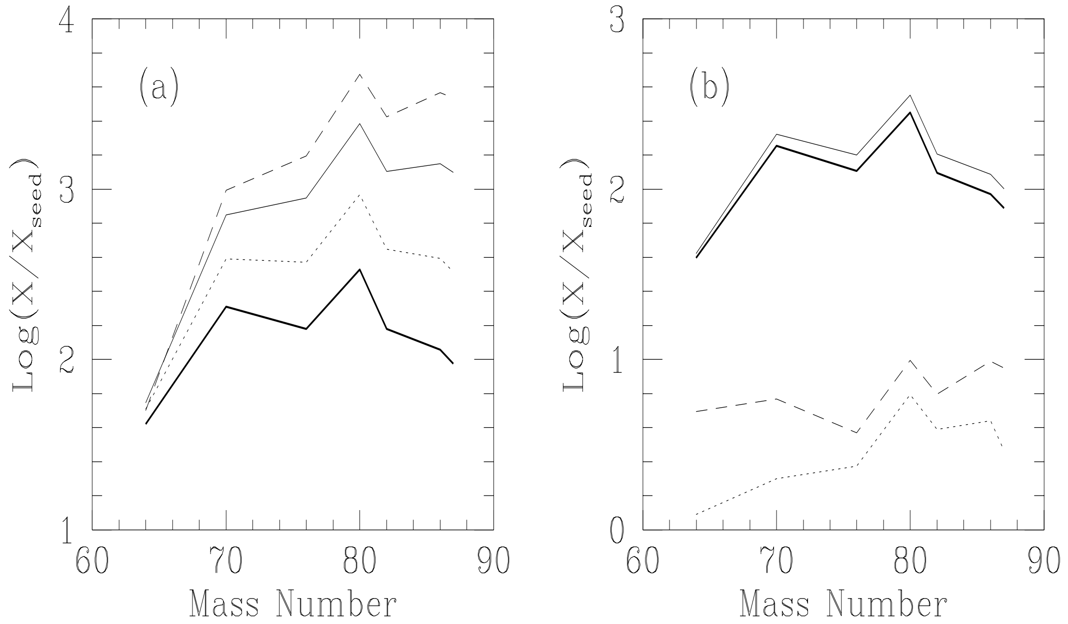

Figure 1: The s-process efficiency, $X/X_{\rm seed}$ for 6 s-only nuclei in the $70 \leq A < 90$ range: (a) with $\sigma_{16} = 0.2\,\mu$b[6], (b) with $\sigma_{16} = 34\,\mu$b[1], and for different metallicities: $z/z_\odot = 1$ (thick solid line), $z/z_\odot = 10^{-1}$ (thin solid line), $z/z_\odot = 10^{-2}$ (dashed line), $z/z_\odot = 10^{-3}$ (dotted line)

for $z/z_\odot < 10^{-2}$. On the other hand, with $\sigma_{16} = 34\,\mu$b, we observe that between $z/z_\odot = 1$ and 10^{-1} the efficiency remains almost constant, neutron captures on ^{16}O compensating the increase in the *source/seed* ratio, while it drops dramatically at lower metallicities.

References

[1] Igashira M., Nagai Y., Masuda K., Ohsaki T., Kitasawa H., 1995, ApJ 441, L89

[2] Prantzos N., Hashimoto M., Nomoto K., 1990, A&A 234, 211

[3] Nomoto K., Hashimoto M., 1988, Phys. Rep. 163, 13

[4] Rayet M., Hashimoto M.,1998, in *Tours Symposium on Nuclear Physics III*, eds. M. Arnould et al. (American Institute of Physics: New York), p. 605

[5] Travaglio C., Gallino R., Arlandini C., Busso M., 1997, preprint

[6] Bao Z.Y., Käppeler F., 1987, ADNDT 36, 411

Explosive Nucleosynthesis: Coupling Reaction Networks to AMR Hydrodynamics

K. Kifonidis[1], *T. Plewa*[2,1], *E. Müller*[1]

[1] *Max-Planck-Institut für Astrophysik, Karl-Schwarzschild-Strasse 1, D-85740 Garching, Germany*
[2] *Nicolaus Copernicus Astronomical Center, Bartycka 18, 00716 Warsaw, Poland*

1.1 Introduction

Observations of SN 1987A revealed that extensive mixing had taken place in the exploding envelope of the progenitor Sk -69 202. Especially the early detection of X and γ-rays [7], [15], the broad profiles of infrared Fe II and Co II lines [6], [9] as well as modelling of the light curve [1], [22] indicated that ^{56}Ni was mixed from the layers close to the collapsed core, where it was explosively synthesized, out to the hydrogen envelope where the highest expansion velocities occurred.

Multidimensional hydrodynamic models of the late phases of the explosion (starting several minutes after core bounce) while successful in confirming that mixing due to Rayleigh-Taylor instabilities did indeed occur after the explosion shock had passed the C,O/He and He/H interfaces, have hitherto failed to yield the amount of mixing observed [8], [10], [17]. However, Herant and Benz [11] have shown that velocities in line with the observations could be obtained if one *artificially* mixed ^{56}Ni in the very early phases of the explosion out to layers which later suffer from the Rayleigh-Taylor instabilities.

In the light of results from recent multidimensional simulations of the (neutrino driven) explosion mechanism itself which revealed large scale anisotropies, mixing and overturn due to convective motions taking place within about one second after core bounce behind the revived supernova shock, it has been argued [12], [14] that a physically satisfactory mechanism has been found which might lead to the required amount of "premixing" and thus resolve the nickel problem. However, only very preliminary multidimensional computations exist to date which attempt to follow the mixing of nickel from the moment of nucleosynthesis until it appears in the hydrogen envelope of the exploding star [18]. Despite constant growth in computer resources and steady advances in numerical algorithms such simulations still pose a formidable task due to the large range of spatial and temporal scales which have to be resolved. Therefore, most of the computations hitherto performed started from artificial *spherical* models of the explosion itself.

In recent years the technique of Adaptive Mesh Refinement (AMR) has been applied to several astrophysical problems (cf. [5], [19]) and should allow a consistent modelling of the complete evolution in two dimensions. In this contribution we address some of the computational difficulties encountered when trying to apply AMR to explosive nucleosynthesis and supernova envelope ejection.

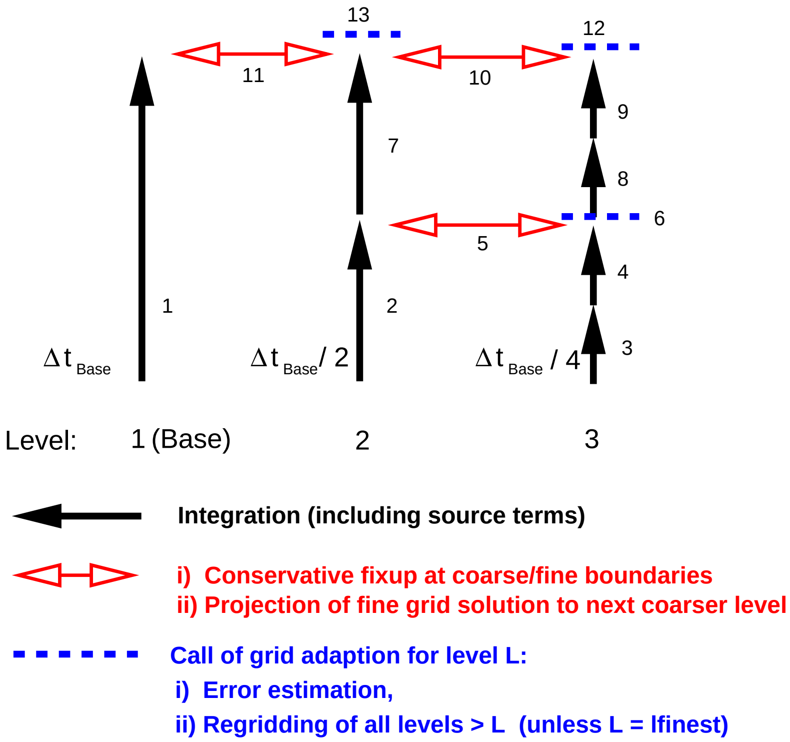

Figure 1: Integration of the grid hierarchy over a single base level time step for 3 levels of refinement with a constant refinement factor $r = 2$. Note that grids at level $l+1$ have to be evolved with time steps $\Delta t_l / r$. The numbers indicate the actual sequence of operations to be carried out. A regridding frequency of $K = 2$ was chosen in this example.

1.2 Adaptive Mesh Refinement

AMR is an algorithm for the efficient solution of systems of time-dependent, hyperbolic partial differential equations [2]. An extended version of the basic AMR algorithm applied to the Euler equations of ideal, compressible flows has been discussed in [3]. In essence, AMR provides a way to automatically adjust the computational grid resulting from the discretization of the differential equations subject to the estimated error of the solution. Since in many cases this error is large only in some regions of the computational domain AMR usually offers large savings in CPU time and memory usage.

The AMR algorithm constructs and continuously updates a tree of nested grid meshes or patches located on different *levels* in the tree hierarchy. Each level can be formed out of one or more patches with the resolution changing between levels from lower (coarse) to higher (fine) levels by arbitrary (but integer) factors in each dimension. Patches forming a single level may partially overlap each other or may cover distinct regions of the computational domain, but those belonging to different levels must necessarily be “properly nested”, i.e. patches on a given level must be totally covered by one or more patches located on the next coarser level.

Integration of the grids proceeds starting from the base level grid of the lowest resolution, which covers the entire computational domain, and recursively continues through the higher levels of the grid hierarchy (Fig. 1). Some amount of communication between the different levels is needed in order to obtain a consistent solution. This includes averaging of the solution obtained on fine patches and its projection down to parent patches. Furthermore, special attention is required at boundaries separating coarse and fine grid cells. The integration of fine grids is carried out using boundary (ghost) zones which might have to be initialized by interpolating data from coarser levels. In the general case, numerical fluxes calculated with higher resolution will differ from fluxes calculated with lower resolution. To ensure global conservation a correction pass over all coarser grid cells abutting fine grid cells is needed once both grid levels have been integrated to the same time. We refer the reader to [3] for a more detailed description of this procedure.

Finally, every K time steps on a given level an error estimation procedure is invoked, which yields an estimate of the local truncation error. The regions where this value exceeds some predefined threshold, ϵ, are marked and later covered with new grid patches of higher resolution. Thereby flow features requiring high resolution like shocks, contact discontinuities or strong gradients in the solution are always followed with the higher level grids while regions where the flow is essentially smooth are calculated at lower resolution. It is important to note in this context that newly created fine grids might have to be initialized with data obtained by interpolation from underlying coarser grids. As we will show below this procedure may lead to serious numerical problems especially for multi-component flows.

1.3 Numerical tests

In our numerical investigations we considered the problem of a supernova explosion for a $15\,M_\odot$ model progenitor of Woosley, Pinto and Ensman [23] in one dimension assuming spherical symmetry and using the AMRA code [20]. The hydrodynamic equations were solved with the direct Eulerian version of the Piecewise Parabolic Method (PPM) as implemented in the PROMETHEUS code [8] although AMRA can be used in conjunction with any hydrodynamic scheme.

After removing the model's iron core the explosion was initiated by depositing an energy of 10^{51} ergs in form of a thermal bomb into the innermost region of the silicon shell. We used five levels of refinement, with 256 zones on the base grid (level 1) and refinement factors of 2, 4, 6, and 8 for patches on levels 2, 3, 4, 5 respectively. This gave us an effective resolution of 98 304 equidistant zones. The computational domain extended from 1.4×10^8 cm up to 3.8×10^{11} cm and covered about the inner 1/10th of the star. Besides ^{1}H, the 13 α-nuclei from ^{4}He to ^{56}Ni were included. A realistic equation of state was used that contained contributions from all considered nuclei as well as electrons, photons and e^+/e^--pairs. Gravity was taken into account and included the contribution from the collapsed central core as well as self-gravity of the envelope. The code was optimized to run efficiently on CRAY shared memory systems.

The solution of the coupled system of hydrodynamic and nuclear rate equations neccessitates a detailed description of the chemical composition within the hydrodynamic scheme. In PROMETHEUS this is achieved by solving additional continuity equations for each fluid component, with the partial densities, ρX_i, (where X_i denotes the mass fraction of species i) as state variables. This extension of basic PPM is reflected within AMRA in

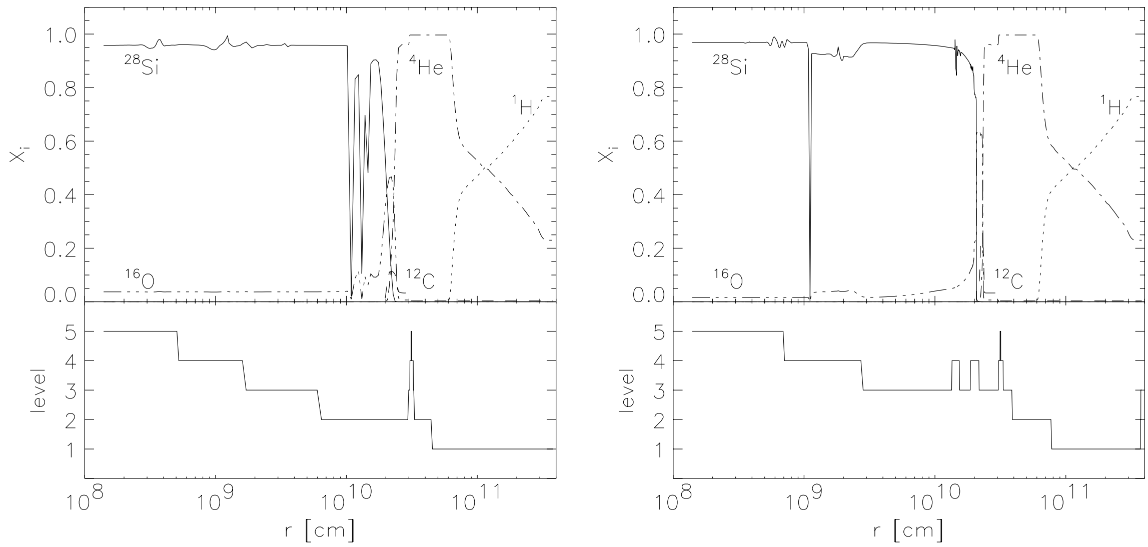

Figure 2: Left: Mass fraction profiles for our test problem after 34.9 s of evolution. By this time the shock has reached a radius slightly larger than 3×10^{10} cm and is tracked with a single level 5 patch. The error estimation algorithm was applied only to $(\rho, \rho u, \rho E_{\rm tot})$ and a local truncation error of $\epsilon = 0.1$ was used. Large errors in mass fractions can clearly be seen in the central region of the grid. Right: Same as left panel but with $\epsilon = 0.01$. In spite of the increased accuracy (by a factor of ten) the solution is still flawed.

two ways. Firstly, the fixup procedure for fluxes at fine-coarse boundaries is done for the partial densities in a similar way as for the other conserved quantities. Secondly, fractional masses are interpolated conservatively when boundary data for fine patches are needed or when the hydrodynamic state for the interior of a newly created fine patch has to be provided. Both steps may lead to serious numerical problems due to the fact that the interpolation scheme does *not* guarantee that the total gas density will remain equal to the sum of partial densities after interpolation. One might expect that the magnitude of this problem will be large whenever the new patch is created in regions where the partial densities vary significantly. Furthermore, the degree of mismatch between the total and partial densities should decrease with increasing degree of smoothness. The latter can efficiently be controlled using the threshold for truncation error. In what follows we ignore for the moment nuclear reactions and focus on this interpolation problem by presenting results obtained for the same initial data but varying truncation error thresholds.

Figure 2 displays the chemical profiles obtained when the truncation error is estimated only for the conserved quantities $(\rho,\ \rho u,\ \rho E_{\rm tot})$ with $\epsilon = 0.1$ and $\epsilon = 0.01$ in the left and right panel, respectively. In both cases large errors in the distribution of species are visible. Using a smaller ϵ helps in resolving the outer edge of the silicon shell ($r \approx 1-2\times 10^{10}$ cm), but some low-amplitude noise can still be seen at $r \approx 1.5\times 10^{10}$ cm. However, the computed distribution of ^{28}Si in the core does not seem to be sensitive to this mild improvement in overall accuracy and in addition to low-amplitude noise a conspicuous undershoot is present at $r \approx 10^9$ cm for the $\epsilon = 0.01$ case. The quality of the solution improves when

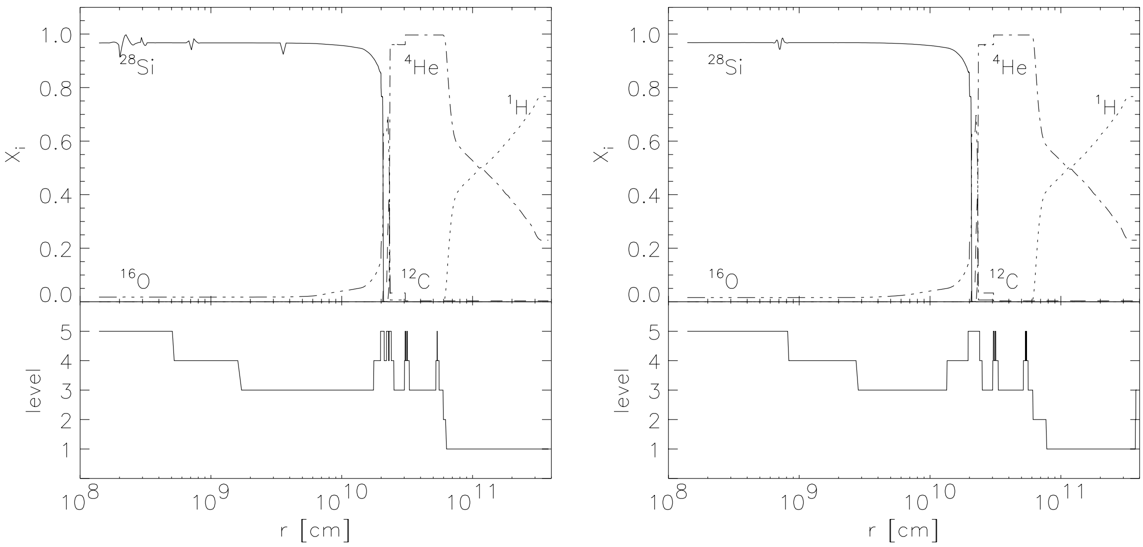

Figure 3: Left: Same as Fig. 2 but with $\epsilon = 0.1$ for $(\rho, \rho u, \rho E_{\rm tot})$ and additional flagging of the partial densities, ρX_i, with $\epsilon_X = 0.1$. Right: Same as left panel but with $\epsilon = 0.01$ and $\epsilon_X = 0.01$.

in addition to the error estimation for $(\rho, \rho u, \rho E_{\rm tot})$ we also estimate the truncation error for the partial densities (Fig. 3). With $\epsilon = 0.1$ and $\epsilon_X = 0.1$ most of the material interfaces located just below the helium shell are resolved and no large errors in the silicon distribution are present. With increased accuracy ($\epsilon = 0.01$, $\epsilon_X = 0.01$) the finest level patches extend from the centre of the grid further out and help in keeping the chemical composition smooth. The outer edge of the silicon core is now covered with level 4 patches and all chemical discontinuities are modelled using the highest resolution. However, the errors are not totally eliminated. The silicon abundance is still affected near $r \approx 7\times10^8$ cm. From our numerical experiments we found that using $\epsilon = 0.001$ and $\epsilon_X = 0.01$ finally eliminates the problem (cf. the left panel of Fig. 4) with patches on the finest level now extending from the inner boundary to radii slightly above $r \approx 10^9$ cm.

In the right panel of Fig. 4 we finally present results obtained with an α-chain network of 27 reactions for our 13 α-nuclei. The network was coupled to the hydrodynamics as described in [16]. The same explosion energy as for the other runs was also adopted for this setup. However, the computational domain extended from $r = 1.4 \times 10^8$ cm to $r = 1.2 \times 10^{11}$ cm. Five levels of refinement, 120 zones on the base grid and refinement factors of 2, 4, 4 and 8 were used. The truncation error thresholds were set to $\epsilon = 0.001$ and $\epsilon_X = 0.01$. In addition flagging of density contrasts above 0.1 was employed. The obtained solution does not differ from a corresponding single grid model computed using 30 720 equidistant zones and demonstrates that with a cautious use of the AMR technique it is possible to obtain physically correct results. Moreover, the speedup achieved in calculating the first 6.4×10^{-2} s of evolution as compared to the single grid run amounted to a factor of 8.4 on a single node of an IBM SP2. We note here that there is some overhead associated with AMR because the source terms have to be computed also in the error estimation procedures. This is especially important during this early phase, when

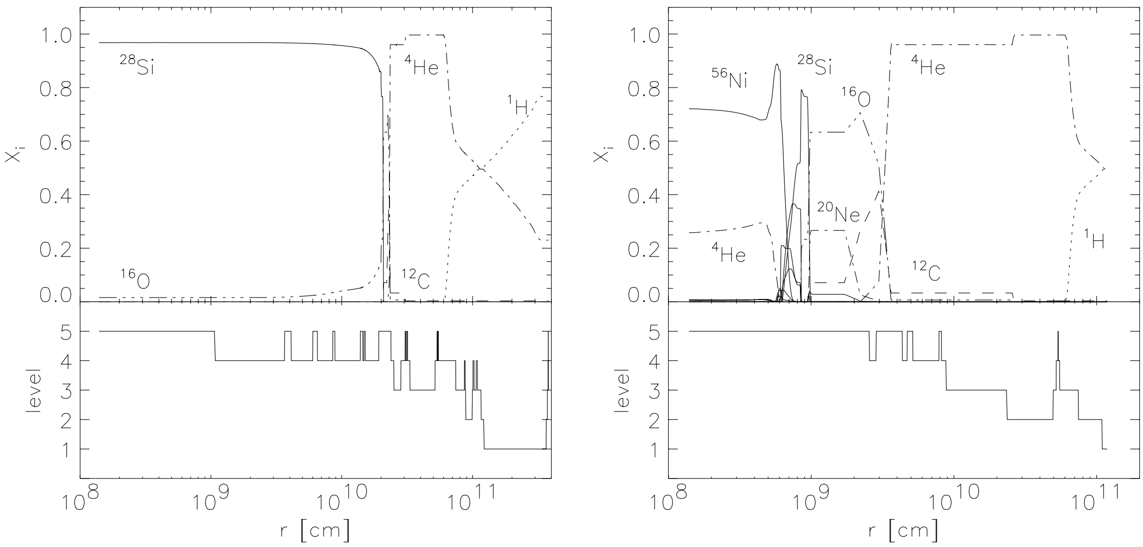

Figure 4: Left: Same as Fig. 2 but with $\epsilon = 10^{-3}$ and $\epsilon_X = 10^{-2}$. All errors have disappeared. Note the changes in the distribution of grid patches. The larger number of level 4 and level 5 patches resulted in an increase in CPU-time of about a factor of 5 and 3.6 as compared to the first and second case shown in Fig. 2, respectively. Right: Chemical composition at $t = 0.5\,\mathrm{s}$ for our run including nuclear burning (see text). At this time nearly all nuclear reactions have frozen out. Nucleosynthesis has taken place mainly in the former silicon shell. The entropy in the innermost zones was sufficiently high to synthesize ^{56}Ni and produce an α-rich freeze-out (cf. [21]). Following these layers incomplete silicon burning has led to a zone dominated by ^{32}S, ^{36}Ar, and ^{40}Ca. The C/O-core of the star is almost completely covered with the finest resolution ($\Delta r \approx 39\,\mathrm{km}$). Abrupt changes in composition in this region are a consequence of coarse zoning in the initial model. Note that, in contrast to the other runs, the entire grid extends up to $1.2 \times 10^6\,\mathrm{km}$ in this case.

the solution of the nuclear network dominates the computational time. But since cooling due to the strong expansion leads to a rapid freezeout of nuclear reactions, we may expect AMR to offer even larger savings in CPU time during the late evolutionary phases. We were not able to continue this comparison further in time, however, as the computational cost for the single grid run turned out to be prohibitively high.

In the future, we plan to use AMRA to study the problem of nucleosynthesis and mixing in two dimensions starting shortly after shock stagnation, when shock revival due to neutrino heating and convective motion begins, through the stage where the aspherical shock overruns the Si and O shells leading to an aspherical distribution of newly synthesized nuclei, up to the development of the Rayleigh-Taylor instability. Current multidimensional simulations of the delayed explosion mechanism (cf. [13], [4], [14]) indicate that explosive burning will partly proceed for electron fractions well below $Y_e \approx 0.5$ and thus results in neutron rich isotopes. In order to avoid a contamination of the interstellar medium with the wrong nucleosynthetic products, fallback of this material onto the central remnant in the late stages of the explosion was suggested. Therefore, another goal of such computations is to determine the actual location of the mass cut and to provide the link needed to test the current ideas behind the delayed explosion mechanism by confronting the ejected nucleosynthesis products with observations.

Acknowledgements

We are very grateful to Stanford Woosley for providing us with various progenitor models which we have used to construct our initial data. The work of TP was partly supported by the grant KBN 2.P03D.004.13 from the Polish Committee for Scientific Research. The simulations were performed on the IBM SP2-P2SC and CRAY J916/16512 located at the Rechenzentrum Garching.

References

[1] W.D. Arnett, J.N. Bahcall, R.P. Kirshner, S.E. Woosley, Ann. Rev. Astron. Astrophys. **27** (1989) 341.

[2] M. Berger and J. Oliger, J. Comp. Phys. **53** (1984) 484.

[3] M. Berger and P. Colella, J. Comp. Phys. **82** (1989) 64.

[4] A. Burrows, J. Hayes, B.A. Fryxell, ApJ **450** (1995) 830.

[5] R. Cid-Fernandes, T. Plewa, M. Różyczka, J. Franco, R. Terlevich, G. Tenorio-Tagle, W. Miller, MNRAS **283** (1996) 419.

[6] S.W.J. Colgan, M.R. Haas, E.F. Erickson, S.D. Lord, D.J. Hollenbach, ApJ **427** (1994) 874.

[7] T. Dotani et al., Nature **330** (1987) 230.

[8] B.A. Fryxell, E. Müller, W.D. Arnett, ApJ **367** (1991) 619.

[9] M.R. Haas, S.W.J. Colgan, E.F. Erickson, S.D. Lord, M.G. Burton, D.J. Hollenbach, ApJ **360** (1990) 257.

[10] M. Herant and W. Benz, ApJ **370** (1991) L81.

[11] M. Herant and W. Benz, ApJ **387** (1992) 294.

[12] M. Herant, W. Benz, S. Colgate, ApJ **395** (1992) 642.

[13] M. Herant, W. Benz, W.R. Hix, C.L. Fryer, S. Colgate, ApJ **435** (1994) 339.

[14] H.-Th. Janka and E. Müller, A&A **306** (1996) 167.

[15] S.M. Matz, G.H. Share, M.D. Leising, E.L. Chupp, W.T. Vestrand, W.R. Purcell, M.S. Strickman, C. Reppin, Nature **331** (1988) 416.

[16] E. Müller, A&A **162** (1986) 103.

[17] E. Müller, B.A. Fryxell, W.D. Arnett, A&A **251** (1991) 505.

[18] S. Nagataki, T.M. Shimizu, K. Sato, ApJ **495** (1998) 413.

[19] H. Nussbaumer and R. Walder, A&A **278** (1993) 209.

[20] T. Plewa and E. Müller, in preparation.

[21] F.-K. Thielemann, K. Nomoto, M. Hashimoto, ApJ **460** (1996) 408.

[22] S.E. Woosley, ApJ **330** (1988) 218.

[23] S.E. Woosley, P.A. Pinto, L. Ensman, ApJ **324** (1988) 466.

Stability of Rotating Supermassive Stars in the Presence of Dark Matter

G.S. Bisnovatyi-Kogan[1]

[1] *IKI RAN, Email: gkogan@mx.iki.rssi.ru*

Abstract

Stability of rotating supermassive stars in a hot dark matter background is investigated by an approximate energetic method. Dynamical stages are calculated in similar way, giving a range of exploding stellar masses, which could enrich the intergalactic gas by heavy elements before epoch of a galaxy formation.

1.1 Introduction

Observations show, that at red shifts as large as $z \sim 5$, where distant quasars are observed, the concentration of heavy elements Z (starting from ^{12}C) is not so different from the solar one, and may be much larger, than in some old stars in our Galaxy. Even more impressive is a high concentration of heavy elements in the intergalactic gas of rich galactic clusters, where X-ray Fe lines are observed. The formation of elements in quasars may be connected with dense stellar clusters, giving origin to the supermassive black holes, and at the same time responsible for production of elements. It is, nevertheless, rather striking, that different quasars has a similar composition, if the element production had a local origin. It is rather difficult to imagine a local element production in the intergalactic gas, where similarity between different clusters also takes place. There are different models of the element origin in the intergalactic gas. They could be produced in galaxies, and expelled afterwards outside. It is not easy to perform, because in opposite, inflow of the gas is observed in the form of a "cooling flow". Another models are connected with a very early origin of the heavy elements, before the galaxies themselfs.

The model with large isothermal primordial perturbations is considered for a long time, to give an early birth of objects with a mass $\sim 10^6 M_\odot$, close to the mass of globular clusters. Formation of massive stars in such globular clusters could give origin of heavy elements, and less massive stars could survive from an early epoch with a very small Z concentration. Globular clusters could collect in larger complexes, and stars from their evaporation formed galactic bulges and spherical components. If star formation does not take place in these objects, they form a one supermassive star, which evolution leads to loss of stability, collapse, and possible explosion. Such explosions happening at a pregalactic epoch, could also be responsible for an early Z formation.

1.2 Supermassive stars with a hot dark matter

For $M > 10^4 M_\odot$ the main reason of instability are GR effects. The entropy of such supermassive stars in critical state is so large that the pressure is determined mainly by the radiation with a small admixture of plasma, important for stability, but giving a very short time until the onset of instability. A common way to overcome this instability is to consider rotating superstars, what may postpone the moment of collapse to 3×10^4 years for solid body rotation with angular momentum and mass losses (Bisnovatyi-Kogan, Zeldovich and Novikov, 1967), and much longer for a differentially rotating star evolving with almost constant angular momentum (Fowler, 1966; Bisnovatyi-Kogan and Ruzmaikin, 1973). Formation of supermassive stars on early stages of the Universe expansion, their loss of stability with subsequent collapse or explosion (Bisnovatyi-Kogan, 1968; Fricke, 1973; Fuller et al, 1986) could be important not only for early formation of heavy elements, but also for creation of perturbations for large scale structure formation, influence on small scale fluctuations of microwave background radiation (Peebles, 1987; Cen et al, 1993). A necessity of a presence of a dark matter in modern cosmological models makes it important to include it into stability analysis of supermassive stars. This was done by McLaughlin and Fuller (1996), who dealed with nonrotating superstars. The same problem for rotating superstars, using energetic method, was solved by Bisnovatyi-Kogan (1998). The rotational effects occure to be more important for realistic choice of parameters.

1.2.1 Stability analysis

In supermassive stars with equation of state $P = P_r + P_g = \frac{aT^4}{3} + \rho \mathcal{R} T$ there is $P_r \gg P_g$ due to high entropy of such stars. Besides, such stars are fully convective and entropy is uniform over them, so the spatial structure is well described by a polytropic distribution, corresponding to $\gamma = 4/3$. The influence of a hot dark matter, which density does not change during perturbations, should be taken by account of a newtonian gravitational energy of the star in the dark matter potential, because GR effects of a dark matter are of a higher order of magnitude (McLaughlin, Fuller, 1996). For radiation dominated plasma there is a following expression for the adiabatic index, determining the stability to a collapse

$$\gamma = \left(\frac{\partial \log P}{\partial \log \rho}\right)_S \approx \frac{4}{3}\left(1 + \frac{\mathcal{R}}{2S}\right) = \frac{4}{3} + \frac{\beta}{6}, \tag{1}$$

where $\beta = \frac{P_g}{P} = \frac{4\mathcal{R}}{S}$. In the radiationaly dominated supermassive star there is a unique connection between its mass M and entropy per unit mass S (Zeldovich and Novikov, 1965)

$$M = 4.44 \left(\frac{a}{3G}\right)^{3/2} \left(\frac{3S}{4a}\right)^2, \tag{2}$$

where a is a constant of the radiation energy density, and numerical coefficient is related to the polytropic density distribution with $\gamma = 4/3$. At the point of a loss of stability the critical value of an average adiabatic index $< \gamma >$ in selfgravitating nonrotating star with account of post-newtonian corrections is determined by a relation (Zeldovich and Novikov, 1965)

$$< \gamma >_{crs} = \frac{4}{3} + \delta_{GR} = \frac{4}{3} + \frac{2}{3}\frac{\varepsilon_{GR}}{\varepsilon_G} \approx \frac{4}{3} + 0.99\frac{GM^{2/3}\rho_c^{1/3}}{c^2}. \tag{3}$$

Here averaging is done over a volume, with a pressure as a weight function . ¿From comparison between (1) and (3) we get a well known relation for a critical central density of a supermassive star stabilized by plasma

$$\rho_c = 0.10\frac{\mathcal{R}^3 c^6}{G^{21/4}a^{3/4}}M^{-7/2} \approx 1.8 \times 10^{18}\left(\frac{M_\odot}{M}\right)^{7/2} \text{g/cm}^3. \tag{4}$$

Here and below we consider for simplicity a pure hydrogen plasma. Newtonian energy of a superstar ε_{nd} in the gravitational field of uniformly distributed dark matter with a density ρ_d is written as

$$\varepsilon_{nd} = \int_0^M \varphi_d dm. \tag{5}$$

The gravitational potential of a uniform dark matter φ_d is written as

$$\varphi_d = \frac{2\pi}{3}G\rho_d r^2 - \frac{3}{2}\frac{GM_d}{R_d}, \tag{6}$$

where R_d is much larger then stellar radius R, and M_d is a total mass of the dark matter halo. Stability does not depend on normalization of the gravitational potential so we shall omit the constant value in (5). It follows from (5) and (6) that during variations $\varepsilon_{nd} \sim \rho_c^{-2/3}$, while $\varepsilon_{GR} \sim \rho_c^{2/3}$ and $\varepsilon_G \sim \rho_c^{1/3}$ (Zeldovich and Novikov, 1965). For nonrotating superstar in presence of a dark matter the critical value of an average adiabatic index $< \gamma >_{crnrot}$ is determined by

$$< \gamma >_{crnrot} = < \gamma >_{crs} + \delta_{dm} = \frac{4}{3} + \frac{2}{3}\frac{\varepsilon_{GR}}{\varepsilon_G} - 2\frac{\varepsilon_{nd}}{|\varepsilon_G|}. \tag{7}$$

The relation for a critical density in presence of a dark matter is obtained by comparison of (1) and (7), giving

$$2.8 \times 10^{-3}\left(\frac{M}{M_6}\right)^{2/3}\rho_c^{4/3} = 3.5 \times 10^{-4}\left(\frac{M_6}{M}\right)^{1/2}\rho_c + \rho_d. \tag{8}$$

Solution of (8) is presented in Fig.1.

1.2.2 Stability of rotating stars

Consider a rigid rotation, when its energy is a small correction to the energy of radiation and the energetic method is a good approach. When losses of an angular momentum during evolution are negligible we distinguish between rapidly rotating (RR) and slowly rotating (SR) superstars. In RR case a superstar reaches the state of rotational equatorial

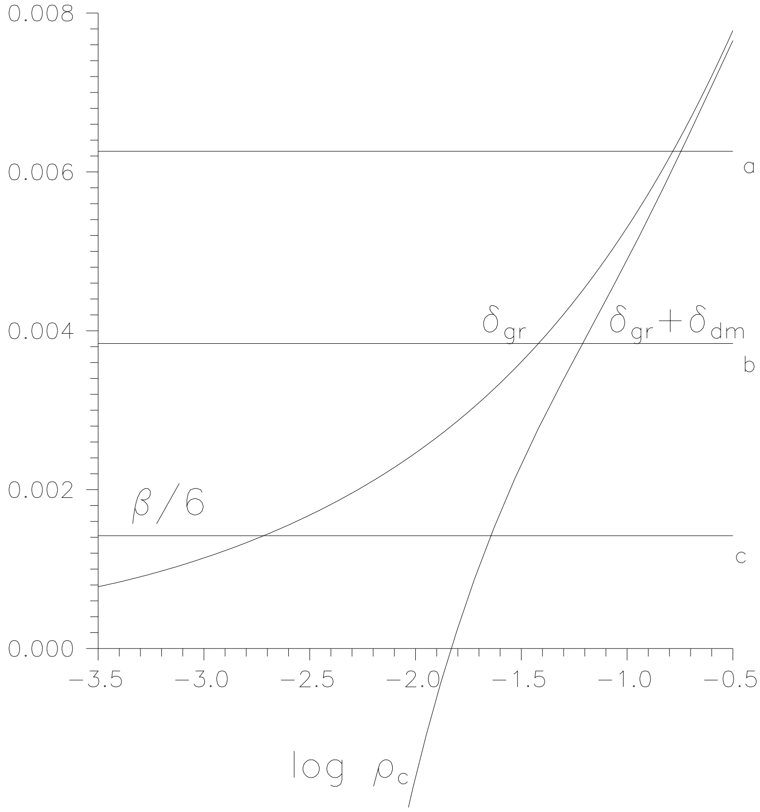

Figure 1: The correction terms δ_{GR} and $\delta_{dm} + \delta_{GR}$, the quantities $\beta/6$ (line c), $\beta/6+(\varepsilon_{rot}/\varepsilon_N)_{sh}/3$ (line b), and $2\beta/6+$ $(\varepsilon_{rot}/\varepsilon_N)_{sh}/3$ (line a), as functions of the central density of a supermassive star with $M = 10^6 M_\odot$, and dark matter density of 10^{-5} g/cm^3. The instability points for nonrotating star occure at intersection of the correction term curves with the line c. Mass shedding in the stable star with angular momentum J_0 (see text) occures at intersection of correction term curves with the line b, and critical point on the mass-shedding curve is determined by a corresponding intersection with the line a.

breaking before loosing its dynamical instability, and in SR case instability comes first. If a superstar has an angular momentum J, then its rotational energy $\varepsilon_{rot} \approx 1.25 J^2 \rho_c^{2/3} M^{-5/3}$, and a ratio $\varepsilon_{rot}/\varepsilon_{GR}$ remains constant during evolution. In presence of rotation and dark matter the critical value of the adiabatic index $< \gamma >_{crrot}$ is written as

$$< \gamma >_{crrot} = \frac{4}{3} + \frac{2}{3}\frac{|\varepsilon_{GR}| - \varepsilon_{rot}}{|\varepsilon_G|} - 2\frac{\varepsilon_{nd}}{|\varepsilon_G|}, \tag{9}$$

and the relations for determination of a critical central density, instead of (8), is written as

$$2.8 \times 10^{-3} \left(\frac{M}{M_6}\right)^{2/3} \rho_c^{4/3} \left(1 - \frac{\varepsilon_{rot}}{|\varepsilon_{GR}|}\right) = 3.5 \times 10^{-4} \left(\frac{M_6}{M}\right)^{1/2} \rho_c + \rho_d. \tag{10}$$

As follows from (10), a superstar does dot loose its stability when $\varepsilon_{rot} > |\varepsilon_{GR}|$. This qualitative result, obtained in the post-newtonian approximation, remains to be valid in a strong gravitational field and reflects a presence of a limiting specific angular momentum $a_{lim} = GM/c$, so that a black holes with a Kerr metric may exist only at $a < a_{lim}$ (Misner, Thorne, Wheeler, 1973).

A RR superstar in a course of the evolution reaches instead a limit of a rotational instability, and equatorial mass shedding begins, leading to a loss of an angular momentum. Such star will loose the stability when the anuglar momentum will become less then the limiting value. The stage of a mass loss was examined by (Bisnovatyi-Kogan, Zeldovich, Novikov, 1967), where it was shown that this stage may last about 10 times longer, then a maximum evolution time to approach the rotational instability point. RR star reaches the stage of a rotational instability at different central densities, depending on J, but the ratio of rotatonal and Newtonan gravitational energy on the mass-shedding curve is constant (Bisnovatyi-Kogan, Zeldovich, Novikov, 1967), neglecting the dark matter gravity,

$$\varepsilon_{rot} = 0.00725|\varepsilon_G|. \tag{11}$$

The energy of a rotating supertar in equilibrium in presence of a hot dark matter may be written as

$$\varepsilon_{eq} = -\varepsilon_{gas} + |\varepsilon_{GR}| - \varepsilon_{rot} + 3\varepsilon_{nd}. \tag{12}$$

In the main term for a superstar in equilibrium a relation is valid

$$\varepsilon_{gas} = \frac{\beta}{2}|\varepsilon_G|. \tag{13}$$

Taking into account (11), (13), we get an expression for an equilibrium energy along the mass-shedding curve (with variable J)

$$\varepsilon_{eq} = -\left(0.00725 + \frac{\beta}{2}\right)|\varepsilon_G| + |\varepsilon_{GR}| + 3\varepsilon_{nd}. \tag{14}$$

The curve $\varepsilon_{eq}(\rho_c)$ has a minimum at the central density, determined by a relation

$$2.8 \times 10^{-3}\left(\frac{M}{M_6}\right)^{2/3}\rho_c^{4/3} = 3.5 \times 10^{-4}\left(\frac{M_6}{M}\right)^{1/2}\rho_c + 5.9 \times 10^{-4}\rho_c + \rho_d. \tag{15}$$

¿From comparison (15) and (10) with account of (11) it is clear, that dynamical instability cannot occure in the minimum of the mass-shedding curve, and after crossing it the evolution proceeds with a substantial mass and angular momentum losses. Central density of the superstar in the minimum of the mass- shedding curve (14) with and without dark matter are represented in the Fig.1. Parameters of a superstar, at which its critical state is situated on the mass-shedding curve satisfy sumultanously the relations (10) and (11). That leads to the equation for determination of a central density

$$2.8 \times 10^{-3}\left(\frac{M}{M_6}\right)^{2/3}\rho_c^{4/3} = 3.5 \times 10^{-4}\left(\frac{M_6}{M}\right)^{1/2}\rho_c + 12 \times 10^{-4}\rho_c + \rho_d. \tag{16}$$

The relation (11) is used for determination of an angular momentum of the superstar $J = J_0$ with ρ_c from (15) and $J = J_1 < J_0$ with ρ_c from (16). Solution of this equation is also given in Fig.1 which shows that stabilizing effect of rotation on the mass-shedding curve at $J = J_1$ is more important, then stabilization by a hot dark matter.

1.3 Collapse and explosions of supermassive stars

To study dynamical processes by the energetic method we use, instead of the energy variation, the energy conservation law in the form

$$d(\varepsilon_{in} + \varepsilon_G + \varepsilon_{GR} + \varepsilon_k) = \int_0^M dQdm = dS\int_0^M Tdm. \tag{17}$$

Here $\varepsilon_k = \frac{1}{2}\int_0^M v^2 dm$ is the kinetic energy of the superstar. Using thermodynamic relation we get

$$d\varepsilon_{in} = d\int_0^M E(\rho, S)dm = d\rho_c \int_0^M \frac{P}{\rho^2}\frac{d\rho}{d\rho_c}\,dm + dS\int_0^M Tdm. \tag{18}$$

From the mass conservation law, in presence of homologycal motion with the fixed density distribution in space, we obtain a space velocity distribution in the form $v = v_R\frac{r}{R}$, and get a dynamical equation (Bisnovatyi-Kogan, 1968)

$$0.597\frac{d^2(\rho_c^{-1/3})}{dt^2} + 0.639\,G\rho_c^{2/3} + 1.84\,\frac{G^2M^{2/3}}{c^2}\,\rho_c - 3M^{-2/3}\rho_c^{-2/3}\int_0^1 P\frac{d\nu}{\varphi(\nu)} = 0. \tag{19}$$

The equation determining entropy changes is averaged over the star with a weight function ($T^4 \sim E\rho$) for radiation dominated superstar, which entropy is taken homogenous

$$\frac{dS}{dt}\int_0^1 \rho T^5 d\nu = < T^4Q_n > - < T^4Q_\nu > - < T^4Q_r > . \tag{20}$$

Nuclear reactions Q_n of pp and CNO hydrogen burning and 3α helium burning have been included in the calculations of Bisnovatyi-Kogan (1968), as well an neutrino Q_ν, and photon losses Q_r which are nonimportant. The equations (19),(20), together with equations for averaged composition of hydrogen X, helium Y, and equation of state with proper thermodynamics had been solved numerically. Primodial chemical composition with only hydrogen and helium was taken as initial condition. In the process of contraction after a loss of stability, 3α reaction produces ^{12}C, which initiates a CNO hydrogen burning, pp reaction remaining always unimportant. It was obtained that in stars with $M < 1.5\times 10^5 M_\odot$ collapse is reversed, and they explode, enriching the intergalactic and interstellar gas with heavy elements. Such explosions could happen on stages, preceding the epoch of a galaxy formation. Similar calculations made for rotating superstars, and for normal (solar) composition shift the boundary between collapsing and exploding superstars to higher masses (Fricke,1973).

1.4 Formulation of Galerkin method

The Galerkin method allows to find an approximate solution of differential equations. In this method the solution of the partial or ordinary differential equation is reduced to ordinary, or algebraic equation, respectively (Fletcher, 1984). In post-newtonian approximation the density in Galerkin method is written as

$$\rho = \sum_{i=1}^{N} \alpha_i(t)\varphi_i(a) \qquad , \qquad \text{where} \qquad \rho_c = \sum_{i}^{N} \alpha_i(t)\varphi(0) \tag{21}$$

For a function $\varphi_0(a)$ it is convenient to take corresponding Emden profile for one of polytropic indices. For other functions we may choose $\varphi_k = \cos\frac{1+2k}{2}\pi a$. Then satisfaction of the boundary conditions $\varphi_i(A) = 0, \quad A = a(R); \qquad \varphi_i(0) = 1$ will be provided. The minimization of the energy functional for finding an equilibrium model is reduced to zero partial derivatives

$$\frac{\partial \varepsilon}{\partial \alpha_i} = 0, \tag{22}$$

leading in the static case of constant α_i to a set of N algebraic equations for finding equilibrium α_i^{eq}. Stability of a model is found from an evaluation of the second variation $\delta^2\varepsilon$. In the Galerkin method with several scaling functions $\varphi_i(a)$, the second variation $\delta^2\varepsilon$ is represented by a quadratic form

$$\delta^2\varepsilon = \sum_{i,k}^{N} \frac{\partial^2 \varepsilon}{\partial \alpha_i \partial \alpha_k}\delta\alpha_i\delta\alpha_k, \tag{23}$$

The stability is related to positive definiteness of the quadratic form (23), what is provided (Smirnov, 1958) by the positiveness of the determinant

$$\|\frac{\partial^2 \varepsilon}{\partial \alpha_i \partial \alpha_k}\| > 0, \tag{24}$$

and all its main minors. For two functions in (21) the positiveness of the determinant (24), and two partial derivatives $\partial^2\varepsilon/\partial\alpha_1^2 > 0$ and $\partial^2\varepsilon/\partial\alpha_2^2 > 0$ are enough for stellar stability. Loss of stability happens close before the point where the determinant, or one of its main minors becomes zero.

In approximate presentation of the trial function in the Galerkin method, the minimal value of the second energy variation is larger, then its value for a real trial function. So zero values of the determinant (24), or one of its main minors, guarantees the onset of instability. Their positiveness is not an exact guarantee of the stability, but comparison of the energetic method with an exact stability analysis shows a good presicion of this approximate approach in most realistic cases. Energetic method corresponds to a homologeous trial function for displacement $\delta r \sim r$. In the Galerkin method the trial function may be determined with a better precision. In fact, the coefficients $\delta\alpha_i$ for the trial function of a density

$$\delta\rho = \sum_i^N \delta\alpha_i \varphi_i(a) \tag{25}$$

are determined as an eigenvector of a set of uniform linear equations

$$\frac{\partial^2 \varepsilon}{\partial\alpha_i \partial\alpha_k}\delta\alpha_k = \lambda_p \delta\alpha_i. \tag{26}$$

The eigenvector $\delta\alpha_i^e$ is used for obtaining an approximate eigenfunction (25), and eigenvalues λ_p are related to the square eigenfrequencies of the stellar model. The positive definiteness of the quadratic form (23) coincides with the positiveness of all eigenvalues λ_p. Galerkin method for solving dynamical problems in GR was concidered by Bisnovatyi-Kogan and Dorodnitsyn (1998).

Acknowledgements

This work was partly supported by Russian Basic Research Foundation grant No. 96-02-16553 and grant of a Ministry of Science and Technology 1.2.6.5. G.S.B.-K. is grateful to MPA for support to attend this workshop.

References

[1] Bisnovatyi - Kogan G.S.,1968, Azh, **45**, 74

[2] Bisnovatyi - Kogan G.S.,1998, ApJ, **497**, 20 April

[3] Bisnovatyi-Kogan,G.S., Dorodnitsyn A.V., 1998, Gravitation and Cosmology (in press)

[4] Bisnovatyi-Kogan,G.S., Ruzmaikin, A.A., 1973, Astron. Ap., **27**, 209

[5] Bisnovatyi-Kogan,G.S., Zel'dovich,Ya.B., Novikov,I.D. 1967, Astron. Zh. **44** 525

[6] Cen,R., Ostriker,J., Peebles,P.J.E. 1993, ApJ, **415**, 423

[7] Fletcher C.A.J., 1984, Computational Galerkin methods, Springer-Verlag, New York Berlin Heidelberg Tokyo

[8] Fowler,W. 1966, ApJ. **144**, 191

[9] Fuller,G.M., Woosley,S.E., Weaver,T.A. 1986, ApJ, **307**, 675

[10] Fricke,K. 1973, ApJ, **183**, 941

[11] McLaughlin,G., Fuller,G. 1996, ApJ, **456**, 71

[12] Misner Ch.W., Thorne K.S., Wheeler J.A. 1973. Gravitation. W.H.Freeman and Co. San Fransisco.

[13] Peebles,P.J.E. 1987, ApJ, **313**, L73

[14] Smirnov V.I. (1958), Kurs Vysshey Matematiki, vol. 3, part 1. Fizmatgiz, Moscow.

[15] Zel'dovich,Ya.B., Novikov,I.D. (1965), Uspekhi Fiz. Nauk **86** 447

AGB: Evolution and Nucleosynthesis

O. Straniero[1], *A. Chieffi*[2], *M. Limongi*[3]

[1] *Osservatorio Astronomico di Collurania, Teramo, Italy*
[2] *Istituto di Astrofisica Spaziale CNR, Roma, Italy*
[3] *Osservatorio Astronomico di Monteporzio, Monteporzio,Italy*

Abstract

New models of thermally pulsing asymptotic giant branch (AGB) stars of low and intermediate mass ($1 \leq M/M_{\odot} \leq 7$) are presented for a solar chemical composition (namely, Z=0.02 and Y=0.28). The full set of the evolutionary sequences includes more than 300 thermal pulses and it is based on about 2 millions of stellar models. Our main findings are reported.

1.1 Low mass stars: $1 \leq M/M_{\odot} \leq 3$

As it is well known the third dredge-up (TDU) is responsible for the formation of Carbon stars during the AGB phase (see e.g. [1]). The observed luminosity functions of AGB stars in our galaxy and those of the Magellanic Clouds clearly indicate that the C-stars are low mass stars. However, many theoretical investigations of pop I AGB succeeded in finding an envelope enrichment of ^{12}C only if the initial mass is larger then 3-4 $M_{\odot}$ ([2],[3]), unless some kind of extra mixing, whose physics is not well understood, is assumed. In our models, the third dredge-up (TDU) operates self-consistently (i.e. without invoking any extra mixing) for stellar masses as low as 1.5 $M_{\odot}$ ([4]). The amount of C-rich material dredged to the surface by the TDU depends on the mass of the H-exhausted core (M_H) and on the envelope mass (M_E). The minimum core mass for which the TDU occurs is about 0.61 $M_{\odot}$ almost independently of the total mass. Thus the TDU firstly increases, as the core mass increases, and then, owing to the mass loss, it decreases as the envelope mass decreases. When the envelope mass is reduced below approximately 0.5 $M_{\odot}$, the TDU eventually vanishes.

According to previous findings, a linear correlation between the 3α luminosity peek and M_H is obtained before the onset of the TDU phase (see e.g. [2]). However, when the TDU is settled on, the strength of the pulse rapidly increases as the penetration of the convective envelope into the H-exhausted core increases (see figure 1). NO ASYMPTOTIC LIMIT IS FOUND. Thus, unless an extreme mass loss is assumed to be at work from the beginning of the TP-AGB phase ($> 10^6 M_{\odot}/yr$), a C-star is obtained after about 15 TDU episodes, for initial masses $M \geq 1.5 M_{\odot}$. At that time the core mass is about 0.7 $M_{\odot}$ and the luminosity is of the order of $10^4 L_{\odot}$.

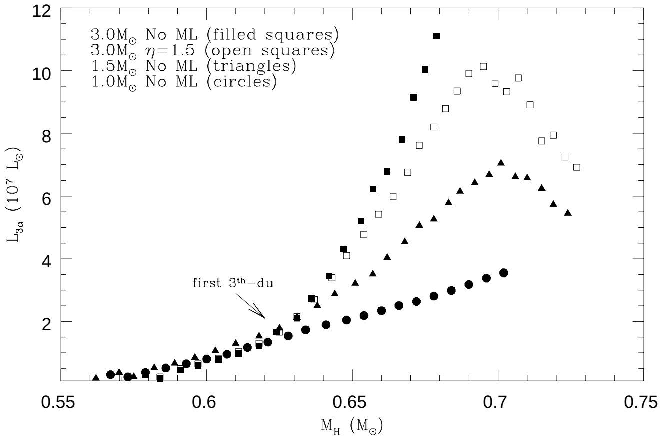

Figure 1: The 3α luminosity peek versus the H-exausted core mass for various TP-AGB evolutionary sequences

1.2 Nucleosynthesis in low mass AGB stars

Evidences of s-process enrichment are found in AGB stars (see e.g. [5]). Many S and MS giants show unstable isotopes (as, for example, ^{99}Tc) which demonstrate that neutron capture episodes are ongoing processes in these stars. For many years the $^{22}Ne(\alpha,n)^{25}Mg$ reaction was considered the most promising source of neutrons for the s-process nucleosynthesis in AGB stars. However, if a certain amount of ^{13}C is synthesized in the He-rich region, an alternative neutron source is provided by the $^{13}C(\alpha,n)^{16}O$ reaction. [1] [6] suggested that such a ^{13}C pocket forms during the post flash, when the H-burning shell is still off and the convective envelope can penetrate it; at that time some protons might diffuse from the H-rich envelope down to the He(and ^{12}C)-rich region, then producing ^{13}C via proton captures on ^{12}C. Thus, following the scenario sketched by these authors, it is commonly assumed that such a ^{13}C pocket is ingested during the subsequent convective pulse, then releasing neutrons suitable for the s-process nucleosynthesis (see e.g. [7]). However, it has been recently found that the typical neutron density, as inferred from Rb measurements in AGB stars, is generally lower than the predictions of the s-nucleosynthesis induced by both the $^{22}Ne(\alpha,n)^{25}Mg$ and the $^{13}C(\alpha,n)^{16}O$ neutron sources operating during the convective pulse (see [8] and [9]).

In the present models for low mass stars, the temperature at the bottom of the convective shell, during a thermal pulse, never exceeds 3×10^8 K, so that the $^{22}Ne(\alpha,n)^{25}Mg$ is only marginally activated. On the contrary, we found that during the interpulse the temperature at the level of the ^{13}C pocket grows enough to activate the $^{13}C(\alpha,n)^{16}O$ reaction ($T\sim10^8$ K), so that the s-process nucleosynthesis occurs well before the onset of the subsequent convective pulse in a radiative environment. In fact, the ^{13}C is fully burned before the end of the interpulse. In such a case the typical neutron density is of the order of 10^7 neutrons/cm^3, which is in very good agreement with the observed Rb abundance in AGB stars ([9]). In figure 2 we show the best fit to the solar system s-process main component, as derived from our models ([10], [4]; [11]). Note that filled diamonds refer to s-only nuclei, open squares to nuclei with an s-process contribution in excess of 80%, open rhombs to nuclei with an s-process contribution between 60% and 80%, and small crosses to all the others.

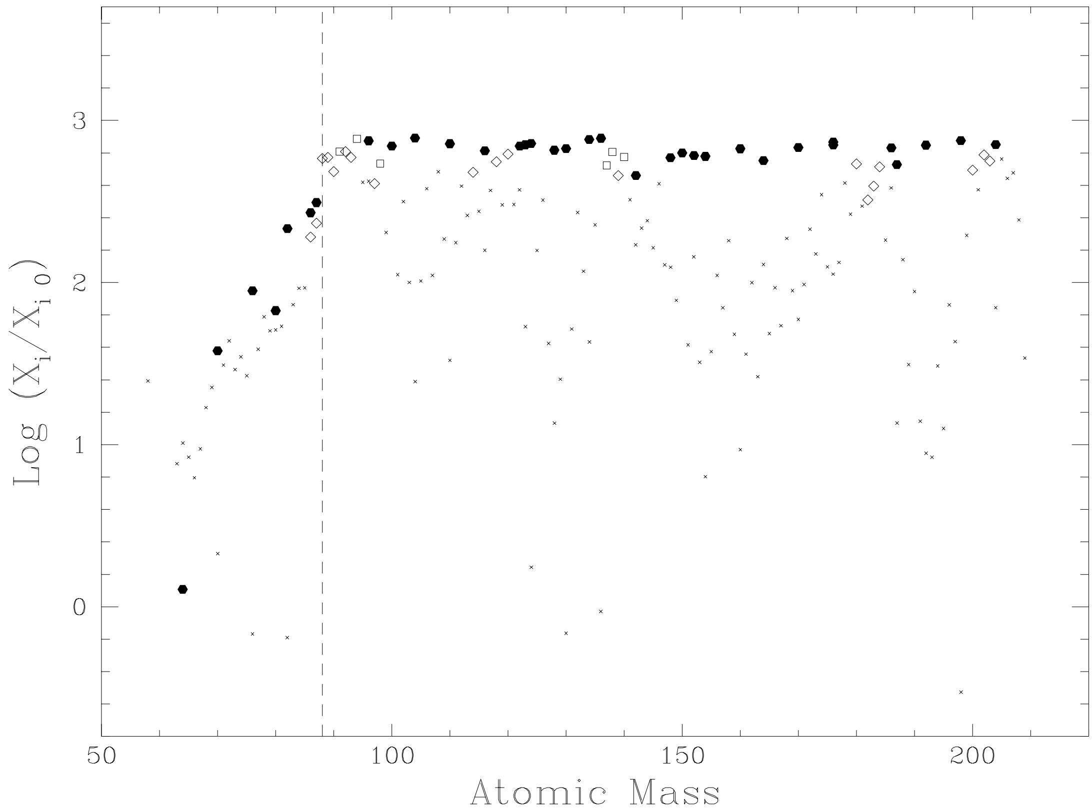

Figure 2: The best fit to the solar s-process main component as derived in the case of the 3 $M_\odot$

1.3 Intermediate Mass Stars

Bright AGB stars are characterized by a strong mass loss (up to 10^4 $M_\odot$/yr), so that they might be obscured by the ejected material. For this reason, before the most recent satellite infrared mission (IRAS), their luminosity function was poorly known. Now it has been understood that the AGB tip is located at approximately $M_{bol} = -7m$ (see [13]). However it is rather surprising that such a limit coincides with the AGB tip predicted by the famous core mass-luminosity relation ([12]) when a core mass of 1.4 $M_\odot$ (i.e. the Chandrasekhar mass) is attained. In fact it has been early recognized that an hot bottom burning occurs at the base of the convective envelope during the interpulse of an intermediate mass stars ([14]). As a consequence of the surplus of nuclear energy released by the H-burning shell, a breakdown of the core mass-luminosity relation is expected. Such a breakdown was recently found in stellar models computation by various authors ([15] [16]). They found that the luminosity of a 7 $M_\odot$ TP-AGB stars rapidly exceeds the classical limit, in contrast with the observed AGB tip ([13]). Our models removes such a controversy. In the following we summarized our main findings:

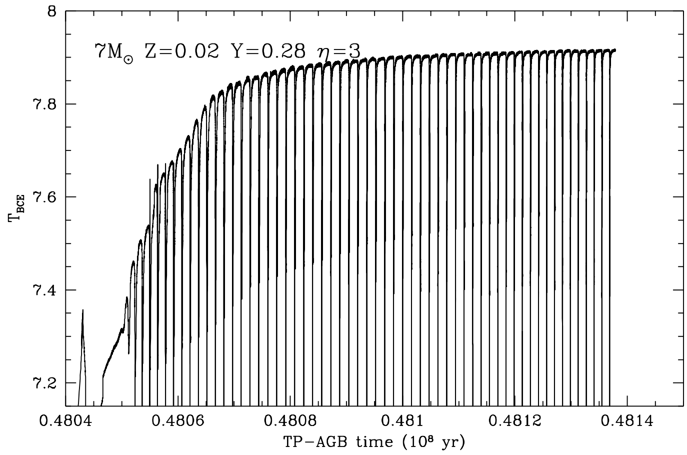

Figure 3: The evolution of the temperature of the inner boundery of the convective envelope in the case of the 7 $M_{\odot}$

1) A significant hot bottom burning was found in the 7 $M_{\odot}$. The typical temperatures at the base of the convective envelope (T_{BCE}) is 8$\times$10^7 K. On the contrary, in the 5 $M_{\odot}$ this temperature never exceed 3$\times$10^7 K. In figure 3 we show the evolution of T_{BCE} in the 7 $M_{\odot}$ sequence.

2) The stronger the hot bottom burning the smaller the amount of matter brought to the surface by the third dredge-up. For this reason, and because the ^{12}C is converted in ^{14}N during the interpulse, stars with $M > 4M_{\odot}$ never become C-stars. This is in agreement with the observed luminosity functions of C-stars in the Milky Way and in the Magellanic Clouds. As for the low mass stars, the reduced efficiency of TDU is correlated with a minor intensity of the pulse strength.

3) As a consequence of the hot bottom burning, a significant deviation from the classical core mass-luminosity relation is found for those stars having a mass close to the limit for the Carbon ignition in the core ($M_{up} \sim 7 - 8M_{\odot}$). In figure 4 we report the maximum interpulse luminosity of our models of 7 $M_{\odot}$ (squares). They are compared to the classical core mass-luminosity relations ([12], dashed line; [17], solid line). The observed AGB tip is also reported (heavy solid line). Note that the luminosity of our 7 $M_{\odot}$ sequence of models clearly deviates from the classical relations, but, at variance with previous claims, the expected final luminosity, is very close to, and never exceeds, the observed AGB tip. Note, in addition, that this tip luminosity accidentally coincides with the one predicted by the Paczynski relation when the core mass is equal to 1.4 $M_{\odot}$. In fact, in our 7 $M_{\odot}$ model the final core mass is just 1.05 $M_{\odot}$.

1.4 Nucleosynthesis in intermediate mass AGB stars

We report here just the preliminary results of our investigation of the s-process nucleosynthesis in intermediate mass stars. This is a project in collaboration with the Torino

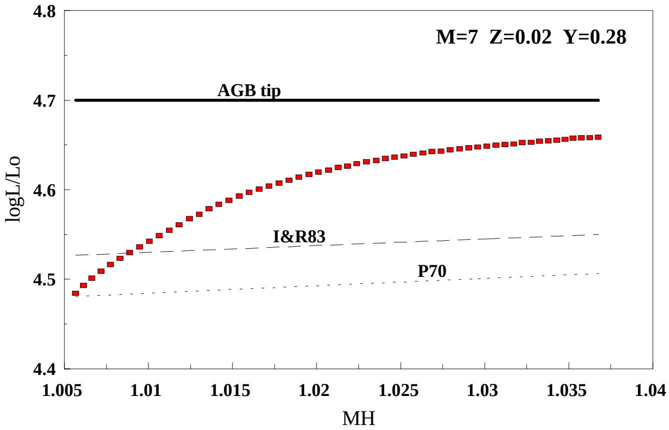

Figure 4: Maximum interpulse luminosity versus M_H for the 7 $M_\odot$ sequence

group: Gallino, Busso & coworkers. As in the case of the low mass stars, if a certain amount of protons is left below the convective envelope at the time of the TDU, the resulting ^{13}C is fully burned during the interpulse by the α captures. The resulting s-process nucleosinthesys is then characterized by a low neutron density (10^6-10^7 neutrons/cm^3). However, the maximum temperature at the base of the convective shell during the pulse is now larger then that found in the low mass stellar models, namely about 3.5×10^8 K. In such a condition the $^{22}Ne(\alpha,n)^{25}Mg$ neutron source provides a significant contribution to the s-process nucleosynthesis and the resulting neutron density is extremely large, up to 3×10^{11} neutrons/cm^3 with major consequences on some critical branching. This implies, in particular, an overabundance of some non s-only isotopes, which are commonly associated to the r-processes, with respect to the solar system distribution of the heavy elements. Let us finally mention that we are now becoming to explore the nucleosynthesis occurring at the base of the convective envelope during the interpulse as a consequence of the hot bottom burning.

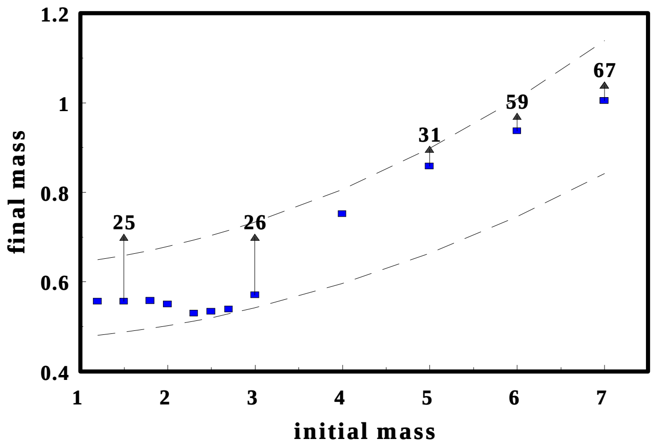

Figure 5: Theoretical (arrows) and semi-empirical (lines) initial-final mass relations

1.5 The final masses

One of the most important goal of the present study is the derivation of the theoretical initial-final mass relation. It depends on many uncertain ingredients of the modern stellar evolution: the efficiency of convection, semiconvection and overshooting, which determine the core mass at the beginning of the TP-AGB phase, the strength of the mass loss and its evolution during the AGB, the rapid spin up of the contracting C-O core which might reduce the efficiency of the 2nd dredge-up thus increasing the Early-AGB lifetime ([18]). In figure 5 we summarize our preferred theoretical scenario. Each arrow indicates the evolution of the core mass during the AGB for different initial masses. Then the squares represent the core masses at the beginning of the TP phase. For $M \leq 3M_{\odot}$, the tip of the arrow indicates the core mass at the time of the C-star formation, whereas for the intermediate mass stars the arrow terminates when the complete envelope removal occurrs, as derived by assuming the [19] prescription for the mass loss rate The label above each arrow indicates the number of the thermal pulses computed up to the tip of the AGB, for the various masses. Finally, the dashed lines represent the lower and the upper limits of the semi-empirical relation obtained by [20].

References

[1] Iben, I. Jr, & Renzini, A. 1982, ApJ, 263, L188

[2] Boothroyd, A.I., & Sackmann, I-J. 1988a, ApJ, 328, 653

[3] Vassiliadis, E., & Wood, P.R. 1993, ApJ, 413, 641

[4] Straniero, O., Chieffi, A., Limongi, M., Busso, M., Gallino, R., Arlandini C., 1997, ApJ. 478,332

[5] Smith, V.V., & Lambert, D.L. 1990, ApJS, 72, 387

[6] Hollowell, D., & Iben, I. Jr. 1989, ApJ, 340, 966

[7] Gallino, R., Busso, M., Picchio, G., Raiteri, C.M., & Renzini, A. 1988, ApJ, 334, L45

[8] Busso, M., Lambert, D.L., Beglio, L., Gallino, R., Raiteri, C. M., & Smith, V.V. 1995, ApJ, 446, 775

[9] Lambert L.D., Smith V.V., Busso M., Gallino R., Straniero O. 1995, ApJ, 450, 302

[10] Straniero, O., Gallino, R., Busso, M., Chieffi, A., Limongi, M., & Salaris, M. 1995, ApJ, 440, L85

[11] Gallino R., Busso M, ApJ 498...

[12] Paczyński, B. 1970, Acta Astron. 20:47, 20:287

[13] Wood P.R, Whiteoack J.B., Hughes S.M.G., Bessel M.S.,Gardner F.F., Guglielmo F., 1992 ApJ 397,552

[14] Renzini, A., & Voli, M. 1981, A&A, 94, 175

[15] Blöcker, T., & Schönberner, D. 1991, A&A, 244, L43

[16] Boothroyd, A.I., & Sackmann, I-J. 1992, ApJ, 392, L71

[17] Iben, I. Jr, & Renzini, A. 1983, ARA&A, 21, 271

[18] Dominguez I., Straniero O., Isern J., Tornambe' A., 1996 ApJ

[19] Groenewegen M.A.T., de Jong T., 1994, A&A 463,468

[20] Weidemann, V. 1987, A&A, 188, 74

Nucleosynthesis Constraints from γ-Ray Astronomy

Roland Diehl

Max Planck Institut für extraterrestrische Physik, D-85740 Garching

Abstract

Gamma-ray line observations have been demonstrated to provide insight into the operation of nucleosynthetic reaction networks in astrophysical objects. The longlived ^{26}Al isotope promises to provide a direct and unocculted tracer of sites of massive-star formation in the Galaxy. For the nearby γ^2Vel system WR models predict higher ^{26}Al yields than observed. The ^{44}Ti isotope detection from Cas A with its halflife of 60 years testifies ejection of inner-core material in core-collapse supernovae, and may be visible throughout the Galaxy for historic supernovae. ^{56}Ni56 production in thermonuclear supernovae still awaits a clear calibration through γ-ray lines, from a nearby ($\leq$ 14Mpc) event.

^{26}Al Radioactivity

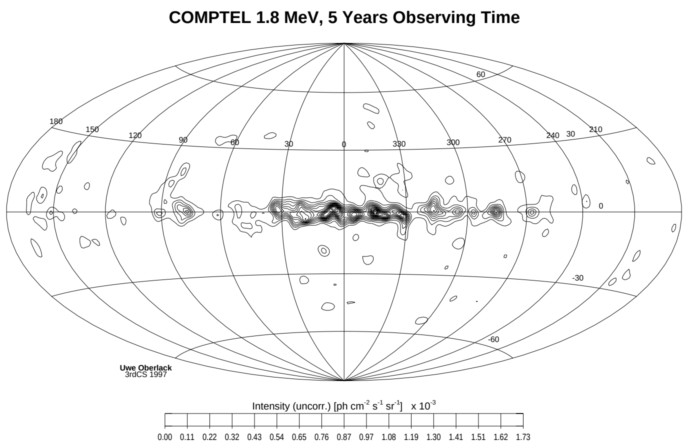

Figure 1: The COMPTEL 1.8 MeV image shows that Galactic-plane sources dominate the ^{26}Al production[10].

With its one-million year decay time, ^{26}Al accumulates in the interstellar medium from many source events, thus addressing current average nucleosynthesis activity in the Galaxy and solar vicinity[9]. Images from COMPTEL measurements[10] show the spatial structure of the emission: The ridge of the Galactic plane dominates, but there are several prominent regions of emission such as Vela, and Cygnus, and possibly the anticenter region (Fig. 1). Simulations of expected images from plausible source imaging techniques, all confirm those features of the 1.809 MeV sky[10, 6]. Yet those also reveal that the apparent irregularity and asymmetries can be instrumental artifacts from fluctuations of the dominating background. Nevertheless, correlation with candidate tracers massive stars probably dominate the ^{26}Al production, as suggested from 1.8 MeV data correlation with spiral structure, dust emission, and in particular free-free emission[6]. For the latter, consistency between the ionizing Lyman continuum luminosity and the ^{26}Al yields from massive stars had been demonstrated[6], and a Lyc calibration for the entire Galaxy yields a Galactic amount of 2.4 $M_\odot$, quite consistent with amounts determined from other considerations.

The $\simeq$ 500 km/sec broadening of the 1.809 MeV line suggested from GRIS measurements appears difficult to reconcile, both with plausibility checks for a physical mechanism[2], and with the COMPTEL latitude profile width of $\leq 5°$. However, if the sources are distributed like a narrow (CO) disk, a kinetic broadening of a few 100 km/sec cannot be ruled out by COMPTEL's image. INTEGRAL's 2-keV spectral resolution[11] imaging should clarify.

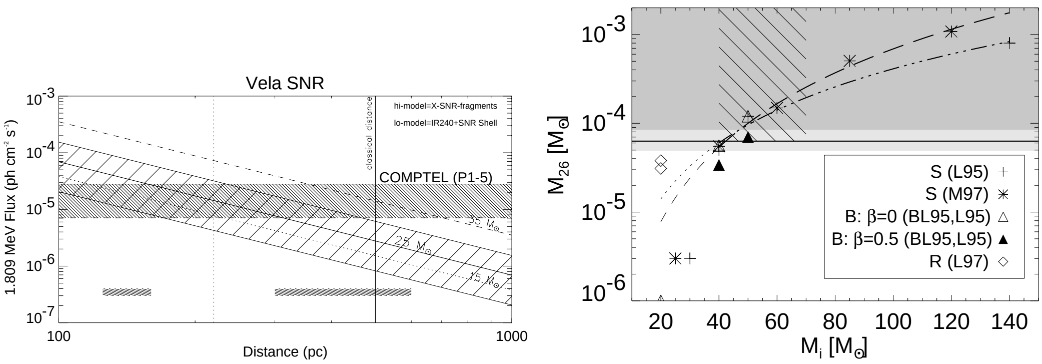

Figure 2: Vela region object limits for ^{26}Al yield models: The Vela SNR models are consistent with the 1.809 MeV flux for distances out to 500 pc (left). The updated WR model yields however appear a factor of 2 or more too high for the case of γ^2Vel(right)

A direct calibration of core-collapse supernova nucleosynthesis with the Vela SNR, (a tantalizing prospect two years ago Diehl et al. 1995), now appears less constraining (Fig. 2 left), as the improved 1.8 MeV image shows structures which may reflect superimposed other sources (a newly discovered young supernova remnant, and/or from OB associations and shell-like extended objects at larger distances). The other prominent candidate source in the Vela region is the binary system γ^2 Velorum, the Wolf Rayet star "WR11" closest to the sun with an O star companion. Recent Hipparcos parallax measurements suggest that this system is at a distance of 250-310 pc only, much closer than previous estimates of 300-450 pc. At this closer distance the absence of a signal from γ^2 Velorum in the COMPTEL 1.8 MeV data is unexpected (Oberlack et al., in preparation, (Fig. 2 right), particularly since recent models have increased the expected ^{26}Al yields for this object[7].

Open issues still are the relative contributions from explosive and wind release of ^{26}Al into the interstellar medium; here the obervations / tighter upper limits from ^{60}Fe could help to disentangle those two massive-star ^{26}Al sources[3]. From classical novae, a smooth distribution of the emission with a pronounced peak in the central bulge region would be expected. The upper limit for such contribution is probably 1 $M_\odot$ of ^{26}Al. On the other hand, Ne-rich novae in our Galaxy may occur more frequently in the disk, hence be less clearly dscriminated against massive stars in general. For the AGB contribution a similar problem is expected, since *massive* AGB stars $M \geq 3M_\odot$) are most likely candidate sources of ^{26}Al.

1.1 Other Radioactivities

From the inner regions of supernovae, models predict ^{44}Ti yields of typically $\sim 3\times10^{-5}$ $M_\odot$ for the Type II models, or twice that value for the Type Ib models; type Ia supernovae of the sub-Chandrasekhar model could also be important sources. The discovery of 1.157 MeV γ-rays from the $\sim$ 300 year-old Cas A supernova remnant appears consolidated[5], although the flux value remains uncertain, at $3 \pm 1 \times 10^{-5}$ ph cm^{-2} s^{-1} implying $\simeq 2\times10^{-4}$ $M_\odot$ of ^{44}Ti. The ^{44}Ti decay time had been controversial until very recently, but now settled at 89 years[4, 1]. Large uncertainties in ^{44}Ti mass estimates may however still remain from a residual uncertainty of the inhibited β-decay of ^{44}Ti if the nucleus remains fully ionized (Hillebrandt, discussed at the meeting).

The order of magnitude of $\sim 10^{-4}$ $M_\odot$ of ^{44}Ti inferred to have been ejected in SN 1987A and in Cas A is surprisingly similar. If this ^{44}Ti ejection should be typical, core collapse supernovae could be revealed even from embedded and hence occulted sites through their ^{44}Ti decay gamma-ray lines. The COMPTEL search for additional ^{44}Ti sources in the Galaxy from 1991-today's data are in progress, and may be constraining the Galactic supernova rate.

Radioactive ^{56}Ni56 and ^{56}Co from supernovae, mainly from type Ia events, still has not been clearly detected. The COMPTEL marginally significant detection converts into a surprisingly large ^{56}Ni56 mass, however, between 1.3 $M_\odot$and 2.3 $M_\odot$for distances of 13 and 17 Mpc, respectively. This requires that almost all of the Chandrasekhar mass white dwarf must be turned into radioactive ^{56}Ni56, unlikely even for an exeptional event such as SN1991T undoubtedly has been.

Acknowledgements

These results emerge from the efforts of the COMPTEL Team, where contributions by Uwe Oberlack, Jürgen Knödlseder, and Hans Bloemen are particularly acknowledged.

References

[1] Ahmad et al., 1998, Phys. Rev. Lett. **80**, 2550

[2] Chen W., et al., 1997, ESA SP-382, 105

[3] Diehl R., & Timmes F.X., 1998, PASP, in press

[4] Görres J., et al., 1998 Phys. Rev. Lett. **80**, 2554

[5] Iyudin, A. F., et al., 1997, ESA SP-382, 37

[6] Knödlseder J., 1998, Ph.D. Thesis, CESR/UPS Toulouse

[7] Meynet, G., et al., 1997, A&A, **320**, 460

[8] Morris D. J., et al., 1997, AIP,**410**, New York, p 1084

[9] Prantzos N. & Diehl R., 1996, Phys. Rep., 267, 1

[10] Oberlack U., 1998, Ph.D. Thesis, TU München

[11] Winkler, C., 1995, Exp. Astron., 6, 71

Nucleosynthesis in classical CO and ONe novae

M. Hernanz, J. José

Institut d'Estudis Espacials de Catalunya (IEEC)
Edifici Nexus, Gran Capità 2-4, 08034 Barcelona, SPAIN

Nova outbursts occur in white dwarfs accreting H-rich matter in a close binary system, as a result of Roche lobe overflow of the main sequence companion. The accreted hydrogen is compressed up to degenerate ignition conditions, leading to a thermonuclear runaway. The explosive H-burning produces β^+-unstable nuclei (^{13}N, ^{14}O, ^{15}O, ^{17}F, ^{18}F), which are transported by convection to the outer envelope where they decay (because $\tau_{\rm conv} < \tau$). The energy released through these decays is at the origin of envelope expansion, luminosity increase and final mass ejection.

A one dimensional implicit hydrodynamical code has been developed to analyze classical nova explosions, from the onset of accretion up to the expansion and ejection stages. A reaction network following the evolution of more than 100 nuclei (from ^{1}H to ^{40}Ca) with updated rates has been included. This has allowed us to model detailed nucleosynthesis during nova explosions, together with the general properties of the explosion [1].

Nucleosynthesis in classical novae has implications for the chemical evolution of the Galaxy. An order of magnitude estimate indicates that novae can eject a total mass of around 7×10^6M$_\odot$ during the whole life of the Galaxy ($\sim2\times10^{-5}$ M$_\odot$/nova, a nova rate of $\sim$35 yr^{-1} and and age of the Galaxy of 10 Gyr lead to this approximate value). Thus, a lower limit (since the ejected mass observed in novae seems to be higher than the theoretical value used above) to the percentage of interstellar medium enriched by novae is 0.03%. This means that novae can account for a significant fraction of the abundance levels of elements which are overproduced by factors larger than $\sim$3000.

Classical novae nucleosynthesis has also implications for γ-ray astronomy. Some medium and long-lived radioactive nuclei are synthesized in novae: ^{7}Be (τ=77 days), ^{22}Na (τ=3.75 yr) and ^{26}Al (τ=10^6 yr)([2], [3]). They decay by emitting photons of 478, 1275 and 1809 keV, respectively. Furthermore, some of the short-lived nuclei mentioned before (^{13}N and ^{18}F) originate annihilation radiation at 511 keV and below at the very beginning of the explosion [4].

A wide range of initial conditions, concerning mass of the white dwarf and degree of mixing of the accreted envelope with the underlying core, has been considered. Carbon oxygen (CO) as well as oxygen-neon (ONe) novae have been computed, with an accretion rate of 2×10^{-10} M$_\odot$ yr^{-1} and luminosity 10^{-2} L$_\odot$. Realisitic chemical compositions for the underlying core have been adopted. In the case of ONe novae, for instance, recent abundance determinations from [5] and [6] indicate that ONe white dwarfs are almost devoid of magnesium and are much richer in ^{16}O than in ^{20}Ne, in contradiction with previous estimates from hydrostatic carbon burning made by [7]. This issue is crucial for the final abundances of some important elements in the nova ejecta.

A summary of the nucleosynthesis obtained for CO and ONe novae of 1.15 M$_\odot$ with initial enrichment of 50% is shown in figure 1, in the form of overabundances with respect to solar ones (see [1] for more details). Because of the difference in initial abundances, elements of the Ne-Na and the Mg-Al group are more abundant in ONe ejecta than in CO ones. Also, as the mass of the underlying white dwarf increases elements with higher Z are synthesized in larger amounts, because the peak temperatures attained are higher. However, some elements can also be destroyed more heavily (as is the case for the important ^{26}Al, see [1] and [8]). The elements that are overproduced by huge factors in almost all models belong to the CNO-group. ^{13}C is overproduced by factors greater than 1000 in all CO models, whereas ^{17}O is overproduced by the same factors in CO novae and even by larger ones in ONe novae. Therefore, novae can account for a significant fraction of the Galactic ^{17}O, and also for some Galactic ^{13}C. Concerning ^{7}Li, the daughter nucleus of ^{7}Be, it is overproduced in CO novae in large amounts (a maximum of ~900), but some extra source is needed to explain its Galactic content. Another element that is significantly overproduced is ^{15}N, but an extra source is also required.

The yields we have obtained fit the abundances observed in some particular novae, such as V693 CrA 1981, V1370 Aql 1982, QU Vul 1984, PW Vul 1984 and V1688 Cyg 1978. But in order to reproduce the wide range of metallicites observed in these and in other novae, a range of mixing levels between the core and the envelope has to be assumed, being its origin still unclear.

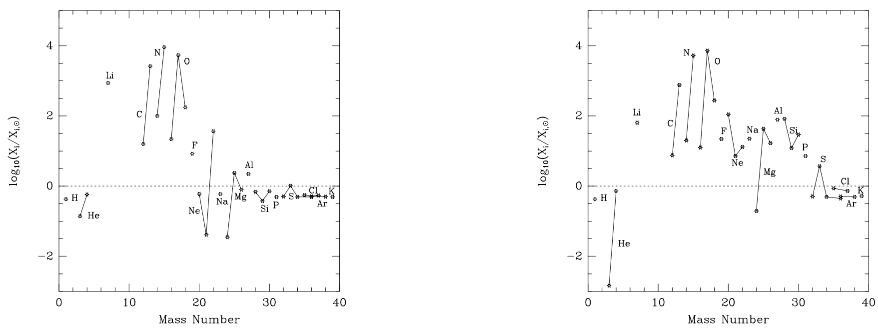

Figure 1: Overproduction factors relative to solar abundances versus mass number for CO (left) and ONe (right) novae of 1.15 $M_\odot$

Acknowledgements

This research has been partially supported by the CICYT (ESP95-0091) and the DGICYT (PB94-0827-C02-02).

References

[1] J. José and M. Hernanz, ApJ **494** (1998) 680.

[2] M. Hernanz, J. José, A. Coc and J. Isern, ApJ **465** (1996) L27.

[3] J. José, M. Hernanz and A. Coc, ApJ **479** (1997) L55.

[4] J. Gómez-Gomar, M. Hernanz, J. José and J. Isern, MNRAS (1998) in press (astro-ph/9711322).

[5] I. Domínguez, A. Tornambè and J. Isern, ApJ **419** (1993) 268.

[6] C. Ritossa, E. García-Berro and I. Iben, ApJ **460** (1996) 489.

[7] D.W. Arnett and J.M. Truran, ApJ **157** (1969) 339.

[8] S. Starrfield, J.W. Truran, M.C. Wiescher and W.M. Sparks, MNRAS (1998) in press.

Two- and Three-Dimensional Simulations of the Thermonuclear Runaway in an Accreted Atmosphere of a C+O White Dwarf

A. Kercek[1], *W. Hillebrandt*[1] *and J.W. Truran*[2]

[1] *Max Planck Institut für Astrophysik, Karl-Schwarzschild-Strasse 1, D-85740 Garching, Germany*
[2] *Department of Astronomy and Astrophysics, Enrico Fermi Institute, University of Chicago, Chicago, IL 60637, USA*

Abstract

We present the results of two- and three-dimensional calculations of turbulent nuclear burning of hydrogen-rich material accreted onto a white dwarf of 1.0 $M_\odot$. The main aim of the present paper is to investigate the question as to whether and how the general properties of the burning are affected by dimensionality and numerical resolution effects. In particular, we want to see whether or not convective overshooting into the surface layers of the C+O white dwarf can lead to self-enrichment of the initially solar composition of the hydrogen-rich envelope with carbon and oxygen from the underlying white dwarf core.

1.1 General Considerations

Today, we know that novae are white dwarfs in close binary systems with a main sequence star as their companion. The white dwarf collects hydrogen-rich material from the companion which first settles into an accretion disk and is then accreted onto the white dwarf's surface. Due to compressional heating this envelope can reach temperatures sufficiently high to burn hydrogen into helium, first by the proton-proton chain and later by the CNO-cycles, where C, N and O nuclei act as catalysts for the burning of hydrogen. Numerical simulations have shown that these reactions can fuse all H into He and eject the envelope, provided the matter is electron degenerate and the CNO-abundances are sufficiently high, several times the solar values [8, 9]. If these conditions are met, the outburst resembles the observed properties of classical novae very well.

It is an important feature that the presence of C, N, and O nuclei enhances the energy production during the violent stages of the nova outburst dramatically. Spherically symmetric hydro-dynamical simulations of the accretion process and the following outburst [10, 2] have shown that it is crucial to have large overabundance of CNO nuclei in the H-rich envelope already at the onset of the violent burning phase in order to get a thermonuclear runaway (TNR) at all. According to these calculations a mass fraction of CNO nuclei close to 30 % is required for a strong outburst and a fast nova. The crucial question is then: Can we explain the huge CNO abundances in the accreted envelope of the white dwarf? Here N is not a problem since it is directly produced from C and O during H-burning. The problem are C and O.

Several ideas have been put forward for mixing C and O from the white dwarf into the envelope already during the accretion phase . One is simply diffusion of hydrogen into the white dwarf accompanied by diffusion of C and O into the envelope [6]. However, because of the long diffusion time-scales this process can only work in exceptional cases with very low accretion rates. Another idea is mixing due to shear instabilities since material is accreted from a disk with high orbital angular momentum [1, 5]. Finally, because the envelope becomes convectively unstable during the accretion stage it is also possible that the penetration of convective motions into the surface of the white dwarf lead to some dredge-up of C and O.

On the other hand side, one might suspect that *during* the TNR violent convective and turbulent motions driven by nuclear reactions may lead to very efficient mixing on short time-scales caused by shear flows or convective overshooting. To be more precise, one may hope that convective motions can dig into the white dwarf and mix some C and O into the envelope. The enhancement of C and O could increase the burning rate generating more violent motions with even more dredge-up and mixing. It is obvious that modeling this effect requires multi-dimensional simulations of a reacting fluid under extreme conditions. Recently, the results of some simulations have been published which indeed show considerable self-enrichment and a fast nova outburst [3, 4].

1.2 Calculations

Here we present the results of simulations we have carried out for a white dwarf of 1 $M_\odot$ accreting hydrogen-rich gas at a rate of 5×10^{-9}M$_\odot$ per year. The calculations were carried out in a carthesian system of coordinates. Only a fraction of the white dwarf's surface was covered by the computational grid, and periodic boundary conditions were implied horizontally. Two-dimensional and three-dimensional calculations were carried out. The dimensions of the calculated domain was 1000 x 1800 km (radial x lateral) and 1000 x 1800 x 1800 km (radial x lateral x lateral) coverd by a grid of the dimensions 100 x 220 and 100 x 220 x 220 for the two-dimensional and three-dimensional simulation, respectively.

The calculations were done with PROMETHEUS, a multi-D Eulerian PPM-hydro code including an equation of state consisting of a non relativistic electron gas with arbitrary degeneracy, the Boltzmann gases of the nuclei and a photon gas. The code also contains a nuclear reaction network including H, He and 12 CNO isotopes. This version of PROMETHEUS was modified to run very efficiently on massively parallel computers such as the CRAY T3E of the Rechenzentrum Garching.

1.3 Results

First simulations were done in two spatial dimensions, assuming that all physical quantities are independent of the third dimension. In this symmetry convective eddies are represented by infinitely long rolls. Some of our results are displayed in Fig.1 and 2. Fig.1 shows snapshots of the absolute value of the velocities obtained in this 2D simulation. A small temperature increase was imposed on one zone as an initial perturbation. Already 14 seconds later sound waves emerging from the ignition region ignited the whole bottom layer of the envelope (Fig.1a). As time progresses quasi-stationary axially symmetric flow fields appear (Fig.1b) which dominate the flow patterns after about 100s (Fig.1c). These vortices are very stable and carry a considerable amount of the turbulent kinetic energy, and they disappear only when the nuclear energy generation reaches its maximum after several hundred seconds.

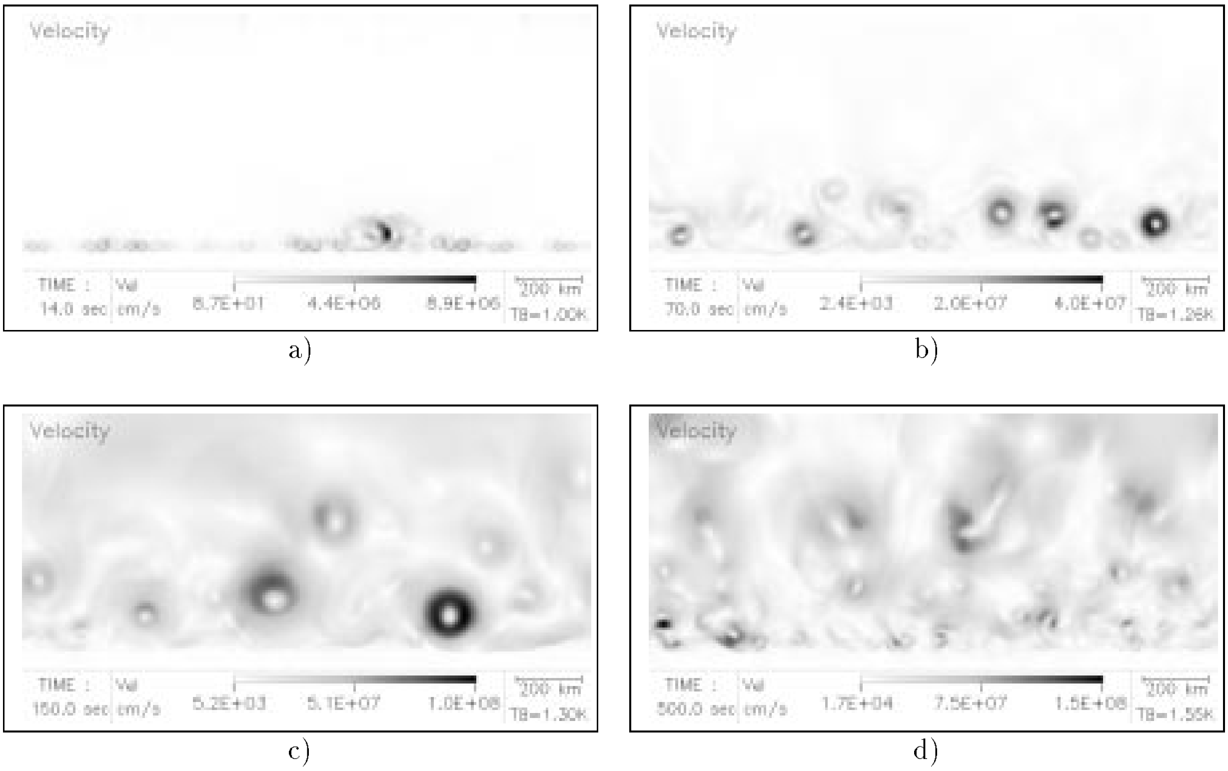

Figure 1: Velocity field at different stages of the evolution for the 2D model explained in the text. Given in color is the absolute value of the velocity at each point. T8 denotes the temperature of the hottest individual zone in units of 10^8K.

The appearance of axi-symmetric quasi-stable structures in 2D flows is not new but has been found earlier in 2D simulations of convection in plane-parallel geometry, and has also been observed in the Earth's atmosphere [7]. It is for the first time however, that such deviations from standard inertially driven turbulence, where the energy is fed into the turbulent eddies on the largest scales, cascades down into the small scales, and is dissipated there by viscosity, are found in astrophysical applications and have important implications there.

As a direct consequence we cannot confirm the results of the simulations of [3, 4]. We find considerably less dredge-up of C and O, mainly because on average less turbulent kinetic energy is available for the largest (and fastest) convective eddies. Although 500 seconds after ignition a considerable amount of ^{12}C can be seen in the envelope (40%) the mixing process has been too slow to yield a strong nova outburst, again in contrast to earlier calculations.

In order to make sure that all relevant scales have been resolved in our simulations

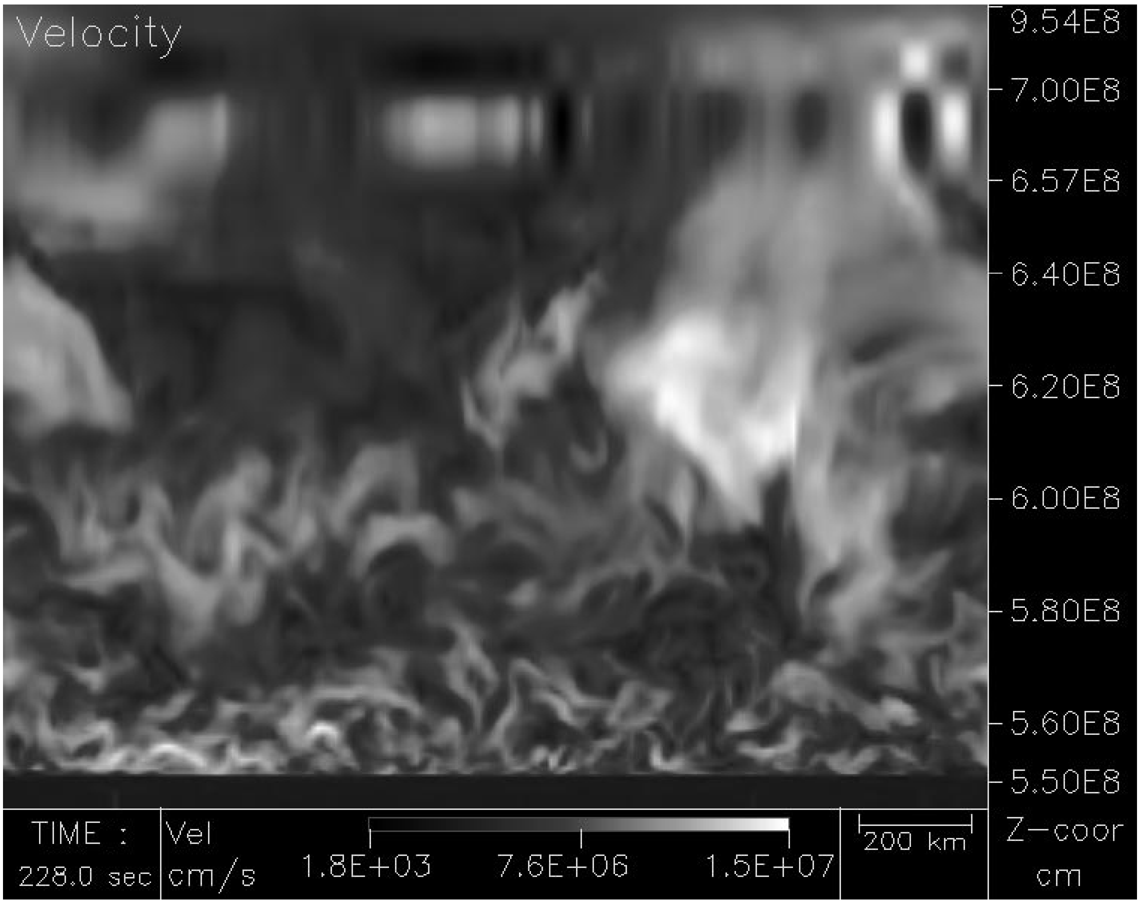

Figure 2: 2D slice of the velocity field of the 3D model at 228 seconds.

we performed one additional run with five times higher spatial resolution, but did not find major differences, as far as the global properties are concerned. Mixing was slightly less efficient than in the model described in some detail here, leading to the conclusion that, at least in 2D, self-enrichment of a nova envelope by violent convective motions is a rather unlikely process. Finally, we also performed first 3D calculations, again with the same input physics and similar resolution as before, but found even less mixing and a completely different flow structure (Fig.2). than in 2D (as might have been suspected), indicating that 3D simulations are indeed necessary.

Our conclusion is, therefore, that nova outbursts require severe enrichment of the H-rich envelope *prior* to the TNR. If for some reason this does not happen the white dwarf will enter into a phase of quiet hydrostatic burning and will, if the envelope fulfills certain requirements, resemble a super-soft X-ray source more than a nova. We also have shown that direct simulations of reaction hydrodynamics have become feasible, even in 3D, and should be done when fuel and ashes are well mixed and burning times are much longer than those of turbulent mixing.

References

[1] R.H. Durisen, ApJ **213** (1977) 145.

[2] M.Y. Fujimoto, ApJ **257** (1982) 752.

[3] S.A. Glasner and E. Livne, ApJ **445** (1995) 149L.

[4] S.A. Glasner, E. Livne and J.W. Truran, ApJ **475** (1997) 754.

[5] R. Kippenhahn and H.-C. Thomas, Astr. Ap.. **63** (1978) 265.

[6] A. Kovetz and D. Prialnik, ApJ **291** (1985) 812.

[7] J.C. McWilliams, J. Fluid Mech. **146** (1984) 367.

[8] S. Starrfield, J.W. Truran, W.M. Sparks and G.G. Kutter, ApJ **176** (1972) 169.

[9] S. Starrfield, W.M. Sparks and J.W. Truran, ApJS **28** (1974) 247.

[10] S. Starrfield, J.W. Truran and W.M. Sparks, ApJ **226** (1978) 186.

Hydrogen accreting carbon-oxygen white dwarfs: An evolutionary scenario

A. Tornambé[1,4], *S. Cassisi*[1,4], *I. Jr. Iben* [2] *& L. Piersanti*[1,3,4]

[1] Osservatorio Astronomico di Teramo, Via M. Maggini, 64100, Teramo, Italy
[2] Astronomy and Physics Departments, University of Illinois, 1002, W. Green Street, Urbana, IL 61801
[3] Dipartimento di Fisica dell'Università degli Studi di Napoli "Federico II", Mostra d'Oltremare, pad. 20, 80125, Napoli, Italy
[4] Dipartimento di Fisica dell'Università degli Studi de L'Aquila, via Vetoio, 67100, L'Aquila, Italy

1.1 Abstract

Results obtained by accreting matter of solar system composition on two initially cool carbon-oxygen (CO) white dwarfs of masses 0.5 $M_\odot$ and 0.8 $M_\odot$, at rates in the range $10^{-8} \leq \dot{M}(M_\odot\ \mathrm{yr}^{-1}) \leq 10^{-6}$, are presented and discussed. Special emphasis is given to two out of the four different hydrogen-burning regimes encountered, namely those in which hydrogen is burned at the same rate at which it is accreted and those in which hydrogen burning proceeds through a series of non-dynamical hydrogen shell flashes. For both cases we present results of several hydrogen-accretion experiments, all but two of which have been continued until a powerful helium shell flash develops.

It is shown that, for a fixed accretion rate, the physical conditions in the growing helium layer are different when (a) the helium layer is built up by the direct accretion of helium and (b) when it is built up by the burning of accreted hydrogen-rich matter. The differences are such that the strength of the helium flash (for the same initial mass and accretion rate) is much smaller in case (b) than in case (a). Nevertheless, even in case (b) experiments, the expansion of the external layers which follows helium ignition is so large that most, if not all, of the previously accreted matter is lost during the event because of the interaction of the expanded envelope with the companion star. For small initial white dwarf masses, the helium flash is so powerful that the convective layer forced by helium burning penetrates deeply into the hydrogen-rich envelope. The introduction of protons into the high temperature parts of the convective shell is expected to induce a complete removal of most of the helium-rich envelope. It is argued that the various events which occur as a consequence of hydrogen accretion onto CO white dwarfs with typical initial masses prevent the mass of the CO white dwarf from growing to the Chandrasekhar limit. Finally, an area in the parameter space of accretion rate and initial mass is identified in which dynamical helium flashes may occur.

1.2 Introduction

Since the early work of Whelan & Iben (1973), white dwarfs accreting hydrogen-rich matter have been considered as possible sources of type Ia supernova explosions (SNeIa). The absence of hydrogen lines in spectra of SNeIa, and various theoretical and observational drawbacks have motivated the search for even more exotic SNeIa progenitor systems. In particular, attention has been focused on systems in which hydrogen has been completely lost during prior evolution. One scenario supposes that the primordial system consists of two intermediate mass stars evolving through a series of common envelope episodes into a final system of two very close CO white dwarfs of combined mass larger than the Chandrasekhar mass (Iben & Tutukov 1984, Webbink 1984). Angular momentum loss by gravitational wave radiation leads to a merger of the white dwarfs and to a possible star-disrupting explosion. Due to several theoretical uncertainties (in particular, the uncertainty as to whether a merger will lead to an explosion or to a collapse into a neutron star, Mochkovich & Livio 1990) and to a perceived lack of appropriately massive close white dwarf pairs (Robinson & Shafter 1987, Bragaglia et al. 1990), this scenario has been challenged for nearly a decade and has led to a reconsideration of the behavior of CO white dwarfs accreting hydrogen from a companion with a hydrogen-rich envelope. Recent discoveries of a relatively high space density of close white dwarf pairs (Marsh 1995, Marsh et al. 1995, and Saffer, Livio, & Yungelson 1998) has demonstrated that appropriately massive and close white dwarf pairs must exist, but the uncertainty as to the outcome of a merger makes the behavior of hydrogen-accreting white dwarfs of continuing interest for an understanding of SNeIa.

A thermonuclear explosion which delivers some 10^{51} erg can be obtained without requiring that the mass of the exploding system exceed the Chandrasekhar mass (the so called "sub-Chandrasekhar" scenario). Nomoto & Sugimoto (1977) first suggested that such an explosion could occur when the total mass of a white dwarf accreting helium at an appropriate rate exceeds $\sim$ 0.65-0.8 $M_\odot$. If helium is accreted onto a cold CO white dwarf at the rate $\sim 3 \times 10^{-8}$ $M_\odot$ yr^{-1}, a violent explosion occurs after the accretion of $\Delta M_{\rm He} \sim 0.15$ $M_\odot$, nearly independent of the initial mass of the underlying white dwarf (Iben & Tutukov 1991). The critical amount of accreted helium depends strongly on the accretion rate, with $\Delta M_{\rm He} > 0.4$ $M_\odot$ for an accretion rate of $\sim 5 \times 10^{-9}$ $M_\odot$ yr^{-1} (Limongi & Tornambé 1991). If the white dwarf is initially cold enough and massive enough, helium burning can evolve into a detonation and an inward moving compression wave can then lead to the detonation of carbon in the core (Tutukov & Khokhlov 1992; Woosley and Weaver 1994).

The development of a critical helium layer above a CO core can be a consequence of the burning of accreted hydrogen-rich matter as well as of the direct accretion of helium from a companion star with a helium-rich envelope. In this contribution, we address the first of these two possibilities. The mass of the critical helium layer and the violence of the explosion differs in the two cases because of the injection of energy from hydrogen burning into the accreting envelope.

Generally speaking, for a fixed initial white dwarf mass, the effect of accreting hydrogen-rich material depends on the accretion rate in the following way. At rates near to or larger than the Eddington limit, the accreted matter will form an expanded configuration, typical of a red giant star (e.g., Nomoto, Nariai, & Sugimoto 1979, Iben 1988).

Lowering the accretion rate, a range of accretion rates is encountered where hydrogen is burned at the base of the accreted layer at the same rate as it is accreted. Lowering the accretion rate still further, a range of accretion rates is encountered where recurrent mild hydrogen shell flashes take place. The accretion rate borderline between steady state burning and flashing behavior increases with the mass of the white dwarf (see, e.g., Fig. 2 in Iben 1982). As the accretion rate is lowered below the borderline, flashes become stronger and stronger, changing from mild, non dynamical events to strong, nova-like outbursts. The precise values of the accretion rate which separate the various zones and the long term evolution of the accreting dwarf have yet to be worked out in adequate detail.

Since the pioneering works of Giannone & Weigert (1967) and Starrfield, Sparks & Truran (1974a,b), the evolution of hydrogen-accreting C-O white dwarfs has been the subject of various extensive investigations (see, for instance, Iben 1982). Nevertheless, the first systematic study of the long term evolution of hydrogen-accreting white dwarfs as a function of accretion rate has been performed by José, Hernanz, & Isern (1993), who used a semi-analytical code in plane-parallel geometry, a choice which considerably simplifies the analysis of long term behavior, but results in the loss of some important details.

We have instituted an investigation of long term behavior using a spherically symmetric quasistatic evolutionary code. The first results of this investigation have been presented by Cassisi et al. (1998). In this communication, we review these results and present results of additional computations.

Two different initial masses for the accreting white dwarf have been taken into account: 0.516 $M_\odot$ and 0.8 $M_\odot$. For each initial mass, several accretion rates have been considered. The first hydrogen shell flash is very strong, and a careful numerical treatment is required to follow its evolution (see Cassisi et al. 1998).

1.3 The evolution of an accreting CO white dwarf of initial mass 0.516 $M_\odot$

In the case of the 0.516 $M_\odot$ initial model, we have chosen accretion rates of 10^{-8}, 2×10^{-8}, 4×10^{-8}, 6×10^{-8}, 10^{-7} and 10^{-6} $M_\odot$ yr^{-1}. Many models experience recurrent hydrogen shell flashes which lead to interesting cyclic excursions in the H-R diagram. The main properties of the various phases along each excursion have been discussed in detail in the literature (see, e.g., Cassisi et al. 1998 and references therein) and will not be repeated here.

Models accreting at the rates $\dot{M} = 10^{-8}$ $M_\odot$ yr^{-1} and $\dot{M} = 2\times10^{-8}$ $M_\odot$ yr^{-1} experience recurrent mild flashes. In about 20 cycles, the leading parameters characterizing a pulse — shape of the light curve, minimum and maximum values of total luminosity, nuclear and gravothermal energy-production rates, and temperature and density in the hydrogen-burning shell — reach asymptotic values. At present, some thousands of complete pulses have been followed for both models. Even so, temperatures near the base of the helium layer are still far from the threshold for the ignition of helium.

A model with $\dot{M} = 4\times10^{-8}$ $M_\odot$ yr^{-1} behaves quite differently, adopting a steady state configuration in which the hydrogen in the accreted matter is burned at the same rate as it is deposited on the surface of the white dwarf. The main physical properties of the model remain almost unchanged until a total mass of 0.6094 $M_\odot$ has been achieved. At this point, recurrent mild hydrogen shell flashes commence. After about 19 pulse cycles, the pulse characteristics approach asymptotic values which are quite different from those of early flashes. (see figure 1a). *This demonstrates that the common practice of assuming that the properties of recurrent novae are similar to those of the 'first' calculated outburst cycle is quite wrong.*

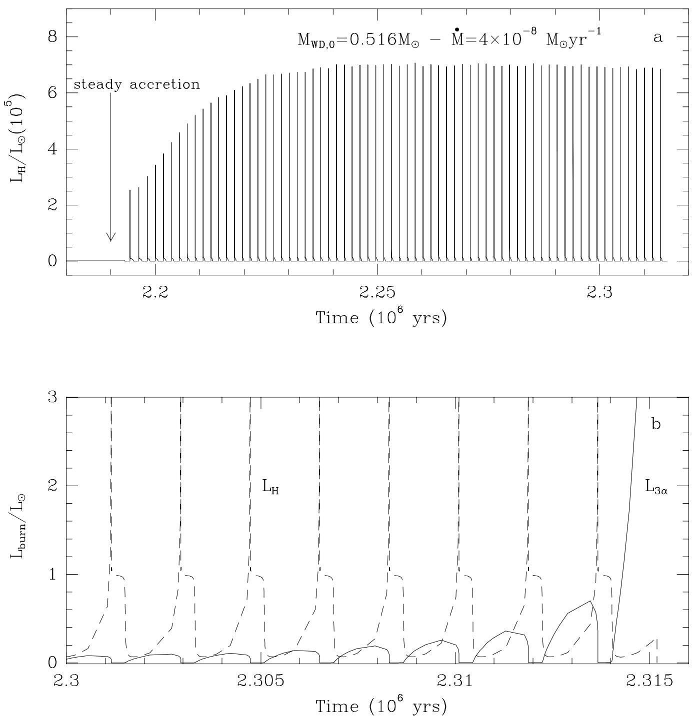

Figure 1: The temporal behaviour of the hydrogen-burning luminosity during the steady state burning and pulsing phases (top panel) and of the hydrogen-burning and the helium-burning luminosities during the last part of the pulsing phase up to the helium-burning thermonuclear runaway for the white dwarf model accreting mass at $\dot{M} = 4 \times 10^{-8}$ $M_\odot$ yr^{-1}

The evolution of the pulsating model has been followed for an additional 49 pulses during the asymptotic regime until helium burning becomes a factor. During the entire evolution, the mass of the helium layer (defined as the region within which the abundance by mass of helium is ≥ 0.5) increases from an original value of 4.3×10^{-4} $M_\odot$ to a final value of 0.127 $M_\odot$.

At the end of the 68$^{\text{th}}$ hydrogen pulse, a very powerful helium shell flash develops (see the far right portion of Fig. 1b). Convection spreads quickly over the entire helium layer. Most of the energy produced by the 3α reactions is used up locally in removing electron degeneracy. External layers expand slightly, and the surface luminosity drops slightly ($\log L$ decreases from 1.6 to 1.2). The flash has been followed until $L_{\text{He}} \sim 5.44 \times 10^6$ $L_\odot$. Computations were terminated at this point because the outer edge of the helium convective layer has reached the inner edge of the hydrogen-rich envelope, necessitating the use of a time-dependent mixing algorithm.

A preliminary investigation of the final fate of this model suggests that it will escape becoming a sub-Chandrasekhar supernova. Moreover, because hydrogen-rich matter ingested by the convective shell is carried deep into the convective region where it burns to release a large amount of energy, one expects the model to expand to giant dimensions. The presence of a close companion leads to common envelope action with the loss of the hydrogen-rich envelope and probably most of the helium layer.

The evolutionary patterns of a model of initial mass 0.516 $M_\odot$ which accretes at the rate 6×10^{-8} $M_\odot$ yr^{-1} differs from that of the previous two models in that a regime of mild hydrogen shell flashing is not encountered before a strong helium shell flash occurs. The phase of steady state hydrogen burning takes place at constant luminosity ($\log L/L_\odot \sim 3.71$) and nearly constant effective temperature ($\log T_e \sim 5.37$). When a total mass of about 0.597 $M_\odot$ has been achieved, the 3α reactions are ignited at the base of the helium layer and the burning develops rapidly into a flash which supports a growing convective layer, as in the previous experiment. The helium burning luminosity reaches a maximum of $L_{\rm He} \sim 2.28 \times 10^6$ $L_\odot$ and thereafter declines. The convective layer continues to grow in mass as $L_{\rm He}$ decreases, and its outer edge eventually enters into hydrogen-rich layers. At this point calculations were terminated, but, once again, one may anticipate diffusion of hydrogen into the helium-rich convective layer until hydrogen ignites and forms a detached convective shell which extends to the surface. And, once again, the model envelope will expand to giant dimensions, leading in the real world to the loss of the hydrogen-rich envelope and most of the helium layer.

A model of initial mass 0.516 $M_\odot$ which accretes at the rate $\dot{M} = 10^{-7}$ $M_\odot$ yr^{-1} reaches the steady state hydrogen-burning phase when $\log L/L_\odot \sim 3.86$ and $\log T_e \sim 5.0$. When a total mass equal to 0.578 $M_\odot$ is achieved, a helium shell flash develops. This time, the maximum helium-burning luminosity is $L_{\rm He} \sim 1.58 \times 10^5$ $L_\odot$. Again, the convective layer continues to grow in mass until its outer edge reaches and ingests hydrogen-rich matter.

The model with $\dot{M} = 10^{-7}$ $M_\odot$ yr^{-1} is initially right at the borderline between models which can burn at a steady rate at fixed luminosity and nearly fixed surface temperature and those which evolve into red giants. To illustrate the phenomenon of evolution into a red giant, an additional experiment with an accretion rate of $\dot{M} = 10^{-6}$ $M_\odot$ yr^{-1} has been performed. After about 100 years, the model reaches the Hayashi track ($\log T_e \sim 3.5$), as expected, and begins to climb upward along this track as a red giant.

1.4 The evolutionary patterns of an accreting CO white dwarf of initial mass 0.8 $M_\odot$

The 0.8 $M_\odot$ CO white dwarf model is subjected to accretion at the rates 10^{-8}, 4×10^{-8}, 10^{-7}, 1.6×10^{-7} and 4×10^{-7} $M_\odot$ yr^{-1}. For $\dot{M} = 10^{-8}$ $M_\odot$ yr^{-1}, hydrogen burns via recurrent pulses, but numerical difficulties during the second hydrogen shell flash prevented us from exploring the asymptotic properties of the pulses. Indeed, this model is very near the borderline for the occurrence of strong pulses as defined by Iben (1982). Anyway, we can try to foresee the final fate of the model. The large radius attained by the model during its evolution suggests that, in a close binary system, mass loss from the system due to Roche-lobe overflow and common envelope action will be extensive and make the accretion process very inefficient (i.e., a large fraction of the matter accreted between hydrogen shell flashes is lost during the envelope expansion phase of the outburst cycle).

Accretion at the rate $4 \times 10^{-8}\ M_\odot\ \mathrm{yr}^{-1}$ leads to mild recurrent hydrogen-flash outbursts with a period of about 480 yr. The computations have been carried out until the asymptotic regime in the pulse properties has been achieved.

A quite similar behavior occurs when $\dot{M} = 10^{-7} M_\odot\ \mathrm{yr}^{-1}$. This time, evolution has been followed through several hundred hydrogen-burning pulse episodes until helium burning accelerates into a thermonuclear runaway after $\sim 6.46 \times 10^4$ yr of accretion, when the white dwarf mass has reached $0.8105\ M_\odot$. A small convective layer supported by helium burning appears, but the outer edge of this layer is unable to reach the hydrogen-rich matter in the outer envelope. Nevertheless, as a consequence of the helium-burning energy release, the entire helium envelope expands to red giant dimensions. Therefore, in the real close binary system, the accretor will fill its Roche lobe and one can once again expect that a large amount of the helium envelope will be lost from the system, thus reducing significantly the efficiency at which the CO core can grow secularly in mass.

The evolutionary behavior of the model accretor when $\dot{M} = 1.6 \times 10^{-7}\ M_\odot\ \mathrm{yr}^{-1}$ is quite similar to the one previously described. In this case the expansion has been studied in detail (Piersanti 1996). The onset of a non dynamical helium flash causes the expansion of the helium layer well beyond the Roche lobe ($R_{max} \simeq 600\ R_\odot$). The mass loss induced by the interaction with the companion has been estimated to remove at least 60% of the accreted matter.

Finally, for $\dot{M} = 4 \times 10^{-7}\ M_\odot\ \mathrm{yr}^{-1}$, the model soon adopts an expanded red giant configuration.

1.5 Helium-accreting *versus* hydrogen-accreting white dwarfs.

It has been known since the work of José et al. (1993) that a difference exists in the structural properties of the helium layer of a mass-accreting white dwarf when helium is accreted directly from when it is accreted, at the same rate, via hydrogen burning by product. This is because, in the hydrogen-accretion models, the helium layer is generally maintained at a higher temperature by the release of nuclear energy during hydrogen shell flashes.

To investigate this property in more detail, we performed additional numerical experiments in which hydrogen-free matter is accreted onto a CO white dwarf. In figure 2, the structure of a helium-accreting white dwarf is compared in the ρ-T plane to the structure of a hydrogen-accreting model of the same mass. The accretion rate is the same for both models. The presence of the hydrogen shell produces a different boundary condition for the helium layer which leads to a higher temperature at any given density.

When the helium-burning runway occurs, the mass of the helium layer in the helium-accreting models is about $0.128\ M_\odot$, which is $\sim 0.035\ M_\odot$, or ~37%, larger than the corresponding quantity for the hydrogen-accreting structure. As a corollary, all other things being equal, the strength of the helium shell flash is smaller when hydrogen-rich material is accreted.

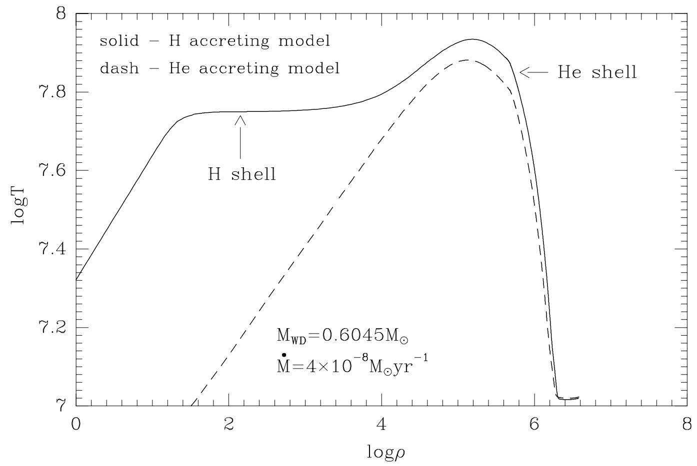

Figure 2: Structure in the ρ-T plane for two white dwarf models of the same initial mass and accretion rate (as labeled) but accreting, in one case, hydrogen-rich matter and, in the other, helium-rich matter.

Another interesting feature is that the difference in the masses of the helium layers built up in the hydrogen-accreting case and the helium-accreting case before the start of a helium flash increases as the initial mass of the CO white dwarf increases. This means that, the larger the white dwarf mass, the larger is the fraction of hydrogen-burning energy that is converted into heat remaining in the star (see Cassisi et al. 1998 for a more detailed discussion).

1.6 Discussion of the results and final remarks.

Figure 3 summarizes the results and describes schematically the outcomes encountered for the various models discussed in the previous sections. The meaning of the various adopted symbols is clarified in the figure.

It is evident that, for a constant hydrogen-accretion rate, the larger the initial mass of the white dwarf, the smaller is the mass of the helium layer required to produce a helium shell flash. Therefore, the larger the CO core mass, the smaller is the total power of the helium shell flash, even if the peak luminosity is larger. For example, during the helium shell flash in models of mass $M_{\rm WD,0} = 0.516\ M_\odot$ and $M_{\rm WD,0} = 0.8\ M_\odot$ accreting at the rate $\dot{M} \sim 10^{-7}\ M_\odot\ {\rm yr}^{-1}$, the total energy output of the model of smaller mass is larger ($\sim 0.3 \times 10^{42}$ erg) than in the model of larger mass ($\sim 0.5 \times 10^{41}$ erg). Nevertheless, the specific energy deposited in the envelope at the peak of the helium flash is larger in the model of larger mass due to the smaller mass of the helium layer: $E_{\rm sp} \sim 0.5 \times 10^{10}$ erg g^{-1} in the model of smaller mass and $E_{\rm sp} \sim 7.1 \times 10^{10}$ erg g^{-1} in the model of larger mass.

One of the main goals of this work was to examine the paths that a hydrogen-accreting CO white dwarf might follow to become a supernova which either ignites carbon at the center of a degenerate CO core or ignites helium in a degenerate helium layer above a CO core. With the aim of enlarging the size of the explored parameter-space, present results

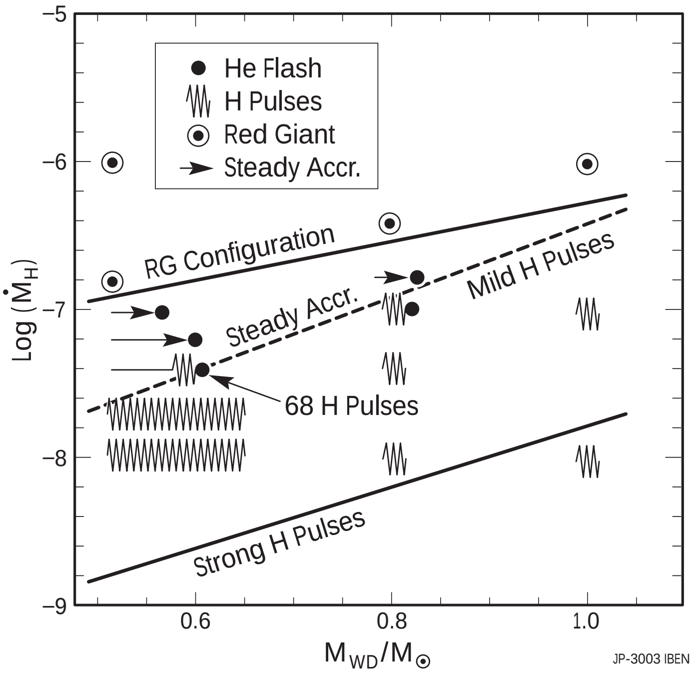

Figure 3: The parameter space $\dot{M} - M_{WD}$ explored so far. Various symbols mark the different outcomes experienced by the various computed models, depending on initial white dwarf mass and accretion rate. The results of accretion experiments onto a $1M_\odot$ white dwarf performed by Livio et al. (1989) are also displayed.

have been implemented with those of Livio et al. (1989) for accretion onto a white dwarf of initial mass $M_{\rm WD,0} = 1\ M_\odot$.

Due to wind mass loss and the formation of a common envelope when helium ignites, it is probable that SNeIa are not the consequence of accretion of hydrogen-rich matter at rates above the line labeled "RG configuration" in Figure 3 (see Livio et al. 1990, Kato & Hachisu 1994, and Iben & Tutukov 1996)

A second region which is probably also excluded is the one which lies below the line labeled "Strong H pulses" ($\dot{M} \sim [1 \rightarrow 10] \times 10^{-9}\ M_\odot\ {\rm yr}^{-1}$, depending on the mass of the white dwarf). A large body of theoretical work together with observational evidence provide strong evidence that, during recurrent outburst cycles, the mass lost by a combination of wind mass loss and common envelope action is larger than the accreted mass, with the consequence that the global mass of the white dwarf decreases secularly with time.

In the regime of intermediate mass-accretion rates, beginning with white dwarfs of small mass (say, $0.5 \leq M/M_\odot \leq 0.65$), it is clear that, for accretion rates smaller than some critical value (say, $\dot{M} \sim 3 \times 10^{-8}\ M_\odot\ {\rm yr}^{-1}$), explosive helium ignition certainly occurs. However, whether this explosion leads to a "super nova" with the dynamical ejection of the helium layer or whether it evolves into a quiescent burning phase with a more gradual expansion to giant dimensions of the helium layer requires hydrodynamic calculations with appropriate initial conditions (e.g., Tutukov & Khochlov 1992; Woosley & Weaver 1994; Livne & Arnett 1995; Livne 1997). In any case, evolution is interrupted before the white dwarf attains the Chandrasekhar mass, preventing the formation of a SNIa due to ignition of carbon at the center.

For higher accretion rates, still inside the strip and for the selected range of masses, a non-dynamical off-center helium flash occurs, with diffusion of hydrogen into the helium-burning convective zone and the formation of a detached convective shell burning hydrogen at its base. One can reasonably expect that in such a case the envelope expands beyond the Roche lobe and most of it is lost.

Models lying in the central part of the strip (say, $0.7 \leq M/M_{\odot} \leq 0.9$), if accreting at rates smaller than $\sim 2 \times 10^{-8}$ $M_{\odot}$ yr^{-1}, may produce dynamic ejection of the helium envelope. To establish this possibility more securely is quite a difficult task due to the tremendously large number of mild hydrogen-burning pulses which take place before a helium shell flash occurs. When accretion rates are larger than $\sim 10^{-7}$ $M_{\odot}$ yr^{-1}, models experience a non dynamical helium shell flash and are subject to a huge expansion of the layers surrounding the helium-burning shell; the expanded configuration is maintained also after the quenching of the helium flash. The consequence of this behavior in a real binary system is the loss of the helium-rich and hydrogen-rich outer layers of the white dwarf by interaction with the companion.

We conclude that scenarios in which a CO white dwarf accreting hydrogen at a realistic rate increases in mass to the Chandrasekhar limit are not viable. However, a long term accretion process at rates in the range $1 \rightarrow 4 \times 10^{-8}$ $M_{\odot}$ yr^{-1} is able to produce a helium shell flash whose properties may be close to those of a sub-Chandrasekhar super nova event.

References

[1] A. Bragaglia, L. Greggio, A. Renzini and S. D'Odorico, ApJ **365** (1990) L13

[2] S. Cassisi, I.Jr. Iben and A. Tornambè, ApJ **496** (1998) 376

[3] P. Giannone and A. Weigert, ZsAp. **67** (1967) 41

[4] I.Jr. Iben, ApJ **259** (1982) 244

[5] I.Jr. Iben, ApJ **324** (1988) 355

[6] I.Jr. Iben and A.V. Tutukov, ApJS **54** (1984) 335

[7] I.Jr. Iben and A.V. Tutukov, ApJ **370** (1991) 615

[8] I.Jr. Iben and A.V. Tutukov, ApJS **105** (1996) 145

[9] J. José, M. Hernanz and J. Isern, A&A **269** (1993) 291

[10] M. Kato and I. Hachisu, ApJ **437** (1994) 802

[11] M. Limongi and A. Tornambé, ApJ **371** (1991) 317

[12] M. Livio, D. Prialnik and O. Regev, ApJ **341** (1989) 299

[13] M. Livio, A. Shankar, A. Burkert and J.W. Truran, ApJ **356** (1990) 250

[14] E. Livne, in *Thermonuclear Supernovae* ed. P. Ruiz-Lapuente, R. Canal and J. Isern (Dordrecht: Kluwer) (1997) 425

[15] E. Livne and D. Arnett, ApJ **452** (1995) 62

[16] T.R. Marsh, MNRAS **275** (1995) L1

[17] T.R. Marsh, V.S. Dhillon and S.R. Duck, MNRAS **275** (1995) 828

[18] R. Mochkovich. and M. Livio, A&A, **236** (1990) 378

[19] K. Nomoto, K. Nariai and D. Sugimoto, PASJ **31** (1979) 287

[20] K. Nomoto and D. Sugimoto, PASJ **29** (1977) 765

[21] L. Piersanti, *Degree Thesis* (1996)

[22] E.L. Robinson and A.W. Shafter, ApJ **332** (1987) 296

[23] R. Saffer, M. Livio and L. R. Yungelson, in progress (1998)

[24] S. Starrfield, W.M. Sparks and J.W. Truran, ApJS **28** (1974a) 247

[25] S. Starrfield, W.M. Sparks and J.W. Truran, ApJ **192** (1974b) 647

[26] A.V. Tutukov and A.M. Khokhlov, Soviet Astron. **36** (1992) 401

[27] R.F. Webbink, ApJ **277** (1984) 355

[28] J.C. Whelan and I. Jr. Iben, ApJ **186** (1973) 1007 .

[29] S.E. Woosley and T.A. Weaver, ApJ **423** (1994) 371

Hydrogen Consumption in X-ray Bursts

J.-F. Rembges[1], *M. Liebendörfer*[1], *T. Rauscher*[1], *F.-K. Thielemann*[1], *H. Schatz*[2]

[1] *Departement für Physik und Astronomie, Universität Basel, CH-4056 Basel, Schweiz*
[2] *Forschungszentrum Karlsruhe, IK3, D-76021 Karlsruhe, Deutschland*

1.1 Introduction

X-ray bursts (for an observational overview see [1]) occur when a neutron star accretes hydrogen-rich material from a close companion. After a critical mass ΔM of unburned transferred matter is accumulated on the surface of the neutron star, ignition sets in, typically under degenerate conditions. The critical mass of the hydrogen layer before ignition can be as small as 10^{-12} $M_\odot$. Temperatures $T\approx$(1-2)$\times 10^9$ K and densities $\rho\approx 10^6$–10^7 g cm^{-3} are attained (see e.g. [3, 4]). This explosive burning with rise times of about 5 seconds leads to the release of 10^{39}–10^{40} ergs. The burst period is typically in the range of a few hours [1].

On the one hand, our aim was to reproduce the calculations by Woosley and Weaver [3] and Taam et al. (see [4] and the references therein). On the other hand we investigated how material can be processed beyond ^{56}Ni and how much accreted hydrogen can be burnt in one burst.

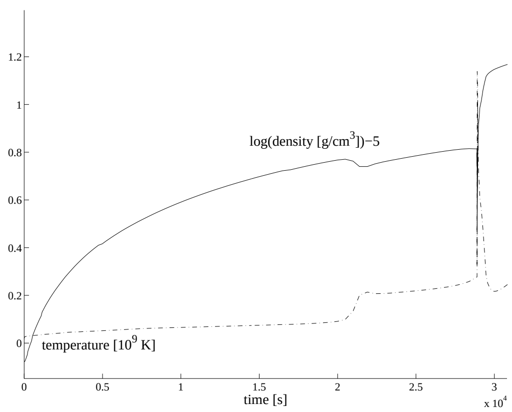

Figure 1: Temperature and density evolution of the hot burning layer in the accretion shell. The significant change in temperature at $t \approx 2.2 \times 10^4$ s is due to the onset of CNO-burning.

1.2 Method and Results

The results shown here were performed with an implicit, one dimensional (general relativistic) hydro-code [5, 6] which was modified for the X-ray burst problem mainly by including an approximation scheme for the rp-process nucleosynthesis [7]. The network was completed by the PP-chain reactions. Also 2-proton capture reactions [8] were considered in a full hydro calculaton for the first time. These sequences were treated as "quasi nuclei" [7], using the fact that, at temperatures sufficiently high, the abundances of the nuclei in such a sequence are kept in equilibrium by very fast proton-capture reactions. The 2-proton capture reactions are important, because they can bridge the slow β^+-decay of the waiting point nuclei ^{68}Se, ^{72}Kr, ^{76}Sr and ^{80}Zr. Consequently, material can be processed efficiently very far beyond ^{56}Ni, leading to an enhanced nuclear energy production $\dot{\epsilon}_{nuc}$ and maybe to different burst behavior as presently assumed.

Due to the implicit nature of the code, it was possible to follow the evolution of the accretion shell over a long period of time and simultaneously resolve the individual bursts with very high accuracy (Figure 1). The surface of the neutron star was considered by inner boundary conditions: R(NS-surface)=10 km, L(NS-surface)=0 erg/s, M(NS)= 1 $M_{\odot}$. The outer boundary condition for the temperature was updated, when the difference to the next inner shell was more than 10 per cent.

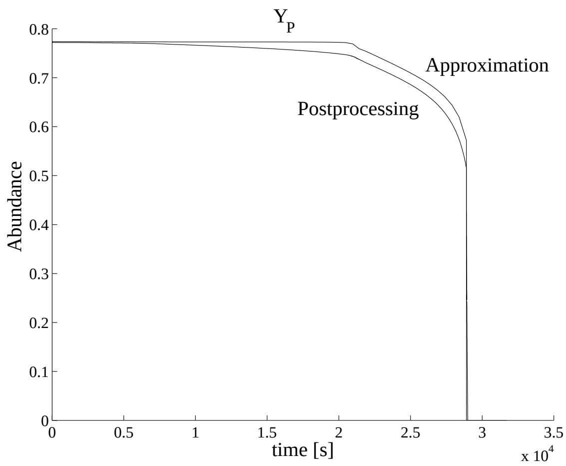

Figure 2: Evolution of the hydrogen abundance before and during the burst. In the hot burning zone, all hydrogen is consumed in one burst.

In Figure 2, the Y_p evolution of the hot burning region is shown. We see that all the initial hydrogen is burnt in one burst. This result is confirmed by postprocessing calculations. The reason is the production of ^{15}O by the 3α-reaction just before thermonuclear ignition (Figure 3). When temperature starts to rise in the explosion, ^{15}O will be processed to heavier nuclei via the rp-process, *before* (α,p)-process becomes effective. Consequently, more hydrogen is burnt than heliyum.

Furthermore it may be possible that a considerable amount of elements heavier than

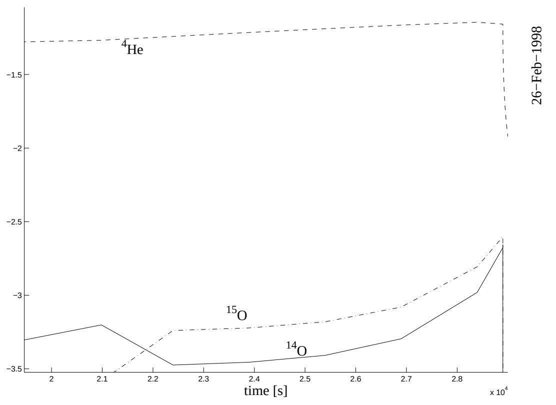

Figure 3: Evolution of Y(^{4}He), Y(^{14}O) and Y(^{15}O) shortly before ignition sets in. We see that a considerable amount of ^{15}O is produced.

^{56}Ni can be produced in only one burst. Among other things, the knowledge of the heavy element composition is important because it will influence the frequency spectrum of ocean g-modes [2].

Our calculation shows that hydrogen exhaustion may occur before appropriate densities for deep hydrogen burning [4] are attained. However, a more reliable result can only be given when convection as well as turbulence in the accretion layer are taken into account; a problem which we have still to solve.

Acknowledgements

This work was supported by the Swiss Science Foundation grant 20-47252.96.

References

[1] W. H. G. Lewin, J. van Paradijs, and R. E. Taam, Space Sci. Rev. **62**, 223 (1993).

[2] L. Bildsten and A. Cumming, ApJ (1998), submitted.

[3] S. E. Woosley and T. A. Weaver, in *High Energy Transcients in Astrophysics*, Vol. 115 of

AIP Conf. Proc., edited by S. E. Woosley (AIP Press, New York, 1985), p. 273.

[4] R. E. Taam, S. E. Woosley, and D. Q. Lamb, ApJ **459**, 271 (1996).

[5] L. G. Henyey *et al.*, ApJ **129**, 628 (1959).

[6] M. Liebendörfer, progress report, 1995, unpublished.

[7] J.-F. Rembges *et al.*, ApJ **484**, 412 (1997).

[8] H. Schatz *et al.*, Phys. Rev. C **294**, 167 (1998).

Gravitational Radiation and Rotation of Accreting Neutron Stars

Lars Bildsten

Department of Physics and Department of Astronomy 366 LeConte Hall, University of California, Berkeley, CA 94720 email: bildsten@fire.berkeley.edu

Abstract

Recent discoveries by the *Rossi X-Ray Timing Explorer* indicate that most of the rapidly accreting ($\dot{M} > 10^{-11} M_{\odot}$ yr^{-1}) weakly magnetic ($B \ll 10^{11}$ G) neutron stars in the Galaxy are rotating at spin frequencies $\nu_s > 250$ Hz. Remarkably, they all rotate in a narrow range of frequencies (no more than a factor of two, with many within 20% of 300 Hz). I suggest that these stars rotate fast enough so that, on average, the angular momentum added by accretion is lost to gravitational radiation. The strong ν_s dependence of the angular momentum loss rate from gravitational radiation then provides a natural reason for similar spin frequencies. Provided that the interior temperature has a large scale asymmetry misaligned from the spin axis, then the temperature sensitive electron captures in the deep crust can provide the quadrupole needed ($\sim 10^{-7} MR^2$) to reach this limiting situation at $\nu_s \approx 300$ Hz. This quadrupole is only present during accretion and makes it difficult to form radio pulsars with $\nu_s > (600-800)$ Hz by accreting at $\dot{M} > 10^{-10} M_{\odot}$ yr^{-1}. The gravity wave strength is $h_c \sim (0.5-1) \times 10^{-26}$ from many of these neutron stars and $> 2 \times 10^{-26}$ for Sco X-1. Prior knowledge of the position, spin frequency and orbital periods will allow for deep searches for these periodic signals with gravitational wave interferometers (LIGO, VIRGO and the "dual-recycled" GEO 600 detector) and experimenters need to take such sources into account. Sco X-1 will most likely be detected first.

Paper to Appear in The Astrophysical Journal Letters, 1998

On the Systematics of Core–Collapse Explosions

A. Burrows[1]

[1] *Department of Astronomy, The University of Arizona, Tucson, AZ 85721*

Abstract

Recent observations of supernovae, supernova remnants, and radio pulsars suggest that there are correlations between pulsar kicks and spins, infrared and gamma-ray line profiles, supernova polarizations, and ejecta debris fields. A framework is emerging in which explosion asymmetries play a central role. The new perspective meshes recent multi–dimensional theoretical investigations of the explosion mechanism with trends in ^{56}Ni yields and explosion kinetic energies. These trends imply that the mass above which black holes form after collapse is $\sim$30 $M_{\odot}$ and that supernova explosion energies may vary by as much as a factor of four. In addition, new neutrino–matter opacity calculations reveal that the inner cores of protoneutron stars are more transparent than hitherto suspected. This may have consequences for the delayed neutrino–driven mechanism of explosion itself. Be that as it may, as the millenium dawns a surprising array of new data and theoretical results are challenging supernova modelers as never before.

1.1 Introduction

Summarizing the important issues surrounding supernova theory is a daunting task and fraught with dangers [1, 2], but I will attempt here to highlight some of the recent developments that I find interesting and hope that the reader will be patient with the manifest limitations of this exercise. In the process, some potential systematics will be discussed and new connections between disparate classes of observations will be suggested. It is now not unreasonable to imagine a theory that unifies the spins and velocities of neutron stars, the anisotropies observed in supernova ejecta, and stellar collapse and explosion. These may be connected in a given supernova, with the debris asymmetries correlated with the kick directions and the neutrino and gravitational wave emissions related to both.

1.2 Status of Explosion Modeling

All groups that do multi–D hydrodynamic modeling of supernovae obtain vigorous convection in the semi–transparent mantle bounded by the stalled shock [3, 4, 5, 7, 6, 8]. There is a consensus that the neutrinos drive the explosion [9] after a delay whose magnitude has yet to be determined, but that may be between 100 and 1000 milliseconds. Whether any convective motion or hydrodynamic instability is central to the explosion mechanism is not clear, with five groups [3, 4, 5, 6, 8] voting yes or maybe and one group [7] voting no. The negative vote is from a group that is taking pains to handle the transport with a minimum of approximations. However, this group opted to do the transport in 1–D, save the result, and impose this history on the 2–D calculation, without feedback. This prescription is suspect, but so are the prescriptions of all the other groups, which compromised in different ways. Hence, a definitive calculation in either two and three dimensions has not yet been performed.

It should be noted that it is not trivial to diagnose the differences between the various calculations of the major groups, nor to reproduce the algorithms they employ. In this regard, one should be cautious of facile comparisons that purport to explain the results of others. For instance, to ascribe the explosions that some groups obtain to the use of the "gray" approximation says next to nothing. There is no one "gray" approximation, though all share the dubious characteristic of not being multi–energy–group. There are many implicit spectra and spectral forms that can be assumed, various flux limiters, a variety of source terms, a number of algorithms to merge opaque and transparent regimes, different approximations for the integrals of the Pauli blocking factors, and different cross sections averages, to name only the most obvious. Furthermore, the differences between a multi–group flux–limited calculation and a full transport calculation can be larger than the differences between a well–chosen "non–gray" calculation and the latter. The range of possible sets of choices under the rubric of "non–gray" is vast and each set entails painstaking evaluation. Therein lies the major problem: it is harder to assemble a "non–gray" code that attempts to cover all the limits than to do the problem correctly. It is only in an effort to speed up the calculation that an integral approach is attempted and doing the full problem is always preferable if sufficient computational resources are available. In addition, it is more difficult to have confidence in a patchwork of approximations than to trust a code that incorporates the full equations, though poor angular, energy, and spatial zoning can severely compromise even an otherwise virtuous scheme.

1.3 Many–Body Correlations

To focus exclusively on numerical and transport matters is frequently to lose sight of the important issues. After the ultimate algorithm is implemented, the results will depend on the initial progenitor models and the microphysics, in particular the neutrino cross sections. In this regard, the recent explorations into the effects of many–body correlations on neutrino–matter opacities at high densities are germane [10, 11, 12, 13]. Though the final numbers have not yet been derived, indications are that we have been overestimating the neutral–current and the charged–current cross sections above 10^{14} gm cm^{-3} by factors of from two to ten, depending upon density and the equation of state. The many–body corrections increase with density, decrease with temperature, and for neutral–current scattering are roughly independent of incident neutrino energy. Furthermore, the spectrum of energy transfers in neutrino scattering is considerably broadened by the interactions in the medium. An identifiable component of this broadening comes from the absorption and emission of quanta of collective modes akin to the Gamow–Teller and Giant–Dipole resonances in nuclei (zero-sound; spin sound), with Čerenkov kinematics. This implies that all scattering processes may need to be handled with the full energy redistribution formalism and that ν–matter scattering at high densities can not be considered elastic. One consequence of this reevaluation is that the late–time (≥ 500 milliseconds) neutrino luminosities may be as much as 50% larger for more than a second than heretofore estimated. These luminosities reflect more the deep protoneutron star interiors than the early post–bounce luminosities of the outer mantle and the accretion phase. Since neutrinos drive the explosion, this may have a bearing on the specifics of the mechanism, but it is too soon to tell.

1.4 Systematics

Unfortunately, theory is not yet adequate to determine the systematics with progenitor mass of the explosion energies, residue masses, ^{56}Ni yields, kicks, or, in fact, almost any parameter of a real supernova explosion. Despite this, there are hints, both observational and theoretical, some of which I would like to touch on here. The gravitational binding energy ($B.E.$) exterior to a given interior mass is an increasing function of progenitor mass, ranging at 1.5 $M_{\odot}$ interior mass from about 10^{50} ergs for a 10 $M_{\odot}$ progenitor to as much as 3×10^{51} ergs for a 40 $M_{\odot}$ progenitor [3, 14]. This large range must affect the viability of explosion and its energy. It is not unreasonable to conclude, in a very crude way, that $B.E.$ sets the scale for the supernova explosion energy. When the "available" energy exceeds the "necessary" binding energy, both very poorly defined quantities at this stage, explosion is more "likely." However, how does the supernova, launched in the inner protoneutron star, know what binding energy it will be called upon to overcome when achieving larger radii? Since the post–bounce, pre-explosion accretion rate ($\dot{M}$) is a function of the star's inner density profile, as is the inner $B.E.$, and since a large $\dot{M}$ seems to inhibit explosion, it may be via $\dot{M}$ that $B.E.$, at least that of the inner star, is sensed. Furthermore, a neutrino–driven explosion requires a neutrino–absorbing mass and there is more mass available in the denser core of a more massive progenitor. One might think that binding energy and absorbing mass partially compensate or that a more massive progenitor can just wait longer to explode, until its binding energy problems are buried in the protoneutron star and $\dot{M}$ has subsided. The net effect in both cases may be similar explosion energies for different progenitors, though the residue mass could be systematically higher for the more massive stars. However, if these effects do not compensate, the fact that binding energy and absorbing mass are increasing functions of progenitor mass hints that the supernova explosion energy may also be an increasing function of mass. Since $B.E.$ varies so much along the progenitor continuum, the range in the explosion energy may not be small. Curiously, the amount of ^{56}Ni produced explosively also depends upon the mass between the residue and the radius at which the shock temperature goes below the explosive Si–burning temperature, a radius that depends upon explosion energy. Hence, the amount of ^{56}Ni produced may also increase with progenitor mass. Thermonuclear energy only partially compensates for the binding energy to be overcome, the former being about 10^{50} ergs for every 0.1 $M_{\odot}$ of ^{56}Ni produced.

Not all ^{56}Ni produced need be ejected. Fallback is possible and whether there is significant fallback must depend upon the binding energy profile. Personally, I think that there is not much fallback for the lighter progenitors, perhaps for masses below 15 $M_{\odot}$, but that there is significant fallback for the heaviest progenitors. The transition between the two classes may be abrupt. I base this surmise on the miniscule binding energies and tenuous envelopes of the lightest massive stars and on the theoretical prejudice that the r–process, or some fraction of it, originates in the protoneutron winds that follow the explosion for the lightest massive stars [15]. If there were significant fallback, these winds and their products would be smothered.

If there is significant fallback, the supernova may be in jeopardy and much of the ^{56}Ni produced will reimplode. There may be a narrow range of progenitor mass over which the supernova is still viable, while fallback is significant and both the mass of ^{56}Ni *ejected* and the supernova energy are decreasing. Above this mass range, a black hole may form. Hence, both low–mass and high–mass supernova progenitors may have low ^{56}Ni yields. Recently, two Type IIp supernovae have been detected, SN1994W [16] and SN1997D [17], which have very low ^{56}Ni yields ($\leq 0.0026\,M_{\odot}$ and $\leq 0.002\,M_{\odot}$, respectively), long–duration plateaus, and large inferred ejecta masses ($\geq 25 M_{\odot}$). The estimated explosion energy for SN1997D is a slight 0.4×10^{51} ergs. (SN1987A's explosion energy was $1.5 \pm 0.5 \times 10^{51}$ ergs and its ^{56}Ni yield was 0.07 $M_{\odot}$.) These two supernovae may reside in the fallback gap and imply that the black hole cut–off is near 30 $M_{\odot}$.

In sum, supernova ^{56}Ni yields may vary by a factor of $\sim$100 and may peak at some intermediate progenitor mass, the supernova explosion energy may vary by a factor of ~ 4 and also may peak at some intermediate progenitor mass, and the black hole hole cut–off mass may be near 30 $M_{\odot}$. However, and importantly, whether real theoretical calculations will bear out these hinted–at systematics is as yet very unclear.

1.5 Young Supernovae and Supernova Remnants

There are many observational indications that supernova explosions are indeed aspherical. Fabry–Perot spectroscopy of the young supernova remnant Cas A, formed around 1680 A.D., reveals that its calcium, sulfur, and oxygen element distributions are clumped and have gross back–front asymmetries [18]. No simple shells are seen. Many supernova remnants, such as N132D, Cas A, E0102.2-7219, and SN0540-69.3, have systemic velocities relative to the local ISM of up to 900 km s^{-1} [19]. X–ray data taken by ROSAT of the Vela remnant reveal bits of shrapnel with bow shocks [20]. The supernova, SN1987A, is a case study in asphericity: 1) its X–ray, gamma–ray, and optical fluxes and light curves require that shards of the radioactive isotope ^{56}Ni were flung far from the core in which they were created, 2) the infrared line profiles of its oxygen, iron, cobalt, nickel, and hydrogen are ragged and show a pronounced red–blue asymmetry, 3) its light is polarized, and 4) recent Hubble Space Telescope pictures of its inner debris reveal large clumps and hint at a preferred direction [21]. Furthermore, radio pictures of the supernova SN1993J, which also has polarized optical spectral features, depict a broken shell. One of the most intriguing recent finds is the supernova SN1997X, which is a so–called Type Ic explosion. This supernova shows the greatest optical polarization of any to date (Lifan Wang, private communication). Type Ic supernovae are thought to be explosions of the bare carbon/oxygen cores of massive star progenitors stripped of their envelopes. As such, SN1997X's large polarization implies that the inner supernova cores, and, hence, the explosions themselves, are fundamentally asymmetrical. No doubt, instabilities in the outer envelopes of supernova progenitors clump and mix debris clouds and shatter spherical shells. The observation of hydrogen deep in SN1987A's ejecta [22] strongly suggests the work of such mantle instabilities. However, the data collectively, particularly for the heavier elements produced in the inner core, are pointing to asymmetries in the central engine of explosion itself.

1.6 Neutron Star Kicks

Strong evidence that neutron stars experience a net kick at birth has been mounting for years. In 1993 [23, 24], it was demonstrated that the pulsars are the fastest population in the galaxy ($< v > \sim 450$ km s^{-1}). Such speeds are far larger than can result generically from orbital motion due to birth in a binary (the "so–called" Blaauw effect). An extra "kick" is required, probably during the supernova explosion itself [25]. In the pulsar binaries, PSR J0045-7319 and PSR 1913+16, the spin axes and the orbital axes are misaligned, suggesting that the explosions that created the pulsars were not spherical [26, 27]. In fact, for the former the orbital motion seems retrograde relative to the spin [28] and the explosion may have kicked the pulsar backwards. In addition, the orbital eccentricities of Be star/pulsar binaries are higher than one would expect from a spherical explosion, also implying an extra kick [29]. Furthermore, low–mass X–ray binaries (LMXB) are bound neutron star/low-mass star systems that would have been completely disrupted during the supernova explosion that left the neutron star, had that explosion been spherical [30]. In those few cases, a countervailing kick may have been required to keep the system bound. The kick had to act on a timescale shorter than the orbit period and the explosion orbit crossing time. Otherwise, the process would have been uselessly adiabatic. One is tempted to evoke as further proof the fact that pulsars seen around young (age $\leq 10^4$ years) supernova remnants are on average far from the remnant centers, but here ambiguities in the pulsar ages and distances and legitimate questions concerning the reality of many of the associations make this argument rather less convincing [31, 32]. However, the ROSAT observations of the 3700 year–old supernova remnant Puppis A show an X–ray spot that has been interpreted as its neutron star [33]. This object has a large X–ray to optical flux ratio, but no pulsations are seen. If this interpretation is legitimate, then the inferred neutron star transverse speed is $\sim$1000 km s^{-1}. Interestingly, the spot is opposite to the position of the fast, oxygen–rich knots, as one might expect in some models of neutron star recoil during the supernova explosion. Whatever the correct interpretation of the Puppis A data, it is clear that many neutron stars are given a hefty extra kick at birth (though the distribution of these kicks is broad) and that it is reasonable to implicate asymmetries in the supernova explosion itself.

1.7 Theories of Kicks

Supernova theorists have determined that protoneutron star/supernova cores are indeed grossly unstable to Rayleigh–Taylor–like instabilities [3, 4, 5]. During the post–bounce delay to explosion that might last 100 to 1000 milliseconds, these cores with 100– to 200–kilometer radii are strongly convective, boiling and churning at sonic ($\sim 3 \times 10^4$ km s^{-1}) speeds. Any slight asymmetry in collapse can amplify this jostling and result in vigorous kicks and torques [3, 34, 35] to the residue that can be either systematic or stochastic. Whatever the details, it would seem odd if the nascent neutron star were not left with a net recoil and spin, though whether pulsar speeds as high as 1500 km s^{-1} (*cf.* the Guitar Nebula) can be reached through this mechanism is unknown. Furthermore, asymmetries in the matter field may result in asymmetries in the emission of the neutrinos that carry away most of the binding energy of the neutron star. A net angular asymmetry in the neutrino radiation of only 1% would give the residue a recoil of $\sim$300 km s^{-1}. Not surprisingly, many theorists have focussed on producing such a net asymmetry in the neutrino field, either evoking anisotropic accretion, exotic neutrino flavor physics, or the influence of strong magnetic fields on neutrino cross sections and transport. The latter is particularly interesting, but generally requires magnetic fields of 10^{14} to 10^{16} gauss [36], far larger than the canonical pulsar surface field of 10^{12} gauss. Perhaps, the pre–explosion convective motions themselves can generate via dynamo action the required fields. Perhaps, these fields are transient and subside to the observed fields after the agitation of the explosive phase. It would be hard to hide large fields of 10^{15} gauss in the inner core of an old neutron star, while still maintaining standard surface fields of 10^{12} gauss. In this context, it is interesting to note that surface fields as high as 10^{15} gauss are very indirectly being inferred for the so–called soft gamma repeaters [37], but these are a very small fraction of all neutron stars. If such large fields are necessary to impart, via anisotropic neutrino emission, the kicks observed, then the coincidence that Spruit & Phinney [35] note between the fields needed to enforce slow pre–collapse rotation and those observed in pulsars after flux freezing amplification is of less significance.

Whether the kick mechanism is hydrodynamic or due to neutrino momentum, one might expect that the more massive progenitors would give birth to speedier neutron stars. More massive progenitors generally have more massive cores. If the kick mechanism relies on the anisotropic ejection of matter [34], then for a given explosion energy and degree of anisotropy we might expect the core ejecta mass and, hence, the dipole component of the ejecta momentum to be larger ("$p \sim \sqrt{2ME}$"), resulting in a larger kick. The explosion energy itself may also be larger for the more massive progenitors, enhancing the effect. If the mechanism relies on anisotropic neutrino emission, the residues of more massive progenitors are likely to be more massive and have a greater binding energy ($E_B \propto M_{NS}^2$) to radiate. Hence, for a given degree of neutrino anisotropy, the impulse and kick ($\propto E_B/M_{NS}$) would be greater. In either case, despite the primitive nature of our current understanding of kick mechanisms, given the above arguements it is not unreasonable to speculate that the heaviest massive stars might yield the fastest neutron stars.

Acknowledgements

I would like to acknowledge productive conversations with F. Thielemann, K. Nomoto, E. Müller, W. Hillebrandt, R. Hoffman, S. Reddy, M. Prakash, B. Schmidt, R. Kirshner, P. Pinto, and C. Wheeler, as well as support from the NSF under grant No. AST-96-17494. I would also like to acknowledge the facilitating environment of the Santa Barbara Institute for Theoretical Physics, supported by the NSF under grant No. PHY94-07194.

References

[1] A. Burrows, to be published in the proceedings of the 18'th Texas Symposium on Relativisitc Astrophysics, ed. A. Olinto, J. Frieman, & D. Schramm (World Scientific Press, 1998).

[2] A. Burrows, to be published in the proceedings of the 5'th CTIO/ESO/LCO Workshop "SN1987A: Ten Years Later," eds. M.M. Phillips & N.B. Suntzeff, held in La Serena, Chile, February 24–28, 1997.

[3] A. Burrows, J. Hayes, & B.A. Fryxell, Astrophys. J. **450** (1995) 830.

[4] M. Herant, W. Benz, J. Hix, C. Fryer, & S.A. Colgate, Astrophys. J. **435** (1994) 339.

[5] H.-T. Janka & E. Müller, Astron. & Astrophys. **290** (1994) 496.

[6] D.S. Miller, J.R. Wilson, & R.W. Mayle, Astrophys. J. **415** (1993) 278.

[7] A. Mezzacappa, *et al.*, Astrophys. J. **495** (1998) 911.

[8] I. Lichtenstadt, A. Kholkhov, & J.C. Wheeler, Astrophys. J., (1998) submitted.

[9] H. Bethe & J.R. Wilson, Bethe, Astrophys. J. **295** (1985) 14.

[10] A. Burrows & R. Sawyer, Phys. Rev. C, (1998) in press.

[11] A. Burrows & R. Sawyer, Phys. Rev. Letters, (1998) submitted.

[12] S. Reddy, M. Prakash, & J.M. Lattimer, Phys. Rev. D, (1998) in press.

[13] S. Yamada, (1998) this conference.

[14] T.A. Weaver & S.E. Woosley, Astrophys. J. Suppl. **101** (1995) 181.

[15] G. Mathews, G. Bazan, & J. Cowan, Astrophys. J. **391** (1992) 719.

[16] J. Sollerman, *et al.*, Astrophys. J. **493** (1998) 933.

[17] M. Turatto, *et al.*, Astrophys. J. Letters, (1998) submitted.

[18] S.S. Lawrence, *et al.*, Astron. J. **109** (1995) 2635.

[19] R.P. Kirshner, J.A. Morse, P.F. Winkler, & J.P. Blair, Astrophys. J. **342** (1989) 260.

[20] R. Strom, H.M. Johnston, F. Verbunt & B. Aschenbach, Nature **373** (1994) 590.

[21] C.S.J. Pun, R.P. Kirshner, P.M. Garnavich, & P.Challis, B.A.A.S. **191** (1998) 9901.

[22] D.H. Wooden, *et al.*, Astrophys. J. Suppl. **88** (1993) 477.

[23] P.A. Harrison, A.G. Lyne, & B. Anderson, Mon. Not. R. Astron. Soc. **261** (1993) 113.

[24] A. Lyne & D.R. Lorimer, Nature **369** (1994) 127.

[25] C. Fryer, A. Burrows, & W. Benz, Astrophys. J., (1998) in press.

[26] I. Wasserman, J. Cordes, & D. Chernoff, (1998) in preparation.

[27] V.M. Kaspi, *et al.*, Nature **381** (1996) 584.

[28] D. Lai, L. Bildsten, & V.M. Kaspi, Astrophys. J. **452** (1995) 819.

[29] E.P.J. van den Heuvel & S. Rappaport, in *I.A.U. Colloquium 92*, eds. A. Slettebak & T.D. Snow (Cambridge Univ. Press), (1987) pp. 291–308.

[30] V. Kalogera, Pub. Astron. Soc. Pac. **109** (1997) 1394.

[31] P. Caraveo, Astrophys. J. **415** (1993) L111.

[32] D.A. Frail, W.M. Goss, & J.B.Z. Whiteoak, Astrophys. J. **437** (1994) 781.

[33] R. Petre, C.M. Becker, & P.F. Winkler, Astrophys. J. **465** (1996) L43.

[34] A. Burrows & J. Hayes, Phys. Rev. Lett. **76** (1996) 352.

[35] H. Spruit & E.S. Phinney, Nature, (1998) in press.

[36] D. Lai & Y.-Z. Qian, Astrophys. J., (1998) in press.

[37] M. Duncan & C. Thompson, B.A.A.S. **191** (1997) 119.08.

Prediction of nuclear reaction rates for astrophysics

Thomas Rauscher

Departement für Physik und Astronomie, Universität Basel,
Klingelbergstr. 82, CH-4056 Basel, Switzerland

The investigation of explosive nuclear burning in astrophysical environments is a challenge for both theoretical and experimental nuclear physicists. Highly unstable nuclei are produced in such processes which again can be targets for subsequent reactions. The majority of reactions can be described in the framework of the statistical model (compound nucleus mechanism, Hauser–Feshbach approach), provided that the level density of the compound nucleus is sufficiently large in the contributing energy window [1]. Among the nuclear properties needed in this treatment are masses, optical potentials, level densities, resonance energies and widths of the GDR. All these necessary ingredients have to be provided in as reliable a way as possible, also for nuclei where no such information is available experimentally.

A recent experiment [2] has underlined that the low-energy extrapolation of the widely used optical α+nucleus potentials may still have to be improved. Currently, there are only few global parametrizations for optical α+nucleus potentials at astrophysical energies. Most global potentials are of the Saxon–Woods form, parametrized at energies above about 70 MeV, e.g. [3]. The high Coloumb barrier makes a direct experimental approach very difficult at low energies. More recently, there were attempts to extend those parametrizations to energies below 70 MeV [4]. Early astrophysical statistical model calculations [5, 6] made use of simplified equivalent square well potentials and the black nucleus approximation. Improved calculations [7] employed a phenomenological Woods–Saxon potential [8], based on extensive data [9]. However, it was not clear how well all these potentials would work for heavy targets with $A > 60$ or in the thermonuclear energy range.

Most recent experimental investigations [10, 11] found a systematic mass– and energy–dependence of the optical potentials and were very successful in describing experimental scattering data, as well as bound and quasi–bound states and $B(\mathrm{E2})$ values, with folding potentials. Based on that work, a global parametrization of the volume integrals can be found [12]. In this description, the real part of the nuclear potential is given by a folding potential $V_f(r,E)$. The imaginary part $W(r,E)$ is of Woods–Saxon shape with a strongly energy–dependent depth. Nuclear structure and deformation information determines the shape of the energy–dependence by including level density dependent terms [12].

It is easy to show that the final transmission coefficients are not only sensitive to the strength of the potential but also to its geometry. Experimental data seemed to indicate that the geometry may also be energy–dependent [4, 13]. At low energies, the diffuseness of the standard volume Woods–Saxon potential had to be set to smaller values, while the radius parameter was increased, in order to be able to describe experimental scattering data. This can be understood in terms of the semi–classical theory of elastic scattering [14] which shows that the relative importance of contributions from different radial parts of the potential depends on the energy. It was shown [15] that the predicted enhanced surface absorption at low energies can be described by an increased surface Woods–Saxon term. Thus, the artificial change in geometry in the description of scattering data results from the use of a volume term only. Consequently, the optical potential proposed here contains an imaginary part which is given by the sum of a volume Woods–Saxon term and a surface term:

$$V(r,E) = V_C(r) + V_f(r,E) + i\left(W_v(E)f(r,R,a) - W_s(E)\frac{d}{dr}f(r,R,a)\right) \qquad (27)$$

with

$$f(r,R,a) = \left[1+e^{\frac{r-R}{a}}\right]^{-1}, \quad W_v(E) = C - \alpha e^{-\beta E}, \quad W_s(E) = D + \gamma e^{-\delta E} \quad . \qquad (28)$$

The depths of the potentials are exponentially dependent on the energy, with the volume depth W_v increasing and the surface depth W_s decreasing when going to higher energies. An increasingly dominant surface term at low energies leads to similar effects as reducing the diffuseness of a pure volume Woods–Saxon potential. The coefficients are related to the height of the Coulomb barrier and the microscopic and deformation corrections as used in Ref. [12]. The total volume integral is still given by the relation derived in Ref. [12]. The energy–dependence of the ^{144}Sm(α,γ)^{148}Gd excitation curve [2] at low energies can be reproduced by such a description. Nevertheless, more experimental data is needed which should be consistently analyzed at different energies with optical potential parametrizations similar to the one used in Ref. [15].

Based on the well–known code SMOKER [7], an improved code for the prediction of astrophysical cross sections and reaction rates in the statistical model has been developed [16]. Among other changes, it includes an improved level density description [1], updated data sets of experimental level information, as well as the new α+nucleus potential. It also allows to treat isospin effects which are especially important in α capture reactions on self–conjugate target nuclei and in proton capture reactions above the neutron separation energy. For a more detailed presentation of the code and possible isospin effects, see [16].

Acknowledgements

TR is an APART fellow of the Austrian Academy of Sciences.

References

[1] T. Rauscher, F.-K. Thielemann, and K.-L. Kratz, Phys. Rev. C **56** (1997) 1613.

[2] E. Somorjai, Zs. Fülöp, Á.Z. Kiss, C.E. Rolfs, H.P. Trautvetter, U. Greife, M. Junker, S. Goriely, M. Arnould, M. Rayet, T. Rauscher, and H. Oberhummer, A&A **333** (1998) 1112

[3] M. Nolte, H. Machner and J. Bojowald, Phys. Rev. C **36** (1987) 1312.

[4] V. Avrigeanu, P.E. Hodgson, M. Avrigeanu, Phys. Rev. C **49** (1994) 2136.

[5] M. Arnould, A&A **19** (1972) 92.

[6] S.E. Woosley, W.A. Fowler, J.A. Holmes, and B.A. Zimmerman, At. Data Nucl. Data Tables **22** (1978) 371.

[7] F.-K. Thielemann, M. Arnould and J.W. Truran, in *Advances in Nuclear Astrophysics*, ed. E. Vangioni–Flam, Gif sur Yvette 1987, Editions Frontière, p. 525.

[8] F.M. Mann, 1978, Hanford Engineering, report HEDL-TME 78–83.

[9] L. McFadden and G.R. Satchler, Nucl. Phys. **84** (1966) 177.

[10] P. Mohr, H. Abele, U. Atzrott, G. Staudt, R. Bieber, K. Grün, H. Oberhummer, T. Rauscher, and E. Somorjai, in *Proc. Europ. Workshop on Heavy Element Nucleosynthesis*, eds. E. Somorjai and Zs. Fülöp, Institute of Nuclear Research, Debrecen 1994, p. 176.

[11] U. Atzrott, P. Mohr, H. Abele, C. Hillenmayer, and G. Staudt, Phys. Rev. C **53** (1996) 1336.

[12] T. Rauscher, in *Nuclear Astrophysics, Proc. Int. Workshop XXVI on Gross Properties of Nuclei and Nuclear Excitations*, eds. M. Buballa et al., GSI, Darmstadt 1998, p. 288.

[13] P. Mohr, T. Rauscher, H. Oberhummer, Z. Máté, Zs. Fülöp, E. Somorjai, M. Jaeger, and G. Staudt, Phys. Rev. C **55** (1997) 1523.

[14] D.M. Brink and N. Takigawa, Nucl. Phys. **A279** (1977) 159.

[15] A. Budzanowski et al., Phys. Rev. C **17** (1978) 951.

[16] T. Rauscher and F.-K. Thielemann, in *Proc. 2nd Oak Ridge Symp. on Atomic and Nuclear Astrophysics*, ed. A. Mezzacappa, IOP Publishing, in press;
preprint nucl-th/9802040.

Direct measurement of reaction rates relevant to Nuclear Astrophysics

U. Greife

Institut für Exp.Phys. III, Ruhr-Universität Bochum, Germany

Due to the Coulomb Barrier involved in the nuclear fusion reactions, the cross section of a nuclear reaction drops nearly exponentially at energies which are lower than the Coulomb Barrier, leading to a low-energy limit of the feasible cross section measurements in a laboratory at the earth surface. Since this energy limit has up to now always been far above the thermal energy region of the sun, the high energy data have been extrapolated down to the energy region of interest.

The low-energy studies of thermonuclear reactions in a laboratory at the earth's surface are hampered predominantly by the effects of cosmic rays in the detectors. Passive shielding around the detectors provides a reduction of gammas and neutrons from the environment, but it produces at the same time an increase of gammas and neutrons due to the cosmic-ray interactions in the shielding itself. A 4π active shielding can only partially reduce the problem of cosmic-ray activation. The best solution is to install an accelerator facility in a laboratory deep underground. The worldwide first underground accelerator facility has been installed at the Laboratori Nazionali del Gran Sasso (LNGS) in Italy, based on a 50 kV accelerator. This pilot project is called LUNA and has been supported since 1992 by INFN, BMBF, DAAD-VIGONI and NSF/NATO.

The major aim of the LUNA pilot project is to measure the cross section of ^{3}He(^{3}He,2p)^{4}He which is one of the major sources of uncertainties for the calculation of the neutrino source power of the sun. It had been studied previously down to about $E_{\rm cm}$=25 keV, but there remains the possibility of a narrow resonance at lower energies that could enhance the rate of path I of the pp-chain at the expense of the alternative paths that produce the high-energies neutrinos ($E_\nu > 0.8$ MeV). The LUNA–collaboration has now studied this important reaction over the full range of the solar Gamow Peak, where the cross section is as low as 8 pbarn at $E_{\rm cm}$=25 keV and about 20 fbarn at $E_{\rm cm}$=17 keV.

Also the other key reactions of the pp–chain like ^{3}He(α,γ)^{7}Be and ^{7}Be(p,γ)^{8}B and the key reaction of the CNO–cycles, ^{14}N(p,γ)^{15}O, have never been studied in or even near their solar Gamow peaks. All these reactions are critical to the solar neutrino puzzle. The reaction rate of ^{14}N(p,γ)^{15}O is also one of the ingredients needed to determine the theoretical scenario used to constrain both the age and the distance of the oldest stellar system in our galaxy, namely the Globular Clusters.

Due to the higher Coulomb barrier the 50 kV LUNA accelerator is not suited to investigate these reactions but a 400 kV machine is needed to get an overlap with the previous measurements. In addition, a new 400 kV accelerator will give the possibility to study many (p,γ) reactions of the NeNa and MgAl cycles below an incident proton energy $E_{\rm p}$=200 keV. Experimental data about these channels, very important for the understanding of nucleosynthesis processes in massive stars, are today still missing or very uncertain. The NeNa cycle may play a role in understanding the ^{22}Ne abundance found in meteorites samples, while the MgAl cycle may provide the mechanisms for production of ^{26}Al, which is observed via gamma astronomy. All the involved (p,γ) cross sections of these cycles are scarcely known at low energies. For example the strength of the low lying resonances in the reaction ^{25}Mg(p,γ)^{26}Al, which is crucial for the production of ^{26}Al, could be experimentally determined for the first time. Also other reactions of these cycles like ^{26}Mg(p,γ)^{27}Al and ^{27}Al(p,γ)^{28}Si can be investigated using accelerator and detector systems in the next phase of the LUNA experiment.

Special care has to be taken for the choice of the detectors for the new underground accelerator. As the measured cross sections are of the order of a some 100 fbarn or lower high efficiency detection systems are required. In addition the background counting rate of the detectors must be reduced as much as possible. The aim of the development is to detect count rates as low as a few events per day in the region of interest. While cosmic ray background is suppressed efficiently due to the massive shielding provided by the Gran Sasso rock, background events from environmental and intrinsic radioactivity must be eliminated as well as events caused by electronic noise.

The LUNA II collaboration is currently investigating the different aspects of the detection setup in order to have it available on completion of the new 400 kV LUNA Accelerator at LNGS.

There are however limitations to the underground accelerator approach in the measurement of radiative capture reactions A(x,γ)B which are among the most important reactions for the formation of the elements. They are usually studied in the laboratory by detecting the emitted γ-rays. If the capture cross section is small, one of the nuclei involved is radioactive and/or competing reactions produce a high γ-ray background, even measurements with high-resolution Ge detectors have reached their limitations. It has been shown that the direct detection of the recoiling nucleus B can greatly improve the experimental sensitivity. In summer 1994 the NABONA project was initiated to combine the two fields of nuclear astrophysics and accelerator mass spectrometry with the aim to determine reaction rates of radiative capture reactions important for nuclear astrophysics.

The absolute cross section $\sigma(E)$ of the reaction ^{7}Be(p,γ)^{8}B influences sensitivly the calculated flux of high energy solar neutrinos and must therefore be known with adequate precision. Using a radioactive ^{7}Be target ($T_{1/2} = 53.29$ d) the $\sigma(E)$ data were derived from the β-delayed α-decay of ^{8}B. The work of several investigators led to a fairly consistent picture of the energy dependence of $\sigma(E)$ - or equivalently of the astrophysical S(E) factor - but not on the absolute value: the extrapolated absolute S(0) factor ranges from 16 to 45 eV b. The discrepancy is most likely to be found in the complicated target stoichiometry of the ^{7}Be target (produced via hot chemistry). Recent theoretical and and experimental investigations have found new problems which will make renormalisations of all published solid target measurements necessary.

It is the aim of a project at the 3 MV TTT-3 tandem accelerator in Naples to provide an improved $\sigma(E)$ value in the nonresonant region, i.e. at $E_{\mathrm{c.m.}} = 1.0$ MeV. The reaction is studied in inverse kinematics, p(^{7}Be,γ)^{8}B, i.e. a radioactive ^{7}Be ion beam of $E_{\mathrm{lab}} = 8.0$ MeV is guided into a windowless gas target system filled with H_2 gas (pressure p(H_2) = 5.0 mbar), thus avoiding the above problems of target stoichiometry. As a novel technique the ^{8}B residual nuclides are detected directly in an efficient recoil separator. Since the elastic scattering yield is observed concurrently with the ^{8}B yield, $\sigma(E)$

is related ultimately to the Rutherford scattering cross section ("relative measurement"). Due to the low capture cross section (about 0.5 μb) and the low target density (about 10^{19} atoms/cm^2) a ^{7}Be beam intensity of about 100 ppA is needed in order to achieve sufficient statistical accuracy in a finite time. Moreover, a high purity of the beam, and in particular the absence of isobaric contaminants (for a unique analysis of the p+^{7}Be elastic scattering yields), is needed. The setup including the recoil separator was tested with the H(^{12}C,γ)^{13}N radiative capture reaction and the result was in excellent agreement with preyious work.

The ^{7}Be nuclides were produced in a Li$_2$O matrix via the ^{7}Li$(p,n)^7$Be reaction using a 13 MeV proton beam (about 10 μA) from the KIZ-cyclotron at Karlsruhe. In the sputter source, the ^{7}Be nuclides in the Li$_2$O matrix were extracted in form of a ^{7}BeO$^-$ molecular ion beam. Setting the 35° injection magnet to mass-23 ions, this beam was accompanied by an intense ^{7}LiO$^-$ molecular beam. Both beams were focused by two gridded lenses and accelerated to the terminal voltage $U = 2.42$ MV of the tandem. After stripping in a 3 μg/cm^2 thick C foil, the 8.0 MeV ions of ^{7}Be^{3+} and ^{7}Li^{3+} emerging from the accelerator were focused by a magnetic quadrupole doublet on the object slits of a 90° analysing magnet and this double focusing magnet focused the beam on the image slits. Inserting a post-stripper C foil near the object slits, fully stripped ^{7}Be^{4+} ions were produced. These ^{7}Be^{4+} ions were selected by the analysing magnet, while the accompanying intense ^{7}Li^{3+} ions were filtered. The analysed ^{7}Be^{4+} current amounted up to 70 pA and lasted for about 48 hours. With a 50 % transmission through the gas target system a time-averaged ^{7}Be^{4+} current of about 18 pA was available in the target zone. The ^{8}B residual nuclides from $p(^7$Be,$\gamma)^8$B at $E_{\rm lab} = 8$ MeV were produced in the H$_2$ gas target and guided through the recoil separator with a 100 % efficiency. For the above ^{7}Be current, p(H$_2$) = 5.0 mbar, and $\sigma = 0.5$ μb one expects a ^{8}B count rate of about 1 event per 3 hours, consistent with observation: the 5 events per 12 hours were clearly resolved in the recoil detector. Further improvements, especially the use of hot chemistry in the cathode production, will be implemented in order to obtain sufficient statictics.

The next aim of the NABONA collaboration is the determination of the cross section for the reaction ^{12}C(α,γ)^{16}O in inverse kinematics. The experimental setup will consist of a pointlike gas jet target, a large acceptance recoil spectrometer and a detector array for the measurement of γ-recoil coincedences. For the future use with radioactive ion beams the advantages of this approach are even more apparent. Through several collaborations the experience gained in this development project will be an important input for the RIB laboratories which are installing a dedicated recoil mass spectrometer for nuclear astrophysics.

Further information is available at:

HTTP://www.ep3.ruhr-uni-bochum.de/astro/astro.html
HTTP://www.lngs.infn.it/lngs/htexts/luna/luna.html

Uncertainties in the solar r-abundance distribution

S. GORIELY

Institut d'Astronomie et d'Astrophysique
Université Libre de Bruxelles, Campus de la Plaine, CP 226
B-1050 Bruxelles, Belgium

1. The solar r-abundances and the multi-event s-process model

The slow neutron-capture process (or s-process) and the rapid neutron-capture process (or r-process) are known to be the 2 major nucleosynthetic mechanisms responsible for the production of the elements heavier than iron observed in nature. Though both processes invoked neutron captures on light seed nuclei to produce the heavy elements, they take place in completely different astrophysical environments and on very different timescales. About 30 nuclei, called s-only isotopes, are exclusively synthesized during the low-neutron-densities ($N_n \simeq 10^8 \mathrm{cm}^{-3}$) events characteristic of the s-process. Most of the neutron-rich stable isotopes cannot be produced by the s-process and the high neutron densities ($N_n > 10^{20} \mathrm{cm}^{-3}$) found in the r-process are called for to explain their origin. In addition to these s-only and r-only nuclei, a large number of stable isotopes (called sr-isotopes) are potentially produced by both processes. In order to understand these 2 very different nucleosynthetic mechanisms, it is of first importance to decompose the observed solar system abundance distribution into its s- and r-components. To do so, the s-contribution is obtained by fitting parametric s-process models to the abundance of the s-only isotopes. Such a fit defines the s-component of the sr-nuclei, and consequently the solar r-abundance distribution by a simple subtraction of the s-contribution from the observed solar values.

For this specific purpose, fully parametric s-process models, free of all astrophysical constraints, have been introduced. A new approach to the parametric s-process models, called the multi-event model, has been recently developed [1]. Such a model considers the superposition of a large number of canonical events taking place in different thermodynamic conditions. Each canonical event is characterized by a given neutron irradiation on the ^{56}Fe seed nuclei during a time t at a constant temperature T and a constant neutron density N_n. The combination of s-process events that provides the best fit to the solar abundances of the s-only isotopes is derived with the aid of an iterative inversion procedure described in [1] and defines the s-component to the solar abundances of the sr-nuclei, and consequently enables the determination of the solar r-abundance distribution. It should be stressed that in contrast to the classical exponential model, the multi-event model is particularly well suited to an analysis of the impact of the different uncertainties on the solar s- and r-abundance distribution, since it offers the advantage of deriving, for a given input, the best fit to the abundances of the s-only isotopes. Through the iterative inversion procedure, a modification of the input parameters automatically leads to a renormalization of the thermodynamic conditions required to fit the s-only abundances. In the present work, thermodynamic conditions in the $1.5 \le T[10^8\mathrm{K}] \le 4$ and $7.5 \le \log N_n[\mathrm{cm}^{-3}] \le 10$ ranges are considered. More technical details on the multi-event model can be found in [1].

2. Uncertainties in the solar r-abundance distribution

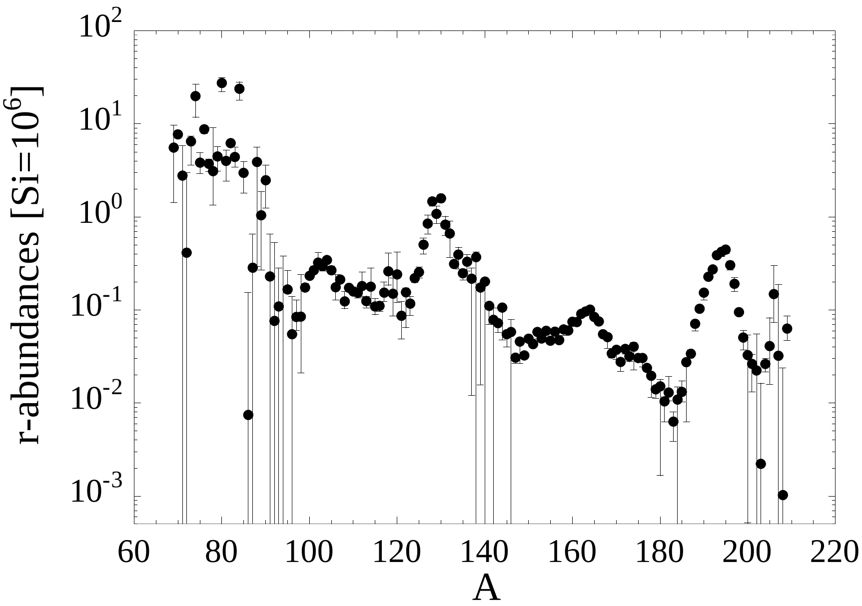

Figure 1: Isotopic r-abundance distribution in the solar system. The error bars reflect uncertainties affecting observational data and experimental and theoretical (n, γ) rates.

Various uncertainties still affect the determination of the solar r-abundance distribution. First, the quality of the observational data which inevitably depends on the spectroscopic or physico-chemical peculiarities of each species [2] plays a crucial role in the determination of the s-contribution to the abundance of the sr-nuclei. Second, nuclear uncertainties in the s-process model also influence the relative s- and r-contributions to the solar abundances. These concern mainly the estimate of the neutron capture and β-decay rates. Since the uncertainties on the stellar β-decay rates remain difficult to derive systematically, the study of their impact on the s- and r-splitting of the solar abundances is postponed to a future work. As regards the neutron capture rates, effects due to experimental and theoretical imprecisions are analyzed. To do so, the latest experimental neutron capture cross sections and their prescribed error bars are included in the multi-event s-process approach (note that thermalization effects are considered, but not added to the experimental uncertainties at this stage). When not available experimentally, the cross sections are calculated within the updated statistical Hauser-Feshbach model called MOST [3]. However, to test the sensitivity of the solar r-abundance distribution to the predicted (n, γ) rates, calculations are also made with an older version of the statistical model [4] based on a different nuclear physics input.

Observational and nuclear uncertainties in the multi-event s-process calculations are studied simultaneously by considering the two different predictions of the theoretical (n, γ) rates and by allowing various random selections among the upper and lower limits of each observed abundance and each experimental (n, γ) rate. Their impact on the solar r-abundance distribution is shown in Fig. 1. As seen in Fig. 1, the solar r-abundances can be considered as relatively well determined around the r-only isotopes corresponding to

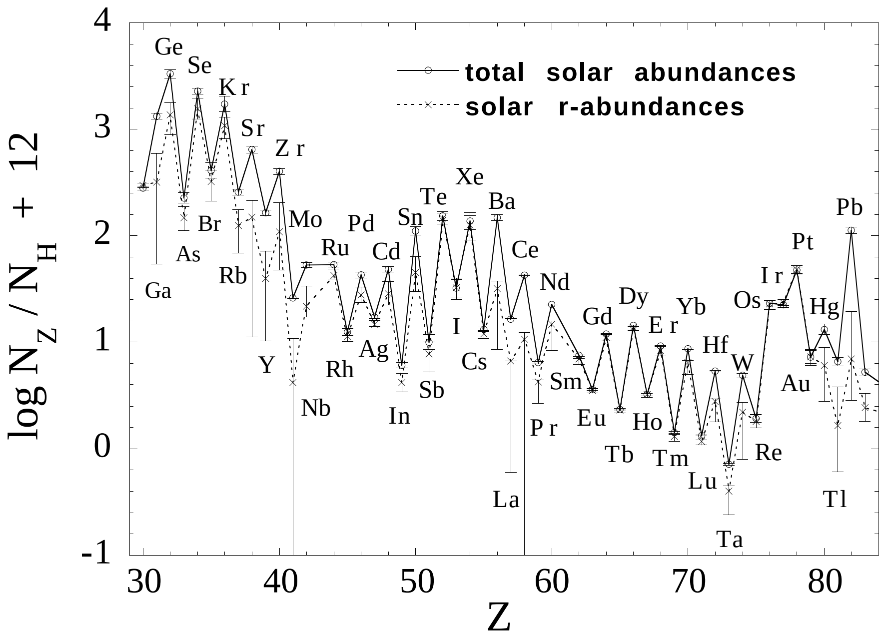

Figure 2: Elemental abundance distribution in the solar system (total and r-component). The error bars reflect uncertainties affecting observational data and experimental and theoretical (n, γ) rates.

the $A \simeq 130$ and $A \simeq 195$ peaks and the $A \simeq 160$ hill. Unfortunately, our predictions of the r-contribution to the abundance of the s-dominant nuclei in the $A \simeq 90, 120, 140, 180$ and 200 regions still suffer from large uncertainties in observational data and nuclear input to the s-process model. The corresponding elemental r-abundance distribution is shown in Fig. 2. It is seen that the r-contribution to the solar abundance of nuclei, such as Rb, Sr, Y, Zr and Ba, La, Ce, is not known with a high degree of accuracy. This feature does not facilitate our understanding concerning the origin of such heavy nuclei observed in ultra-metal-poor stars.

Finally, it should be recalled that other uncertain factors in the s-modelling have not been considered here and could also exert influence on the splitting of the solar abundances into their s- and r-components. These mainly concern nuclear uncertainties in the β-decay rates and most of the assumptions inherent to the canonical s-process model, i.e. the seed abundance distribution, the range of thermodynamic conditions to be considered and the time-independent thermodynamic profiles.

References

[1] S. Goriely, A&A **327** (1997) 845;

[2] E. Anders,N. Grevesse, Geochim. Cosmochim. Acta **53** (1989) 197;

[3] S. Goriely, in: G. Reffo et al. (eds.) Nuclear Data for Science and Technology, Societa Italiana di Fisica, Bologna (1997) p. 811;

[4] F.-K. Thielemann, M. Arnould and J.W. Truran, in: E. Vangioni-Flam et al. (eds.) Advances in Nuclear Astrophysics, Editions Frontières, Gif-sur-Yvette (1986) p. 525.

Merging compact objects — gamma-ray bursts and nucleosynthesis

H.-Thomas Janka[1], *Maximilian Ruffert*[2]

[1] *MPI für Astrophysik, Postfach 1523, 85740 Garching, Germany*
[2] *Institute of Astronomy, Madingley Road, Cambridge CB3 0HA, U.K.*

1.1 Introduction

Coalescing compact binary neutron stars or neutron star, black hole binaries are among the strongest known sources of gravitational-wave emission and as such are promising targets for the new generation of gravitational-wave interferometers currently being constructed in Europe (VIRGO, GEO600), the US (LIGO), and Japan (TAMA) (for a review, see, e.g., [1]. In addition, they have repeatedly been suggested as potential sources of r-process nuclei which might be nucleosynthesized in the dynamically ejected material (e.g., [2, 3]). Moreover, because of the huge amount of energy which can potentially be released, because of the compactness of the systems which allows for very short timescales of variability, and because of an interesting rate between 10^{-6} and 10^{-4} events per year per galaxy [4, 5], merging compact binaries have been speculated to be an (the?) origin of the gamma-ray bursts, powered by neutrino-antineutrino annihilation or by magnetically driven jets either during the merging process or afterwards when an accretion torus around the central black hole has formed (e.g., [6, 7]).

In an ongoing project, we simulate the coalescence and collisions of two neutron stars [3, 8] and the mergings of neutron star, black hole binaries [9] with the aims to compute neutrino and gravitational-wave emission, to determine the amount of material ejected from these systems, and to investigate the possibility to power gamma-ray bursts by neutrino-antineutrino annihilation in the surroundings of the merger events. To this end, the three-dimensional Newtonian equations of hydrodynamics are integrated with the 'Piecewise Parabolic Method'. We take into account the effects of the emission of gravitational waves and the corresponding backreaction on the hydrodynamics. The properties of neutron star matter are described by the equation of state of Lattimer and Swesty [10]. Energy loss and changes of the electron abundance due to the emission of neutrinos are taken into account by an elaborate "neutrino leakage scheme", which is based on a careful evaluation of the lepton number and energy source terms of all neutrino and antineutrino flavors and which includes the effects of a finite diffusion time of neutrinos out of optically thick regions.

The results of a large number of models with different parameters such as neutron star or black hole masses, mass ratios, impact parameters of the components, and initial physical conditions inside the merging neutron stars, shed light on the accessable physical parameters during the merger. For example, we obtain information about the conversion of energy into gravitational-wave and neutrino emission, about the gas mass which is dynamically expelled from the systems during the mergings, about the mass which ends up in an accretion torus around the black hole that is present in the system or assumed to be

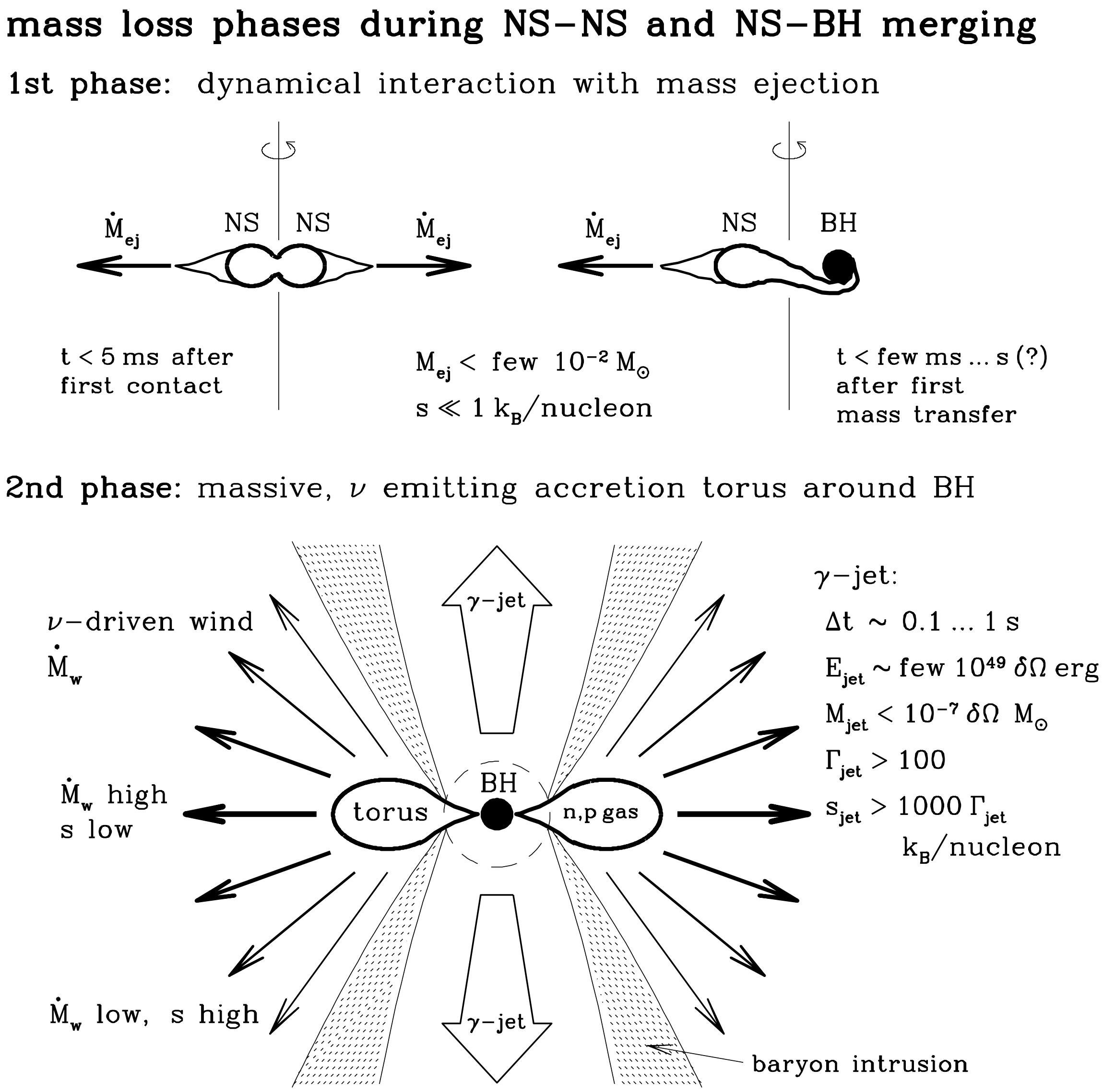

Figure 1: Mass-loss phases during NS-NS and NS-BH merging and the subsequent evolution of the massive accretion torus around the BH. During the phase of dynamical interaction between the binary components only low-entropy (dense and cold) material is ejected. In addition, the intense neutrino fluxes from a hot accretion torus could power a relativistic plasma jet that expands along the system axis. At the same time the neutrinos will drive an outflow of high-entropy, baryonic gas outside the jet cone.

formed after the merging, and about the efficiency with which neutrinos and antineutrinos annihilate into electron-positron pairs in the vicinity of the merged stars. The dynamics of the dense accretion torus of neutron matter is also followed until a quasi-stationary state is reached where the further evolution of the torus will be governed by the shear viscosity which leads to angular momentum transport outward.

Compared to our previously published calculations [3], the new models of merging or colliding neutron stars [8] have been extended with respect to the employed numerical procedures and the parameter space for the initial conditions. The former includes the use of up to 5 nested grids to cover a larger computational volume [$(300\,\mathrm{km})^3$ to $(400\,\mathrm{km})^3$] without losing resolution in the neutron stars, the latter concerns lower initial temperatures in the neutron stars and lower minimum densities at their surfaces. The simulations of neutron star black hole coalescence are done with the improved version of the code.

1.2 Some results

1.2.1 Mass loss phases and implications for nucleosynthesis

We find that during the merging of the compact binaries between about $10^{-4}\,M_\odot$ and a few $10^{-2}\,M_\odot$ of low-entropy gas ($s \ll 1\,k_\mathrm{B}$/nucleon) can be dynamically ejected. This gas is flung out into extended spiral arms because of the angular momentum transferred by the torque which is excerted by the gravitational forces of the bulk of the system matter. The amount of mass loss depends moderately on the neutron star mass ratio or the ratio of the neutron star mass to the black hole mass, respectively. However, the mass loss is extremely sensitive to the total angular momentum of the system which is a function of the assumed spins of the components. For anti-spin set-up (i.e., the neutron star spin vectors are opposite to the orbital angular momentum vector), the systems eject more than two orders of magnitude less material than in the case of corotation where the largest mass loss is found. If there is no preferred spin constellation for evolved compact binaries, an average value of $M_\mathrm{ej} \sim 10^{-3}\,M_\odot$ per event seems plausible. With an assumed event rate of 10^{-5} per year this leads to a best estimate of the total yield of about $100\,M_\odot$ of such material in our Galaxy, although with a large uncertainty of at least one order of magnitude up or down associated with the inaccuracy of the event rates. Because of this significant contribution to the nucleosynthetic content of the Galaxy, the composition of the ejecta is a critical issue. In the crust and outer mantle layers of the neutron star, heavy, very neutron-rich nuclei can be present at conditions of beta-equilibrium (zero neutrino chemical potential). These nuclei should start to undergo beta decays as soon as expansion and decompression sets in. If a sufficient number of free neutrons is present, an r-processing might take place which could produce nuclei in the vicinity of the third r-process abundance peak (see [2, 3]). A fair fraction (if not all) of this r-process material in our Galaxy could possibly be explained from such origin.

Preliminary results by Rosswog et al. (this conference) seem to indicate that the abundance pattern of r-process elements beyond $A \gtrsim 120$ might be reproduced promisingly well in the expanding material. However, before these results are conclusive, it has to be shown how they depend on the assumed initial conditions, the timescales of the expansion, and the still incomplete physical description which is applied during the nucleosynthesis

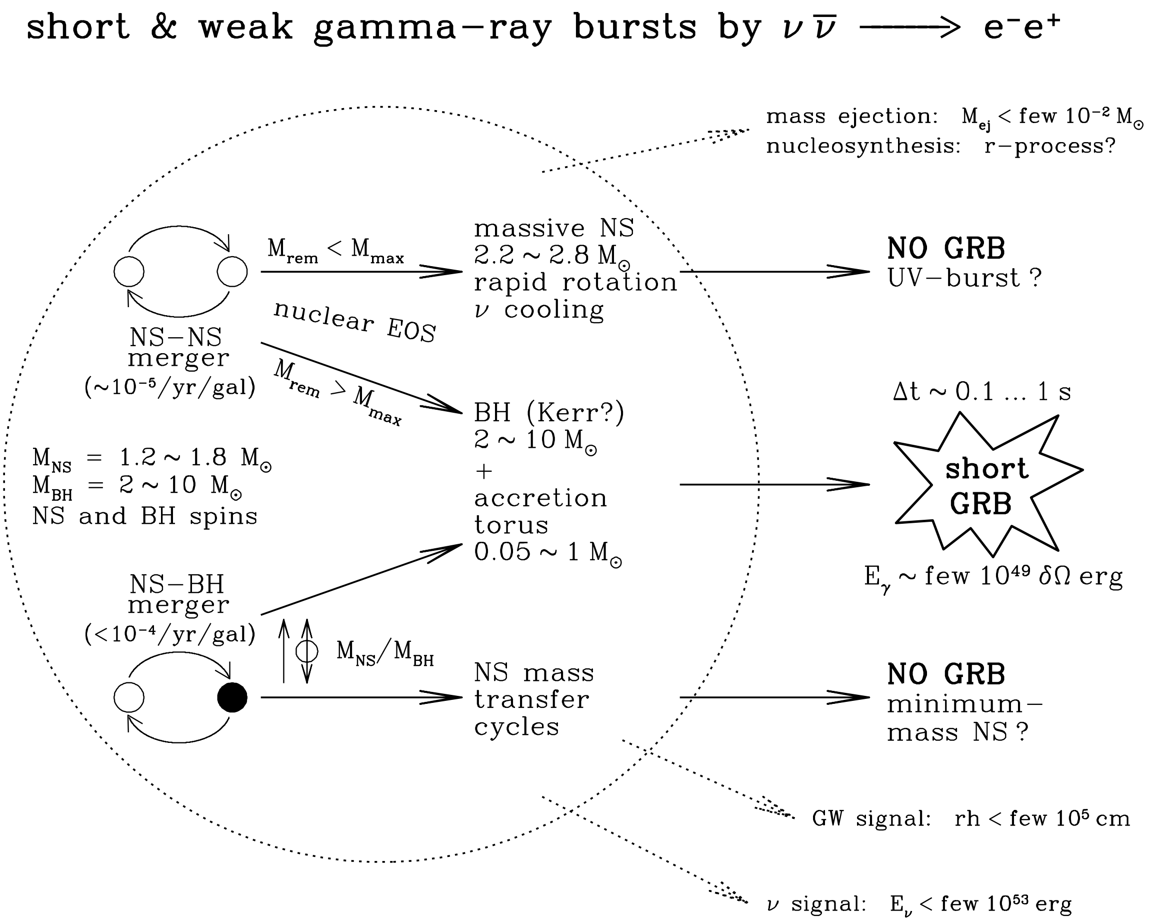

Figure 2: Possible evolution paths from NS-NS and NS-BH mergers to short gamma-ray bursts powered by neutrino-antineutrino annihilation into electron-positron pairs. The evolution tracks depend on the masses of the neutron star(s) and the black hole, on the total angular momentum in the system, and on the stiffness of the nuclear equation of state. Very favorable conditions for an energetic relativistic plasma jet are only obtained if a black hole emerges from the dynamical interaction, which is surrounded by a hot, dense accretion torus, because this torus can emit large neutrino fluxes for a time much longer than the dynamical timescale of the system and with an efficiency of neutrino production that is at least several per cent of the rest-mass energy of the accreted matter. The gamma-ray bursts should be accompanied by the ejection of nucleosynthesis products in considerable amounts, the emission of large numbers of thermal neutrinos, and the production of a gravitational-wave signal which can be detected with the new generation of interferometer experiments. The coincidence of gamma-ray and gravitational-wave measurements would yield a clear identification of the merging of a compact binary as the source of the energy of the relativistic plasma jet which generates the gamma burst.

phase. Also, Rosswog et al. come up with a somewhat larger (about one order of magnitude) number for the average mass of low-entropy ejecta from neutron star mergers than suggested by our simulations.

In our models we find that shocks and shear heating raise the temperatures in the initially cool (or cold) neutron stars as soon as the two components start to fuse. However, the neutrino emission does not become large before shock-heated material with high angular momentum forms an extended dilute cloud ($\rho \sim 10^{12}\,\mathrm{g/cm^3}$) around the massive, much denser body ($\rho \gtrsim 10^{14}\,\mathrm{g/cm^3}$) of the merged stars. This compact core has a mass of around 2.5–3 $M_\odot$ and will collapse into a black hole within milliseconds, unless the nuclear equation of state is stiff enough to prevent gravitational instability. A gas mass of between about $0.02\,M_\odot$ and $0.2\,M_\odot$ obtains enough angular momentum to stay in an accretion torus which transfers gas into the central black hole on a viscous timescale, which is probably 100–1000 times longer than the few milliseconds of dynamical merging. A similar situation develops in case of neutron star, black hole mergers where the torus masses turn out to be somewhat larger, up to about $0.5\,M_\odot$. In particular, in the partially neutrino-transparent torus peak temperatures of more than 10 MeV can be reached and large neutrino luminosities is excess of $10^{53}\,\mathrm{erg/s}$ are produced. These neutrino luminosities can create a neutrino-driven wind by which high-entropy gas is blown off the torus "surface" after it has absorbed energy from the intense neutrino fluxes. The corresponding mass-loss rates are very uncertain, but may well be several 10^{-3} to $10^{-2}\,M_\odot\,\mathrm{s}^{-1}$ for as long as about a second if accretion rates between $10^{-1}\,M_\odot\,\mathrm{s}^{-1}$ and $1\,M_\odot\,\mathrm{s}^{-1}$ are assumed. The latter are favorable for gamma-ray burst scenarios (see below). These neutrino-processed hot ejecta may show a large variety of combinations of entropies and electron (proton) fractions, dependent on the stage of the evolution and the direction of the mass outflow. The detailed properties of this high-entropy component of the mass loss from merging compact binaries have to be revealed by numerical models which take into account the interaction of the emitted neutrinos with the gas in the surface-near regions of the accretion torus. Figure 1 summarizes the essentials of the two stages of mass loss from merging compact binaries.

1.2.2 Short gamma-ray bursts

If the central, massive body did not collapse into a black hole, it would continue to cool down by radiating neutrinos with high luminosities, just like a massive, hot proto-neutron star in a supernova. These neutrinos would deposit a fraction of their energy in the low-density layers near the surface and drive a baryonic wind in which most of the energy is consumed lifting mass in the strong gravitational potential. The expansion is therefore nonrelativistic and there would be no chance to get a fireball which can give rise to a gamma-ray burst powered by neutrino-antineutrino annihilation (see the upper evolution path in Fig. 2).

This unfavorable situation is avoided if the central object collapses into a black hole after the merging of the neutron stars or if a neutron star coalesces with a black hole. In the latter case the region along the system axis stays essentially free of baryons [7, 9], in the former case the axis region cleans out within the free-fall timescale of a few milliseconds as the black hole sucks the baryons away. Thus a nearly baryon-free funnel is produced

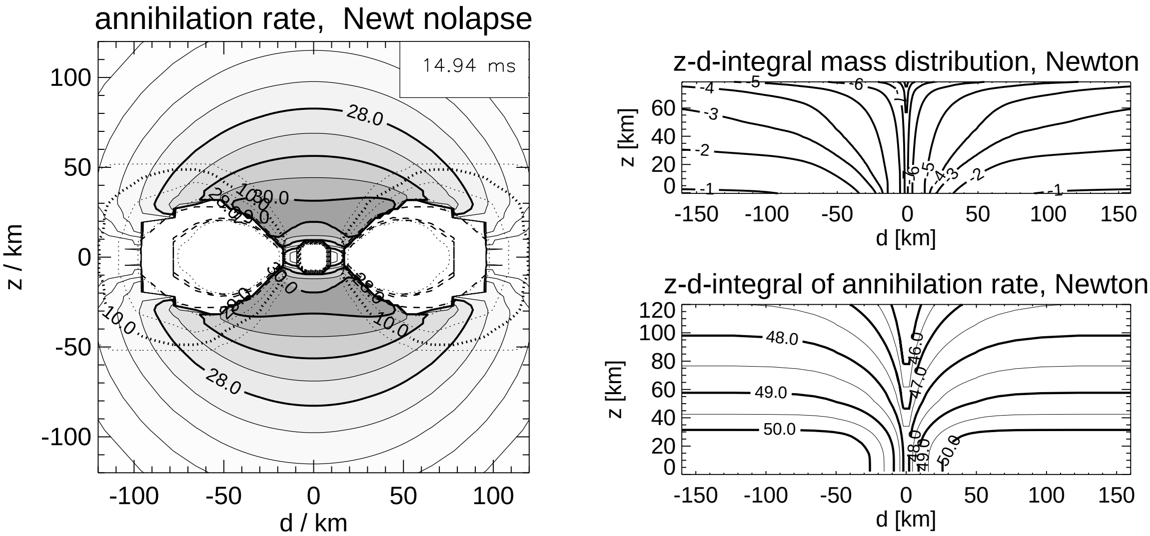

Figure 3: *Left:* Map of the (azimuthally averaged) rate density of energy deposition by $\nu\bar{\nu}$ annihilation into e^+e^- pairs in the surroundings of the accretion torus at a time when the torus has reached a quasi-stationary state. The torus has been formed from the merger of two neutron stars after the massive remnant has collapsed into a black hole. The levels represented by solid contours are spaced logarithmically in steps of 0.5 dex. Darker grey shading indicates higher values of the energy deposition rate, the maximum values are above $10^{30}\,\mathrm{erg\,cm^{-3}\,s^{-1}}$. The dotted lines show isodensity contours of the torus, the dashed lines give the neutrinospheres for the different neutrino and antineutrino flavors (both azimuthally averaged). The white octagonal area around the center represents the black hole. The total integral of the energy deposition rate below a density of $10^{11}\,\mathrm{g/cm^3}$ is $4.9 \times 10^{50}\,\mathrm{erg/s}$.
Right: Contours of constant values of the volume integral $2\pi \int_z^\infty \mathrm{d}\eta \int_0^d \mathrm{d}\xi$ over the mass density (upper panel) and over the rate density of energy deposition by $\nu\bar{\nu}$ annihilation (lower panel) for the torus configuration shown in the left figure. Thus in the upper panel for each point (d, z) the mass inside a cylinder with radius d from z to infinity is given, and in the lower panel the integral rate of energy deposition within this cylindrical volume is displayed.

where further baryon contamination is prevented by centrifugal forces. This provides good conditions for the creation of an $e^{\pm}\gamma$ plasma with little baryonic pollution powered by $\nu\bar{\nu}$-annihilation.

In the described scenario, there is a high baryon density near the equatorial plane due to the presence of the accretion torus which allows only for a collimated expansion of relativistic pair-plasma along the system axis. Using the term "jet" is therefore much more adequate than speaking about a fire-"ball".

If intense neutrino fluxes provide the energy which ultimately causes the observable gamma-ray burst, this burst will inevitably be accompanied by a neutrino-driven outflow of high-entropy, baryonic material outside the narrow cone of the relativistic jet (see Fig. 1). It may be possible that this hot gas, which carries a thermal energy comparable to or even larger than the gamma-burst energy, can give rise to an afterglow as observed in different wavelengths at the locations of gamma-ray bursts (e.g., in case of GRB970228 and GRB970508).

From our torus models we find that the energy deposition rate by $\nu\bar{\nu}$-annihilation into e^+e^- pairs can reach an integral value in the surroundings of the accretion torus as large as $\dot{E}_{\nu\bar{\nu}} \approx 5\times 10^{50}\,$erg/s (Fig. 3, left). The fraction of this energy that is injected into the low-density and low-mass funnel along the system axis (Fig. 3, upper right panel) is several $10^{49}\,$erg/s (Fig. 3, lower right panel). With a neutrino luminosity (in all neutrino and antineutrino flavors) of $L_\nu \approx 10^{53}\,$erg/s the total annihilation efficiency is therefore $\dot{E}_{\nu\bar{\nu}}/L_\nu \approx 5\times 10^{-3}$; the conversion of neutrino energy into the energy of the pair-plasma jet is about 10 times less efficient. Our simulations reveal (Fig. 3, upper right panel) that around 5 ms after the massive remnant of the merger has collapsed into a black hole, the axis region is not yet completely evacuated but still contains a mass of approximately $10^{-5}\,M_\odot$. Although this is very low (and only about one order of magnitude higher than our lower limit of numerical mass resolution), it is still two orders of magnitude above the $\sim 10^{-7}\,M_\odot$ which are desired for relativistic jet expansion with Lorentz factors of , $\approx E_{\rm jet}/(M_{\rm jet}c^2) \sim 100\,(E_{\nu\bar{\nu}}/10^{49}\,{\rm erg})(M_{\rm jet}/10^{-7}\,M_\odot)^{-1}$. Due to the enormous thermal pressure of the $e^{\pm}\gamma$ plasma the jet should be able to drill a hole into the low-density funnel and will push away the $\sim 10^{-5}\,M_\odot$ of baryons, opening up a cleaner funnel for the subsequent pair plasma, which hopefully does not get admixed too many baryons by hydrodynamic instabilities along the boundaries of the jet cone. One can speculate whether the phase of cleaning might show up in a precursor of the actual gamma-ray burst or in a gradual initial hardening of the gamma flux. A number of X-ray precursors to gamma bursts have indeed been detected by the Ginga experiment.

On grounds of our numerical models, we can also make predictions for the discussed scenario on the duration of the energy input from the central engine and on the beaming of the pair-plasma jet. Unless the black hole component of the coalescing binary was already of Kerr type, we find that the black holes which form after the merging will not rotate extremely rapidly (relativistic rotation parameter $a = Jc/(GM^2) \lesssim 0.6$). Therefore the torus matter which is accreted into the black hole can radiate at most about 6% of its rest mass in neutrinos. This gives a total neutrino energy of $E_\nu \sim 10^{52}\,(M_{\rm torus}/0.1\,M_\odot)\,$erg. With a luminosity of $L_\nu \approx 10^{53}\,$erg/s (this numerically determined value agrees well with the "optimum" case calculated analytically in Ref. [3]) we expect a lifetime (accretion time) of the torus of $t_{\rm acc} \approx E_\nu/L_\nu \sim 0.1\,(M_{\rm torus}/0.1\,M_\odot)\,$s. The total jet energy can therefore be estimated to be between several 10^{48} erg and nearly 10^{50} erg at best, which is sufficient to explain the observed gamma fluxes of weak bursts if moderate beaming is involved. With an estimated jet luminosity from $\nu\bar{\nu}$ annihilation of $\dot{E}_{\rm jet} \sim 10^{49}$ erg/s weak gamma bursts with a gamma luminosity of $L_\gamma \sim 10^{50}\, 2\delta\Omega/(4\pi)$ erg/s can be accounted for if the jet covers a volume angle of $\delta\Omega/(4\pi) \sim 1/20$, corresponding to an opening angle of about 26 degrees.

More energetic and long gamma-ray bursts need a different explanation. More energy for the gamma burst and longer accretion times can be achieved if the torus were more massive or if there were a Kerr black hole at the center of the accretion torus. Both may be the case if the torus, black hole geometry results from a failed supernova of a rotating progenitor star ("collapsar" [11] or "micro-quasar" [13]) or from the merging of a black hole, white dwarf binary or of a neutron star or black hole with the helium core of its red giant companion [5].

Acknowledgements

MR is grateful for support by a PPARC Advanced Fellowship, HTJ thanks for support by the "Sonderforschungsbereich 375-95 für Astro-Teilchenphysik" der DFG. Useful discussions with C. Fryer, S. Rosswog, K. Takahashi, R. Wijers, and S. Woosley are acknowledged.

References

[1] Thorne K.S., in: *Proceedings of the Snowmass 95 Summer Study on Particle and Nuclear Astrophysics and Cosmology*, eds. E.W. Kolb, R. Peccei, World Scientific, 398 (1995).

[2] Lattimer J.M., Schramm D.N., ApJ 192, L145 (1974); Lattimer J.M., Schramm D.N., ApJ 210, 549 (1976); Eichler D., Livio M., Piran T., Schramm D.N., Nat 340, 126 (1989); Meyer B.S., ApJ 343, 254 (1989); Davies M.B., Benz W., Piran T., Thielemann F.K., ApJ 431, 742 (1994).

[3] Ruffert M., Janka H.-Th., Schäfer G., A&A 311, 532 (1996); Ruffert M., Janka H.-Th., Takahashi K., Schäfer G., A&A 319, 122 (1997).

[4] Narayan R., Piran T., Shemi A., ApJ 379, L17 (1991); Phinney E.S., ApJ 380, L17 (1991); Tutukov A.V., Yungelson L.R., Iben I., ApJ 386, 197 (1992); Tutukov A.V., Yungelson L.R., MNRAS 260, 675 (1993); Lipunov V.M., Postnov K.A., Prokhorov M.E., Panchenko I.E., Jørgensen H.E., ApJ 454, 593 (1995); Portegies Zwart S., Verbunt F., A&A 309, 179 (1996); Portegies Zwart S., Spreeuw J.N., A&A 312, 670 (1996); Lipunov V.M., Postnov K.A., Prokhorov M.E., MNRAS 288, 245 (1997); Portegies Zwart S., Hut P., McMillan S., Verbunt F., A&A 328, 143 (1997); Portegies Zwart S., Yungelson L., A&A 332, 173 (1998); Bagot J., Portegies Zwart S., Yungelson L., A&A 332, L57 (1998); Bethe H.A., Brown G.E., preprint (1998).

[5] Fryer C.L., Woosley S.E., preprint, astro-ph/9804167 (1998).

[6] Blinnikov S.I., Novikov I.D., Perevodchikova T.V., Polnarev A.G., Sov. Astron. Lett. 10, 177 (1984); Paczyński B., Acta Astron. 41, 257 (1991); Narayan R., Paczyński B., Piran T., ApJ 395, L83 (1992); Mészáros P., Rees M.J., ApJ 397, 570 (1992); Woosley S.E., ApJ 405, 273 (1993); Jaroszyński M., Acta Astron. 43, 183 (1993); Mochkovitch R., Hernanz M., Isern J., Martin X., Nat 361, 236 (1993); Witt H.J., Jaroszyński M., Haensel P., Paczyński B., Wambsganss J., ApJ 422, 219 (1994); Jaroszyński M., A&A 305, 839 (1996); Mochkovitch R., Heranz M., Isern J., Loiseau S., A&A 293, 803 (1995).

[7] Lee W.H., Kluźniak W., Acta Astron. 45, 705 (1995); Kluniak W., Lee W.H., ApJ 494, L53 (1998).

[8] Ruffert M., Janka H.-Th., preprint MPA 1088, astro-ph/9804132 (1998); Ruffert M., Janka H.-Th., in preparation.

[9] Eberl T., Diploma Thesis, Technical University Munich (1998); Eberl T., Ruffert M., Janka H.-Th., in preparation (1998).

[10] Lattimer J.M., Swesty F.D., Nucl. Phys. A535, 331 (1991).

[11] Woosley S.E., ApJ 405, 273 (1993).

[12] Woosley S.E., Baron E., ApJ 391, 228 (1992).

[13] Paczyński B., ApJ 494, L45 (1998).

Coalescing Neutron Stars: A Solution to the R-Process Problem ?

S. Rosswog[1], *F.K. Thielemann*[1], *M.B. Davies*[2], *W. Benz*[3], *T. Piran*[4]

[1] *Departement für Physik und Astronomie, Universität Basel, Switzerland*
[2] *Institute of Astronomy, University of Cambridge, UK*
[3] *Physikalisches Institut, Universität Bern, Switzerland*
[4] *Racah Institute for Physics, Hebrew University, Jerusalem, Israel*

1.1 Introduction

Most recent nucleosynthesis parameter studies [3, 4, 11] place questions on the ability of high entropy neutrino wind scenarios in type II supernovae to produce r-process nuclei for $A < 110$ in correct amounts. In addition, it remains an open question whether the entropies required for the nuclei with $A > 110$ can actually be attained in type II supernova events. Thus, an alternative or supplementary r-process environment is needed, leading possibly to two different production sites for r-process nuclei: a high entropy, high Y_e (neutrino wind in type II supernovae) and a low entropy, low Y_e (decompression of neutron star (ns) material) scenario.
Further indications for a production site possibly different from SN II arise from observations of low metallicity stars [9]. It seems that the production of r-process nuclei is delayed in comparison with the major SN II yields, a fact that would be consistent with the merging scenario of two neutron stars.
The tidal disruption of a ns by a black hole and possible consequences for nucleosynthesis has first been studied by Lattimer and Schramm [6, 7], the merging of a neutron star binary has been discussed by Symbalisty and Schramm [16]. The related decompression of the neutron star material has been investigated by Lattimer et al. [5], Eichler et al. [2], who also discussed various other aspects of such a merging scenario, and by Meyer [10]. In the context of numerical simulations the merging event nucleosynthesis has been discussed by Davies et al. [1] and by Ruffert et al. [15].

1.2 The Calculations

To investigate the possible relevance of neutron star mergers for the r-process nucleosynthesis we perform 3D Newtonian SPH calculations of the hydrodynamics of equal (1.6 $M_\odot$ of baryonic) mass neutron star binary coalescences. Starting with an initial separation of 45 km we follow the evolution of matter for 12.9 ms. We use the physical equation of state of Lattimer and Swesty [8] to model the microphysics of the hot neutron star matter. To test the sensitivity of our results to the chosen approaches and approximations we perform in total 10 different runs where we test each time the sensitivity to one property of our model [14]. We vary the resolution ($\sim$ 21000 and $\sim$ 50000 particles), the equation of state (polytrope), the artificial viscosity scheme [12], the stellar masses (1.4 $M_\odot$ of baryonic matter), we include neutrinos (free-streaming limit), switch off the gravitational backreaction force, and vary the initial stellar spins. In addition we test the influence of the initial configuration, i.e. spherical stars versus corotating equilibrium configurations.

1.3 Results

We find that, dependent on the initial spins and strongly dependent on the EOS, between $4 \cdot 10^{-3}$ and $4 \cdot 10^{-2}$ $M_\odot$ become unbound. Assuming a core collapse supernova rate of $2.2 \cdot 10^{-2}$ (year galaxy) $^{-1}$ [13], one needs 10^{-6} to 10^{-4} $M_\odot$ of ejected r-process material per supernova event to explain the observed abundances if type II supernovae are assumed to be the only source. The rate of neutron star mergers has recently been estimated to be $8 \cdot 10^{-6}$ (year galaxy)$^{-1}$ (see [17]). Taking these numbers, one would hence need $\sim 3 \cdot 10^{-3}$ $M_\odot$ to ~ 0.3 $M_\odot$ for an explanation of the observed r-process material exclusively by neutron star mergers. Thus our results for the ejected mass from $4 \cdot 10^{-3}$ to $3 - 4 \cdot 10^{-2}$ $M_\odot$ look very promising (see Figure 1).

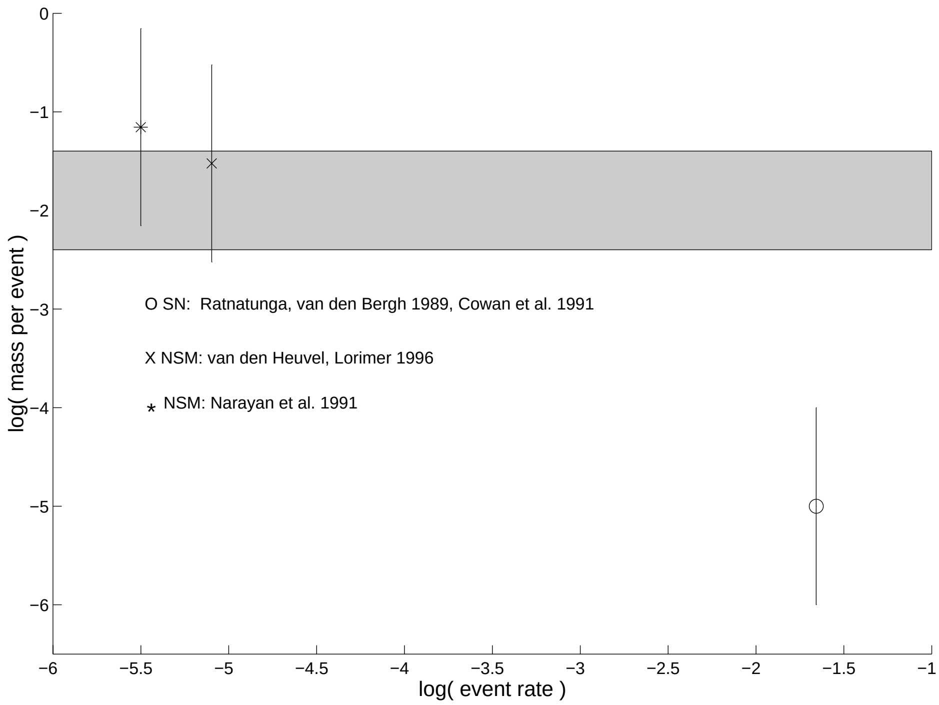

Figure 1: The shaded region shows the amount of ejecta found in our calculations. The circle shows the amount of ejecta needed per event if SN II are assumed to be the only sources of the r-process. The asterisk gives the needed ejecta per merging event for the rate of Narayan et al. (1991), the cross for the estimate of van den Heuvel and Lorimer (1996). The event rate is given in year^{-1} galaxy^{-1}, the ejected mass in solar units.

As a first step we use the mean properties of all ejected particles (initial corotation) for an r-process calculation. We adopt the following approach: in the very first expansion phase (where $\rho > \rho_{drip} \approx 4 \cdot 10^{11}$ g cm^{-3}) we use the abundances of neutrons, protons, alphas and a representative nucleus provided by the LS-EOS. When the density drops below ρ_{drip} we switch over to a treatment of individual nuclei with a full r-process network following all reactions like neutron capture, photo-disintegrations, β-decays etc. as discussed in Freiburghaus et al. [4]. Since the representative nucleus at ρ_{drip} was too neutron rich ($(Z, A) = (26, 155)$), we took the most neutron rich nucleus in the network ($(Z, A) = (26, 73)$) and assumed the remaining neutrons to be free. Following the trajectory given by the hydro calculation (extrapolation for $t > 12.9$ ms) we obtained the abundance pattern that is shown in Figure 2 together with the observed r-process abundances.

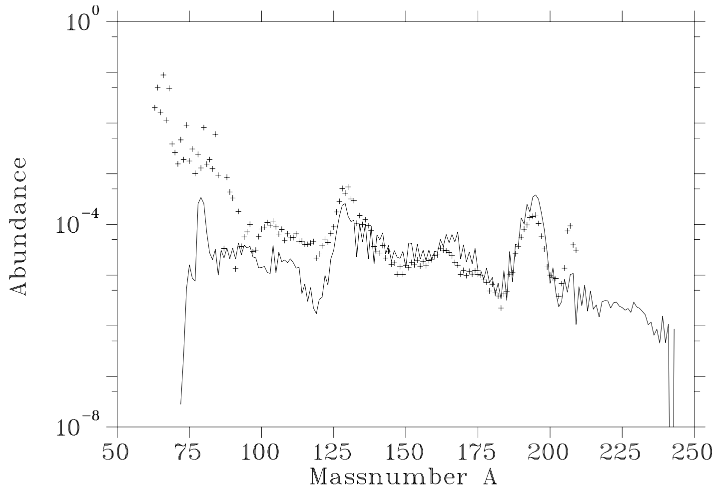

Figure 2: Comparison of the r-process calculations for a corotating system (initial corotation; line) with the observed abundances (crosses).

The observed features of the abundance pattern in the range $125 < A < 200$ are well reproduced. Especially the peak around $A = 195$ is easily reproduced without any tuning of the initial entropy.
This approach has two shortcomings: (i) as long as the LS-EOS is used, only one (representative) nucleus is used instead of an ensemble of nuclei and (ii) weak interactions such as β-decays or e^-−, e^+−captures on protons and neutrons are disregarded in this early phase. For the case of initial corotation this approximation might not be crucial since the ejecta essentially stay cold (until perhaps, at later times, heating by β-decays sets in). For different initial spins, however, weak interactions might change the Y_e of the composition in this early phase.
Clearly, in future investigations these aspects have to be treated in more detail.

Acknowledgements

We thank Ch. Freiburghaus for providing us with Fig.2. S.R. thanks P. Höflich and H.T. Janka for useful discussions.

References

[1] M.B. Davies, W. Benz, T. Piran and F.K. Thielemann, ApJ **431** (1994) 742

[2] D. Eichler, M. Livio, T. Piran and D.N. Schramm, Nature **340** (1989) 126

[3] Ch. Freiburghaus, E. Kolbe, T. Rauscher, F.K. Thielemann, K.-L. Kratz and B. Pfeiffer, in Proc. 4th Int. Symp. on Nuclei in the Cosmos (Univ. of Notre Dame), ed. J. Görres, G. Mathews, S. Shore, & M. Wiescher, Nuc. Phys. **A621** (1997) 405c

[4] Ch. Freiburghaus, J.F. Rembges, E. Kolbe, T. Rauscher, F.K. Thielemann, K.-L. Kratz and B. Pfeiffer, ApJ (1998) submitted

[5] J.M. Lattimer, F. Mackie, D.G. Ravenhall and D.N. Schramm, ApJ **213** (1977) 225

[6] J.M. Lattimer and D.N. Schramm, ApJ **192** (1974) L145

[7] J.M. Lattimer and D.N. Schramm, ApJ **210** (1976) 549

[8] J.M. Lattimer and F.D. Swesty, Nucl. Phys. **A535** (1991) 331

[9] G. Mathews, G. Bazan and J. Cowan, ApJ **391** (1992) 719

[10] B.S. Meyer, ApJ **343** (1989) 254

[11] B.S. Meyer and J.S. Brown, ApJ **S112** (1997) 199

[12] J.P. Morris and J.J. Monaghan, J. Comp. Phys. **136** (1997) 41

[13] K. Ratnatunga and S. van den Berg, ApJ **343** (1989) 713

[14] S. Rosswog, M. Liebendörfer, F.K. Thielemann, M. B. Davies, W. Benz and T. Piran, A & A (1998) submitted

[15] M. Ruffert, H.T. Janka, K. Takahashi and G. Schäfer, A & A **319** (1997) 122

[16] E.M.D. Symbalisty and D.N. Schramm, ApJ **22** (1982) 143

[17] E.P.J. van den Heuvel and D. Lorimer, MNRAS **283** (1996) L37

Nova Explosions: Abundances and Light Curves

James W. Truran[1]

[1] *Department of Astronomy and Astrophysics, Enrico Fermi Institute, University of Chicago*

1.1 Introduction

The outburst mechanism for a classical nova explosion is recognized to be the occurrence of a thermonuclear runaway in an accreted hydrogen-rich envelope on a white dwarf in a close binary system. Buildup of a hydrogen-rich envelope on the white dwarf continues to some critical value, which is strongly dependent upon the white dwarf mass, and runaway ensues.

Numerical hydrodynamic calculations have revealed that many distinguishing characteristics of these events are dictated by a complicated interplay of nuclear reactions and convection during the last few minutes of the runaway [1, 2, 3, 4]. The high temperatures (T $\approx$ 2-3 x 10^8 K) achieved in the runaway drive proton captures on available carbon, nitrogen, and oxygen (CNO) nuclei, forming significant quantities of the proton-rich isotopes ^{13}N, ^{14}O, ^{15}O, and ^{17}F. The positron decay lifetimes of these nuclei ($\sim 10^2$ - 10^3 seconds) constrain further nuclear energy generation on the prevailing hydrodynamic timescale ($\tau_{hyd} \approx$ seconds). (Theoretical studies indicate that novae may represent the source of most of the ^{15}N and ^{17}O in Galactic matter.)

The high temperatures at the base of the envelope also drive convection, which serves to transport the formed radioactivities to the outermost regions of the envelope. Positron decays here play an extremely important role: (1) they provide significant heating in regions far removed from the thermonuclear burning regime, which acts to drive expansion and ejection of these regions at high velocities; (2) they emit gamma rays which may be detectable from relatively nearby novae and thus provide a probe of the runaway physics; and (3) their decays yield stable isotopes of the CNO elements with distinctly non-solar isotopic patterns that may again afford the opportunity for a possible observational test of nova models. Convection may also give rise to overshooting and associated dredge up of matter from the underlying carbon-oxygen (CO) or oxygen-neon (ONe) white dwarf core. Such envelope enrichment is indeed observed, and is demanded for an understanding of the powering of the rapid early developments of the light curves of the fastest classical novae.

Over the past decade, observations of novae spanning a broad range of wavelengths have provided important confirmation of the thermonuclear runaway model and significant clues to the natures of the underlying white dwarfs. IUE and HST observations have confirmed the presence of large abundance enrichments of CNO and ONeMg elements, the products of dredge up, thus establishing the presence of both CO and ONe white dwarfs in nova systems. EXOSAT and ROSAT observations have revealed the continued presence of the constant bolometric luminosity phase (powered by the hydrogen burning shell) at long times, in the form of soft X-ray emission. Compton GRO observations have set limits on gamma ray emission from ^{7}Be and ^{22}Na decay from several recent novae. Infrared observations have confirmed the formation of interesting "stardust" in nova environments.

Such observations have also presented nova theorists with many challenges. We discuss two outstanding questions concerning nova explosions: the early development of the light curves of the most dynamic ("fastest") nova events and the mechanism of envelope enrichment.

1.2 The Early Evolution of Nova Light Curves

Convective mixing and elemental abundance enrichments are crucial to the rapid developments of the light curves of the fastest classical novae. Distinguishing features of fast novae include: (1) luminosities at maximum that can achieve values up to an order of magnitude larger than those predicted by the core-mass-luminosity relation for hydrogen burning shells on degenerate cores [5, 6]; (2) high velocities of ejection ($>$ 1000-2000 km s^{-1}); and (3) a rapid decline from maximum of the visual light curve. It is the correlation of the rate of decline with the peak luminosity that defines the M_B-t_3 relation, which leads to the use of novae as distance indicators. We note in this regard that all fast novae achieve and maintain visual luminosities in excess of those predicted by the core-mass-luminosity relation during the first few days to a week of their outbursts. How might this behavior be understood? Scrutiny of the models [7] reveals that the total energy generated in the convective burning shell is indeed consistent with the occurrence of this high luminosity phase of evolution, of duration $\sim$ 3-7 days. The thermonuclear runaway yields a shell burning temperature T_{shell} which initially is well in excess of that characteristic of quasi-static shell hydrogen burning on a degenerate core. The temperature will relax to $T_{quasi-static}$ on approximately a thermal time scale, of order several days. For the period during which $T_{shell} > T_{quasi-static}$, the high temperature sensitivity of the thermonuclear reactions results in a level of energy generation well above the quasi-static value. This may also hold important implications for early mass loss and the spectral evolution of novae over the first week or two. As convection retreats from the surface, any overlying matter may be expected to be driven off at high velocities, which implies a quite violent phase of mass loss. The theoretical challenge here is to be able to calculate accurately the distribution of this energy into: (1) lift-off energy from the gravitational potential well; (2) kinetic energy of the ejecta; and (3) photon output.

1.3 Envelope Abundance Enrichments and Nucleosynthesis

The high levels of enrichment of nova envelopes in carbon, nitrogen, oxygen, and neon [8, 9] confirm that significant outward mixing must occur, of material from the underlying CO or ONe white dwarf core: typically 30-40 percent of the mass of the ejecta is in the form of such dredged up material [10]. A critical consideration here is that the enrichments of CNO and ONeMg elements must exist during the final stages of the runaway. On the approximately three minute timescale during which the rates of positron decay constrain the operation of the CNO cycles, the nuclear energy available is simply the energy release resulting from the capture of one or two protons on every available CNO nucleus. For matter of solar composition, the maximum allowed energy release on a dynamic timescale

($\approx 2 \times 10^{15}$ ergs g^{-1}) represents only a small fraction of the envelope binding energy ($\sim$ 2-4 x 10^{17} ergs g^{-1}). Ignition occurs, but the violence of the runaway is severely constrained and a relatively slow rise to visual maximum ensues (as the envelope slowly expands). For these conditions, such mass ejection as might result occurs at low velocities. In contrast, the fastest classical novae exhibit rapid early developments of their light curves and the ejection of matter at high velocities ($\gtrsim$ 1000 km s^{-1}). Numerical studies confirm that such behaviors are consistent with the presence of high levels of dredged up CO or ONe white dwarf core matter in nova envelopes.

The demand for a mechanism of heavy element enrichment of nova envelopes thus follows from both theoretical and observational consideration. The three most promising mechanisms for enrichment are shear mixing, diffusion, and convective overshooting. Recent multi-dimensional hydrodynamic studies of reactive flow in nova outbursts have addressed particularly the question of convective overshooting. Glasner, Livne, & Truran [11] studied the thermonuclear evolution during the final stages of the runaway, using the 2D, implicit, hydrodynamic code VULCAN. An important result of this 2D numerical study was the finding that convective overshoot mixing, which acted to dredge up matter from an underlying CO core, may be responsible for the observed levels of heavy element enrichment in nova envelopes. Dredge up occurred during the final stages of the runaway ($T \sim 10^8$ K), yielding a final CNO abundance level of approximately 30 %. An independent 2D study of evolution near the peak of the runaway by Kercek, Hillebrandt, & Truran [12] found a similar level of convective overshoot mixing, but on a longer timescale. These authors used the same starting model as did Glasner *et al.*, but their study was carried out with a modified version of the code PROMETHEUS. The general agreement between the findings of these two 2D investigations at first seemed encouraging, and suggested that convective overshoot mixing may indeed be the mechanism responsible for the envelope abundance enrichments in novae. However, preliminary results recently obtained by Kercek & Hillebrandt [13] from a 3D investigation of a nova-like runaway indicate rather that significant dredge up of core matter by overshooting does not accompany the later stages of the runaway. A firm identification of the mechanism of envelope enrichment in novae is therefor not possible at this time.

References

[1] Truran J W 1982, *Essays in Nuclear Astrophysics*, Eds. C. A. Barnes, D. D. Clayton, & D. N. Schramm (Cambridge: Cambridge University Press), p 467

[2] Starrfield S, Truran J W, Wiescher M C, & Sparks W M 1998, *Mon. Not. Royal Astron. Soc.*, in press

[3] José J & Hernanz M 1998, *Astrophys. J.* **494**, 680

[4] Prialnik D & Kovetz A 1995, *Astrophys. J.* **445**, 789

[5] Paczyński B 1971, *Acta Astron.* **21**, 417

[6] Tuchman I & Truran J W 1998, *Astrophys. J.*, in press

[7] Hayes J 1993, *Ph.D. Thesis*, University of Illinois

[8] Truran J W & Livio M 1986, *Astrophys. J.* **308**, 721

[9] Gehrz R D, Truran J W, Williams R E, & Starrfield S 1998, *PASP* **110**, 3

[10] Livio M & Truran J W 1994, *Astrophys. J.* **425**, 797

[11] Glasner S A, Livne E, & Truran J W 1997, *Astrophys. J.* **475**, 754

[12] Kercek A, Hillebrandt W, & Truran J W 1998, *Astron. Astrophys.*, in press

[13] Kercek A & Hillebrandt W 1998, private communication

Gravitational Collapse with Semi-Implicit Hydrodynamics

M. Liebendörfer, S. Rosswog

University of Basel, Department for Physics and Astronomy, Klingelbergstr. 82, CH-4056 Basel, Switzerland

For the selfconsistent calculation of a core-collapse supernova two reasons recommend an implicit evaluation of the hydrodynamical equations. First the hydrodynamical time scale of the dense proto-neutron star is much smaller than the time scale of neutrino diffusion and the evolution of the outer low-density layers. Therefore it is important to take implicit time steps that are not limited by the Courant-Friedrichs-Lewy condition. Second, general relativistic effects are important in the neighborhood of a neutron star, and the corresponding relativistic constraint equations are easily implemented in an implicit scheme [5, 6, 8, 10]. Additionally, such a scheme offers the option of a selfconsistent adaptive gridding for high shock resolution. Here we give a progress note on the development of such a code.

To guarantee a proper shock handling and for a straightforward application of the adaptive grid technique the hydrodynamical equations are formulated in conservative form for Eulerian observers. We use the system of equations as presented by Romero et al. (see [4] and references therein). The spherical symmetric general relativistic equations are written in radial gauge and polar time slicing.

For the test calculation we take a cold equation of state (EOS) that was available from previous static calculations of neutron star profiles. The enormous density range from $10^5 - 10^{15} g/cm^3$ is covered by three different EOS: Harrison-Wheeler for the low density range, Negele-Vautherin around the neutron drip and Weber-Weigel for the high density range (see [9] and references therein). There is still an urgent need of a smooth EOS for hot matter covering as well the neutron drip densities as the high density range.

We integrate the hydrodynamical equations with our code AGILE [3]. It implements an adaptive grid technique following Dorfi and Drury [2]. The time integration is performed by an extrapolation method based on the semi-implicit midpoint rule of Bader and Deuflhard [1]. In comparison to a fully implicit time integration the new method reduces drastically numerical diffusion (at no increase in the number of expensive evaluations of the Jacobian). The new advection scheme of AGILE was successfully transfered to the general relativistic equations without conceptual changes. Based on a careful estimation of the accumulated advected error in each zone it regulates the insertion of artificial diffusion. Artificial tensor viscosity was implemented in a nonrelativistic manner following Tscharnuter and Winkler [7].

The test calculation starts with a one solar mass cold white dwarf in static equilibrium. Matter is accreted until onset of instability. As it is well known from core-collapse supernovae the collapse proceeds in a homologous manner. At about the density of the neutron drip almost complete deleptonization occurs in our calculation due to the neglection of neutrino trapping and the corresponding Pauli-blocking of the deleptonization reactions.

This changes the Chandrasekhar mass to a very small value and only the innermost part of the core continues to collapse homologously. Therefore the shock is formed near the center after bounce. It turns quickly into a pure accretion shock riding on an oscillating core.

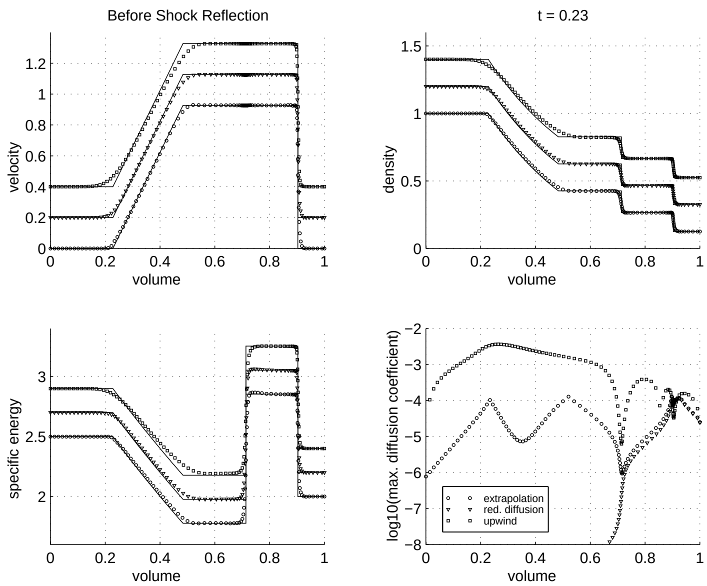

Figure 1: Calculation of Sod's nonrelativistic shock tube problem. Squares in the uppermost curve show a calculation with upwind differencing and implicit time steps. The triangles show the benefit of the new advection scheme replacing upwind differencing (both shifted in the vertical axis). For the circles in the lowermost curve, the extrapolation method was switched on. All three calculations need about the same number of function evaluations. The solid line is the exact solution.

We would like to express our thanks for useful discussions to F.-K. Thielemann, Ernst Dorfi, Ewald Müller and Wolfgang Hillebrandt.

References

[1] G. Bader and P. Deuflhard, Numer. Math. **41** (1983) 373.

[2] E.A. Dorfi and L.O'C. Drury, J. Comp. Phys. **69** (1987) 175.

[3] M. Liebendörfer, S. Rosswog and F.-K. Thielemann, submitted to J. Comp. Phys. (1998).

[4] J.V. Romero, J.M. Ibanez, J.M. Marti and J.A. Miralles, Ap J. **462** (1996) 839.

[5] P.J. Schinder, S.A. Bludman and T. Piran, Phys. Rev. **37D** (1988) 2722.

[6] F.D. Swesty, Ap. J. **445** (1995) 811.

[7] W.M. Tscharnuter and K.-H. Winkler, Comput. Phys. Communications **18** (1979) 171.

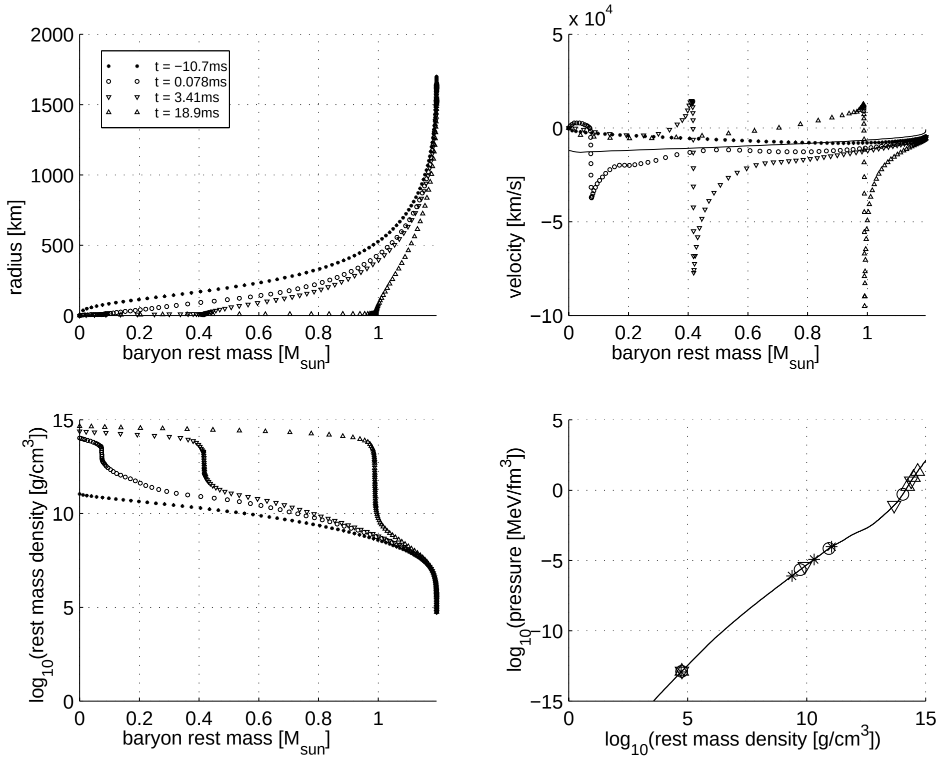

Figure 2: Shown is a collapse test calculation. Four different snapshots are plotted: homologous collapse (stars), bounce (circles), and two positions of the accretion shock (triangles). The solid line in the upper right plot is the local velocity of sound cutting the collapsing matter into a sonic and supersonic part. In the lower right plot the equation of state is shown with baryon markers. This figures are aimed to show the performance of the adaptive grid technique as well as the ability of the code to calculate collapse problems. For physical relevance the inclusion of neutrino physics and a finite temperature EOS is indispensable.

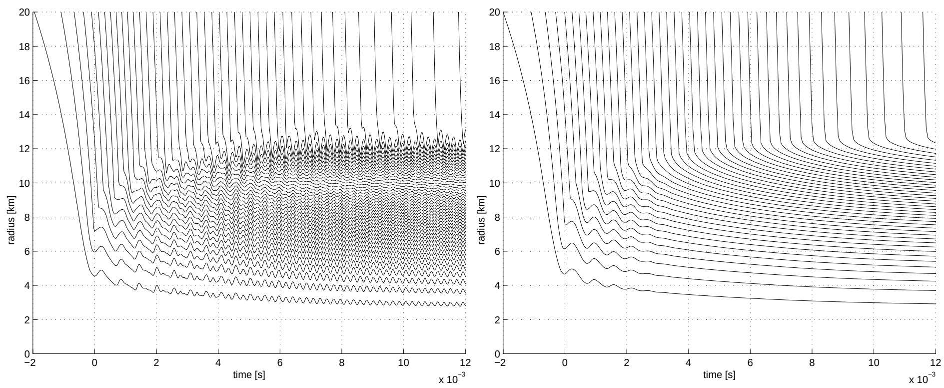

Figure 3: This figure shows baryon traces in the innermost $20km$. The left plot is calculated with the extrapolation method, the right one with fully implicit time steps. The latter introduces considerable numerical diffusion, core oscillations are damped out quickly. The former tracks the oscillations properly and shows a transition from the fundamental mode to the first overtone. After bounce however the timestep is limited by the oscillation frequency.

[8] K.A. Van Riper, Ap. J. **232** (1979) 558

[9] F. Weber and M.K. Weigel, Nuc. Phys. **A505** (1989) 779.

[10] S. Yamada, Ap. J. **475** (1997) 720.

Modification of Neutrino Reaction Rates in Hot Dense Matter

S. Yamada

Department of Physics, Graduate School of Science, the University of Tokyo

1.1 Introduction

The neutrino-nucleon scattering is one of the major sources of opacity for all types of neutrinos in the supernova core. Recently some authors are paying their attention to possible modifications of this reaction rate in the hot and dense medium in the supernova core. Since the success of explosion in the neutrino heating scenario is very sensitive to the neutrino luminosity and energy, it is important to calculate the neutrino transport in the supernova core. However, the reaction rates of neutrinos with nucleons in the hot and dense medium are uncertain. When the matter density exceeds $\sim 10^{13}\mathrm{g/cm^3}$ and the temperature is $\sim$ 10MeV, the typical wave length of neutrinos is larger than the average separation of nucleons. On the other hand, the nucleon-nucleon scattering rate becomes roughly of the same order as the typical transferred energy between a neutrino and a nucleon. Hence, the spatial and temporal correlations should be taken into account in calculating the reaction rate. Here in this work, we consider two possible mechanisms to modify this rate, that is, the screening effect and the temporal spin density correlation by the nucleon-nucleon scattering. It is shown that both of them could be important.

1.2 Formulation

The neutrino nucleon scattering rate is most conveniently formulated with the dynamical structure function of the nucleon:

$$R(q_\nu^{in}, q_\nu^{out}) = \frac{G_F^2}{2} N_{\alpha\beta}(q_\nu^{in}, q_\nu^{out})\ S_N^{\alpha\beta}(k) \quad .$$

In the above equation, q_ν^{in} and q_ν^{out} are the four momenta of the incident and scattered neutrinos, respectively, $k = q^{in} - q^{out}$, G_F is the Fermi coupling constant and $N_{\alpha\beta}$ is the tensor for the neutrino sector. The dynamical structure function of the nucleon is defined as a thermal ensemble average of the nucleon weak neutral current $J_N^\mu(x) \equiv \overline{\psi}_N(x)\,\gamma^\mu(h_V^N - h_A^N\gamma_5)\ \psi_N(x)$ as

$$S_N^{\alpha\beta}(k) \equiv \int d^4x\, e^{ikx}\ \ < J_N^\alpha(x)\, J_N^\beta(0) > \quad .$$

Taking the contraction, we find that the reaction rate has in general three contributions.

$$\begin{aligned} R(E_\nu^{in}, E_\nu^{out}, \cos\theta) \;&=\; 4\, G_F^2\, E_\nu^{in}\, E_\nu^{out}\, [R_1(k)\,(1+\cos\theta) \;+\; R_2(k)\,(3-\cos\theta) \\ &-\; 2\,(E_\nu^{in} + E_\nu^{out})\, R_5(k)\,(1-\cos\theta)] \quad , \end{aligned}$$

where θ is a scattering angle, E_ν^{in} and E_ν^{out} are the energies of the incident and outgoing neutrinos, respectively. Since $R_5(k)$ is much smaller than the other two contributions in general, we ignore it in the following. The meaning of the other two terms becomes clearer when we take the non-relativistic limit. $R_1(k)$ comes mainly from the vector part of the nucleon weak current and nothing but a density correlation function of nucleons $R_1(k) \sim (h_V^N)^2 \int d^4x\, e^{ikx} < \rho_N(x)\, \rho_N(0) >$, while $R_2(k)$ stems chiefly from the axial vector part and a spin density correlation function of nucleons $R_2(k) \sim (h_V^N)^2 \int d^4x\, e^{ikx} < \boldsymbol{s}_N^i(x)\, \boldsymbol{s}_N^i(0) >$. So the problem is now reduced to the calculation of these correlation functions with many body effects included somehow.

1.3 RPA

What we have to study first is the response of the mean nucleon field to the disturbance induced by a neutrino. This is easily done by summing up the so called ring diagrams and this approximation is also called the random phase approximation. In this work we used for a nuclear potential a parameterized G-matrix obtained by Boersma & Malfliet and worked in the relativistic frame work. The typical modification of the correlation function is shown for R_2 in figure 1a, where the dashed line is the no correlation case and the solid line represents the correlation case. It is clear that the amplitude of the correlation function is reduced by this screening effect. The total cross section is calculated by integrating the structure functions over the kinematically allowed region of the transferred four momenta under the assumption that the neutrino is not degenerate. In figure 1b we show the contour of the suppression factor of the total cross section against the Bruenn's approximation formula. It is clear that the suppression becomes remarkable as the density increases or the temperature is decreased.

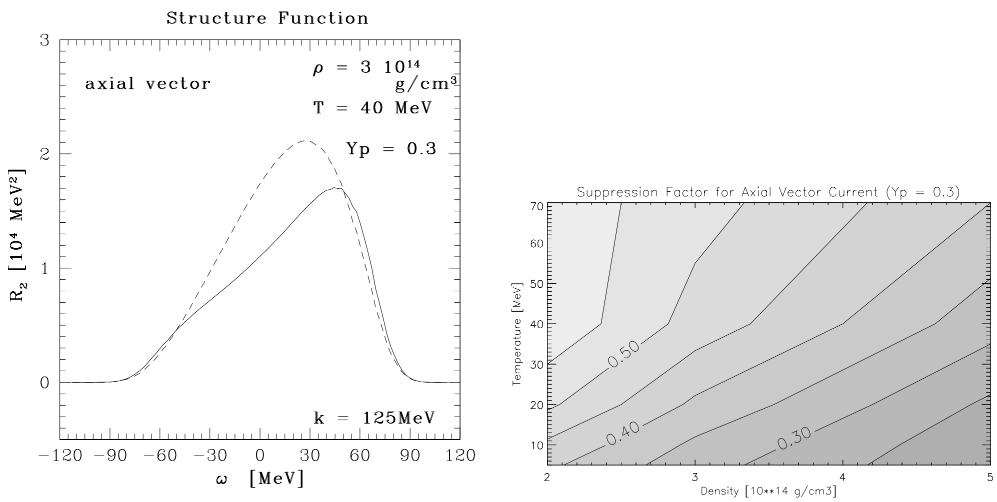

Figure 1: a. the structure function R_2. b. the suppression factor.

1.4 Scattering effect

As mentioned in introduction, the nucleon-nucleon scattering time scale is of the same order as the energy transfer between neutrino and nucleon. This implies that the temporal correlation induced by the nucleon-nucleon scattering could be important. This effect is supposed to broaden the width of the structure function. In order to estimate this effect, we summed up the ladder diagrams to obtain the self-energy of the nucleon which originates from this scattering process and the imaginary part of which is responsible for the broadening of the spectral function of the nucleon. Here we used a simple Yamaguchi potential and worked in the non-relativistic frame work since we are mainly interested in the low density regime. Figure 2a shows a neutron spectral function for $\rho = 6\times 10^{13}\mathrm{g/cm}^3$, $T = 10\mathrm{MeV}$ and $Y_p = 0.1$. The peak of the spectrum corresponds to the on-shell energy of a neutron. It is seen that the spectrum is considerably broadened by scattering. Note that the spectrum for a free nucleon is a delta function of energy with the peak at the on-shell energy. With this width taken into account, we calculated the spin correlation function to the lowest one-loop diagram. The typical result is shown in figure 2b as a function of the transferred energy for different transfer momenta. As expected the structure function is broadened by an amount of the typical nucleon-nucleon scattering rate. This has two implications. Firstly, the neutrino-nucleon scattering could be more anisoenergetic. As a result, ν_μ and ν_τ could be more thermalized and their energy would be much closer to that of ν_e. The second effect is to reduce the total cross section further.

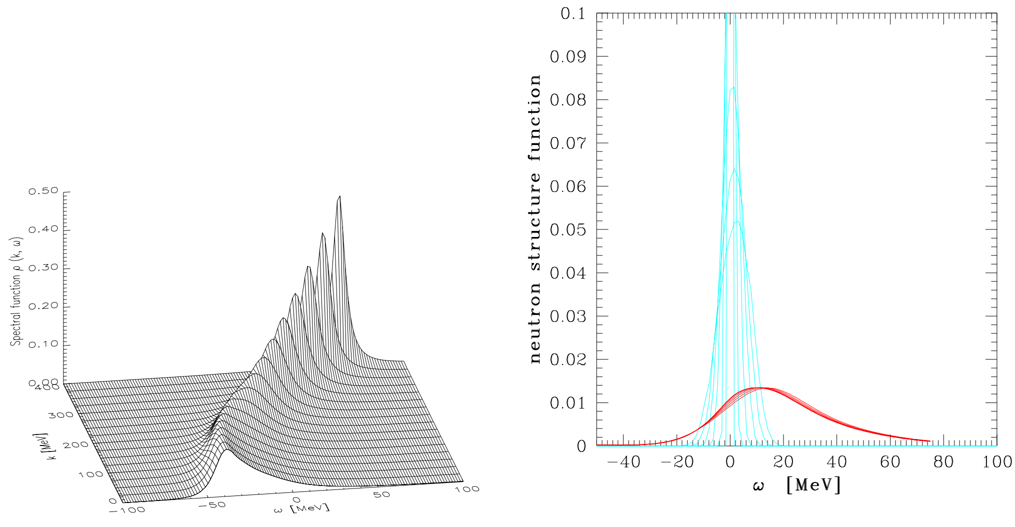

Figure 2: a. the neutron spectral function. b. the normalized neutron spin density correlation function for $\rho = 3\times 10^{13}\mathrm{g/cm}^3$, $T = 10\mathrm{MeV}$ and $Y_p = 0.4$. The tall lines represent the no correlation cases with $k = 0, 10, 20, 30, 40, 50\mathrm{MeV}$ from inside, while the lower lines are for the correlation cases for the same $k's$ from left to right, although they are almost degenerate.

1.5 Conclusion

We considered two mechanisms to modify the structure function of nucleons in hot and dense medium. It was demonstrated that both of them could be important. However, the results obtained here are far from satisfactory, since both of them should be treated simultaneously and consistently with the EOS we use in the simulations of the supernova and the protoneutron star. The charged current reactions should be treated on the same basis. These improvements are currently underway.

Neutrino-Induced Synthesis of ^{7}Li in He-shell

D.K. Nadyozhin

Institute for Theoretical and Experimental Physics
Moscow, 117259, Russia

An appreciable amount of ^{7}Li can be produced in the helium shell of a presupernova irradiated by the neutrino flux from a collapsing stellar core. The key reaction is the excitation of ^{4}He by μ and τ neutrinos and antineutrinos with subsequent decay of ^{4}He* through two almost equally probable channels

$$^4\mathrm{He}^* \longrightarrow {}^3\mathrm{He} + \mathrm{n}, \qquad {}^4\mathrm{He}^* \longrightarrow {}^3\mathrm{H} + \mathrm{p}\,. \tag{29}$$

^{3}He and ^{3}H interact with ^{4}He to produce ^{7}Li and its counterpart ^{7}Be mostly by means of reactions $^4\mathrm{He}(^3\mathrm{H},\gamma)^7\mathrm{Li}$ and $^4\mathrm{He}(^3\mathrm{He},\gamma)^7\mathrm{Be}$. The relative number of ^{4}He destroyed by neutrinos is given by

$$\frac{\delta n_{\mathrm{He}}}{n_{\mathrm{He}}} = N_\nu \frac{<\sigma_{\nu\mathrm{He}}>}{4\pi r^2} \approx 1.2\times10^{-5}\,, \tag{30}$$

where N_ν is the total number of neutrinos having crossed the helium shell of radius r and $<\sigma_{\nu\mathrm{He}}>$ is the energy-averaged cross section of the neutrino-helium breakup. The numerical estimate in Eq. (30) stands for typical value $N_\nu = 8.8\times10^{57}$, $r = 7\times10^9\,\mathrm{cm}$ (15M$_\odot$ presupernova model of Woosley and Weaver), and $<\sigma_{\nu\mathrm{He}}> = 0.86\times10^{-42}\,\mathrm{cm}^2$ for the mean energy of individual neutrinos 25 MeV [1]. If there were no other thermonuclear reactions apart from those mentioned above, the maximum yield of ^{7}Li + ^{7}Be, $n_7 \equiv n_{\mathrm{Li7}} + n_{\mathrm{Be7}} \equiv \rho N_{\mathrm{A}} Y_7$, would equal to

$$Y_{7\mathrm{max}} = \frac{\delta n_{\mathrm{He}}}{\rho N_{\mathrm{A}}} = \frac{1}{4} N_\nu \frac{<\sigma_{\nu\mathrm{He}}>}{4\pi r^2} \approx 3\times10^{-6}\,. \tag{31}$$

However, a bulk of the destroyed ^{4}He happens to be reassembled back in ^{4}He. In addition, Li and Be are destroyed — mostly in the reactions $^7\mathrm{Li}(^4\mathrm{He},\gamma)^{11}\mathrm{B}$, $^7\mathrm{Li}(p,{}^4\mathrm{He})^4\mathrm{He}$, $^7\mathrm{Be}(^4\mathrm{He},\gamma)^{11}\mathrm{C}$, and $^7\mathrm{Be}(p,\gamma)^8\mathrm{B}$ accelerated especially owing to an increase in temperature when the supernova shock wave crosses over the helium shell. As a result, the actual yield of ^{7}Li happens to be at least by 1–2 orders of magnitude lower than $Y_{7\mathrm{max}}$ from Eq. (31).

Here we report the preliminary results of our study of the ^{7}Li production in the helium shell. Our code takes into account some 100 reactions between light nuclides from neutrons and protons from the neutrino break up of ^{4}He up to ^{16}O. It is connected through the neutron channel with much more sophisticated network (for about 3200 heavy nuclides) which controls the temporal behavior of free neutrons participating in the neutrino-induced r-process on Fe-seeds in the He-shell (see details in [2]). Figure 1 shows Y_7 for three representative sets of the ^{4}He shell properties:

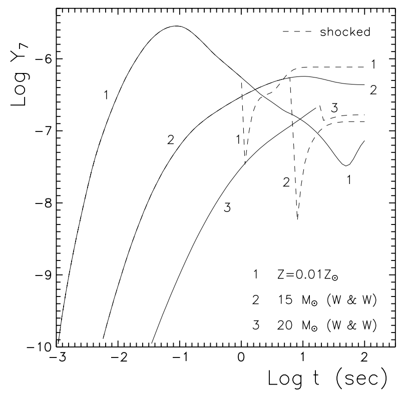

Figure 1: The temporal behavior of $Y_7 = Y_{\mathrm{Li7}} + Y_{\mathrm{Be7}}$. Time is measured from the beginning of the neutrino pulse ($t = 0$, note the logarithmic scale). The dashed parts of the curves correspond to reprocessing after the heating of the He-shell by a shock wave.

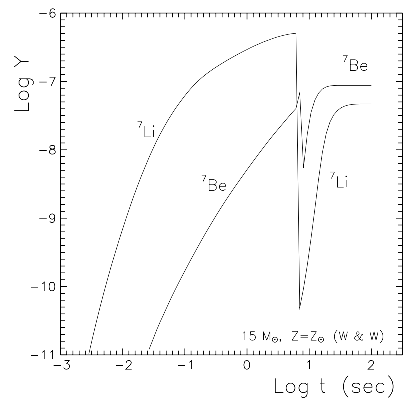

Figure 2: Same as in Fig. 1 but separately for ^{7}Li and ^{7}Be for a 15M$_\odot$ model of Woosley and Weaver.

1 Low metallicity ($Z = 0.01\,Z_\odot$) model,
$r = 1\times10^9\,$cm, $\rho = 3\times10^3\,$g cm^{-3}, $T_9 = 0.2$.
2 Solar metallicity Woosley & Weaver's 15 M$_\odot$ model,
$r = 7\times10^9\,$cm, $\rho = 2\times10^2\,$g cm^{-3}, $T_9 = 0.17$.
3 Solar metallicity Woosley & Weaver's 20 M$_\odot$ model,
$r = 1.5\times10^{10}\,$cm, $\rho = 55$g cm^{-3}, $T_9 = 0.1$.

Figure 2 shows the interplay of ^{7}Li and ^{7}Be at $t \approx 7$sec when the shock wave crosses the helium shell with a typical velocity $D \approx 10^9$cm/s and a temperature jump up to $T_9 \approx 0.4$. At the beginning, ^{7}Li and ^{7}Be have to undergo a strong depletion mostly owing to the interaction with ^{4}He and protons. Then, however, as the temperature of shocked matter falls slowly down due to the expansion, Y_{Li7} and Y_{Be7} begin to grow again — the neutrino flux still continues to supply fresh ^{3}He and ^{3}H!

The final yield is $Y_7 \approx 10^{-7}$. Thus, the total mass of ejected ^{7}Li + ^{7}Be is equal to $7Y_7\Delta M_{\rm He} \approx 10^{-6}{\rm M}_\odot$, where the He shell mass $\Delta M_{\rm He} \approx 1.7{\rm M}_\odot$ for a $15{\rm M}_\odot$ presupernova model. This result is in a good agreement with calculations of Woosley and Weaver [3].

The neutrino-induced nucleosynthesis of the light elements in He shell deserves further detailed study.

Acknowledgements

It is a pleasure to thank the Organizing Committee for the invitation to attend the Workshop and the Max-Planck- Institut für Astrophysik for hospitality and financial support. I am grateful to S. Woosley and T. Weaver for the permission to use their presupernova models. The work was also supported by grants Nos. 96-02-17604 and 96-02-16352 of Russian Foundation of Fundamental Research (RFFI), ISTC Project No 370-97, and the Swiss National Science Foundation.

References

[1] S.E. Woosley, D.H. Hartmann, R.D. Hoffman, and W.C. Haxton, ApJ **356** (1990) 272.

[2] D.K. Nadyozhin, I.V. Panov, and S.I. Blinnikov, A&A (1998) accepted.

[3] S.E. Woosley and T.A. Weaver, ApJS **101** (1995) 181.

Modelling the hydrogen emission of supernova 1987A

V.P. Utrobin[1], *N.N. Chugai*[2]

[1] *Institute of Theoretical and Experimental Physics, 117259 Moscow, Russia*
[2] *Institute of Astronomy of Russian Academy of Sciences, 109017 Moscow, Russia*

Abstract

We construct a self-consistent atmosphere model and succeed in reproducing the optical and infrared continuum and the luminosity of hydrogen emission lines observed from supernova 1987A on days 128 and 498 taking account of a quasi continuum of optical and infrared emission lines, produced by the splitting of non-thermal ultraviolet photons. We find that a depletion of the primary composition in the inner layers of the supernova envelope is needed to provide a better fit to the observations. We conclude that a total hydrogen mass in the supernova envelope is $\sim 5.6\ M_\odot$, and estimate a core mass of heavy elements in the presupernova as $\sim 8\ M_\odot$.

1.1 Introduction

The close proximity of supernova (SN) 1987A in the Large Magellanic Cloud (LMC) provided a unique opportunity for the study of supernovae resulted in unprecedented coverage in both wavelength and time. SN 1987A is the first supernova bright enough for long-term ultraviolet (UV) and infrared (IR) observations [1-3] which complement the optical data [4, 5].

At late times a supernova becomes transparent so that the observed flux, dominated by emission lines, originates from an increasing range of depths. For SN 1987A this phase begins at nearly day 130 [6]. The period between day 130 and day 530, when dust forms [7], is a particularly important phase to study the interior of the expanding envelope.

It is a great deal of the observational data for SN 1987A and the existence of the above phase in its evolution that has motivated this work. Our main goal is to reproduce the most prominent features of the observations at this stage — the optical and infrared continuum and the hydrogen emission lines.

1.2 Atmosphere model

We construct a self-consistent atmosphere model, using as starting point a hydrodynamic model similar to those of SN 1987A that show a good agreement with the observations [6]. Our spherical model has an envelope mass of 15 $M_\odot$ and gives the density of matter as a function of velocity for the stage of homologous expansion when pressure forces are negligible in the supernova envelope. At this stage any mass element of gas expands with a constant velocity of $v(m)$ and has a radius given by a simple relation of $r(m,t) = v(m)t$, where t is the time since the supernova explosion. A gas density is given by $\rho(m,t) = \rho(m,t_0)(t_0/t)^3$, where t_0 is any other time of free expansion stage and $\rho(m,t_0)$ is the gas density at this time.

It is well established that at late times an energy source in the envelope of SN 1987A is mainly the radioactive decay of nickel and cobalt nuclides. The iron-group elements are known to extend to $\sim$ 3000 km/s and possibly even up to $\sim$ 5000 km/s [8, 9]. We distribute a 0.085 $M_\odot$ mass of ^{56}Ni according to these indications and fit this distribution to the evolution of the 847 keV ^{56}Co line observed by [10]. We assume that freshly synthesized iron-group elements and hydrogen are physically segregated, and are mixed only macroscopically.

According to [11], in spherically symmetric atmosphere the equation of transfer for the radiative specific intensity I_ν of the photon frequency ν with an angle-averaged frequency redistribution in the comoving frame can be written as

$$\mu\frac{\partial I_\nu}{\partial r} + \frac{1-\mu^2}{r}\frac{\partial I_\nu}{\partial \mu} = -\chi_\nu I_\nu + \eta_\nu^c + \eta_\nu^t + \sigma_\nu J_\nu + \sigma_0(r)\int_0^\infty \mathcal{R}(\nu',\nu)J(\nu')d\nu', \tag{32}$$

where $\chi_\nu = \kappa_\nu + \sigma_\nu + \sigma_0(r)\varphi(\nu)$ is the total monochromatic extinction and $\mathcal{R}(\nu',\nu) = \varphi(\nu')\psi(\nu',\nu)$ is an arbitrary angle-averaged redistribution function represented by a product of the normalized absorption profile $\varphi(\nu')$ and the normalized emission profile $\psi(\nu',\nu)$. Here r is the local radius; μ is the cosine of the angle between the direction of propagation and the local radius vector at radius r; η_ν^c is the emissivity of continuum photons; η_ν^t is the total thermal emissivity, resulting from bound-free and free-free transitions and two-photons decays; κ_ν is the monochromatic absorption coefficient corrected for stimulated emission; $\sigma_\nu = \sigma_e + \sigma_R(\nu)$ is the monochromatic isotropic scattering coefficient, including the Thomson scattering by free electrons and the Rayleigh scattering by hydrogen atoms (Lyman sequence) with the radiative damping; $\sigma_0(r)$ is the scattering coefficient of the isotropic frequency redistribution; and $J_\nu = \frac{1}{2}\int_{-1}^{1} I_\nu d\mu$ is the angle-averaged mean intensity.

In the expanding envelope of supernova the non-thermal excitation and ionization of atoms and ions result mainly in the UV emission. The UV radiation is blocked by scattering in numerous resonance lines of metals and converted by fluorescence into a quasi continuum of optical and infrared emission lines [12]. We model the generation of the non-thermal UV radiation by specifying the emissivity of continuum photons, η_ν^c, and the fluorescence of UV radiation by specifying the isotropic frequency redistribution function, $\mathcal{R}(\nu',\nu)$. The absorption profile of the redistribution function, $\varphi(\nu')$, is taken similar to the emission profile of the non-thermal continuum photons, so that most of these photons suffer the fluorescence.

At late times the characteristic expansion velocity in the supernova envelope is much larger than the thermal velocity of the matter. Therefore, a modified Sobolev approximation [13, 14] can be used to take the radiative transfer of the lines into account. This approximation utilizes information about the local continuum radiation field outside the line-forming region and yields the solution of the radiative transfer of a line as

$$J_{lu}^L = (1 - \beta_{ul})S_{lu} + \beta_{ul}J^c(\nu_{lu}), \tag{33}$$

where J_{lu}^L is the line frequency-averaged mean intensity, β_{ul} is the photon escape probability, and S_{lu} is the line source function. The continuum angle-averaged mean intensity, $J^c(\nu_{lu})$, at the line frequency ν_{lu} is obtained from the solution of Eq. (32). An escaping line photon may be nevertheless destroyed by continuum absorption in the bound-free and free-free transitions. To take this continuum absorption into account, we solve the equation of transfer for the net line intensity.

The following elements are included in the non-LTE gas equation of state: H, He, C, N, O, Ne, Na, Mg, Si, S, Ar, Ca, and Fe. All but H are treated with the three ionization stages. The level populations are calculated for a number of atoms and ions and the rest of them are assumed to consist of the ground state and continuum. All atomic levels under consideration are treated as non-LTE and the adequate equations of statistical equilibrium for them are solved. Both the ionization balance equations and the equations of statistical equilibrium include the non-thermal excitation and ionization [15].

In a steady state the gas energy equation, the first law of thermodynamics for the material, includes an adiabatic cooling in the supernova envelope expanding homologously, the net rates of radiative losses in continuum and the lines, and the energy input dominated by the non-thermal excitation, ionization, and heating. The balance of these cooling processes and the energy input determines the electron temperature in the supernova envelope.

A simultaneous solution of the transfer, gas energy, and non-LTE statistical equilibrium equations is achieved by performing a two-step iteration. The first step of the numerical procedure is solving the transfer equation for the continuum radiative intensity and the lines. Its solution is then used in the second step, which is to solve the non-LTE equations of statistical equilibrium and the gas energy equation. The iteration is stopped when the change in basic quantities from one cycle to the next is less than 0.01.

1.3 Results

We have computed atmosphere solutions for SN 1987A at day 128 and day 498 after the core collapse, assuming a distance to the LMC of 50 kpc and a color excess of 0.2. With a density distribution taken from the adequate hydrodynamic model and a radioactive ^{56}Ni distribution fitted to the observations, there are only two basic parameters: the emission profile of the redistribution function and the radial distribution of hydrogen.

The emission profile of the redistribution function, $\psi(\nu', \nu)$, is adjusted to fit the calculated emergent flux in continuum to that observed from SN 1987A. The result of such a fitting is shown in Fig. 1a for day 498 when the supernova envelope is transparent in optical band. The hydrogen emission lines are diagnostic mainly of the hydrogen distribution and energy deposition. Here we focus on the Hα and Brγ lines which are strong and apparently isolated. With the uniform radial distribution of hydrogen the calculated luminosities of these hydrogen emission lines exceed the observed ones. So, hydrogen content in the supernova envelope should be reduced and a natural way is to deplete it in the inner layers adjusting a filling factor of the hydrogen-rich material with the LMC composition. The filling factor distribution shown in Fig. 1b leads to a good agreement with the observed luminosities of hydrogen emission lines in Fig. 2.

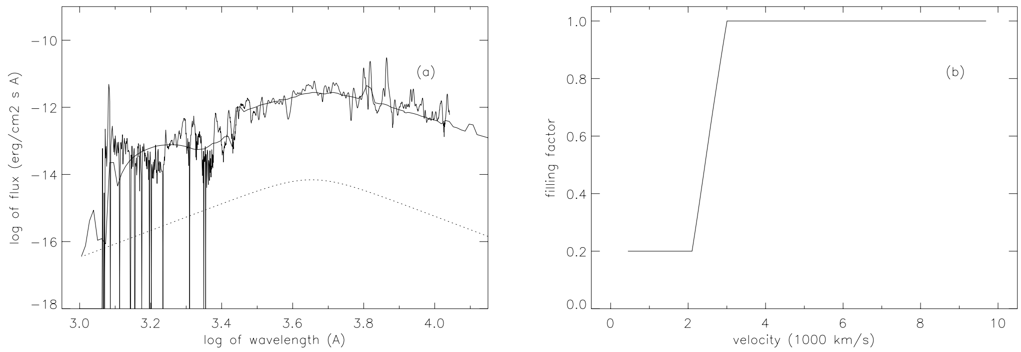

Figure 1: (a) The combined UV and optical spectra of SN 1987A [1] (thin solid line) and the calculated emergent flux (thick solid line) for day 498. The shape of the emission profile of the redistribution function is shown by dotted line. (b) The filling factor of hydrogen as a function of velocity.

1.4 Discussion and conclusions

Previous attempts of modelling the hydrogen emission lines in the nebular phase were the simple approach discussed in [16] and the self-consistent time-dependent model represented recently by [17]. There are several limitations to the first model. The most serious are the neglect of the radial structure, the radiative transport in continuum, and the thermal balance. As a result, it is inconsistent with the Hα observations of SN 1987A [16]. The second model is a more refined approach and free of the above limitations. However, it is unable to reproduce well the hydrogen emission lines during the phase under consideration too.

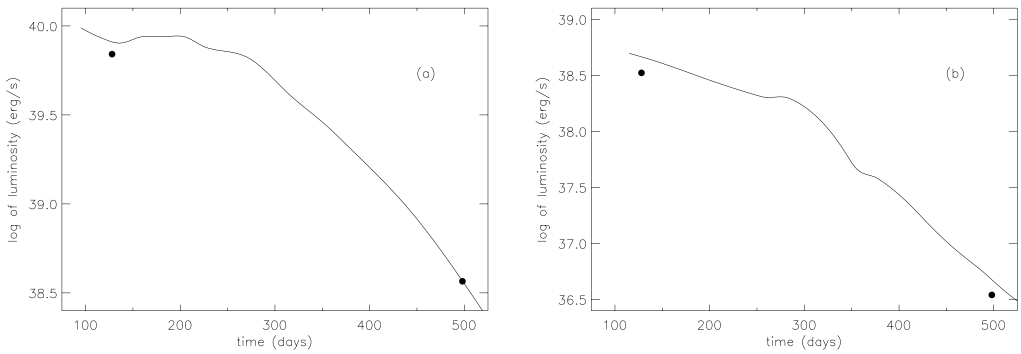

Figure 2: Comparison of the calculated luminosities (black circles) with those observed from SN 1987A (solid line) [2, 3, 5] for Hα (a) and Brγ (b) lines.

Our self-consistent atmosphere model succeeds in reproducing the observed luminosity of hydrogen emission lines on day 128 and day 498. We include a quasi continuum originated from optical and IR emission lines in order to reproduce the observed optical and IR continuum. By fitting our atmosphere model to the optical and infrared data, we can derive information about the hydrogen content and its distribution within the ejecta. A depletion of the primary composition in the inner layers of the supernova envelope is required to explain the observed luminosity of hydrogen emission lines. We conclude that a total hydrogen mass is $\sim 5.6\ M_{\odot}$ and estimate a core mass of heavy elements in the presupernova as $\sim 8\ M_{\odot}$. Note that our simple treatment of the splitting of UV photons does not strongly affect our calculation of the luminosity of hydrogen emission lines and the total hydrogen mass.

Acknowledgements

One of us (V.P.U.) would like to thank the MPA for the opportunity to announce this work at Ninth Workshop on nuclear astrophysics at the Ringberg Castle and for the financial support of his participation at this workshop and staying at the MPA. The work in Russia is partially supported by RFFI (projects 96-02-19756 and 98-02-16404) and ISTC (project 370-97).

References

[1] C.S.J. Pun et al., Astrophys. J. Suppl. Ser. **99** (1995) 223.

[2] W.P.S. Meikle, D.A. Allen, J. Spyromilio, G.-F. Varani, Mon. Not. Roy. Astron. Soc. **238** (1989) 193.

[3] W.P.S. Meikle, J. Spyromilio, D.A. Allen, G.-F. Varani, R.J. Cumming, Mon. Not. Roy. Astron. Soc. **261** (1993) 535.

[4] N.B. Suntzeff, M.M. Phillips, D.L. Depoy, J.H. Elias, A.R. Walker, Astron. J. **102** (1991) 1118.

[5] J.W. Menzies, In: I.J. Danziger, K. Kjär. (eds.) Proc. ESO/EIPC Workshop, Supernova 1987A and other supernovae. ESO, Garching (1991) p. 209.

[6] V.P. Utrobin, Astron. and Astrophys. **270** (1993) 249.

[7] L. Lucy, I.J. Danziger, C. Gouiffes, P. Bouchet, In: S.E. Woosley. (ed) Supernovae. Springer-Verlag, New York (1991) p. 82.

[8] M.R. Haas, et al., Astrophys. J. **360** (1990) 257.

[9] V.P. Utrobin, N.N. Chugai, A.A. Andronova, Astron. and Astrophys. **295** (1995) 129.

[10] M.D. Leising, G.H. Share, Astrophys. J. **357** (1990) 638.

[11] D. Mihalas, Stellar Atmospheres. Freeman, San-Francisco (1978).

[12] H. Li, R. McCray, Astrophys. J. **456** (1996) 370.

[13] V.V. Sobolev, Moving envelopes of stars. Harvard University Press, Cambridge (1960).

[14] J.I. Castor, Mon. Not. Roy. Astron. Soc. **149** (1970) 111.

[15] C. Kozma, C. Fransson, Astrophys. J. **390** (1992) 602.

[16] Y. Xu, R. McCray, E. Oliva, S. Randich, Astrophys. J. **386** (1992) 181.

[17] C. Kozma, C. Fransson, Astrophys. J. **496** (1998) 946; **497** (1998) 431.

Bolometric Light Curves of Type Ia Supernovae

G. Contardo[1,2], *B. Leibundgut*[1]

[1] *European Southern Observatory, Karl-Schwarzschild-Straße 2, D-85748 Garching, Germany*
[2] *Max-Planck-Institut für Astrophysik, Karl-Schwarzschild-Straße 1, D-85748 Garching, Germany*

1.1 Light Curves of Type Ia Supernovae

Substantial information about the processes in supernovae is contained in their light curves. They track the temporal evolution of the energy release. The energy is generated in the explosion by burning matter to nuclear statistical equilibrium, goes into unbinding the white dwarf and is stored in radioactive material. The light curve itself is defined by the conversion of the γ-rays from the radioactive decays into lower energy photons and by the escape of the latter from the ejecta.

Because of their apparent uniformity SNe Ia were used as standard candles for distance determination and to measure cosmological parameters [1]. The standard candle approach is the simplest method. But the light curves of SNe Ia show significant differences in their shapes and maximum luminosities. Phillips [2] showed a relation between maximum brightness and $\Delta m_{15}(B)$, the difference in brightness in the B-band at its maximum and 15 days after. Hamuy et al. [3] confirmed this relation. Another one parameter model is the Multicolor Light Curve Shape (MLCS) method of Riess et al. [4], which uses a training set of well observed SNe to span a range of light curves, described by one parameter.

1.2 Fitting Method

A different approach is fitting the filter light curves independently to avoid intrinsic assumptions made in template-fitting techniques. Therefore it is ideally suited for investigating the non-uniformity of SN Ia explosions. For each supernova the light curve shape parameters (like rise time, shape around maximum, late decline etc.) are derived individually and can be searched for correlations. A descriptive model has been fitted to light curves of supernovae from the Calán/Tololo survey [5], a set of supernovae from Riess et al. [6] and other well observed, high quality data. The time evolution of the observed magnitudes is modeled as a Gaussian (for the peak phase) atop a linear decay (for the late-time decline), a second Gaussian in the V, R, and I-band (for the secondary maximum found in that curves) and an exponential rise function (for the pre-maximum segment), as applied to SN 1994D by Vacca and Leibundgut [7].

1.3 Epoches of Maxima

With these fits, parameters derived from the light curve shape can be compared more easily. For example the distribution of the times of maximum light in the different filter

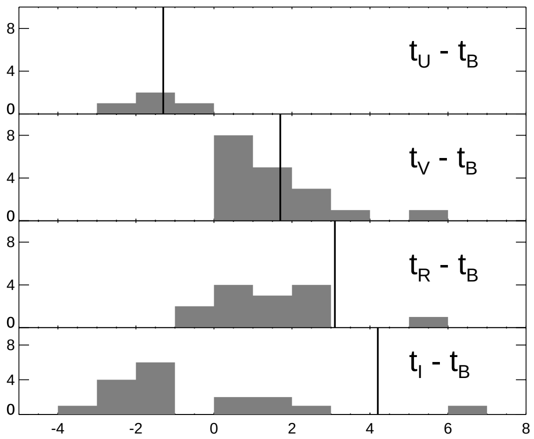

Figure 1: Relative times of maximum light in different filters. The vertical lines show an expanding, adiabatic cooling sphere [9].

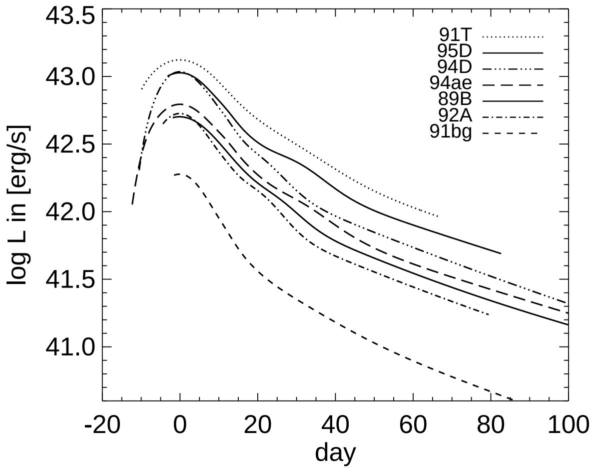

Figure 2: Bolometric luminosities.

light curves can be examined, as shown in Figure 1. While the U-band light curve peaks before the B maximum and V and R follow the B, the I light curve reaches maximum even earlier than the U light curve. This trend is also confirmed by the IR light curves [8]. This is a very clear sign of the non-thermal nature of the radiation emitted by SNe Ia. A simple model of an expanding, adiabatic cooling sphere according to Arnett [9] gives the vertical lines in Figure 1. The maxima at longer wavelengths are reached at later epoches in this model. This is clearly not seen for most SNe Ia.

1.4 Bolometric Light Curves of Type Ia Supernovae

As nearly 80 % of the bolometric luminosity is emitted in the range from 3000 to 10000 Å [10], the $UBVRI$ integrated flux is a physically meaningful quantity. It depends on the nickel production, the energy deposition and the γ-ray escape, but not on the wavelengths of the emitted photons. The theoretical calculation of the bolometric light curve is much simpler than the calculation of the filter light curves, as complicated multi-group calculations of the complete spectrum can be avoided.

But not all SNe are observed in all five bands. In a first approximation it is assumed that the flux distribution is the same for all SNe. A well observed supernova (SN 1994D) is used to calculate correction factors for missing pass bands.

If this correction is applied to other SNe, and the distance moduli and reddening are taken into account [3, 4], one obtains the $UBVRI$ bolometric light curves displayed in Figure 2. The absolute peak luminosities differ by a factor of 10. The second bump, which can be seen in the R and I light curves of several SNe, is still visible in the bolometric light curves. These results show, that there are fundamental differences in the energy release among individual SNe Ia.

How reliable are these bolometric luminosities and by which quantities are they affected? In a forthcoming paper [11] a more extended discussion of the errors will be given.

The distance modulus only changes the absolute luminosity. As all distances used here are scaled to a Hubble constant of $H_0 = 65\,\mathrm{km\,s^{-1}\,Mpc^{-1}}$, the luminosity differences are only affected by errors in the determination of the distance modulus and not by offsets due to the different methods. If the distance modulus changes by 0.1 mag, the bolometric luminosity changes by 9 %. Reddening changes the absolute luminosity as well as the shape of the light curve. Reddening of $E(B-V) = 0.05$ still gives 85 % (88 %) of the unreddened bolometric luminosity at $t = t_{\max}$ ($t = 20\,$days $\approx$ time of second maximum in R and I), whereas at reddening of $E(B-V) = 0.35$ only 33 % (44 %) of the unreddened bolometric luminosity remains at $t = t_{\max}$ ($t = 20\,$days). Differences among independent data sets introduce additional uncertainties. For typical values of < 0.05 mag [6], however, we find changes of less than 3 %. We have tested also the influence of applying the fitting routine on the individual filter light curves before constructing the bolometric luminosities by comparing it to bolometric luminosities calculated directly from the observational data. The integration method and normalization influence the bolometric luminosities up to 2 %. Finally, the error introduced by the correction factors for missing U-band is < 10 %, as has been tested by constructing artificially data with missing pass bands for SNe which are observed in U, B, V, R, and I.

1.5 Conclusions and Future Work

A sample of supernovae has been used to construct bolometric light curves from observations. These bolometric light curves can be compared to theoretical models more easily than filter light curves. Therefore, bolometric light curves are one step from observations to theoretical models.

In the future, a comparison of the bolometric light curves from observations with those from theoretical models can supply us with information about the physical processes in SNe Ia. We will derive the light curve corrections with bolometric light curves instead of filter light curves to move from an empirical classification to physically meaningful relations.

References

[1] D. Branch and G. A. Tammann, Ann. Rev. Astron. Astrophys. **30** (1992) 359

[2] M.M. Phillips, Astrophys. J. Lett. **413** (1993) 105

[3] M. Hamuy, M.M. Phillips, R.A. Schommer, N.B. Suntzeff, J. Maza and R. Avilés, Astron. J. **112** (1996) 2391

[4] A.G. Riess, W.H. Press and R.P. Kirshner, Astrophys. J. **473** (1996) 88

[5] M. Hamuy et al. Astron. J. **112** (1996) 2408

[6] A.G. Riess, PhD thesis, Cambridge: Harvard University (1996)

[7] W.D. Vacca and B. Leibundgut, Astrophys. J. Lett. **471** (1996) 37

[8] J.H. Elias, K. Matthews, G. Neugebauer and S.E. Persson, Astrophys. J. **296** (1985) 379

[9] W.D. Arnett, Astophys. J. **253** (1982) 785

[10] N.B. Suntzeff, in IAU Colloquium, Vol. 145, Supernovae and Supernova Remnants, ed. R. McCray & Z. Wang, Cambridge: Cambridge University Press (1996) 41

[11] G. Contardo, B. Leibundgut and W.D. Vacca, in preparation

Models for Type Ia Supernovae: Influence of the Description forthe Deflagration Front

P. Höflich[1], *I. Dominguez* [1,2]

[1] *Dept. of Astronomy, University of Texas, Austin, TX 78712 USA*
[2] *Dept. of Astronomy, University of Grenada, Grenada, Spain*

1.1 Introduction

The standard scenario for Type Ia Supernovae consists of massive carbon-oxygen white dwarfs (WDs) with a mass close to the Chandrasekhar mass which accrete through Roche-lobe overflow from an evolved companion star (Nomoto & Sugimoto 1977; Nomoto 1982). In these accretion models, the explosion is triggered by compressional heating. From the theoretical standpoint, the key questions are how the flame ignites and propagates through the white dwarf. Several models within this general scenario have been proposed in the past including detonations, deflagrations and the delayed detonations, which assume that the flame starts as a deflagration and turns into a detonation later on (Khokhlov 1991, Yamaoka et al 1992, Woosley & Weaver 1995). The latter scenario and its variation "pulsating delayed detonation", seems to be the most promising one, because, from the general properties and the individual light curves and spectra, it can account for the majority of SNe Ia events (e.g. Höflich & Khokhlov 1996, Nomoto et al. 1997, and references therein). We note that with the discovery of the supersoft X-ray sources, potential progenitors have been found (e.g. van den Heuvel et al. 1992; Rappaport et al. 1994).

What we observe as a supernova event is not the explosion itself but the light emitted from a rapidly expanding envelope produced by the stellar explosion. As the photosphere recedes, deeper layers of the ejecta become visible. A detailed analysis of the light curves and spectra gives us the opportunity to determine the density, velocity and composition structure of the ejecta and provide a direct link between observations. A successful application of observational constrains requires both accurate early LC and spectral observations and detailed theoretical models which are coupled tightly to the hydrodynamical calculations as became available during the last few years (Höflich et al. 1991, Harkness et al. 1991, Bravo et al 1995).

During the last years, we have constructed a large set of 1-dimensional models which are consistent with respect to the explosion, the optical and infrared light curves, and the spectral evolution based on detailed NLTE atmospheres This leaves the density and chemical structure of the initial WD, and the description of the burning front the only free parameters from which the light curves and spectral evolution follows. A comparison with observations allows to test existing scenarios. According to our results, normal bright, fast SNeIa can be explained by delayed detonation and pulsating delayed detonation models (e.g. SN 94D, Höflich 1995). During the deflagration phase, the mean deflagration velocity is 3 % of the sound speed. In general, a transition from deflagration to detonation is required at densities of about 2.5 10^7 $g\ cm^{-3}$. Central densities of the initial WDs range from 2. to 3.5 $10^9 g\ cm^{-3}$. As a tendency, models at the lower end of this range give better fits. Despite their success, the hydrodynamical models are limited by the parametized description of the burning front and the ad hoc adjustment of the density at which the deflagration turns into a detonation.

Very recently, significant progress has been made towards a better understanding of the propagation of nuclear burning fronts. First multidimensional hydrodynamic calculations of the deflagration fronts have been performed (e.g. Khokhlov 1995, Niemeyer & Hillebrandt 1995) and a basic, qualitative understanding of the mechanism which leads to a transition from a deflagration to a detonation phase has been achieved (Khokhlov, Oran & Wheeler 1997ab, Niemeyer & Woosley 1997). Qualitatively, the results agree between different hydrodynamical numerical simulations but a full description of the deflagration in the entire white dwarf and the consistent calculations of the transition requires high resolution in 3-D which are beyond the current state of the art. Moreover, the transition from a deflagration to a detonation is still not well understood.

Here, the question is addressed how our results of the explosions vary if we use descriptions for the deflagration front which use functional relations derived from 3-D calculations.

1.2 Hydrodynamics

The explosions are calculated using a one-dimensional radiation-hydro code, including nuclear networks (Höflich & Khokhlov 1996, and references therein). This code solves the hydrodynamical equations explicitly by the piecewise parabolic method (Collela & Woodward 1984) and includes the solution of the frequency-averaged radiation transport implicitly via moment equations, expansion opacities, and a detailed equation of state. The frequency-averaged variable Eddington factors and mean opacities are calculated by solving the frequency-dependent transport equations. About one thousand frequencies (in one hundred frequency groups) and about five hundred depth points are used. Nuclear burning is taken into account using a network which has been tested in many explosive environments (see Thielemann, Nomoto & Hashimoto 1996, and references therein).

1.3 Description of the Burning Front

We have considered three cases:

Case 1) $v_{burn} = const.\ v_{sound}$. In our previous investigations, const=0.03 has been found to give the best fits to observations.

Case 2 & 3) Here we assumed that $v_b = max(v_t, v_l)$ where v_l and v_t are the laminar and turbulent velocities, respectively.

Intrinsically, turbulent combustion is a three-dimensional problem. It is driven on large scales by the buoyancy of the burning products. The turbulent cascade penetrates down to very small scales, and makes the rate of deflagration independent of the microphysics. Turbulent combustion in a uniform gravitational field and static conditions singles out the propagation of the flame agains gravity. Both from experiments in and numerical simulations for flux tubes, the propagation speed can be described by

$$v_{turb} = C\ \sqrt{\alpha_T\ g\ L_f};\quad C = 0.5; \alpha_T = (\alpha - 1)/(\alpha + 1),\ \ \alpha = \rho^+(r_{burn})/\rho^-(r_{burn}) \qquad Eq.[1]$$

where ρ^+ and ρ^- are the densities in front and behind the front, respectively. However, despite the success in terrestial experiments, the basic assumptions of both a uniform gravitational field and static conditions is violated in the rapidly expanding envelopes of SNe Ia. The main effect of expansion is the freeze out of the turbulence on scales L_f where the turbulent velocity due to Rayleigh Taylor instabilities is comparable to the differential expansion velocities on those scales, i.e.

$$v_{turb} \approx v_{exp} = L_f/\tau_{ex} \qquad Eq.[2]$$

Based on this idea, Khokhlov et al. (1997b) suggested to use the average turbulent velocity (eq. 1), use α for uniform, static conditions, and to use the mean expansion time scale determined by one dimensional simulations $\tau_{exp} \approx dt/d\ ln\ R_{WD}$. He found for the propagation speed of the turbulent burning front

$$v_t = 474 * sqrt(g\ L_f) \qquad Eq.[3]$$

As third option for the description, we followed the recipe of Khokhlov but did some modifications (Dominguez et al. 1998) by taking α, L_f and τ_{exp} directly from the hydro at the location of the burning front. Freeze-out was assumed when the radius of a mass element has doubled after being burned. C in equation [1] has been varied. Note that a variation in C is equivalent to scaling the relative length scale for the freeze out.

1.4 Results

The influence of the description of the deflagration front has been studied at the example of a set of delayed detonation model based on the same C/O WD with a mass of 1.39 $M_\odot$ and a central density $\rho_c = 2.0\ 10^9 g\ cm^{-3}$. In all cases, a transition density ρ_{tr} of $2.3\ 10^7 g\ cm^{-3}$ has been assumed. The description of the deflagration front has been varied. The deflagration velocity is taken to be 3 % of the speed of sound and the approximation of Khokhlov is used for *m2z02y24i5* and *m2z02y24i4*, respectively. Eq. (1) has been used for models *m2z02y24i1-3* with C=0.15, 0.20 and 0.25.

In figure 1, the velocity of the burning front is shown as a function of time. In general, the speed of the burning front is mainly determined by the turbulent speed but the very early time. As can be expected, the transition density is reached later in time for smaller v_{turb} because the lower energy production per time and, consequently, the slower preexpansion.

The final density, velocity and chemical structures are given in Fig. 2. Overall, the structures are very similar because the total energy release depends on the amount of the released energy and the initial structure of the WD. Even the chemical structure or, more precisely, the location of transition between different regimes of burning (e.g. from partial to total Si-burning) changes by only ≈ 5 % as a function of the final expansion velocity.

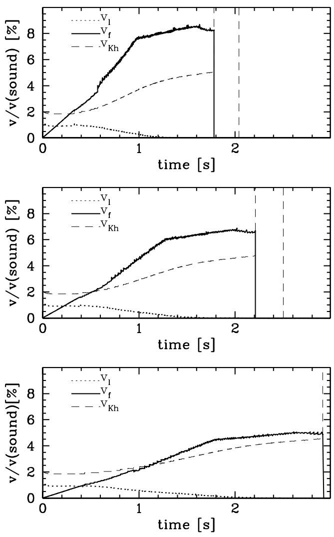

Figure 1: Laminar and turbulent velocities at the burning front for models m2z02y24i1 to 3 (top to bottom). For comparison, v_{Kh} is gives the velocity of the burning front according to Khokhlov (eq. 2, m2z02y24i1).

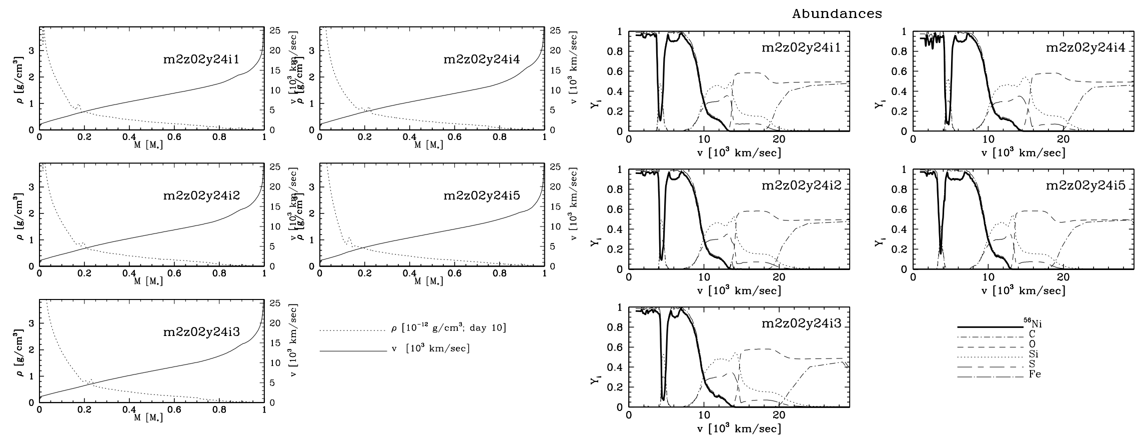

Figure 2: Final density and velocity (left) and chemical composition (right) as a function of mass and expansion velocity, respectively.

The total production the production of the most abundant elements changes by only 4 % and 2 % for ^{56}Ni and Si, respectively.

The rather small sensitivity of the final models on details of the description of the burning front can be understood by the two competing effects. The chemical pattern depends mainly on the preexpansion of the WD during the deflagration phase. The preexpansion increases with the duration of the deflagration phase but decreases with the reduced energy release per time. Note, however, that the amount of burning under high density transitions and, consequently, the production of neutron rich isotopes in the central region depends sensitively on the burning front. For a systematic study of different flame speeds for case 1, see Brachwitz et al. (1998), and for a detailed description of the influence of the description of the deflagration front see Dominguez et al. (1998).

1.5 Conclusions

Overall, the final model is rather insensitive to the detailed description of the burning front during the deflagration phase. The relative change over the entire range of parameterizations corresponds to a change in the transition density of $\approx 10\%$. Basic parameters found by Höflich & Khokhlov (1996) will hardly change. This leaves us with the puzzle why the theoretical estimates for the transition density are lower by a factor of about 0.7 (Khokhlov et al. 1997b) and 0.4 (Niemeyer et al. 1997). For reasons, we can only speculate. The differences between the latter values may indicate the size of the uncertainties in our understanding of this transition process. Other, not yet considered microscopic effects may be involved. Another possibility may be that we measure two different things. To derived the model parameters from the observations, we measure the mean density at the burning front when the transition occurs whereas the theoretical considerations provide information on the location where the transition occurs. Maybe the fragmentation of the burning front causes that the transition occurs somewhat ahead of the mean front. If this interpretation is correct, this may indicate that the detonation is started at about 10 to 20 % (in radius) ahead of the mean front. In either case, a clarification needs further investigations and, certainly, will provide new inside into the properties of nuclear burning fronts. For more details, light curves and spectra see Dominguez et al. (1998).

References

[1] Bravo E., Tornambe A., Dominguez I. Isern J., 1995 AA, 306, 811

[2] Brachwitz F., Thielemann F.K. 1998, A&A, in preparation

[3] Collela P., Woodward P.R. 1984, J.Comp.Phys., 54, 174

[4] Dominguez I., Höflich P., Wheeler J.C. 1998, ApJ, in preparation

[5] Harkness, R.P. 1991, in: SN1987A, ed. I.J. Danziger, ESO, Garching, p.447

[6] Höflich, P., Khokhlov, A., Müller, E. 1991, A&A, 248, L7

[7] Höflich, P. 1995, ApJ, 443, 533

[8] Höflich P., Khokhlov A. 1996, ApJ, 457, 500

[9] Khokhlov A. 1991, A&A, 245, 114

[10] Khokhlov A. 1995, ApJ, 449, 695

[11] Khokhlov A., Oran E.S., Wheeler J.C. 1997a, ApJ 478, 678

[12] Khokhlov A., Oran E.S., Wheeler J.C. 1997b, in: Thermonuclear Supernovae, eds. Canal et al., Kluwer Academic Publisher, Vol. 486, 475

[13] Niemeyer J.C., Hillebrandt W. 1995, ApJ 452, 779

[14] Niemeyer J.C., Woosley S. 1997, ApJ 475, 740

[15] Nomoto K., Sugimoto D. 1977, PASJ, 29, 765

[16] Nomoto K. 1982, ApJ, 253, 798

[17] Nomoto K., Yamaoka H., Shigeyama T., Iwamoto K. 1997, in: Thermonuclear Supernovae, eds. Canal et al., Kluwer Academic Publisher, Vol. 486, 349

[18] Rappaport S., Chiang E., Kallman T., Malina R. 1994 , ApJ, 431, 237

[19] Thielemann F.K., Nomoto K., Hashimoto M. 1996, ApJ, 460, 408

[20] Woosley S. E., Weaver T. A. 1994, in: Supernovae, Elsevier, Amsterdam, 423

[21] Van den Heuvel E.P.J., Bhattacharya D., Nomoto K., Rappaport S. 1992, A&A, 262, 97

[22] Yamaoka H., Nomoto K., Shigeyama T., Thielemann F. 1992, A&A, 393, 55

Light Curve Modeling of the Type Ib/Ic Supernova 1997ef

Koichi Iwamoto[1], *Ken'ichi Nomoto*[1], *Peter Garnavich*[2], *and Robert Kirshner*[2]

[1] *Department of Astronomy, School of Science, University of Tokyo, Tokyo 113, Japan*
[2] *Harvard-Smithsonian Center for Astrophysics, Cambridge, MA 02138, USA*

Abstract

The optical display of core collapse supernovae from relatively massive C+O star progenitors is studied as a possible model for the recent Type Ic(-like) supernova 1997ef. The light curve is found to be well reproduced by an explosion of a 6 $M_\odot$ C+O star. The evolution of the overall spectral shape is also in a qualitatively good agreement with the prediction from the model. With a distance of 52.3 Mpc ($\mu = 33.6$) and $A_V = 0.15$, the inferred mass of ejected ^{56}Ni is found to be 0.15 ± 0.03 $M_\odot$. This is an interesting case that suggests there exist not only fast Type Ic supernovae(SNe Ic) like SN 1994I but also such a slow class of SNe Ic, which might originate from the progenitors in different mass ranges.

1.1 Introduction

The supernova 1997ef (SN 1997ef) was discovered November 25, 1997 at R-magnitude of 16.7 near the UGC4107. Later, further photometric and spectroscopic follow-ups have been made to give good resolution optical spectra and light curves (Garnavich et al. 1997,1998; Fillipenko et al. 1997; Wang et al. 1997). The spectra are dominated by broad oxygen lines and did not show any clear feature of hydrogen or silicon(Garnavich et al. 1997; Fillipenko et al. 1997) so that SN 1997ef has been identified as Type Ib/Ic. SN 1997ef seems more likely to be a Type Ic due to if any its weakness of a possible He feature(Filippenko 1997).

The light curve of SN 1997ef has quite a flat peak that lasted for $\sim$ 25 days and an exponential tail that declines slightly faster than ^{56}Co decay rate. The similarity in the light curve shape to SN1993J motivated us to study a possibility of core collapse supernova from an envelope-stripped massive star for the progenitor of SN 1997ef. We determine the basic parameters of the progenitor star such as the explosion energy, the ejecta mass, and the mass of ejected ^{56}Ni by modeling the light curves and spectra. The implications on the possible evolutionary scenarios are discussed in the forthcoming paper(Iwamoto et al. 1998).

1.2 Progenitor Model

In order to estimate the progenitor mass, we first compare the light curve of SN 1997ef with that of SN 1993J. The width of the flat peak ($\tau_{\rm peak}$) can be approximately given by a simple analysis, equating the time scale of photon diffusion $\tau_{\rm diff} \sim \kappa\rho R^2/c$ to the dynamical time scale of explosion $\tau_{\rm dyn} \sim R/v$. Then we have a relation $\tau_{\rm peak} \sim (\kappa/c)^{1/2} M_{\rm ej}^{3/4} E_{\rm exp}^{-1/4}$, where the explosion energy is approximated by $E_{\rm exp} \sim 1/2 M_{\rm ej} v^2$ and κ and c are the opacity and the speed of light, respectively. Equation (1) shows that the time scale depends mainly on the ejcta mass. SN 1993J had a peak with $\tau_{\rm peak} \sim 15$ days, which was well reproduced by the ejecta of 2–2.5 $M_\odot$. To have a broader peak with $\tau_{\rm peak} \sim 25$ days, the scaled mass turns out to be around ~ 6 $M_\odot$.

If SN 1997ef actually does not have a He layer, a possible progenitor would be 6 $M_\odot$ C+O star. According to the stellar evolution calculations (Nomoto & Hashimoto 1988), a main-sequence star of 25 $M_\odot$ develops an 8 $M_\odot$ He core and subsequently a 6 $M_\odot$ C+O core inside. If both the hydrogen-rich and He layers are stripped off by either a wind or Roche lobe overflow, the resultant C+O star would be a good candidate for SN 1997ef.

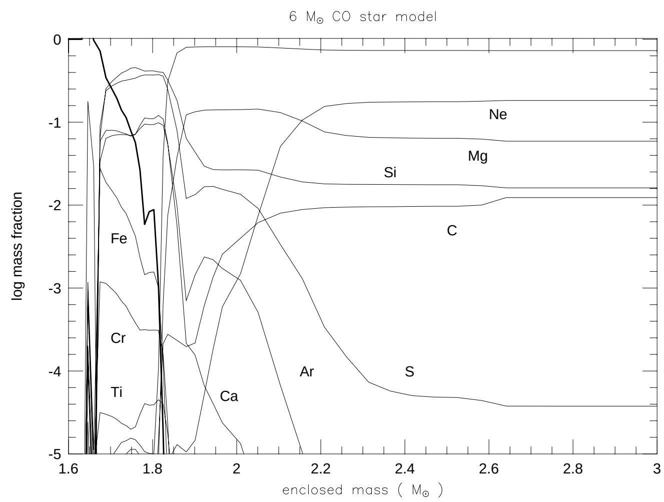

Figure 1: Composition structure in the ejecta of 6 $M_\odot$ C+O star model

1.3 Light Curves and Spectra

The hydrodynamics of explosion at earlier phases was simulated by using a Lagrangian PPM code with a simple nuclear reaction network including 13 elements(Müller 1986). The light curve is calculated with a one-dimensional spherically symmetric radiation transfer code(Iwamoto 1997, 1998). The multi-frequency radiative transfer equation for the specific intensity I_ν (2) is solved simultaneously with the energy equation for the radiation plus gas, and a set of moment equations for frequency-integrated radiation energy density E and flux F, including all the terms up to the first order of v/c.

$$\begin{aligned}\frac{1}{c}\frac{DI_\nu}{Dt} &+ \frac{\mu}{r^2}\frac{\partial}{\partial r}(r^2 I_\nu) + \frac{\partial}{\partial \mu}\left\{(1-\mu^2)\left[\frac{1}{r}+\frac{\mu}{c}\left(\frac{v}{r}-\frac{\partial v}{\partial r}\right)\right] I_\nu\right\} \\ &- \frac{\partial}{\partial \nu}\left\{\nu\left[(1-\mu^2)\frac{v}{cr}+\frac{\mu^2}{c}\frac{\partial v}{\partial r}\right] I_\nu\right\} + \left[(3-\mu^2)\frac{v}{cr}+\frac{1+\mu^2}{c}\frac{\partial v}{\partial r}\right] I_\nu \\ &= j_\nu - \kappa_\nu I_\nu - \sigma_\nu I_\nu + \frac{1}{4\pi}\int \sigma_\nu I_\nu d\Omega. \end{aligned} \tag{34}$$

To calculate opacities, we assumed LTE(Local Thermodynamic Equilibrium) to determine the ionization balances and level populations of each ion. The energy deposition due to the radioactive decays is calculated by a one energy-group gamma-ray transfer code. We assumed the absorptive opacity $\kappa_\gamma = 0.04$ for the gamma-rays and the complete trapping of positrons. The rest frame flux is calculated from the comoving frame intensities following the transformation law of the special relativity.

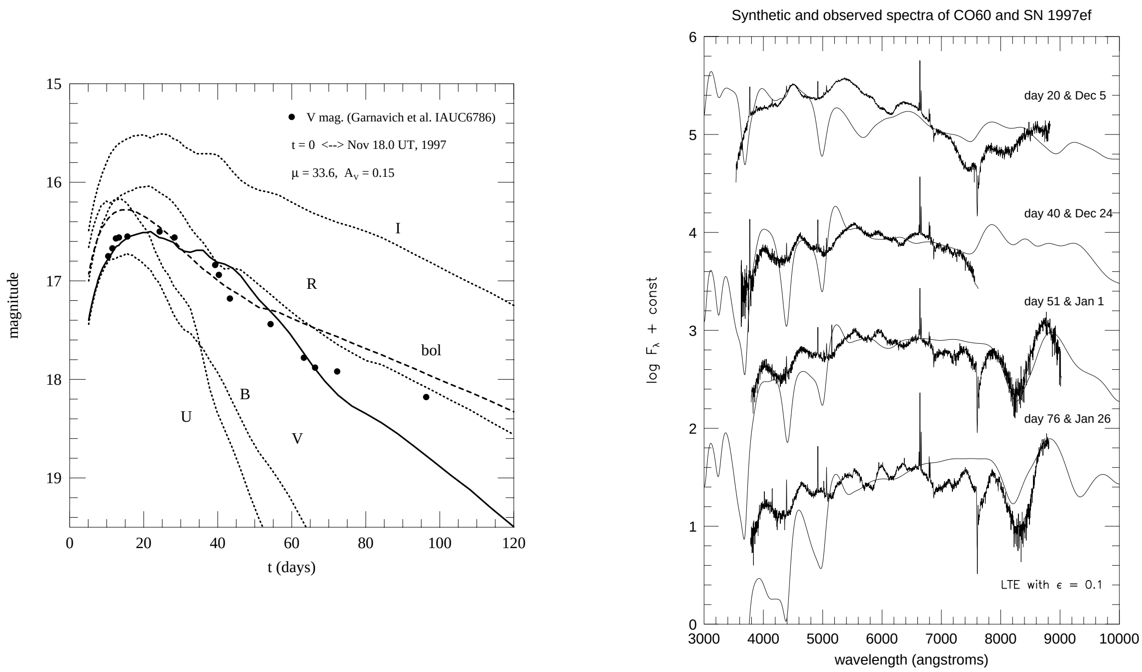

Figure 2: Calculated light curves and spectra compared with those of SN 1997ef

$$F_{\nu,\mathrm{rest}} = 2\pi\int_{-1}^{1}(\mu+\beta)I\left(\mu, \frac{\nu}{1+\beta\mu}\right)d\mu, \qquad F_{\lambda,\mathrm{rest}} = \frac{\nu^2}{c}F_{\nu,\mathrm{rest}}. \tag{35}$$

The left panel in Figure 2 shows that the calculated visual light curve fits well to the observation until day 60 and then declines a bit too faster in its tail region. After the very epoch at $\sim$ day 60, the ejecta is entering the nebula phase so that the LTE becomes a poor approximation. We take a distance of 52.3 Mpc, or 33.6 in distance modulus, which is obtained from the recession velocity 3,400 km sec^{-1} (Garnavich et al. 1997) and the Hubble constant 65. The reddening is expected to be small because of the weak absorption feature due to interstellar Na I D lines. We assume $A_V = 0.15$ to fit the light curve with a nickel mass of 0.15 $M_\odot$. The right panel in Figure 2 shows the observed and calculated spectra for several epochs corresponding to the light curve ages of 20, 40, 51, and 76 days after the explosion. The overall continuum shape and the basic line features, the position of line centers and their broadness, are well reproduced at least qualitatively. The more detailed spectrum analysis with non-LTE treatment is left to be done.

Acknowledgements

We would like to thank Drs. Paolo Mazzali, Hideyuki Umeda, Nobert Langer, and Ewald Müller for useful discussion. This work has been supported in part by the grant-in-Aid for Scientific Research (05242102, 06233101) and COE research (07CE2002) of the Ministry of Education, Science, and Culture in Japan, and the fellowship of the Japan Society for the Promotion of Science for Japanese Junior Scientists (6728).

References

[1] Filippenko, A.V., Moran, E.C., 1997, IAU Circ. No.6809; Filippenko, A.V., 1997, IAU Circ. No.6783.

[2] Garnavich, P., Jha, S., Kirshner, R., & Challis, P., 1997, IAU Circ. No.6778, 6786, 6798.

[3] Iwamoto, K., 1997, Ph.D. Thesis, University of Tokyo

[4] Iwamoto, K., Nomoto, K., Garnavich, P., & Kirshner, R., 1998, submitted.

[5] Müller, E., 1986, A&A, 162, 103.

[6] Nomoto, K., & Hashimoto, M., 1988, Phys.Rep., 163, 13.

[7] Wang, L., Howell, D.A., & Wheeler, J.C., 1997, IAU Circ. No.6820.

Progenitors of Type Ia Supernovae and the Chemical evolution of Galaxies

T. Tsujimoto[1], *C. Kobayashi*[2], *K. Nomoto*[2]

[1] *National Astronomical Observatory, Mitaka, Tokyo 181, Japan*
[2] *Department of Astronomy, School of Science, University of Tokyo, Bunkyo-ku, Tokyo 113, Japan*

1.1 Introduction

It is difficult to estimate the evolutionary timescale of Type Ia supernova (SN Ia) progenitors from purely theoretical arguments due to difficulties in identifying the binary companions of SNe Ia progenitors (e.g., [1] for a recent review). For example, their evolutionary timescale would either be related to the lifetime of the low mass companion in a binary system if Roche lobe overflow replenishes the white dwarf by accretion, or their timescale would depend on the initial separation of the double white dwarfs if a merging scenario ([2]; [3]) is adopted. Under these circumstances, Yoshii, Tsujimoto, & Nomoto ([4]:YTN) constrain the evolutionary timescale of SN Ia progenitors from the observational features in the solar neighborhood, i.e., both the observed break in the abunadance ratio [O/Fe] which certainly imprints an onset of secondary iron release from SNe Ia and the [Fe/H] abundance distribution function of long-lived stars. They conclude from a full survey in the parameter space that the range of their evolutionary timescale is strictly confined within 0.5–3 Gyr.

On the other hand, SNe Ia are found in the elliptical galaxies (Es) which have already stopped the star formation. How Es formed and have evolved is very puzzling, represented by the two competing scenarios; the dissipative collapse of a protogalactic cloud with a single star burst at very early epoch and the hierarchial clustering where Es form continuously by the merger of galaxies. In any event the color evolution up to $z \sim 1$ brought by HST suggests that Es formed early, at least $z > 1$ ([5]), which is incompaible with the evolutionary timescale of SN Ia progenitors determined by YTN in explaining the present SN Ia occurrence in Es.

Recently a new model for progenitor systems for SNe Ia basaed on a single degenerate scenario was presented by [6]. Adopting this model, Li & van den Heuvel ([7]) find there are two types of systems that can produce SNe Ia. The two systems consist of the close binaries with ~ 2 to $\sim 3.5\ M_\odot$ main-sequence or subgiant companions and the wide binaries with low-mass (0.9–1.2 $M_\odot$) red giant companions. The former yields the evolutionary timescale of several 10^8 years to ~ 1 Gyr, whereas the latter yields several Gyrs to a Hubble time. There is a possibility that such a mixture of two distributions of SN Ia progenitors can resolve the above discrepancy, different from the one continuous distribution function adopted by YTN. We therefore investigate the distribution of the SN Ia progenitors which can explain the chemical evolution in the solar neighborhood and the present SN Ia rate in Es simaltaneously, assuming the two systems of SN Ia progenitors exist.

Furthermore we show that the difference in the observed relative ratio of SNe II rate to SNe Ia rate between early spirals and late spirals revealed by [8] gives a constrain on the distribution of the evolutionary timescale of SN Ia progenitors.

1.2 Results

(i) *the chemical evolution in the solar neighborhood*

Assuming a mixture of two systems, we try to find the mass range of a donar star which can reproduce the evolutionary change in [O/Fe] and by a full survey in the parameter space we obtain the mass range of 1.5–$2M_\odot$ & 0.8–$1.2M_\odot$. The mass range for the close binary is completely shifted to lower mass. If the mass range predicted by the binary evolution model is adopted, it results in the [O/Fe] break point starting at lower [Fe/H] and deviating from the data because the close binary has an evolutionary timescale less than 1 Gyr. For reference, we show the cases including only wide or close binary for SN Ia progenitors (the upper panel on the left).

In the single degenerate scenario proposed by [6], optically thick winds from the mass accreting white dwarf play an essential role to stabilize the mass transfer and to escape from forming a common envelope. The optically thick winds are driven by a strong peak of OPAL opacity at $\log T(\mathrm{K}) \sim 5.2$. Since the peak is due to iron lines, the optically thick winds depend strongly on the metallicity. If the metallicity is low, an opacity decreases and a wind does not occur, which means that SNe Ia cannot be produced. Introducing such a metallicty effect on SN Ia progenitors results in reproducing the evolutionary change in [O/Fe]. It is noted that the double degenerate scenario is not accepetable with a 81 % K-S confidence from a view point of the chemical evolution in the solar neighborhood (the upper panel on the right).

(ii) *the SN Ia rate in the elliptical galaxies*

The present occurrence of SNe Ia in the elliptical galaxies (Es) means that there should exist a binary system for SN Ia progenitors which has an evolutionary timescale of several Gyrs to a Hubble time because the star formation in Es is likely to stop at $z > 1$. Therefore the wide binary system for SN Ia progenitors is inevitably necessary. Whether the rate of a wide system derived from the chemical evolution in the solar neighborhood is compatible with the observed current SN Ia rate in Es or not should be checked (the lower panel on the left).

(iii) *the relative frequencies between SN Ia and SN II in early/late-type spiral galaxies*

There exists a difference in the star formation history between early-type and late-type spiral galaxies (Ss). Early Ss evolved faster than late Ss, so that in the early phase, early Ss have much higher star formation rate than late Ss, whereas at present is reversed. Such a difference in the star formation history results in the difference in the present SN rate between early Ss and late Ss. The observed SN II rate in late Ss is about twice larger than the rate in early Ss. On the other hand, the observed SN Ia rates for both are nearly equal. Such relative frequencies among Ss can be reproduced by a mixture of two systems having different evolutionary timescales for SN Ia progenitors. The lower panel on the right shows the change in the relative frequencies over the star formation history from Sa to Sd galaxies.

1.3 Conclusion

The observational features in galaxies such as the abundance pattern of long-lived, low-mass stars and the current supernova rates present us the crucial information on the evolutionary timescale of supernova progenitors. Based on the recent progress on theoretical binary evolution models for SN Ia progenitors, we determine the distribution of SN Ia progenitors by reproducing the chemical evolution in the solar neighborhood, together with the current SN Ia rate in the elliptical galaxies. We find that a mixture of two systems for SN Ia progenitors having different evolutionary timescales is inevitably required. The one system has an evolutionary timescale of several Gyrs to a Hubble time, whereas the characteristic timescale of the other is $\sim$1.5 Gyr. The latter timescale can be shifted to several 10^8 years if the metallicity effect on SN Ia progenitors is introduced. Our results also give a solution for explaining the observed equality in the occurrence frequency of SNe Ia between early-type and late-type spiral galaxies which imposes another constraint on the distribution of SN Ia progenitors.

References

[1] Branch, D., Yungelson, L. R., Boffi, F. R., Livio, M., & Baron, E. PASP, **107** (1995), 1019

[2] Iben, I. Jr., & Tutukov, A. ApJS, **54** (1984), 335

[3] Webbink, R. ApJ, **277** (1984), 355

[4] Yoshii, Y., Tsujimoto, T., & Nomoto, K. ApJ, **462** (1996), 266

[5] Schade, D., Barrientos, L. F., & López-Cruz, O. ApJ, **477** (1997), L17

[6] Hachisu, I., Kato, M. & Nomoto, K. ApJ, **470**, L97

[7] Li, X.-D. & van den Heuvel, E.P.J., A&A, **322** (1997), L9.

[8] Cappellaro, E., Turatto, M., Tsvetkov, D. Yu., Bartunov, O. S., Pollas, C., Evans, R., & Hamuy, M. A&A, **322** (1997), 431

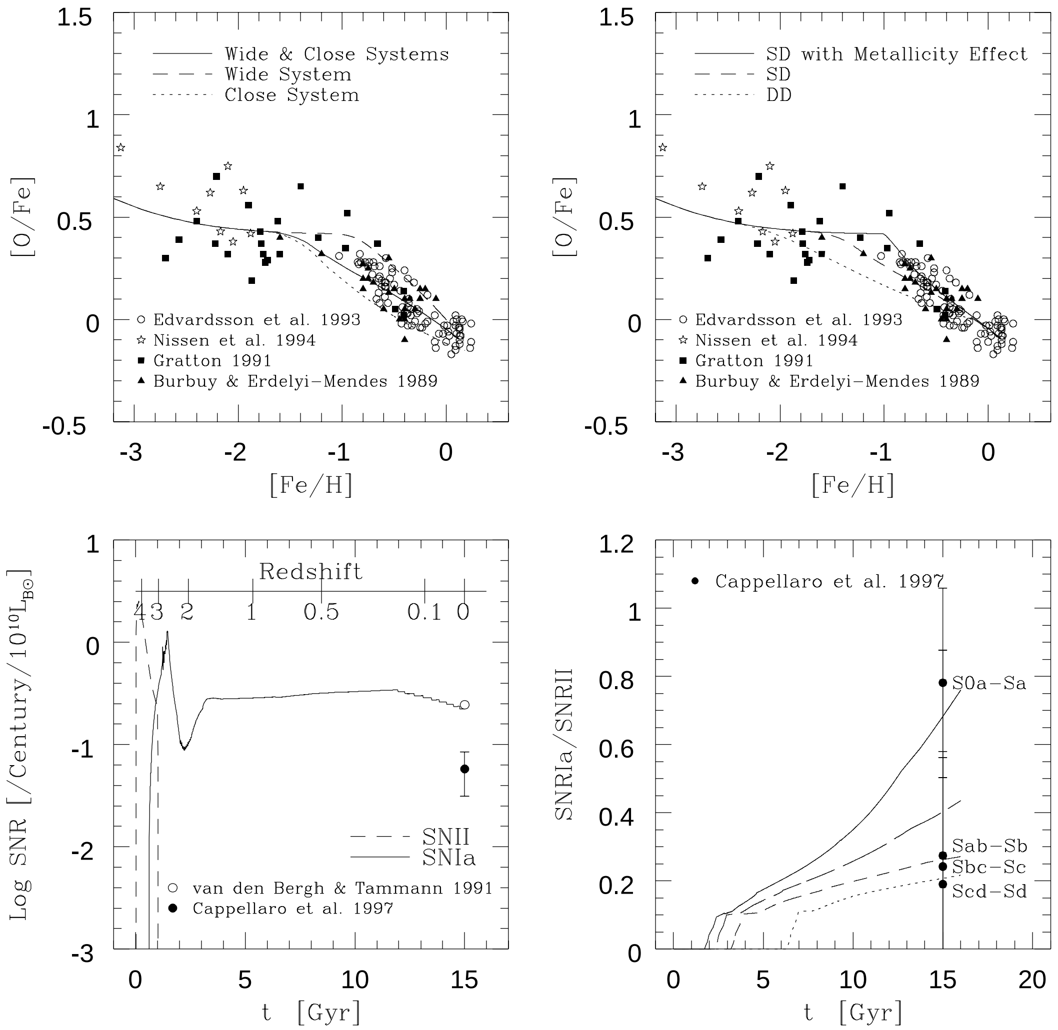

Figure 1: The evolutionary changes in [O/Fe] against [Fe/H] in the solar neighborhood (the upper panels) and the supernova rate histories for elliptical galaxies (the lower panel on the left) and Sa - Sd type spiral galaxies (the lower panel on the right).

One–Dimensional Models of Turbulent Thermonuclear Flames

A. M. Lisewski[1], *W. Hillebrandt*[1]

[1] *Max Planck Institut für Astrophysik, Karl-Schwarzschild-Str. 1, 85748 Garching, Germany*

Abstract

We present a model which shows the influence of turbulence to a thermonuclear flame during a Type Ia Supernova (Type Ia SN). Based on a statistical description of turbulence, it provides a method for investigating the physics in the distributed burning regime. Possible consequences for a deflagration to detonation transition (DDT) are discussed.

Introduction

Explosion mechanisms of a Chandrasekhar Mass White Dwarf have been subject to numerous investigations. However, despite the fact that there are different plausible models explaining the history of the explosion, many important details remain unclear. Thermonuclear reactions provide the energy source which possibly unbinds the White Dwarf. Thus, it is the physics of thermonuclear flames propagating through the star that characterizes a Type Ia SN event. The physical conditions governing the structure of this flame vary drastically during the different temporal and spatial stages of a Type Ia SN. A better understanding of these conditions, their interaction with the flame, and finally their consequences regarding the explosion itself are still important issues from the theoretical point of view.

Here, we focus on the interaction between the thermonuclear flame and turbulence taking place during the burning process. Turbulence is caused by instabilities (like shear instabilities or Rayleigh-Taylor instability) that occur on different length sales during the explosion. Rough estimates give a Reynolds number of $\mathrm{R} \sim 10^{14}$ and an integral scale of $\mathrm{L} \sim 100\,\mathrm{km}$. Consequently the Kolmogorov scale η, i.e. the scale where microscopic dissipation becomes important, is about $10^{-4}\,\mathrm{cm}$. It is this wide dynamical range that makes a representation at least by means of numerical models practically impossible.

In order to make an attempt to resolve turbulent dynamics, we first present a method, formulated in one spatial dimension, which provides essential features of three dimensional homogenous turbulence. It consists of a statistical description of turbulent mixing and a deterministic evolution of the underlying microphysics. Using this method we numerically investigate the influence of turbulence on thermonuclear flames. In particular, we give first and preliminary results, how this interaction could cause a transition between two originally well separated modes of combustion, namely the transition from deflagration to detonation. Since there is evidence from theoretical predictions and observational data for such a scenario during a SN Ia, we hope that the model presented here is able to give further insight into the physical conditions under which a DDT is possible. Apart from this special situation the model allows a systematical study of burning fronts in turbulent media.

One Dimensional Turbulence (ODT)

The fact, that fundamental aspects of turbulence can be recovered from the knowledge of the statistical moments and correlations of the velocity flow has made the statistical approach to turbulence particulary appealing. In this context we introduce a certain model of turbulence [1]. A stochastic method, implemented as a Monte Carlo simulation, is used to compute statistical properties of velocity, passive-scalars in stationary and decaying turbulence. It consists of a transverse velocity profile that evolves in time due to molecular viscosity and of a random sequence of profile rearrangements representing turbulent eddies. For the sake of simplicity we discuss homogenous shear driven turbulence only.
Given a transverse velocity profile $u(y,t)$ the mapping modelling the action of an individual eddy on u reads

$$\hat{u}(y,t) = \begin{cases} u(y_0 + f_1(y-y_0), t) \\ u(y_0 + f_2 l - (f_2 - f_1)(y-y_0), t) \\ u(y_0 + f_2 l - (1-f_2)(y-y_0), t) \end{cases} \tag{36}$$

where y_0 denotes the location and l the size of an eddy. With $f_1 = 1/3 = 1 - f_2$, this three valued map represents the action of an eddy to a velocity or passive scalar field, namely rotation and compression. Now, each random map defines an 'eddy time scale', $\tau(y_0, l, t)$, via

$$\tau(y_0, l, t) = \frac{l}{2|u_l(y_0,t) - u_l(y_0 + l/2, t)|}\,. \tag{37}$$

Here, u_l is taken to be the boxcar averaged profile u on length scale l. Following the physical fact that vortical kinetic energy density is fed by the kinetic energy of the local shear one is lead to the 'eddy rate distribution'

$$\lambda(y_0, l, t) := A/[l^2 \tau(y_0, l, t)]\,. \tag{38}$$

It represents the assumption that eddies of size l at y_0 (with tolerances dl, dy) are governed by a Poisson process with mean event rate $\lambda(y_0, l, t)\, dl\, dy$. A is the only model independent parameter, which has to be fixed empirically. In addition, the viscous transport of the profile is represented by a diffusion equation $u_t = \nu\, u_{yy}$, where ν is the kinematic viscosity.
The numerical implementation of this model reproduces typical features of homogenous turbulence. For instance, power spectra of the velocity and of possible passive scalars show the self similar $(-5/3)$ power law and the scales where the transition to dissipation takes place.
An obvious advantage of this ansatz is the high spatial resolution of turbulence compared to numerical models in three spatial dimensions. With moderate numerical effort Reynolds numbers of $\sim 10^6$ can be achieved. On the other hand ODT does not consider any pressure gradients (dynamical or external) in the temporal evolution of the velocity profile. The reason for this artefact is the inherent conservation of kinetic energy in only one spatial velocity component due to equation (38). As a consequence, pressure waves cannot be generated in the framework of ODT.

Turbulent Flames in Type Ia SNe

The physics of undisturbed laminar flames in the dense matter of a White Dwarf is well understood. The state of unburned matter, e.g. density and nuclear composition, uniquely defines the propagation velocity of the flame. For a temperature range of 10^7K to 10^{10}K and to 10% of accuracy the flame speed is given by [2]

$$s_{lam} = 92.0 \left(\frac{\rho}{2 \times 10^9}\right)^{0.805} \left[\frac{\mathrm{X}(^{12}\mathrm{C})}{0.5}\right]^{0.889} \ \mathrm{km\,s^{-1}} \,. \tag{39}$$

In addition, the width of the flame essentially depends on the density, too. Higher densities cause shorter nuclear reaction timescales. Thus, in low density regions the flame is broader than in the higher ones. Now, there is a length scale l_g (Gibson scale), which can be used as a measure of how strong turbulence affects the small scale structure of a laminar flame. If $v_{tur}(l)$ is the rms-velocity of turbulent fluctuations on a length scale l, then l_g is defined by the equation

$$s_{lam} = v_{tur}(l_g) \,. \tag{40}$$

Turbulence will disturb the laminar flame only if l_g becomes comparable or smaller than the thickness of the flame itself. Taking into account that v_{tur} obeys Kolmogorov scaling and that $v_{tur}(l = 10^6\,\mathrm{cm}) \sim 10^7\,\mathrm{cm\ s^{-1}}$, one finds that within a density range of $1 \times 10^7\mathrm{g\ cm^{-3}} \le \rho \le 5 \times 10^7\,\mathrm{g\ cm^{-3}}$ the Gibson scale is $10^{-4}\,\mathrm{cm} \le l_g \le 0.2\,\mathrm{cm}$, whereas the flame thickness decreases from 4 cm to 0.5 cm [2]. In other words, only in the late stages of a supernova explosion, where the flame has reached the low density outer layers of the White Dwarf, turbulence causes a different kind of nuclear burning, where turbulent mixing can carry away material from the interior of the flame before it is burned. This scenario is called the *distributed regime* [3]. In order to model this situation, we set up a conductive flame at a density of $\rho = 2.3 \times 10^7\,\mathrm{g\ cm^{-3}}$ propagating into unburned matter which consists half of ^{12}C and half of ^{16}O. Furthermore, turbulence is modelled using ODT. This is done by initializing a transverse velocity profile in such a manner that the turbulent velocity generated by the velocity shear is equal or larger than the laminar speed under these conditions. What is resulting dynamical range needed for an appropriate numerical implementation? Recall that the representation of turbulence via ODT demands the resolution of the Kolmogorov scale $\eta \sim 10^{-4}\,\mathrm{cm}$. The flame thickness at $\rho = 2.3 \times 10^7\,\mathrm{g\ cm^{-3}}$ is about 2 cm. Finally, to watch the flame propagating under the influence of turbulence a spatial range of $\sim$100 cm is desirable. Thus, one ends up with an dynamical range of at least six orders of magnitude. Even for a one dimensional numerical method this is too expensive. The simplest way out of this dilemma would be an artificial increase of the Prandtl number from $\mathrm{Pr} \sim 10^{-4}$ to $\mathrm{Pr} = 1$ corresponding to an increase of the Kolmogorov scale to $\eta \sim 10^{-1}\,\mathrm{cm}$. Of course, this strongly underestimates turbulence. Nevertheless, we use this as a first and simplified model.

Figure 1 shows how, beginning from an step function like initial temperature profile, turbulence distributes the burning region. The interface seperating completely burned material and pure fuel, i.e. $\mathrm{X}(^{12}\mathrm{C}) = 0.5$, gets broader and after 5.3×10^{-5} s it reaches a size of about 10 cm. The second panel shows the resulting power spectra of the velocity and of the temperature as a passive scalar. Up to a constant factor $\mathrm{S}_2(k)$ is the Fourier transform of the second structure function $\mathrm{S}_2(r) := \langle (v_{tur}(0) - v_{tur}(r))^2 \rangle$. The temperature power spectrum is defined in the same way. The formation of a broad interface between fuel and ashes mentioned above gives a first indication of how turbulent mixing in the distributed regime could cause a transition to detonation.

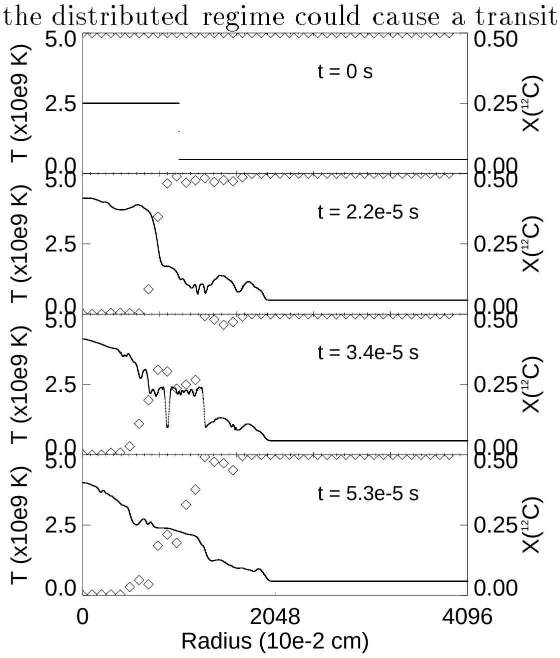

Fig. 1: The temporal evolution of the temperature (–) and the X(^{12}C) profile (◇) at $v_{tur}(l = 10\text{cm}) = 4 \times 10^4\,\text{cm s}^{-1}$.

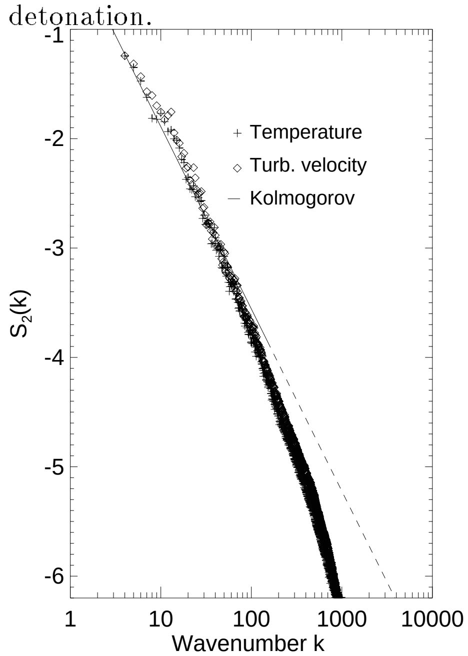

Fig. 2: Power spectra of the velocity and temperature fluctuations compared to the KOLMOGOROV power law.

Khokhlov et al. [4] showed that if this interface reaches a certain size a detonation wave will emerge. In fact, for the density we used here (2.3×10^7 g cm^{-3}) its spatial distribution must have a size of at least 10^4 cm. Unfortunalety this is beyond the scope of our present simulations, but a rough extrapolation shows that turbulence could indeed provide this condition. If the spatial distribution of fuel mass fraction has reached a size of 10 cm after $\sim 5 \times 10^{-5}$s then we can represent this fact by a velocity $w(l = 10\text{cm}) = 10\,\text{cm}/5 \times 10^{-5}\,\text{s} = 2 \times 10^5\,\text{cm s}^{-1}$. Now, if we furthermore assume a naive KOLMOGOROV scaling for $w(l)$ then

$$w(l = 10^4\text{cm}) = (10^3)^{1/3} \times w(l = 10\,\text{cm}) = 2 \times 10^6\,\text{cm s}^{-1}\,. \tag{41}$$

Consequently, the critical length needed for a detonation would form after about 5 ms. This is still much shorter than a typical hydrodynamical timescale in which the star expands.

Acknowledgements

We thank J. Niemeyer and especially S. Woosley for many helpful discussions and for providing essential parts of the numerical code.

References

[1] A.L. Kerstein, submitted to J. Fluid Mech. (1997).

[2] F.X. Timmes and S.E. Woosley, ApJ **396** (1992) 649.

[3] J. C. Niemeyer and S. E. Woosley, ApJ, **475**, (1997) 740.

[4] A.M. Khokhlov, E.S. Oran and J.C. Wheeler, ApJ **478** (1997) 678.

Galactic chemical evolution: from the local disk to the distant Universe

N. Prantzos[1]

[1] *Institut d'Astrophysique de Paris*

Despite more than 30 years of intense theoretical and observational studies, galactic chemical evolution is not yet a mature astrophysical discipline (compared e.g. to stellar evolution). One can identify two main reasons for that situation:

• lack of a galactic equivalent of the HR diagram, that would show unambigously the evolutionary status of galaxies;

• lack of an understanding of the main motor engine of galactic evolution, namely the creation of stars out of galactic gas (compared to our fairly good understanding of the motor of stellar evolution, namely nuclear reactions).

Progress in the theory of galactic chemical evolution has been very slow (almost 20 years after, Tinsley's (1980) review continues to be probably the best on the subject). Since the number of model parameters is, in general, larger than the number of observables, one may sometimes feel that she/he is only constrained by her/his own imagination. This may be the case for most extragalactic systems, but it certainly does not apply to the case of our Galaxy: the wealth of available data, especially in the solar neighborhood, constrain seriously the parameters of simple models of chemical evolution and point to a rather well defined history for the local disk (LD).

In the following, we present a brief review of the observational data for the LD (Sec. 1) and the hints they reveal as to the past history of that region. It turns out that this history allows only for a small depletion of deuterium (D), less than a factor of 3 from its pregalactic value. The observational data for the rest of the Milky Way disk are much less constraining for the models (Sec. 2). They suggest, however, that star formation has been much more vigorous in the inner Galaxy. In consequence, a much larger astration (and, hence, D depletion) has taken place in those regions; the resulting D gradient, measurable by the future *FUSE-LYMAN* mission (to be launched by the end of 1998) should provide invaluable information as to the past history of the disk (Prantzos 1996). Finally, assuming that our Galaxy is a typical spiral, one can calculate the properties of disk galaxies as a function of redshift (in the framework of a given cosmological model) and compare to the observed properties of the extragalactic universe: global star formation rate, gas content and metal abundances in gas clouds. Preliminary conclusions of such a comparison appear in Sect. 3.

1.1 The solar neighborhood

In Fig. 1 we present the main observational constraints on the chemical evolution of the solar neighborhood, compared to the results of a simple model of galactic chemical evolution. The model adopts a stellar initial mass function (IMF) from Kroupa *et al.* (1993), stellar yields from Woosley and Weaver (1995), star formation rate (SFR) $\Psi \propto$

$\Sigma_{Gas}^{1.5}$, and infall (with a gaussian dependence on time). *Left upper panel:* Local surface densities of gas (Σ_G), stars (Σ_*) and total amount of matter (Σ_T). Currently observed values are indicated on the right, between vertical error bars. The corresponding model results are indicated by *solid, dashed* and *dotted* curves, respectively. *Left lower panel:* Rates of infall (*dotted curve*)and star formation (SFR, *solid line*); the latter is to be compared to the currently observed one $\Psi_0 \sim$ 3-5 $M_\odot$ pc^{-2} Gyr^{-1} (vertical error bar on the right). *Middle upper panel:* Age-metallicity relationship in the solar neighborhood (from Table 14 of Edvardsson *et al.* 1993). The data (182 F-type stars) are binned in groups of 0.2 in log(Age), where the age is expressed in Gyr. Metallicities are for stars with galactocentric distances evaluated to 8-9 kpc, *i.e.* appropriate to solar neighborhood only and volume corrected (column 6 in Table 14 of Edvardsson *et al.* 1993). The vertical error bars represent 1 σ dispersion in metallicity for each age group (column 6 of Table 15 in Edvardsson *et al.* 1993). The *solid curve* is the result of the model. *Middle lower panel:* Evolution of deuterium. Data points for pre-solar D/H from Geiss and Gloeckler (1998) and for the local ISM from Linsky (1998). *Right upper panel:* Metallicity distributions of G-type stars in the solar neighborhood. Data from Rocha-Pinto and Machiel (1996, *triangles*) and Wyse and Gilmore (1995, *squares*). *Solid curve:* model results; *dotted curve:* results of a closed box model, shown for illustration purposes. *Right lower panel:* O vs. Fe relationship in the local disk. Data from Edvardsson *et al.* (1993). The observed decline of O/Fe is attributed to the delayed appearance of SNIa, producing ~2/3 of the solar Fe.

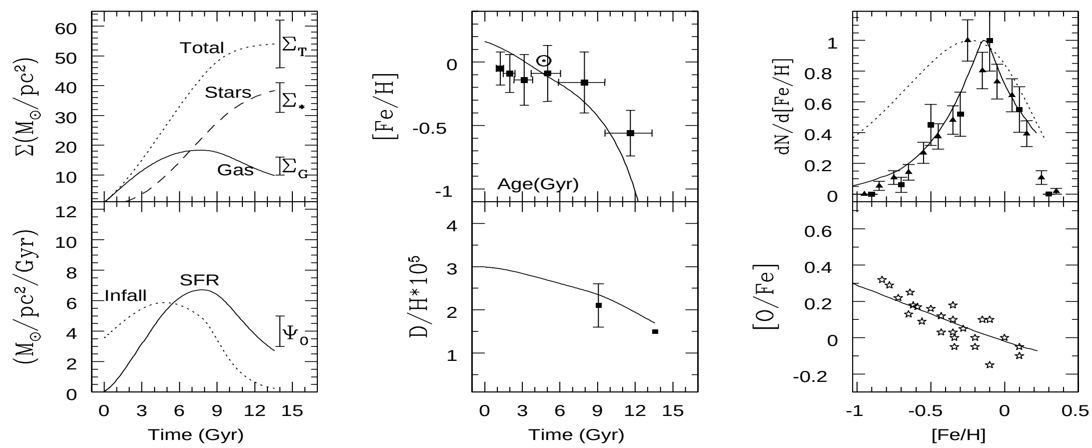

Figure 1: Chemical evolution of the solar neighborhood: model vs. observations

1.2 The Milky Way disk

In Fig. 2 we present the results of a simple (independent ring) model for the chemical evolution of the Milky Way disk at a galactic age T=13 Gyr, and comparison to observations. The adopted SFR is SFR$\propto \Sigma_G^{1.5}$/R and the adopted infall rate is gaussian in time with $\Delta\tau$=6 Gyr in all the zones. *Left*, from top to bottom: final profiles of the surface density of gas, stars and of the gas fraction, respectively. *Solid lines*: model results; *shaded regions* correspond to observations for the disk, and data points at R=8.5 kpc to solar system values. *Right*, from top to bottom: current SFR, O and D profiles, respectively. SFR is normalised to its local value and D to its primordial one D_P. Data for O are from HII regions (*open symbols*, from Shaver et al. 1993) and B-stars (*filled symbols*, from Smart and Rolefston 1997).

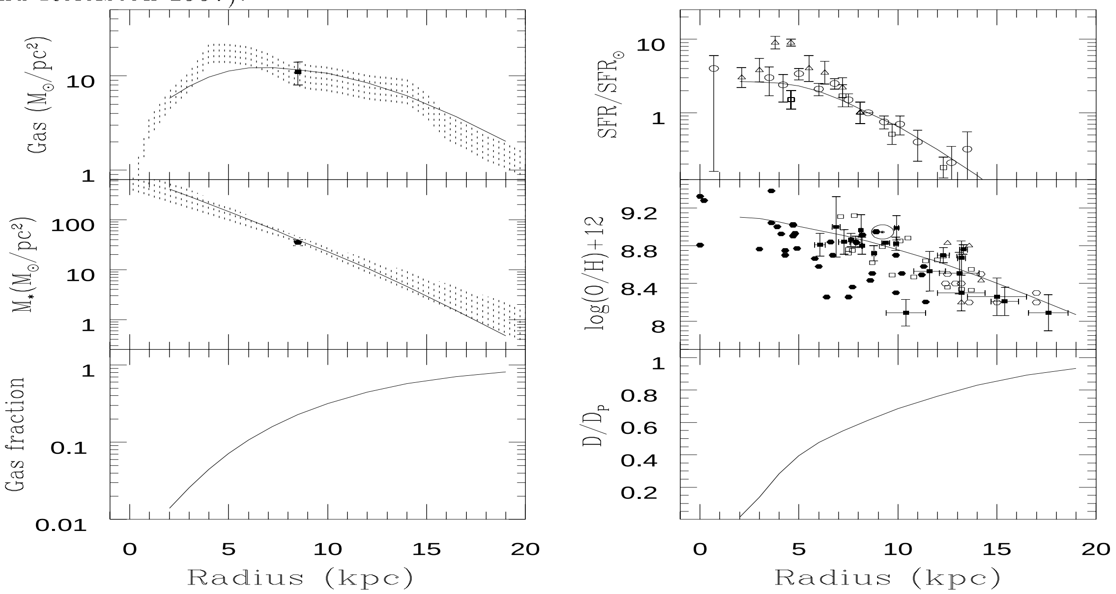

Figure 2: Current density and abundance profiles of the Milky Way disk: model (*solid curves*) vs. observations

1.3 Cosmic chemical evolution

Finally, in Fig. 3 we present the corresponding history of the Milky Way disk as a function of time (*left*) and of redshift (*right*), assuming that our galaxy is a typical spiral; a cosmological model with Ω=0.3, h_0=0.6 and galaxy formation starting 1.0 Gyr after the Big Bang is adopted.

Left, from top to bottom: History of a) Total (disk+bulge) SFR, bulge SFR and total infall rate; b) gaseous, stellar and total mass; c) SNII (*solid* line) and SNIa (*dotted* line) rates; d) overall metallicity in four different zones, at distances of 2, 8.5 and 17 kpc from the galactic center and in the bulge; e) [a/Fe] ratio in the same zones; f) D abundance in the same zones.

Right, from top to bottom: a) the "cosmic" SFR of disk galaxies,when normalised to the current local value (z=0), does not show the steep observed increase back to $z \sim 1$ (although it peaks at $z \sim 1$, as observational data do); other galaxy types (ellipticals ?) should account for the discrepancy between theory (*solid line*: total SFR; *dashed* line: bulge SFR) and observations; data from Madau (1997). b) Evolution of gas and star densities; data for neutral gas (HI + 25% He; *open* symbols) from Natarajan and Pettini (1997); local star density (*filled* symbol) from Briggs (1997). c) cosmic evolution of SNII and SNIa rates; d) The evolution of metallicity, traced by Zn, in various regions of spiral disks (the same regions as on the corresponding panel on the left) brackets well the observed abundances of Zn/H in Lyα absorbers; data from Pettini *et al.* (1997, *open* symbols) and Lu *et al.*

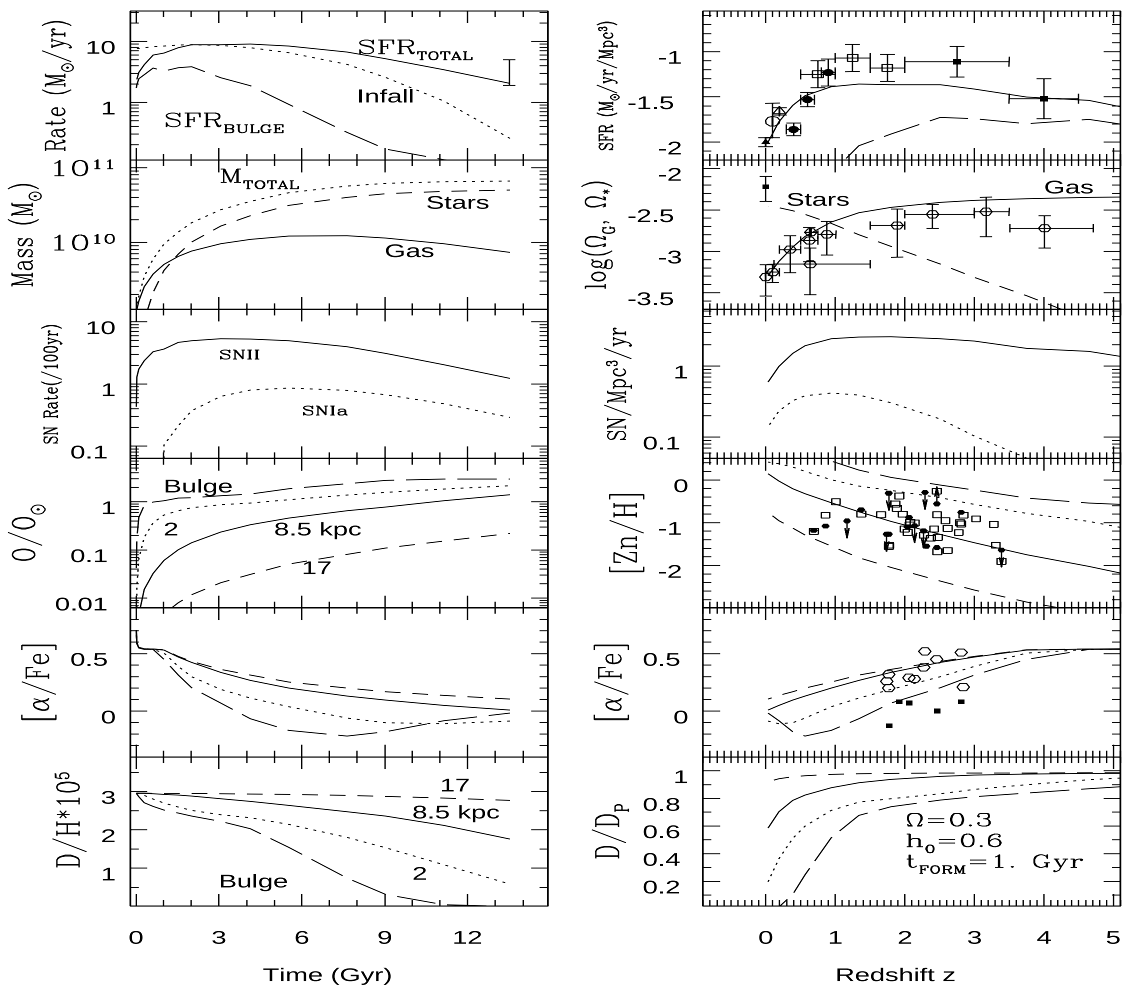

Figure 3: Evolution of the Milky Way disk as a function of time (*left* and of redshift (*right*, compared to observables of cosmic chemical evolution

(1996, *filled* symbols); those systems may well be (proto)galactic disks. e) the [α/Fe] ratio in those same zones declines smoothly from its initial value of ~0.5 at high z (due to SNII) to ~solar values (due to Fe produced by SNIa), at a rate depending on the corresponding SFR; data for Si/Fe from Lu *et al.* (1996, *open* symbols, neglecting dust depletion) and Vladilo (1998, *filled* symbols, corrected for dust effects). f) The corresponding evolution of D shows that considerable depletion may take place in the inner disk regions, but only at low redshifts; abundances measured at high redshifts should be close to the primordial value.

References

[1] Briggs F., 1997, Publ. Astr. Soc. Austr., 14, 31

[2] Edvardsson B., Anderssen J., Gustafsson B., Lambert D., Nissen P. & Tomkin J, 1993, AA, 275, 101

[3] Gallego J., Zamorano J., Aragon-Salamanca A. & Rego M., 1995, ApJ Let., 455, L1

[4] Geiss J. & Gloeckler G., 1998, in *Primordial Nuclei and their Galactic Evolution*, Eds. N. Prantzos, M. Tosi & R. von Steiger (Kluwer), p. 251

[5] Kennicutt R., 1989, ApJ, 344, 685

[6] Kroupa P., Tout C. & Gilmore G., 1993, MNRAS, 262, 545

[7] Linsky D., 1998, in *Primordial Nuclei and their galactic evolution*, Eds. N. Prantzos, M. Tosi & R. von Steiger (Kluwer) p. 283

[8] Lu L., Sargent W., Barlow T., Churchill C. & Vogt S., 1996, ApJ Suppl., 107, 475

[9] Madau P., 1997, astro-ph/9709147

[10] Madau P., 1998, astro-ph/9801005

[11] Matteucci F. & François P., 1989, MNRAS, 239, 885

[12] Natarajan P. & Pettini M., 1997, MNRAS, 291, L28

[13] Pettini M. Smith L., King D. & Hunstead R., 1997, ApJ, 486, 665

[14] Prantzos N., 1996, A&A, 310, 106

[15] Prantzos N., 1998a, in *Primordial Nuclei and their galactic evolution*, Eds. N. Prantzos, M. Tosi & R. von Steiger (Kluwer) p. 225

[16] Prantzos N. & Aubert O., 1995, A&A, 302, 69

[17] Renzini A. & Voli A., 1981, A&A, 94, 175

[18] Rocha-Pinto H., Maciel W., 1996, MNRAS, 279, 447

[19] Samland M., Hensler G. & Theis , 1997, ApJ, 476, 544

[20] Schaller G., Schaerer D., Maeder A. & Meynet G., 1992, A&AS, 96, 269

[21] Shaver P., McGee R., Newton L., Danks A. & Pottasch S., 1983, MNRAS, 204, 53

[22] Smartt S. & Rolleston W., 1997, ApJ Let, 481, L47

[23] Storrie-Lombardi L., McMahon R., Irwin M., 1996, MNRAS, 283, L79

[24] Tinsley B., 1980, Fund. Cosm. Phys., 5, 287

[25] Vilchez J. & Esteban C., 1996, MNRAS, 280, 720

[26] Vladilo G., 1998, ApJ, 493, 583

[27] Woosley S. & Weaver T., 1995, ApJ Suppl., 101. 181

[28] Wyse R. & Gilmore G., 1995, AJ, 110, 2771

[29] Wyse, R. & Silk, J. 1989, ApJ, 339, 700

Light–Element Nucleosynthesis: Big Bang and Later on

J. López–Suárez [1] *and R. Canal* [1,2]

[1] *Dept. Astronomy, Univ. Barcelona, Spain*
[2] *IEEC/UB, Barcelona, Spain*

Production of the light nuclides D, ^{3}He, ^{4}He, and ^{7}Li in their currently inferred primordial abundances by standard, homogeneous big bang nucleosynthesis (SHBBN) would imply a baryon fraction of the cosmic closure density Ω_b in the range:

$$0.04 \leq \Omega_b h_{50}^2 \leq 0.08 \tag{1}$$

where h_{50} is the Hubble constant in units of 50 km s^{-1} Mpc^{-1} [1], [2]. Therefore, for the long–time most generally favored cosmological model with critical matter density and zero cosmological constant ($\Omega_M = 1$, $\Omega_\Lambda = 0$), more than 90% of the matter in the universe should be nonbaryonic. That has led to explore different alternatives to SHBBN (see [3] for a review).

Baryon inhomogeneities generated in a first–order quark–hadron phase transition [4] and resulting in regions with different n/p ratios has been the most thoroughly explored alternative. Agreement with the inferred primordial abundances could only be obtained for Ω_b within the range (1) again, for spherically condensed fluctuations at least [5]. Recently, however, it has been shown that $\Omega_b h_{50}^2$ might be as high as $\simeq 0.2$ in inhomogeneous models if one assumes cylindrical shape for the inhomogeneities together with a very high density contrast [6].

Another approach has been to assume that there are unstable particles X, with masses m_x higher than a few GeV and lifetimes τ_x longer than the standard thermonuclear nucleosynthesis epoch [7]. Gravitinos produced during reheating at the end of inflation might be an example of such particles. Their decay would give rise to both electromagnetic and hadron cascades, and the resulting high–energy photons would mainly photodisintegrate a fraction of the preexisting He whilst the high–energy hadrons would produce light nuclides via spallation–like reactions. A caveat of this model is that it predicts $^6Li/^7Li \gg 1$ whereas observations show that $^6Li/^7Li \leq 0.1$.

Concerning SHBBN, recent determinations of D abundances in high–redshift QSO absorbers, when confronted with the currently inferred primordial ^{4}He abundance, might be in conflict with the predictions for $N_\nu = 3$ [8]. That suggests a temporary abandon at least of SHBBN as a criterion to set bounds to Ω_b. On the other hand, values of Ω_M much lower than the closure density are now being derived from a variety of sources, including high–z supernova searches [9], [10]. The questions of which fraction of Ω_M could be baryonic and of the primordial nucleosynthesis bounds are thus posed in new terms.

Here we explore a composite model: baryon inhomogeneities are first produced at some phase transition prior to thermonuclear nucleosynthesis. The latter, therefore, takes place in two different types of regions: neutron–rich and neutron–poor ones. Then, when the universe has cooled down further and thermonuclear reactions do no longer take place, X–particle decay starts and the resulting electromagnetic and hadronic showers modify the light–nuclide abundances in both regions.

We model the inhomogeneities in a very simple way: there are two types of regions characterized by their density contrast R and by their respective volume fractions f_v and $1-f_v$. Their comoving length scale (d/a) enters in the neutron diffusion rate and is a third parameter of the model. The treatment is the same as in [11]. The X–particles, in turn, are characterized by their half–life τ_x, their mass m_x, the ratio of their number density to that of photons $r \equiv n_x/n_\gamma$, plus their mode of decay. The product rm_x enters in the model as one of the parameters, together with τ_x. The last parameter is the effective baryon ratio r_b^*, which takes into account the dependence of the number of baryons produced in the decays on m_x together with the dependence of the light–element yields on the kinetic energies of the primary shower baryons. A more detailed account of the model can be found in [12] and [13].

We have explored the parameter space of our model and found good agreement with currently inferred primordial abundances for:

a) Density contrasts $500 \leq R \leq 5000$.

b) Volume fractions $0.144 \leq f_v \leq 0.192$.

c) Comoving length scales $(d/a) \simeq 10^{7.5}$ $cm\ Mev$ (little neutron diffusion).

d) Small abundances of the X–particles: $1.5 \times 10^{-12} GeV \leq rm_x \leq 1.5 \times 10^{-11} GeV$.

e) Half–lives of the X–particles: $6.19 \times 10^5 s \leq \tau_x \leq 7.43 \times 10^5 s$.

f) Moderate numbers and energies of the shower baryons: $1.5 \times 10^{-12} \leq r_B^* \leq 1.5 \times 10^{-11}$.

g) Baryon density parameter: $18 \leq \eta_{10} \leq 22$.

Those results are illustrated in Figure 1, where we show the predicted primordial abundances of the light nuclides as a function of τ_x, for $\eta_{10} = 18$, and fixed values of the other parameters taken within the intervals a)–d) and f). The η_{10} range translates into:

$$0.25 \leq \Omega_b h_{50}^2 \leq 0.35 \tag{2}$$

in sharp contrast with (1).

As we also see in the Figure, a testable prediction of the model is the production of a Be abundance $({}^9Be/H)_p \sim 10^{-13}$. The predicted B abundance is much smaller. Production of Be and B is a typical feature of inhomogeneous models. Data on Be and B abundances in halo stars now extend down to metallicites $[Fe/H] \sim -3.0$ and they show a nearly constant B/Be ratio ~ 10 [14] while the smallest Be abundances measured are already of the order of our model prediction. Agreement with the observations would thus require a reversal in the B/Be ratio at still lower metallicities. On the other hand, the apparently primary behaviour of the Be and B abundances in the Galactic halo, together with the Li abundances there, is a still usolved puzzle [15].

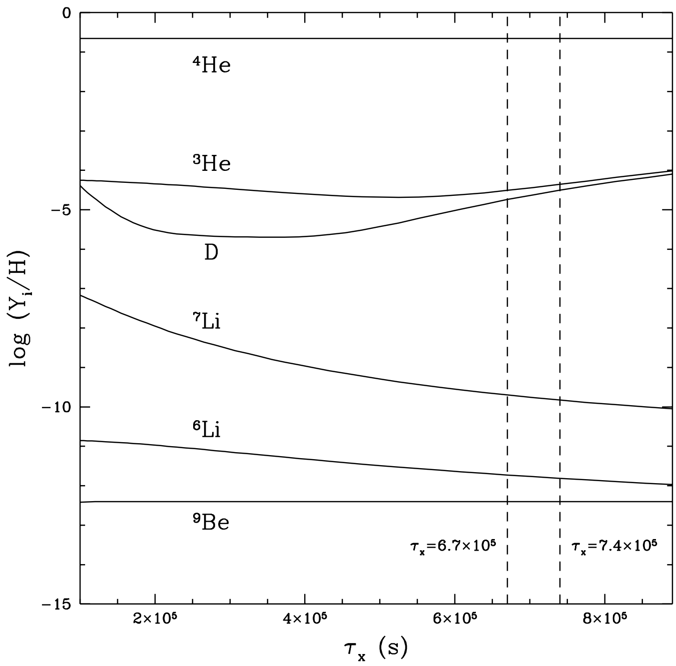

Figure 1: Primordial abundances of the light nuclides as a function of τ_x, the half–life of the X–particles, for fixed values of the other parameters

The model presented here is an example of how comparatively minor deviations from SHBBN might very significantly broaden the range of Ω_b compatible with the primordial abundances inferred from observations. Planned improvements of the model are a more realistic treatment of the inhomogeneities, and also consideration of shorter τ_x for which X–particle decays would occur simultaneously with the thermonuclear reactions.

References

[1] T.P. Walker et al., ApJ, **376** (1991) 51.

[2] C.J. Copi, D.N. Schramm, and M.S. Turner, Science, **267** (1995), 192.

[3] R.A. Malaney and G.J. Mathews, Phys. Rep., **229** (1993), 145

[4] E. Witten, Phys. Rev. D, **30** (1984), 1.

[5] K. Jedamzik, G.M. Fuller, and G.J. Mathews, ApJ, **423** (1994), 50.

[6] M. Orito et al., ApJ, **488** (1997), 515.

[7] S. Dimopoulos et al., ApJ, **330** (1988), 545.

[8] G. Steigman, N. Hata, and J.E. Felten, ApJ, in press (1998).

[9] S. Perlmutter et al., Nature, **391** (1998), 51.

[10] P.M. Garnavich et al., ApJ, **493** (1998), L53.

[11] T. Rauscher et al., ApJ, **429** (1994), 499.

[12] J. López–Suárez, PhD Thesis, Univ. Barcelona (1997).

[13] J. López–Suárez and R. Canal, ApJ (Letters), submitted (1998).

[14] R.J. García–López et al., ApJ, in press (1998).

[15] A. Alibés and R. Canal, in preparation (1998).

Primordial nucleosynthesis in globular clusters, or the puzzling MgAl anticorrelation

P.A. Denissenkov (Univ. of St. Petersburg, Russia), G.S. Da Costa & J.E. Norris (MSSSO, Australia), A. Weiss (MPA, Germany)

1.1 Introduction

Talking about globular clusters' (hereafter, GCs) chemical composition we actually mean the chemical composition of low mass ($M \leq 0.9\,M_\odot$) stars (primarily, red giants on their first ascent along the RGB) in these clusters.

What do observations tell us?

On the one hand, in an arbitrarily chosen GC there are NO star-to-star abundance variations either of [Fe/H][2] (only a few exceptions exist), or of the "heavy" α-elements (Si, Ca, Ti), or of the iron peak elements (Cr and Ni). Hence, those elements were produced and homogeneously distributed throughout a (proto-) GC *primordially*, presumably by SNe II.

On the other hand, in a number of GCs THERE ARE star-to-star abundance variations of C, N, O, Na, Al and Mg. These elements are potential participants (as catalysts) in hydrostatic hydrogen burning (HB in CNO-, NeNa- and MgAl-cycles) and observations do support the idea that HB might be responsible for their abundance variations (low $^{12}C/^{13}C$ ratios, approximate constancy of the sums C+N+O and Mg+Al, anticorrelations of [O/Fe] with [Na/Fe] and [Al/Fe]).

The principal question, however, is whether the abundance variations of C, N, O, Na, Al and Mg are produced directly in the stars we observe or being of primordial origin. The first possibility will be refered to as "the evolutionary scenario" and the second one as "the primordial scenario".

1.1.1 The evolutionary scenario

In a red giant ascending the RGB THERE IS a place where abundances of C, N, O, Na and Al change. This is a small (by mass) region between the HB shell and the base of convective envelope (BCE). Here, Na is produced at the expense of ^{22}Ne and (deeper) of ^{20}Ne, and Al at the expense of ^{25}Mg.

The only problem is how to bring the products of the HB to the BCE. Following Sweigart & Mengel's idea (1979) we assume that some kind of mixing (meridional circulation or something else) does this work. We merely introduce this additional mixing in

[2] We use the standard spectroscopic notation, $[A/B] = \lg(N_A/N_B)_{star} - \lg(N_A/N_B)_\odot$

our calculations by adding diffusion terms to nuclear kinetics equations. We have two free parameters: depth and rate of mixing. Now the question is whether we can explain the whole spectrum of the abundance variations (and correlations) seen in GCs by adjusting the parameters of mixing.

For comparison with observations we chose the GCs ω Cen and M 13. The first cluster belongs to those few exceptions where [Fe/H] varies from star to star but at the same time it is one of a few clusters for which correlations between abundances of several elements are available.

As the initial chemical composition we used the solar abundances scaled down to observed metallicities of ω Cen and M 13 and after that further modified to take into account the abundance patterns revealed in halo dwarfs, for instance, [O/Fe]=+0.4, [Na/Fe]=[Al/Fe]=−0.4 etc., as reviewed by Wheeler et al. (1989). We, however, assumed that [^{22}Ne/Na]=0 and not +0.4 because it is this the initial ^{22}Ne abundance that gives a theoretical O-Na anticorrelation in agreement with observations.

In Fig. 1 results of our calculations are compared with observations for red giants in ω Cen. One can see that the presented observational (anti-) correlations between abundances of C, N, O and Na are reproduced reasonably well in the evolutionary scenario for the same set of the mixing depth and rate. An exception is the O versus Al anticorrelation (Fig. 1, solid line in panel b). A similar conclusion can be made for the cluster M 13: again we reproduce the O vs. Na correlation and fail to explain a rise of Al accompanied by a decline of Mg (Fig. 2, dashed line in panel c).

In red giants Al is mainly produced in the chain of reactions ^{25}Mg(p,γ)^{26}Al$^{\rm g}$(p, γ)^{27}Si ($\beta^+\nu$)^{27}Al. For the accepted initial composition we have ^{24}Mg/^{25}Mg/^{26}Mg = 90/4.5/5.0 (for the Sun 79/10/11). If we assume that in GC red giants the initial abundance of ^{25}Mg is [^{25}Mg/Fe]=1.1 (instead of 0.0) and make the Al producing channel wider by increasing the rate of the reaction ^{26}Al$^{\rm g}$(p,γ)^{27}Si by a factor of $\sim 10^3$ as compared to its rate given by Caughlan & Fowler (1988) (the latter is possible in principle due to a large uncertainty in this reaction rate in the temperature range appropriate to the HB shell in red giants), then we can reproduce the O-Al anticorrelation in the both clusters (Fig. 1, short-dashed line in panel b, and Fig. 2, dot-dashed line in panel c). Since in this case we have a large initial ^{25}Mg abundance we can speculate that the decline of the Mg abundance observed in M 13 is in fact a consequence of a decline of ^{25}Mg in the sum of abundances of the Mg isotopes.

Recently, an unprecendented spectroscopic analysis has been done by Shetrone (1996). He measured the Mg isotopic composition in a small sample (6 stars) of bright red giants in M 13. In 5 giants with enhanced Al he found unusual abundance ratios of the Mg isotopes with the average values $\langle^{24}\mathrm{Mg}\rangle/\langle^{25}\mathrm{Mg}\rangle/\langle^{26}\mathrm{Mg}\rangle = 56/22/22$.

Unfortunately, Shetrone could not separate ^{25}Mg from ^{26}Mg and merely assumed they had equal abundances. Therefore, one could immediately speculate that the 5 peculiar giants in Shetrone's sample have in fact $\langle^{24}\mathrm{Mg}\rangle/\langle^{25}\mathrm{Mg}\rangle/\langle^{26}\mathrm{Mg}\rangle = 56/0/44$, as if the initially abundant ^{25}Mg has been transformed into Al and partially into ^{26}Mg. But this turns out to be not so simply to do because for these 5 stars Shetrone finds $\langle[^{24}\mathrm{Mg/Fe}]\rangle = -0.33$!!!, as if Al has been produced at the expense of ^{24}Mg and not of ^{25}Mg.

<u>The possibilities of how to comply with the new observational data</u>

1. There is still an undetected low energy resonance in the reaction ^{24}Mg(p,γ)^{25}Al, which would give the best solution of the whole MgAl puzzle.
2. Some red giants in GCs had been primordially enriched in ^{25}Mg and at the same time became deficient in ^{24}Mg.
3. In some red giants we observe products of HB at higher (say, $T \geq 70{\cdot}10^6$ K) temperatures than in the standard models ($T \leq 55 \cdot 10^6$ K).

The second possibility is actually "the primordial scenario" we are going to consider next.

1.1.2 The primordial scenario

We have made use of the scenario of GCs' formation proposed by Cayrel (1986) and elaborated upon by Brown et al. (1995). Its main theses are as follows:

◇ The first stars formed in a dense protocluster's core from material having the Big Bang composition were solely massive stars. They evolved quickly and exploded as SNe II.

◇ Later on, stars of the whole mass spectrum formed in a supershell produced by multiple SNe explosions.

◇ In addition, some low mass stars could form from material polluted by ejecta from intermediate-mass AGB stars or acrete such material during their evolution.

According to this scheme we first consider abundances in question ejected by SNe II with $Z = 0$ as functions of SN progenitor's mass (Fig. 3). Data for this figure are taken from Woosley & Weaver (1995). One may pay attention that [^{25}Mg/^{24}Mg] is rather low in Fig. 3.

The abundances from Fig. 3 weighted by a low mass cutoff Salpeter initial mass function were diluted in the supershell. The dilution coefficient can be estimated as $v_s/v_{ej} \sim 10^{-3}$ (for details see Cayrel 1986, and Denissenkov et al. 1998). In Table 1 the final abundances are given. Note that abundances of α-elements are here underestimated by about 0.5 dex because Woosley & Weaver's (1995) models of SNe II overproduce Fe. But for us this is not critical because we are interested in relative abundances of ^{22}Ne, Na, Al and Mg isotopes. With respect to these we find that [^{22}Ne/Na] is too small for Na to be produced from ^{22}Ne in red giants. Similarily, [^{25}Mg+^{26}Mg/Al] is too low for the production of Al from ^{25}Mg.

Considering nucleosynthesis in intermediate-mass AGB stars we have made use of a parametric model which is very like that of Renzini & Voli (1981). It includes hot-bottom burning (HBB), hydrogen shell burning, thermal pulses of the He shell and the third dredge-up. Results of our calculations with this model are shown in Fig. 4 for a $5\,M_\odot$ AGB star after 400 pulses for three values of the HBB temperature. We see that the model gives us what we need, namely:

Table 1: Abundances expected as the result of SNeII explosions

abundance(s)	SNeII
[C/Fe]	−0.25
[N/Fe]	−2.44
[O/Fe]	−0.05
[^{20}Ne/Fe]	+0.10
[Na/Fe]	−0.52
[^{24}Mg/Fe]	−0.05
[^{25}Mg/Fe]	−1.25
[^{26}Mg/Fe]	−1.27
[Mg/Fe]	−0.15
[Al/Fe]	−0.67
[Si/Fe]	−0.15
[Fe/H]	−2.31
[^{22}Ne/Na]	−2.34
[^{25}Mg+^{26}Mg/Al]	−0.59
^{24}Mg/^{25}Mg/^{26}Mg	98/1/1

◇ ^{22}Ne, ^{25}Mg and ^{26}Mg are copiously synthesized (during He pulses !),

◇ ^{23}Na is produced in the reactions ^{22}Ne(n,γ)^{23}Ne($\beta^-\bar{\nu}$)^{23}Na, and the ratio ^{22}Ne/Na increases considerably,

◇ ^{24}Mg is being depleted during HBB, which results in some Al production.

1.1.3 Concluding remarks

¿From inspection of Fig. 4 one could even infer that we do not need the evolutionary scenario at all, but it is not true. In fact, there are very convincing observational arguments in favour of the both scenarios.

The evolutionary scenario is strongly supported by a progressive decline of [C/Fe] with increasing luminosity of a red giant observed in several GCs (see references in Denissenkov et al. 1998). There are also data indicating that the number of Na enriched giants gets larger at higher luminosities in M 13 (Pilachowski et al. 1996). Besides, the primordial scenario alone cannot explain the low O abundances in GC red giants because O must be synthesized from C during He pulses in AGB stars.

The primordial scenario is supported by observations of the CN-bimodality and Na overabundances traced down to the MS turn-off in the GC 47 Tuc (Briley et al. 1996).

Therefore, a solution of the problem may be found in a combined, i.e. “evolutionary+primordial” scenario.

References

[1] Briley M.M., Smith V.V., Suntzeff N.B., Lambert D.L., Bell R.A., Hesser J.E., 1996, Nature 383, 604

[2] Brown J.A., Wallerstein G., 1993, AJ 106, 133

[3] Brown J.H., Burkert A., Truran J.W., 1995, ApJ 440, 666

[4] Caughlan G.R., Fowler W.A., 1988, AD&NDT 40, 283 (CF88)

[5] Cayrel R., 1986, A&A 168, 81

[6] Denissenkov P.A., Da Costa G.S., Norris J.E., Weiss A., 1998, A&A 333, 926

[7] El Eid M.F., Champagne A.E., 1995, ApJ 451, 298

[8] Kraft R.P., Sneden C., Smith G.H., Shetrone M.D., Langer G.E., Pilachowski C.A., 1997, AJ 113, 279

[9] Norris J.E., Da Costa G.S., 1995, ApJ 447, 680 (ND95)

[10] Pilachowski C.A., Sneden C., Kraft R.P., Langer G.E., 1996, AJ 112, 545

[11] Renzini A., Voli M., 1981, A&A 94, 175

[12] Shetrone M.D., 1996, AJ 112, 2639

[13] Sweigart A.V., Mengel J.G., 1979, ApJ 229, 624

[14] Wheeler J.C., Sneden C., Truran J.W., 1989, ARA&A 27, 279

[15] Woosley S.E., Weaver T.A., 1995, ApJ Suppl. Ser. 101, 181

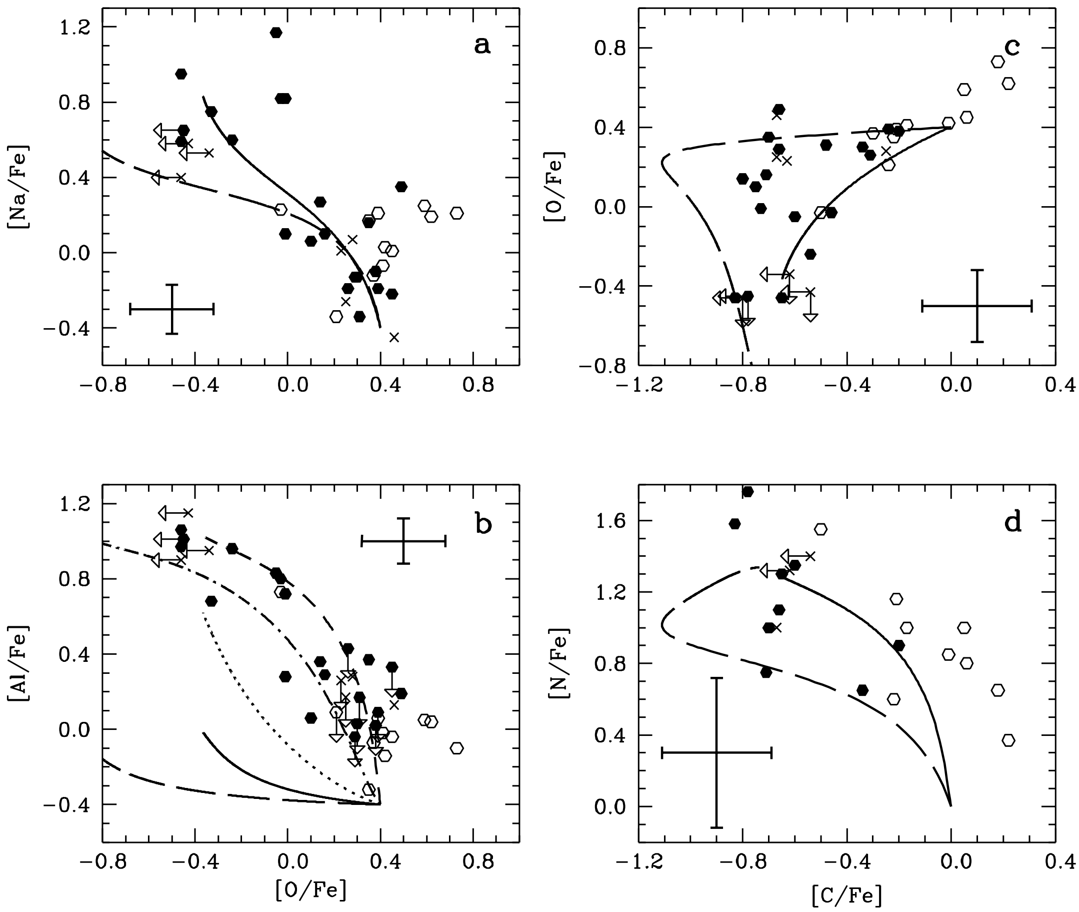

Figure 1: The abundance trends seen in ω Cen giants (symbols; from ND95) are compared with the results of our deep mixing calculations for two sets of mixing depth and rate ($\delta M_{\rm mix}$; $D_{\rm mix}$, cm^2 s^{-1}): (0.05; $5\,10^8$) – solid, dotted and short-dashed lines, (0.06; $2.5\,10^9$) – long-dashed and dot-short-dashed lines. The former pertains to ω Cen while the latter corresponds to the best fit to the anticorrelation of [O/Fe] versus [Na/Fe] in M 13 (Fig. 2). In panel b the dotted line was calculated with an initial abundance [^{25}Mg/Fe]$\,=1.2$, whereas the short-dashed and dot-short-dashed lines were determined with [^{25}Mg/Fe] $= 1.1$ and the ^{26}Al$^{\rm g}$(p,γ)^{27}Si reaction rate increased to 10^3 times the value given by CF88. Open and filled symbols refer to CO-strong and CO-weak stars, and crosses denote stars with unidentified CO status, following ND95. In panel d the N abundances of ND95 have been shifted by $+0.5$ dex (for them to agree better with the data of Brown & Wallerstein (1993))

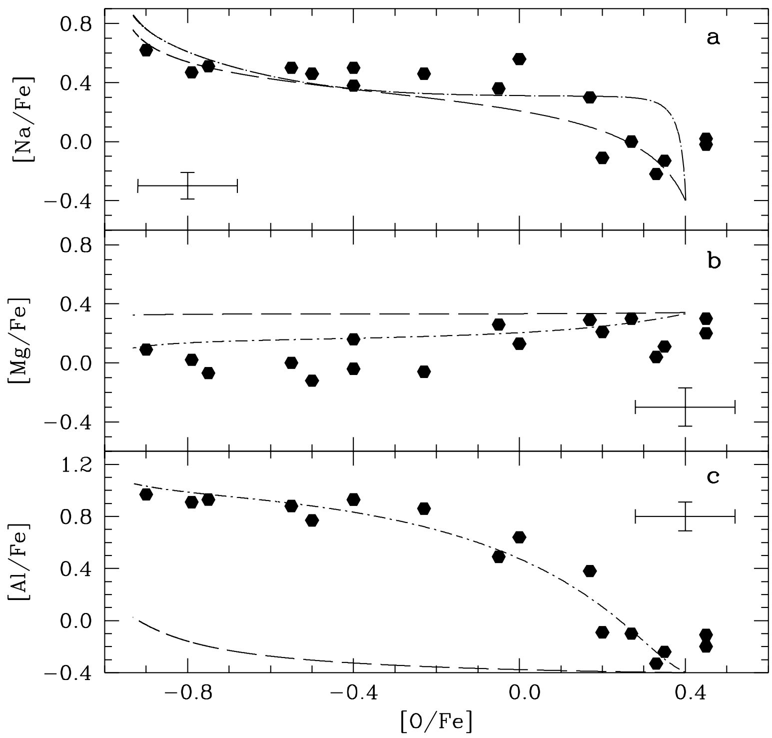

Figure 2: The anticorrelations of [O/Fe] versus [Na/Fe] and [Al/Fe] and the correlation of [O/Fe] versus [Mg/Fe] seen in M 13 giants (symbols) compared with the results of our deep mixing calculations for $\delta M_{\rm mix}= 0.06$ and $D_{\rm mix}= 2.5\,10^{9}\,{\rm cm}^2\,{\rm s}^{-1}$. Observational data are taken from Kraft et al. (1997) with corrections of +0.05 dex and −0.25 dex applied by us to their [Na/Fe] and [Al/Fe] values, respectively, to compensate for differences between their adopted *gf* values and those of ND95. The dashed lines were computed with standard input physics. The dot-long-dashed line in panel a was calculated with the new NeNa-cycle reaction rates from El Eid & Champagne (1995), while the dot-short-dashed lines (panels b and c) were calculated with the initial abundances $[^{24}{\rm Mg/Fe}] = 0$ (as opposed to the value +0.4 while we normally adopt), $[^{25}{\rm Mg/Fe}] = 1.1$ and the $^{26}{\rm Al}^{\rm g}({\rm p},\gamma)^{27}{\rm Si}$ reaction rate increased to 10^3 times the CF88 value

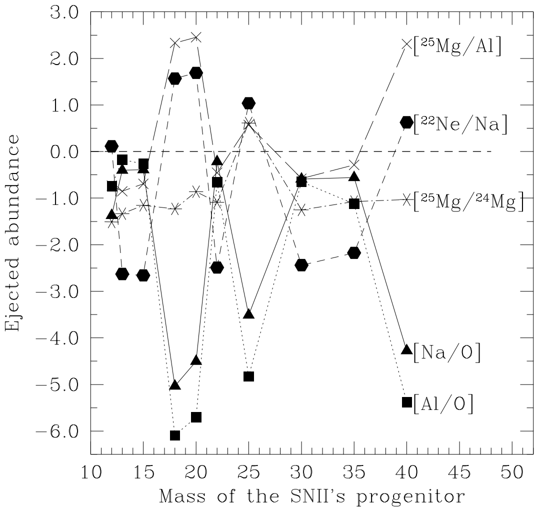

Figure 3: Abundances of some nuclides ejected by SNeII (following Woosley & Weaver 1995)

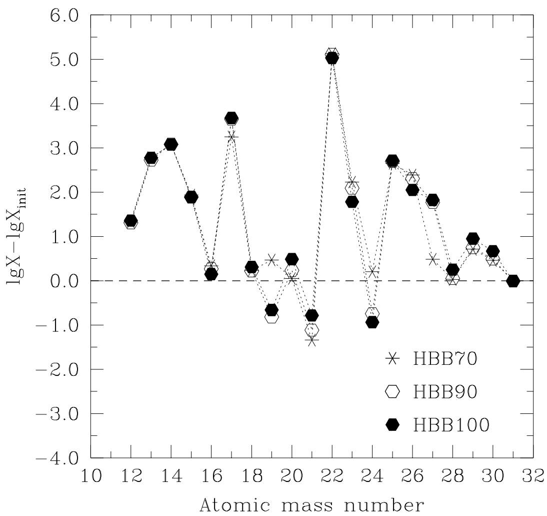

Figure 4: Nucleosynthesis yields of some light nuclides from intermediate mass AGB stars after 400 pulses. The notation HBBT6 signifies that HBB was assumed to occur at the temperature T6 10^6 K. The atomic mass number 26 corresponds to ^{26}Mg. The initial chemical composition was that given in Table 1

R-Process Abundances and Cosmochronometers in Old Metal-Poor Halo Stars

B. Pfeiffer [1], K.-L. Kratz [1], F.-K. Thielemann [2], J.J. Cowan [3], C. Sneden [4], S. Burles [5,6], D. Tytler [5], and T.C. Beers [7]

[1] *Institut für Kernchemie, Universität Mainz, Mainz, Germany*
[2] *Institut für Theoretische Physik, Universität Basel, Basel, Switzerland*
[3] *Department of Physics and Astronomy, University of Oklahoma, USA*
[4] *Department of Astronomy and McDonald Observatory, University of Texas, Austin, USA*
[5] *Department of Physics and Center for Astrophysics and Space Sciences, University of California, San Diego, USA*
[6] *Department of Astronomy and Astrophysics, University of Chicago, Chicago, USA*
[7] *Department of Physics and Astronomy, Michigan State University, East Lansing, USA*

Already 30 years ago, Seeger et al. [1] expressed the idea that the solar system r-process isotopic abundance distribution ($N_{r,\odot}$) is composed of several components. But only on the basis of new experimental and modern theoretical nuclear-physics input, Kratz et al. [2] demonstrated that within the so-called waiting-point approximation a minimum of three components (showing a steady flow of β-decays between magic neutron numbers) can give a reasonable fit to the whole $N_{r,\odot}$. A somewhat better fit can be obtained by a more continuous superposition of exponentially declining neutron number densities [3, 4]. Accordingly, the s-process shows a steady flow of neutron captures in between magic neutron numbers and a good fit is achieved when taking an exponentially declining superposition of exposures. Analyzing with present day almost perfectly known nuclear data in the s-process (as neutron capture and β-decay rates), Goriely [5] recently reproduced this exponential exposure with his "multi-event" model. As there is practically no experimental nuclear input in the r-process we prefer to apply the waiting-point approximation based on a smooth physical behaviour in an exponential model, rather than obtaining spurious results, which are just driven by obtaining a better fit with, however, the wrong physics. Deficiencies in calculated $N_{r,\odot}$-abundances (even using the most recent macroscopic-microscopic mass models FRDM and ETFSI) were attributed to an incorrect trend in neutron separation energies when approaching magic neutron numbers far from stability [2]. The weakening of shell strength near the neutron drip line predicted from astrophysical requirements was recently also obtained by Hartree-Fock-Bogolyubov (HFB) mass calculations with the Skyrme-P force [6]. And indeed, new spectroscopic studies of very neutron-rich Cd-isotopes at CERN/ISOLDE have revealed first experimental evidence for a quenching of the N=82 major shell below ^{132}Sn [7]. Applying these HFB masses around the magic neutron numbers resulted in an eradication of the abundance troughs [4]. As large-scale HFB calculations for deformed nuclear shapes are not yet available, Pearson et al. [8] modified their ETFSI mass model to asymptotically approach the HFB masses at the drip-lines. The $N_{r,\odot}$-abundances calculated with these ETFS-Q masses are shown in

Fig. 1 to give a good fit over the whole range of stable r-process isotopes. This gives confidence to extrapolate the calculations to the unstable actinide isotopes. The abundances prior to α- and β-decay are displayed in Fig. 1 as a dashed line and the final abundances after decay as a solid line. The good reproduction of the Tl-Pb-region (as endproducts of the α-decay chains) let us to conclude that estimates of the initial abundances of the long-lived isotopes ^{232}Th and ^{235,238}U, which are applied as cosmochronometers, can be taken from our r-process model.

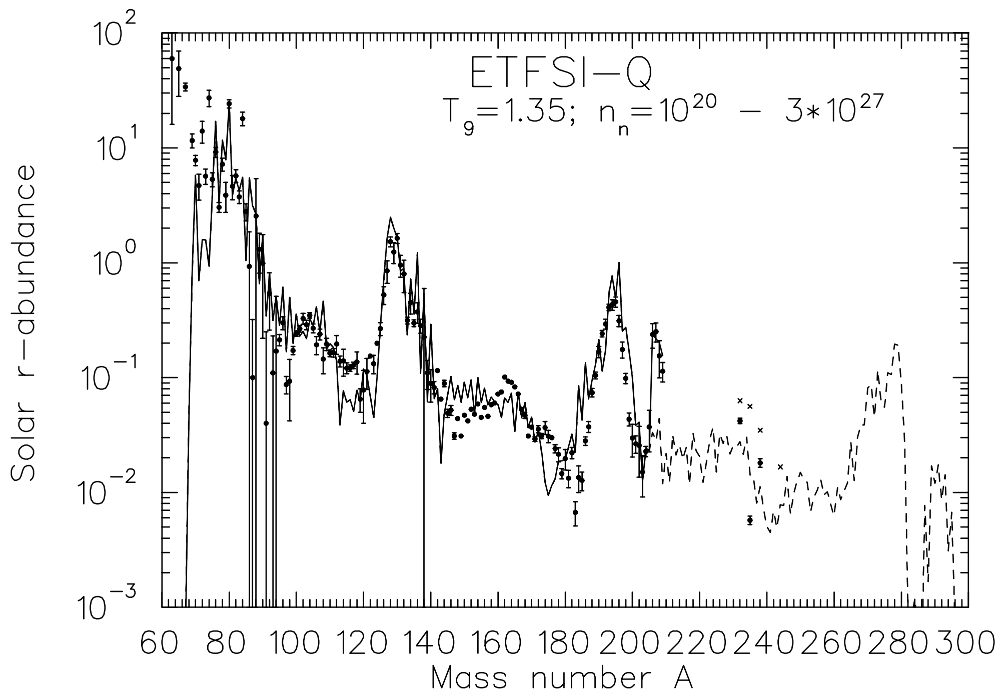

Figure 1: Comparison of theoretical abundances with solar r-process abundances (small filled circles). The dashed line indicates abundances prior to β- and α-decay and the solid line the final abundances after decay. The crosses represent calculated abundances after decay for the nuclei ^{232}Th, ^{235}U, ^{238}U and ^{244}Pu in comparison with the solar values (filled circles) for these nuclei.

Recently, stellar abundances of neutron-capture elements (beyond iron) have been determined over a wide Z-range in the very metal-poor Galactic halo star CS22892-052 [9]. After adjustment to solar metallicity, the values are consistent with the global solar-system r-process abundances as well as with our predictions (see Fig. 2). From this agreement, we concluded that the heavy elements in this star are of pure r-origin and that from the comparison of the observed and calculated Th/Eu abundance ratios an age estimate for the heavy elements of about 13 Gyr can be derived [10, 4]. This indicates, that r-synthesis started early in the Galactic evolution and that there might be a *unique* r-process scenario (at least beyond Z$\simeq$50).

As, evidently, **one** single star cannot stand for the whole low metallicity end of the Galactic halo, further measurements are needed, not only to investigate other stars over a range of metallicities, but essentially to detect additional elements, especially the 3^{rd}-peak elements (Os, Pt, Pb) close to Th and U. These elements have absorption lines in the UV, so that they are best observed from space. Therefore, spectra for three K giant stars (HD115444, HD122563, HD126238) were measured with the Goddard High Resolution Spectrograph on the Hubble Space Telescope [11]. Additional high-resolution spectra were registered with the High Resolution Echelle Spectrometer (HIRES) at the Keck I telescope for the star HD115444 in particular to separate the Th absorption line clearly from a blending ^{13}CH molecular line [11]. The results of these observations are summarized in Fig. 2 as filled squares together with ground-based results (open squares). After proper renormalization, the observed neutron-capture elements in the four stars displayed overlap perfectly with our theoretical r-process curve (solid line) and the solar system distribution (dashed line).

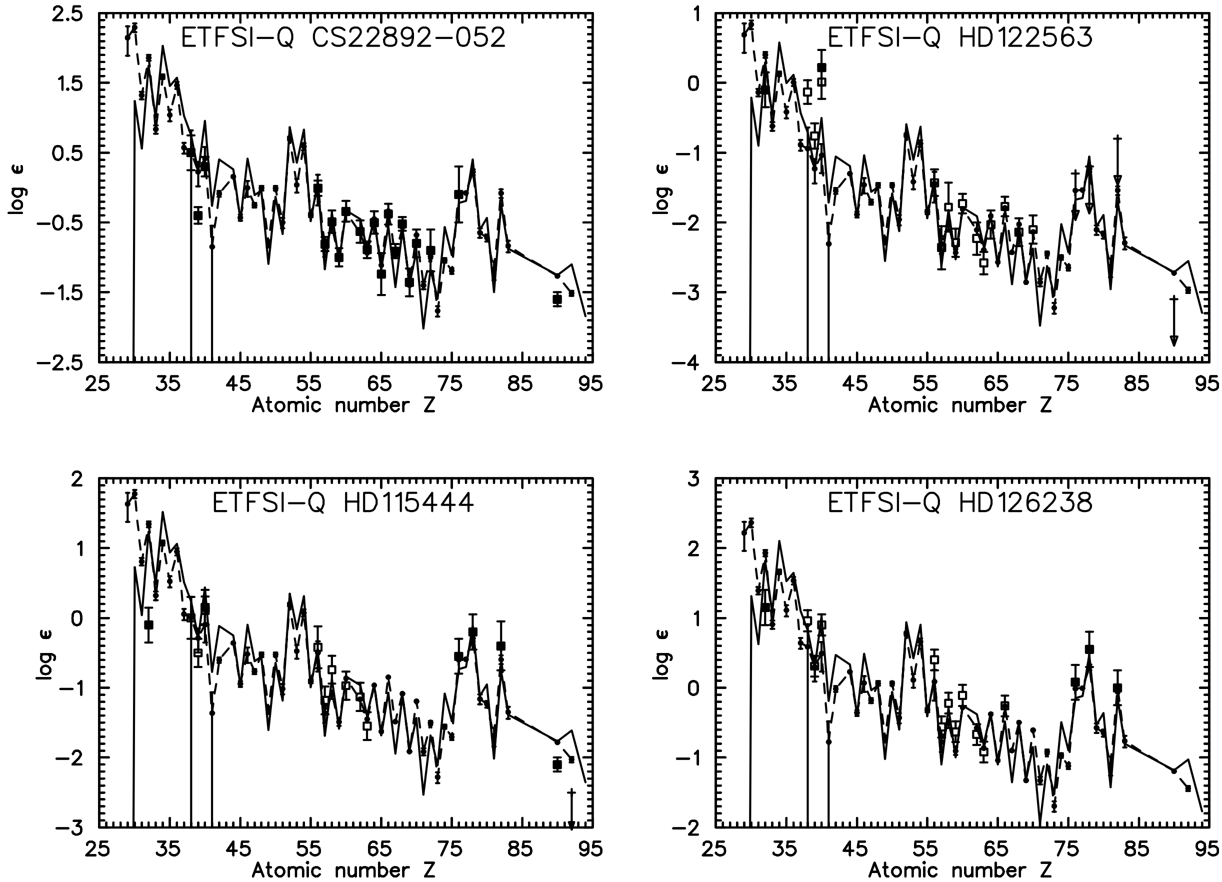

Figure 2: An abundance comparison between the observed neutron-capture elements in four metal-poor halo stars (large squares) and a theoretical r-process (solid line) and a solar system r-process (dashed line) abundance distribution.

In addition to the observation of Th in CS22892-052 mentioned above, the new measurements yielded a firm value for HD115444 as well as an upper limit for HD122563. In the case of the second chronometer U, only an upper limit could be obtained for HD115444. The measured Th/Eu ratios combined with our calculated zero-age value allow to derive

an estimate for the decay age of T=(13 ± 4) Gyr, where the uncertainty takes only in account the counting statistics [12]. This value represents a lower limit for the age of the Galaxy and is in line with a variety of recent age estimates for the Universe.
To summarize, the reproduction of the r-process component of solar abundances in the framework of the "waiting-point approximation" applying nuclear input data calculated from a macroscopic-microscopic mass model with Bogolyubov-enhanced shell "quenching" (ETFSI-Q) gives confidence in extrapolations beyond the stable isotopes to the actinide r-process cosmochronometers. The observation of "solar" neutron-capture element abundance distributions in four metal-poor halo stars indicate to a *unique* r-process site in the Galaxy (at least for Z≥56). This further strenghtens our objections to the conclusions of Goriely and Arnould [13] that a series of several non-solar isotopic abundance distributions might produce a total elemental abundance pattern that fortuitously matches some of the neutron-capture elements in one low-metallicity star. Although the observation of a solar r-process elemental pattern is not an *absolute* proof for isotopic solar r-process abundances, it is nevertheless the most reasonable and probable conclusion.

References

[1] P.A. Seeger et al., ApJS **11** (1965) 121.

[2] K.-L. Kratz et al., ApJ **403** (1993) 216.

[3] B. Chen et al., Phys. Lett. **B355** (1995) 37.

[4] B. Pfeiffer et al., Z. Phys. **A357** (1997) 235.

[5] S. Goriely, A&A **327** (1997) 845.

[6] J. Dobaczewski et al., Phys. Scr. **T56** (1995) 15.

[7] K.-L. Kratz et al., Proc. Int. Conf. on "Fission and Properties of Neutron-Rich Nuclei", Sanibel Island, 1997, World Scientific Press, in print

[8] J.M. Pearson et al., Phys. Lett. **B387** (1996) 455.

[9] C. Sneden et al., ApJ **467** (1996) 819.

[10] J.J. Cowan et al., ApJ **480** (1997) 246.

[11] C. Sneden et al., ApJ **496** (1998) 235.

[12] J.J. Cowan et al., submitted to ApJ.

[13] S. Goriely and M. Arnould, A&A **322** (1997) L29.

Recent Data on ^{187}Re, ^{187}Os and ^{186}Os Abundances

T. FAESTERMANN

Physik Department E12, Technische Universität München,
James-Franck-Str., D-85748 Garching, Germany

Apart from astronomical observations on globular clusters, the age of our galaxy can be estimated from abundancies of longlived radionuclides and their daughters. The pair ^{187}Re and ^{187}Os has been proposed as such a chronometer by Donald Clayton [1] a long time ago and discussed in detail by Yokoi et al. [2]. ^{187}Re has a half-life of 42 Gyr, which exceeds by far the age of the universe. It is produced by the r-process but not its β decay daughter ^{187}Os. This is a great advantage compared with other chronometric pairs like ^{232}Th/^{238}U, where the relative r-process production ratios are required. Naturally we have to know the solar abundances of ^{187}Re and ^{187}Os and also that of ^{186}Os in order to determine the s-process contribution to the ^{187}Os abundance. These are the subject of this talk. Other problems connected with this chronometer, as the alteration of the ^{187}Re/^{187}Os ratio, if the interstellar medium is reprocessed in a new generation of stars, and the galactic chemical evolution are discussed in the talks of Paul Kienle and Kohji Takahashi.

From today's abundances in meteorites we can easily calculate the ^{187}Re and ^{187}Os abundance 4.56 Gyr ago, when the meteorites (and the solar system) formed and were closed off from the admixture of newly synthesized heavy nuclei. But in the commonly used compilation of Anders and Grevesse [3] the abundance ratio is only given with 11% uncertainty. This would restrict in any case the precision of the galactic age derived from this chronometric pair to about 2 Gyr. Therefore we have searched the literature for new data. The best representatives of the solar system composition are the most primitive meteorites, the carbonaceous chondrites, where measurements are apparently difficult. But already from iron meteorites we can deduce important information.

Very precise and reproducible measurements of ^{187}Re and ^{187}Os abundances (normalized to ^{188}Os) in iron meteorites have been reported recently by two groups [4, 5] . In these the Re/Os ratio varies over a large range, but the ^{187}Os/^{188}Os ratio plotted versus the ^{187}Re/^{188}Os ratio defines perfectly a linear relationship, as it should, if all the samples have the same age and the same fraction of the originally present ^{187}Re has decayed to ^{187}Os. The individual measurements are so precise that even slightly different slopes and initials can be deduced for different classes of iron meteorites. These values are shown in the figure as 2σ areas, which are distinctly different for the individual classes. The initial gives the ^{187}Os/^{188}Os ratio at the time when the meteorites formed, the slope equals $(exp(\lambda T) - 1)$ with the ^{187}Re decay constant λ and the age T. Smoliar et al. [4] use the isochrone for the iron meteorites of class IIIA, whose age is dated as (4558 ± 5) Myr to determine the decay constant $\lambda = (1.666 \pm\ 0.010) \times 10^{-11}\mathrm{yr}^{-1}$. This is in agreement with values derived from differently dated meteorites [5, 6, 7], corresponds to a half-life of 41.6 Gyr and is considerably more precise than the only direct determination by Lindner et al. [8]. The initial ^{187}Os/^{188}Os ratio increases for the meteorites which formed later, because it is enriched in the protosolar nebula due to ^{187}Re decay. It amounts to 0.09535(15)

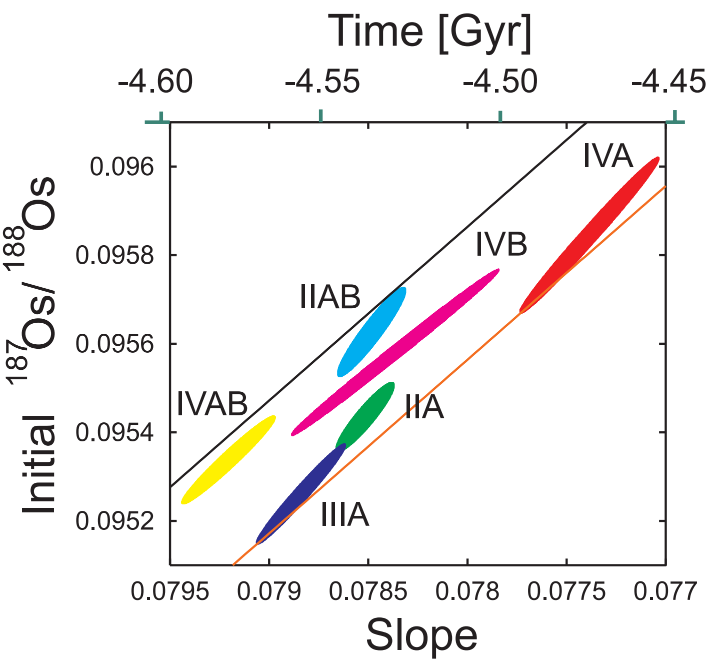

Figure 1: Parameters of the isochrones for different subgroups of iron meteorites [4, 5]. The ellipses show the 2σ contours for the two parameters initial ^{187}Os/^{188}Os at the time of solidification and the slope, which is the fraction of ^{187}Re which has decayed to ^{187}Os during the lifetime of the meteorites. The upper scale is calibrated in time, relative to today, with the help of independently dated meteorites. The two straight lines enclose the well defined range (0.2 %) of the ^{187}Os abundance in the protosolar nebula. (The style of this figure has been adopted from Smoliar et al. [4].)

for the oldest meteorites, like the carbonaceous chondrites, which formed 4.56(1) Gyr ago.

For chondrites even the recent data are not as consistent. Meisel et al. [9] published 5 measurements on CM2 and CV3 carbonaceous chondrites with an average ^{187}Re/^{188}Os ratio of 0.389, significantly lower than the average for ordinary chondrites of about 0.44. These 5 values scatter with an rms value of 2.5 % and Meisel et al. report that the ^{187}Re/^{188}Os in different samples of the same meteorite are not reproducible within the quoted uncertainties, but that the ^{187}Os/^{188}Os ratios are. Therefore they suggest that the latter ratios, which only have a scatter of 0.4 %, reflect the original Re/Os composition, and that the former have been altered just "recently". If this were the case, we could determine the original ^{187}Re from the present ^{187}Os content using the initial value derived from the iron meteorites and arrive at a ^{187}Re/^{188}Os ratio of 0.390(5). But for the time being we use their directly measured values (neglect older measurements by the same group [10]), add the average of recent values for CAI inclusions in the CV3 chondrite Allende [11] and combine them with four recent measurements of CI to CK4 carbonaceous chondrites by Jochum [12] yielding a present day solar abundance ratio and rms deviation of ^{187}Re/^{188}Os$= 0.392 \pm 0.010$. Thus the ^{187}Re/^{187}Os abundance ratio is now determined with a precision better than 3% .

To summarize the results from recent meteoritic data, we now have the input quantities for Re/Os chronometry with much better precision: The halflife of ^{187}Re atoms with 0.6% and the solar abundances at the time of formation of the first meteorites 4.56 Gyrs ago, namely for ^{187}Os/^{188}Os=0.09535 with 0.2% and for ^{187}Re/^{188}Os=0.423 with 2.5%. The ^{186}Os/^{188}Os ratio is well enough known as 0.12035 with an uncertainty below 0.1% .

We would like to acknowledge gratefully the valuable correspondence with G.J. Wasserburg, J.W. Morgan, H. Palme and K.P. Jochum. This work was supported by the "Sonderforschungsbereich 375-95 der Deutschen Forschungsgemeinschaft".

References

[1] D. D. Clayton, Astrophys. Journal **139** (1964) 637

[2] K. Yokoi, K. Takahashi, M. Arnould, Astron. & Astrophys. **117** (1983) 65

[3] E. Anders, N. Grevesse, Geochim. Cosmochim. Acta **53** (1989) 197

[4] M.I. Smoliar, R.J. Walker, J.W. Morgan, Science **271** (1996) 1099

[5] J.J. Shen, D.A. Papanastassiou, G.J. Wasserburg, Geochim. Cosmochim. Acta **60** (1996) 2887

[6] M.I. Smoliar, R.J. Walker, J.W. Morgan, Proc. 60th Meteoritical Society Meeting, Hawai, (1997)

[7] A. Shukolyukov, G. W. Lugmair, Proc. 28th Lunar and Planetary Science Conf., (1997)

[8] M. Lindner et al., Geochim. Cosmochim. Acta **53** (1989) 1597

[9] T. Meisel, R.J. Walker, J.W. Morgan, Nature **383** (1996) 517

[10] R.J. Walker, J.W. Morgan, Science **243** (1989) 519

[11] H. Becker, R.J. Walker et al., Proc. 29th Lunar and Planetary Science Conf., (1998)

[12] K.P. Jochum, Geochim. Cosmochim. Acta **60** (1996) 3353

The ^{187}Re - ^{187}Os Cosmochronometry and Chemical Evolution in the Solar Neighborhood

K. Takahashi[1,2], *T. Faestermann*[2], *P. Kienle*[2], *F. Bosch*[3], *N. Langer*[4], *J. Wagenhuber*[1]

[1] *Max-Planck-Institut für Astrophysik, D-87540 Garching*
[2] *Physik Department E12, Technische Universität München, D-85748 Garching*
[3] *Gesellschaft für Schwerionenforschung, Postfach 110552, D-64220 Darmstadt*
[4] *Institut für Theoretische Physik/Astrophysik, Universität Potsdam, D-14469 Potsdam*

With the use of the solar abundances of ^{187}Re and its β^- decay daughter ^{187}Os, the ^{187}Re - ^{187}Os chronometry aims at setting a stringent lower bound, $T_{\rm G}$, for the age of the Universe ([1, 2]; see [3] for a recent review). One may loosely classify the various requirements it sets out into three categories:

- It requires the *"laboratory" input data,* namely the meteoritic abundances of Re and Os isotopes (see T. Faestermann, this volume), the β^- decay half-lives not only of neutral but also highly-ionized ^{187}Re (P. Kienle, this volume), and the neutron capture cross sections for nuclides in the $A = 184 \sim 187$ mass region (e.g. [4]). Much experimental progress has recently put the chronometry on a safer footing with more reliable input data;

- It requires a *modelling of evolution of various stars,* which is due in the first instance in order to evaluate the effects of "astration" in the stellar interiors – transmutations of ^{187}Re and ^{187}Os by enhanced β^- decays and e^- captures as well as destructions by neutrons of the concerned nuclides. Additionally it provide us with input data that are necessary for a quantitative modelling of chemical evolution (e.g. the stellar lifetimes, remnant masses and possibly the yields of various elements). As far as the ^{187}Re - ^{187}Os chronometry is concerned, the currently available models of stellar evolution may be said to be satisfactorily accurate;

- It requires a *modelling of chemical evolution* of matter from which the solar system was formed. This is the hardest part of all even without referring to the dynamical aspects of the formation of the Galactic disk as we see presently. Being pragmatic and at least for chronometric purposes, however, one may construct simple (largely analytic) models but by imperatively imposing as many observational constraints as possible, a point stressed by Tinsley [5] and concurred by others [2, 3]. [Many attempts to describe the abundances of light elements in the Galactic disk have been made in a similar fashion (most recently: [6]).]

In designing a model of chemical evolution specifically for the chronometry, we adopt here a simple one-zone model with the allowance for "infall." As usual, the star formation is assumed to be separable in time (the star formation rate: SFR) and stellar masses (the initial mass function: IMF). Our working assumptions, which may easily be removed or modified in due course, are that: stellar evolution is independent of (Galactic) time, namely, of metallicity; the instantaneous recycling approximation holds but for astration; and that the infall rate is proportional to SFR (Ψ) being given externally (rather than related to the gas mass), and is metal-free. Under these assumptions, the relevant equations of chemical evolution can easily be solved. The net consumption by star formation of gas mass in the interstellar medium is $(1-R)\Psi$, where R is the "returning" mass fraction of the unit mass enclosed by stars. For β-stable elements such as ^{186}Os or the sum of ^{187}Re+ ^{187}Os, R is to be replaced by $R_{\rm n}$ in consideration of destruction by neutrons in the stellar interiors. As for ^{187}Re, its destruction by ^{187}Re β^- decays has to be taken into account in addition as well as its production by e^- captures of the embedded ^{187}Os. We have first calculated these returning fractions with the use of models of solar metallicty stars ([7] for $M \leq 10$ M$_\odot$ and [8] for $M \geq 10$ M$_\odot$). The weak interaction rates are obtained by the method developed in [9]. The results are shown in Fig. 1, which are then folded by IMF that is obtained from the present-day mass function [10] for each adopted Ψ with the help of the main-sequence lifetimes given by the models.

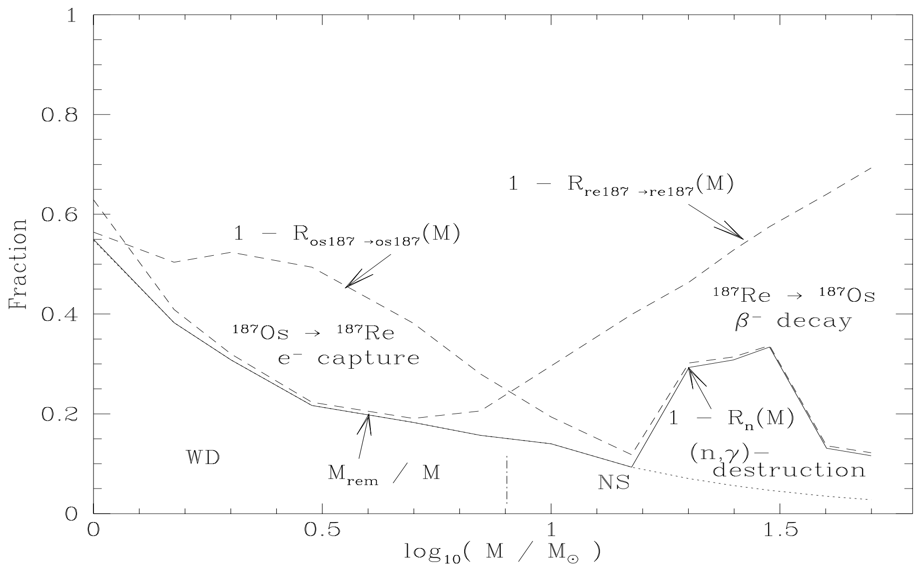

Figure 1: The fates of Re and Os isotopes embedded in stars of the initial mass $M = 1 \sim 50$ M$_\odot$. The dotted line separates the ejecta from the remnants: The "returning" fraction $R(M) = 1 - M_{\rm rem}/M$. The area between the solid and dotted lines represents a fraction that has been destroyed by neutron captures: $R_{\rm n}$ is the returning fraction having survived neutron captures. The area between the dashed and solid lines represents a fraction of ^{187}Re or ^{187}Os that has undergone β^- decays or e^- captures, respectively: Of the unit amount of ^{187}Re (^{187}Os) embedded, $R_{\rm re187\to re187}$ ($R_{\rm os187\to os187}$) is in the ejecta after having survived astration, $R_{\rm n} - R_{\rm re187\to re187}$ ($R_{\rm n} - R_{\rm os187\to os187}$) is found as ^{187}Os (^{187}Re), whereas $1 - R_{\rm n}$ never returns

The β transmutation between ^{187}Re and ^{187}Os occurs most importantly during the main-sequence phase: portions of these elements that encounter higher temperatures in later evolutionary phases are either destroyed by neutrons or eventually absorbed by remnants anyway. At H-burning temperatures, the densities are relatively high in low mass stars such that ^{187}Os e^- captures dominate, whereas in massive stars the effect of ^{187}Re β^- decays becomes appreciable. Neutron captures destroy much of Re and Os isotopes during the core He burning in massive stars. In low mass stars, such destructions occur during the thermal pulse phase but are negligible because only a tiny amount of matter is dredged up. [We are concerned with elements initially existed, and not those freshly produced (and tremendously enhanced) s-process elements.]

We are now left with typically three to four adjustable parameters (one or two for a functional of Ψ, then one for the infall rate, and the other being the initial gas mass. In order to constrain the ranges of parameter values, we adopt the following observational data:

the current total mass of 40 - 60 $M_\odot/pc^2$;
the current gas mass of 5.7 - 7.0 $M_\odot/pc^2$;
the current infall rate of 0.3 - 1.5 $M_\odot/pc^2/Gyr$; and
the current star formation rate of 0.5 - 1.5, relative to its average in the past.

[See the references in [6] for these limits observed in the solar neighborhood. We presume that the solar system had been formed out of material that ended up in the solar neighborhood. If the solar system is atypical, as some assert, then we may have to refer to different numbers.]

Some typical results concerning the metallicity distribution and the age-metallicity relation are compared with observations in Figs. 2 and 3. For a given $T_G = m$ Gyr, the class of models "Sn–m" assumes a step function for Ψ: a constant up to time $m - n$ Gyr and another one at later times, and the model "E-m" an exponential function.

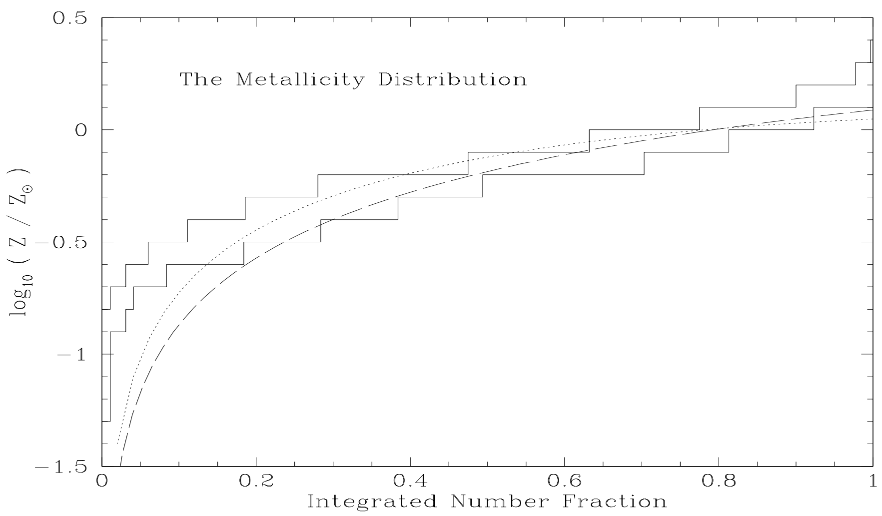

Figure 2: Accumulative metallicity distribution for models S6-13 (dot) and S6-17 (dash). The horizontal axis is the number of stars integrated up to time at which metallicity Z in the ordinate is reached (normalized at the present time). The solid lines define the boundaries set by observed [Fe/H] distribution in G-dwarf stars ([11]). See text for the naming of the models

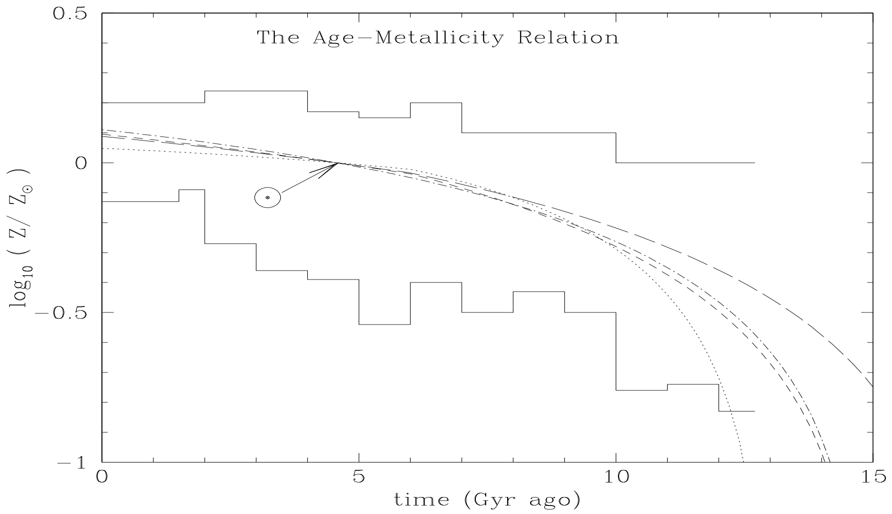

Figure 3: Evolutions of metallicity backward in time for models S6-13 (dot), S6-15 (short dash), S6-17 (long dash) and E-15 (dot-dash). The solid lines define the boundaries set by various observational analyses of [Fe/H] ([12]). See text for the naming of the models

We now proceed to an age determination. For a given trial value of $T_{\rm G}$ and a set of Ψs with constrained parameter values, we first use the ^{186}Os solar abundances to get its bulk (s-process) yield, from which the s-process contribution to the solar ^{187}Os abundance is derived ([4]). We then fit the summed solar abundance of ^{187}Re and ^{187}Os in order to deduce the ^{187}Re r-process yield. Finally, a comparison of the then computed ^{187}Re abundances with the solar value leads to a most probable $T_{\rm G}$ value for each Ψ functional. The results are shown in Fig. 4. The error bars attached there are theoretical and reflect the spreads in the parameter space. It is clear that the ^{187}Re - ^{187}Os chronometry leads as yet to a considerable spread in the derived $T_{\rm G}$ values, particularly owing to the uncertainties in modelling of chemical evolution. On the other hand, it is comforting to find $T_{\rm G}$ in a "reasonable" range, whereas the utter neglect of astration effects would result in $T_{\rm G}$ well beyond 20 Gyr. There are much more observational data that are worth considering in constructing a model of chemical evolution. We add also that the assumptions underlying our models have been introduced just for simplicity, and have to be removed or modified in due course, particularly in relation to chemical evolution in the early, metal-poor (halo) phase.

We should like to dedicate this work to the memory of David N. Schramm with admiration for his important contributions not only to nucleo-cosmochronology but to nuclear astrophysics in general. We thank R. Bender, D. Thomas, W. Hillebrandt and H.-Th. Janka for helpful discussions on the "atypicality" of the Sun in the solar neighborhood. The work was supported by the "Sonderforschungsbereich 375-95 der Deutschen Forschungsgemeinschaft."

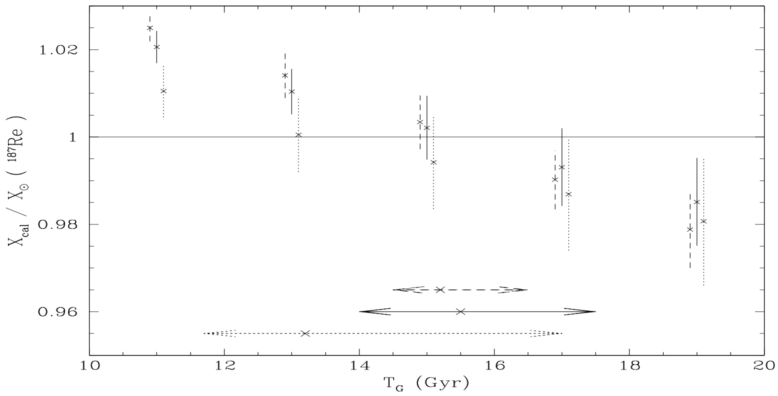

Figure 4: Computed ^{187}Re abundances relative to the solar value and theoretical 1σ errors (vertical lines) for models S6-11 $\sim$ -19 (solid), S9-11 $\sim$ -19 (dotted), and E-11 $\sim$ -19 (dashed). The probable age intervals thus derived are displayed at bottom

References

[1] D.D. Clayton, ApJ **139** (1964) 637.

[2] K. Yokoi, K. Takahashi and M. Arnould, A&A **117** (1983) 65;
D.D. Clayton, MNRAS **234** (1988) 1.

[3] K. Takahashi, in Proc. Tours Symp. on Nuclear Physics III (AIP, 1998) in press.

[4] F. Käppeler et al., ApJ **366** (1991) 605.

[5] B.M. Tinsley, ApJ **216** (1977) 548; Fundam. Cosmic Phys. **5** (1980) 287.

[6] F.X.. Timmes, S.E. Woosley and T.A. Weaver, ApJS **98** (1995) 617;
L. Portinari, C. Chiosi and A. Bressan, A&A (1997) submitted.

[7] J. Wagenhuber, A&A, to be submitted.

[8] N. Langer and C. Henkel, SSR **74** (1995) 343.

[9] K. Takahashi and K. Yokoi, Nucl.Phys. (1983) **A404** 578.

[10] G.E.. Miller and J.M. Scalo, ApJS **41** (1979) 513.

[11] H.J. Rocha-Pinto and W.J. Maciel, MNRAS **279** (1996) 447;
R.F.G. Wyse and G. Gilmore, AJ **110** 2771.

[12] B.A. Twarog, ApJ **242** (1977) 242;
H. Meusinger, H.G. Reimann and B. Stecklum, A&A **245** (1991) 57;
B. Edvardsson et al., A&A **275** (1993) 101.

Status of the Re-Os Cosmochronometry

P. Kienle [1], F. Bosch [3], T. Faestermann [1], K. Takahashi [1,2], E. Wefers[1] in collaboration with the ESR-group of GSI Darmstadt

[1] Physik Department E 12, Technische Universität München, D-85748 Garching
[2] Max-Planck-Institut für Astrophysik, D-85540 Garching
[3] Gesellschaft für Schwerionenforschung, Postfach 110552. D-64220 Darmstadt

The bound-state β-decay of fully ionized ^{187}Re nuclei circulating in a storage ring has been observed. With two independent methods the time dependent growth of hydrogenlike ^{187} Os has been measured and a half life of 32.9 ± 2.0 y for bare ^{187}Re nuclei could be determined, to be compared with 42 Gy for neutral Re atoms. With the resulting log ft value of 7.87 ± 0.03 the half life of ^{187}Re ions in any ionization state can be calculated.

1. Introduction

Boundstate β-decay (β_b) is expected to occur especially in highly ionized atoms in which the decay electron has a high probability to be captured in an empty orbit with a high density at the nuclear origin. It is the time reversed process to orbital electron capture with its decay probability being proportional to the electron density at the nucleus. For fully ionized atoms the Q-value of β_b-decay into K-orbits is given by:

$$Q^K_{\beta_b} = Q_\beta - \Delta\ B^{tot}_e(Z+1,Z) + B^K_e(Z+1) \qquad (1)$$

with Q_β denoting the Q-value for the continuum β-transition of a neutral mother atom with atomic number Z, ΔB^{tot}_e (Z+1,Z) the difference of the total electron binding energies of the neutral daughter- and mother-atoms, and B^K_e (Z+1) the K- electron binding energy in the hydrogen like daughter atom. From equation (1) one notes that β_b becomes energetically favored compared with the continuum β-decay because the binding energy gain B^K_e (Z+1) is always larger than ΔB^{tot}_e. Even nuclei which are stable as neutral atoms, $Q_\beta < 0$, may become energetically unstable if completely ionized when $Q_\beta - \Delta B^{tot}_e + B^K_e$ (Z+1) becomes positive.

Indeed the first observation of boundstate β-decay by our group of completely ionized ^{163}Dy is such a case [1]. This nucleus is stable as a neutral atom (Q_β = -2.565 keV) but when fully ionized it decays with Q_β = 50,3 keV and a half life of 48d to ^{163}Dy. Such β_b-decays play an important role in the hot plasmas of stars in which the atoms may become highly ionized, which was pointed out by Takahashi and Yokoi [2]. Indeed the occurrence of the β_b-decay of ^{163}Dy can explain the unusual high abundance of ^{164}Er, which can be formed following β_b-decay of ^{163}Dy into ^{163}Ho followed by a n-capture and a consecutive β-decay to ^{164}Er.

In this work we will focus on the observation of boundstate β–decay of fully ionized ^{187}Re and its application to calibrate the ^{187}Re - ^{187}Os cosmochronometer. The solar abundances of most elements heavier than iron are the result of prior generations of stellar nucleosynthesis via the s- and r- neutron-capture process.

With models on the effective nucleosynthesis rate, its duration in our galaxy until the formation of the solarsystem can be estimated from the abundances of long lived radioisotopes, such as ^{232}Th, ^{238}U and ^{187}Re. Compared with chronometers like ^{232}Th and ^{238}U, the ^{187}Re-^{187}Os cosmochronometer introduced by Clayton in 1964 [3] has several advantages. One is the very long half life of ^{187}Re of 42Gy [4], but the main advantage is that the longlived ^{187}Re is only produced by the r-process, where as ^{187}Os is shielded against the r-process production by ^{187}Re.

However one uncertainty in the calibration of ^{187}Re - ^{187}Os Chronometer has been pointed out by Takahashi et al [2,5]. ^{187}Re may become highly ionized in the hot plasma of a star during a reastration period with the consequence of a fast β-decay, which decreases its half life up to more than 9 orders of magnitude depending on the ionization state.

The decay modes of fully ionized and neutral ^{187}Re are shown in fig. 1., including the corresponding energetic facts.

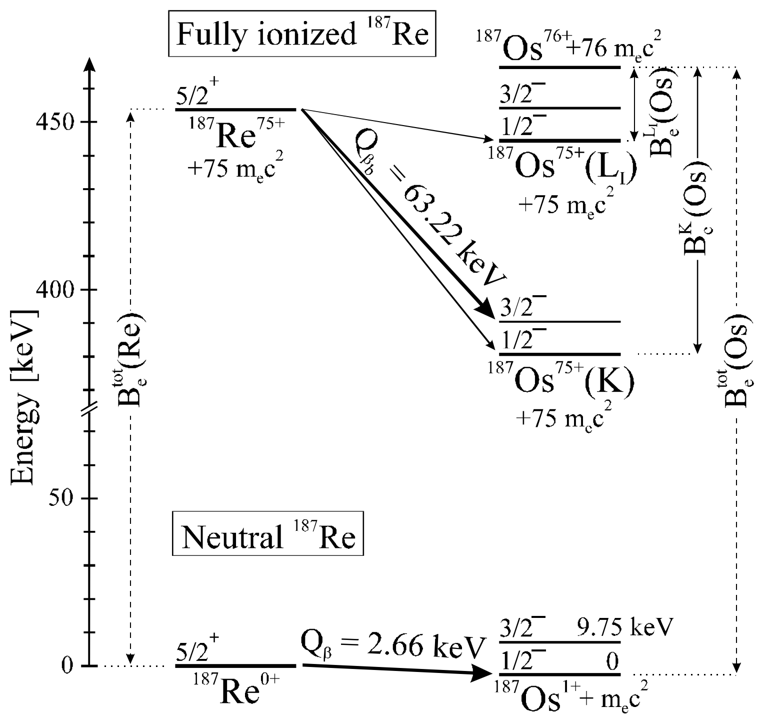

Figure 1. Decay schemes for neutral (bottom) and fully ionized (top) ^{187}Re with the energetically allowed β-transitions indicated by arrows.

For neutral ^{187}Re^0 only the unique, first forbidden transition to the groundstate of ^{187}Os is energetically possible. The small matrixelement and Q-value lead to the long half life of 42 Gy. As the inner orbits are occupied with electrons in neutral Re, β_b-decay contributes less than 1 % [6]. For fully ionized ^{187}Re^{75+}, β-decay to the continuum states of ^{187}Os^{76+} is energetically forbidden, instead bare ^{187}Os^{76+}can decay back to ^{187}Re^{75+} by capturing an electron in the plasma of a star. Bare ^{187}Re^{75+}, however is unstable against β_b-decay with the electron captured in the K - (Q_β = 72.97 keV) [7] or in the L- shell (Q_β = 9.07 keV).

Takahashi, Yokoi and Arnould [5] realized that also the first excited state of ^{187}Re at 9.75 keV can be fed by a non-unique first forbidden transition with a substantially larger matrix element. They made an estimate of the half-life of bare Re of $T_{1/2}$ = 14 y [8], which is more than a billion times shorter than that for neutral ^{187}Re. Thus reastration can change the effective half-life of cosmogenic ^{187}Re appreciably and a measurement of the β-decay of bare ^{187}Re would base the calibration of the ^{187}Re - ^{187}Os clock on safer grounds. Therefore we tried to measure the half life of bare $^{187}Re^{75+}$ in the heavy ion cooler ring ESR of the GSI, Darmstadt, by a procedure similar to that used in the observation of β_b of ^{163}Dy [1].

2. *Observation of boundstate β-decay of $^{187}Re^{75+}$*

$^{187}Re^{50+}$ ions injected into the heavy ion synchrotron SIS were accelerated to an energy of 347 AMeV extracted, stripped with a 100 mg/cm^2 Cu-foil to bare $^{187}Re^{75+}$ with an efficiency of about 75 %, and finally injected into the storage ring ESR, shown in the sketch of Fig 2.

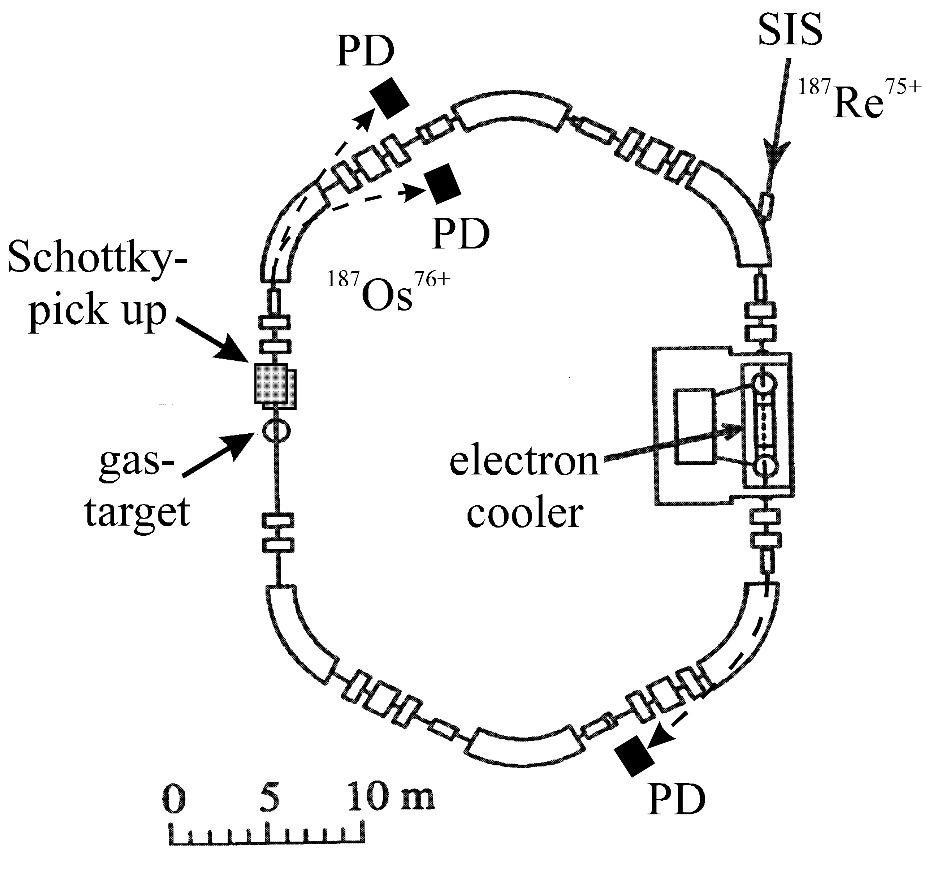

Fig. 2. Sketch of the experimental storage ring (ESR) at GSI. The position of the internal gas jet target, the electron cooler, the Schottky pick up system and the particle detectors (PD) are indicated as well as the path of $^{187}Os^{76+}$.

Electron cooling leads to a small momentum spread (10^{-5}) and a small emittance (0.1 π mm mrad) of the coasting ion beam with currents up to 2mA corresponding to 10^8 bare $^{187}Re^{75+}$ ions.

The storage losses due to collisions with atoms of the residual gas (10^{-11}mb), and atomic charge change reactions in the electron cooler section, lead to an effective storage half life of 4.5 hrs. With about 10^8 stored $^{187}Re^{75+}$ ions, several hundred $^{187}Os^{75+}$ ions were produced by β_b-decays of $^{187}Re^{75+}$ during storage times up to 5 hours.

The $^{187}Os^{75+}$ ions were circulating with nearly the same frequency (within 4ppm) as the main beam due to the small m/q difference. Their number $N_{Os}(t_s)$ grows proportional to the storage time t_s ($t_s << T_{1/2}$), according to the relation

$$N_{Os}(t_s) = (\lambda_{\beta b}/\gamma)\, N_{Re}\,(t_s)\, t_s \qquad (2)$$

$N_{Re}(t_s)$ denotes the number of circulating $^{187}Re^{75+}$ ions at time t_s, $\lambda_{\beta b}$ the decay probability in the $^{187}Re^{75+}$ rest frame and $\gamma = E/mc^2$ the Lorentzfactor, which was determined experimentally to $\gamma = 1.373$ (2).

For separation of hydrogen - like $^{187}Os^{75+}$ ions from the $^{187}Re^{75+}$ mother nuclei, the bound β–decay electron was stripped by turning on a gas jet target which crossed the ion beam and produced $^{187}Os^{76+}$. Two methods were used for the determination of the number of $^{187}Os^{76+}$ ions from the decay of $^{187}Re^{75+}$.

In the first one, the Schottky noise frequency analysis, we measured the number of circulating ions as function of the revolution frequency, which allows a unique identification of $^{187}Os^{76+}$ daughter nuclei. The circulating ions induce a noise signal in a pair of capacitive pick up plates. When Fourier transformed the noise signal reveals the corresponding revolution frequency (or harmonics) of each species of stored ions. This frequency is a unique measure of the mass/charge ratio since the velocity of all ions is forced to be equal to that of the cooler electrons. Fig. 3 shows in the upper part a sketch of the Schottky noise frequency measurement method, and in the lower part a Schottky noise frequence spectrum taken after storing $^{187}Re^{75+}$ for 1.8 h and after stripping the ^{187}Os ions by the gas jet, which was turned on for 200 s containing 3 x 10^{12} Argon atoms/cm^2 .

All lines observed in this spectrum can be assigned to nuclei produced by reactions of ^{187}Re with nuclei in the gas jet (mainly loss of a few nucleons) except for β_b-decay daughter $^{176}Os^{76+}$. Only this line grows linearly with the storage time as demonstrated in the inset of Fig. 3, proving its origin from the β_b-decay of $^{187}Re^{75+}$.

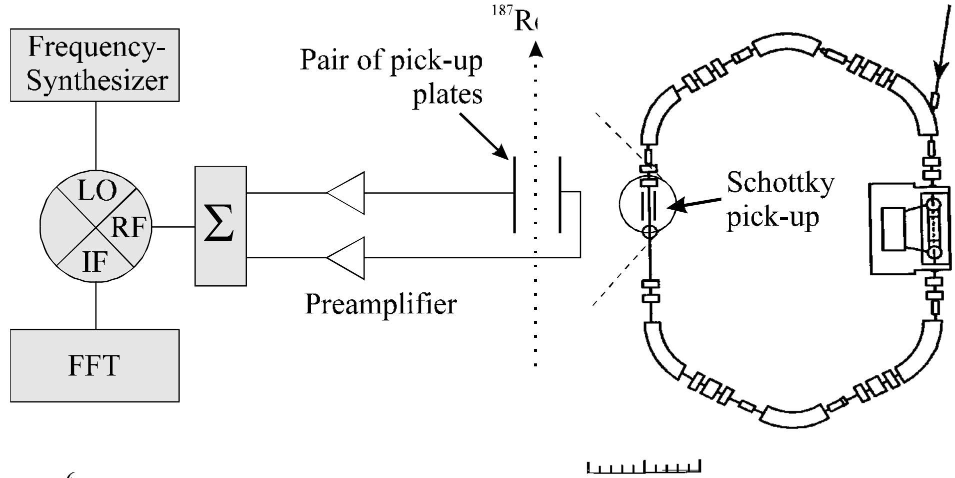

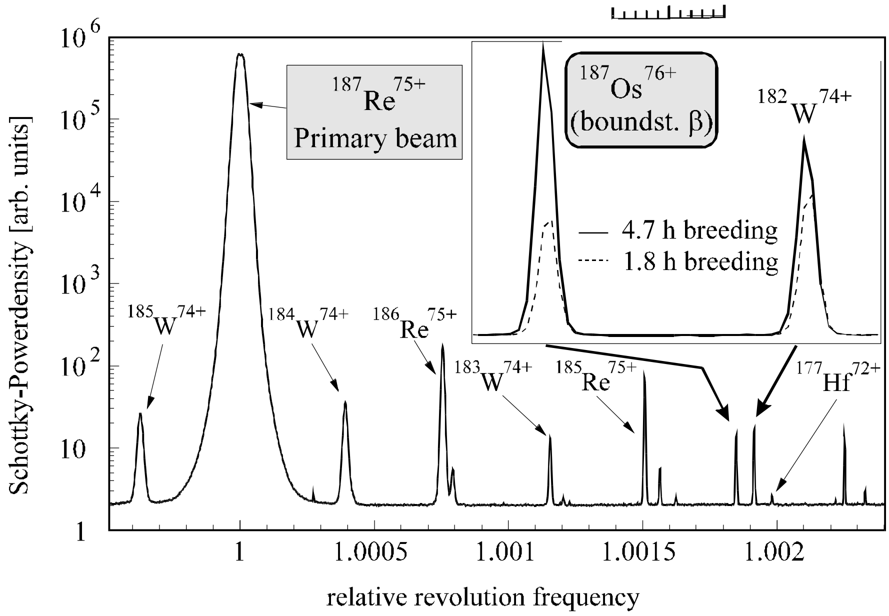

Fig. 3. Schottky noise frequency spectrum after a storage time of 1.8 h and after the reaction of the coasting beam with the jet target. Besides a number of nuclides produced by nuclear reaction the β_b-decay daughter $^{187}Os^{76+}$ is seen. The inset demonstrates that the intensity of the $^{187}Os^{76+}$ line increases expectedly when the storage time is increased from 1.8 h to 4.7 h.

A small ^{187}Os contribution originating from a nuclear charge exchange reaction in ^{187}Re collisions with argon atoms of the gas jet could be determined from the intensity for zero storage time. The absolute number of $^{187}Os^{75+}$ions produced by ^{187}Re β_b-decay, was determined from the area of the Schottky-noise signal of fully ionized $^{187}Os^{76+}$and corrected for the experimentally determined electron stripping efficiency of the gas jet. The area of the Schottky noise lines were calibrated absolutely in terms of particle numbers by measuring currents at particle numbers exceeding 10^5 and counting single ions for very small particle numbers.

In an independent experiment we measured the position of ions that had interacted with the gas jet target and were deflected by the following dipole magnet stronger than the coasting beam.

The dispersion of the magnet displaced $^{187}Os^{76+}$ ions from $^{187}Re^{75+}$ ions by 75 mm at the location of our detector. A gas microstrip counter measured the deflection position with a resolution of 0,4 mm. It was operated with 1 bar of an argon/isobutane (70:30) mixture. In front of this counter and in the same gas volume the energy loss was measured by an ionization chamber. In spite of the small energy loss of 60 MeV we achieved a resolution with respect to the nuclear charge of $\Delta Z = 1.5$. By a condition on the pulse height in the ionization chamber other elements than osmium could be suppressed in the position spectra.

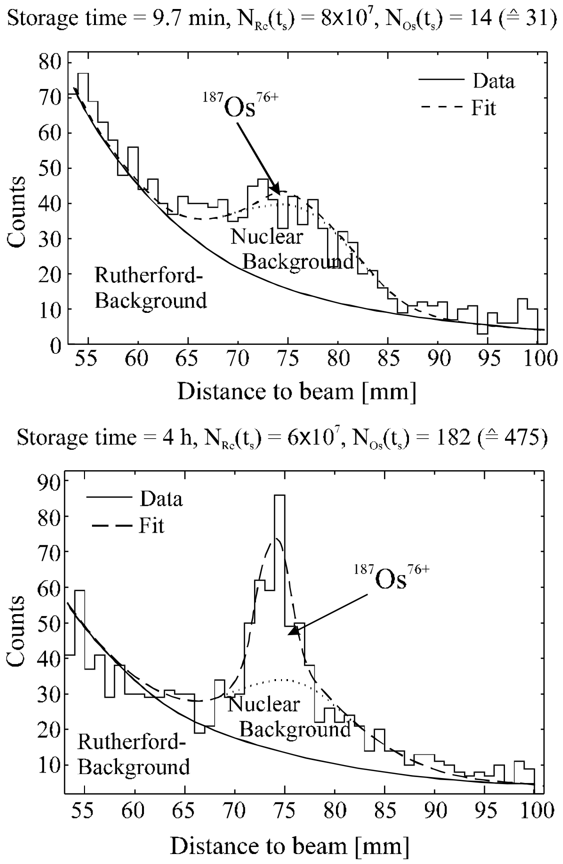

Fig. 4 a and b show positionspectra of particles detected with a multistripgascounter with breeding times of 9.7 min (a) and 4 h (b).

Fig. 4 a,b show position spectra taken with the multistripgascounter with a pulsheight condition from the ionization chamber set such that all elements except osmium being suppressed, taken after a short (a) (9.7m) and a long (b) (4h) breeding time. The spectrum with the short breeding time represents the background due to Rutherfordscattering (continuously decreasing part) and reaction products (broad peak) from interactions with the Ar gas jet. The spectrum with the 4 h breeding time reveals a narrow line at the position for cooled $^{187}Os^{76+}$ daughter nuclei superimposed on the Rutherfordscattering and nuclear reaction background.

With either method a dozen measurements were performed with storage time t_s ranging from $t_s \approx 0$ (determination of background from nuclear reactions) to $t_s \approx 5$ h. After calibrating the areas of the Schottky signals and of the line in the particle detector in absolute particle numbers and after determining the number of primary $^{187}Re^{75+}$ ions (with a beam current transformer), taking into account the various losses, we obtain for the β_b-decay probability $\lambda_{\beta b} = (6.29 \pm 0.19 \pm 0.40) \cdot 10^{-10} s^{-1}$ from the Schottky-noise analysis and $\lambda_{\beta b} = (7.05 \pm 0.28 \pm 0.34) \cdot 10^{-10}\ s^{-1}$ from the position spectra, where first the statistical errors are given and then the estimated systematical errors. Adding these two errors algebraically in each case and then taking the average of both results, we get $\langle \lambda_{\beta b} \rangle = (6.7 \pm 0.4) \cdot 10^{-10}\ s^{-1}$ and $T_{1/2} = (32.9 \pm 2.0)$ y. The measured $\lambda_{\beta b}$ is practically equal to the β_b-decay probability into the K- shell of ^{187}Os, because the decay into the L- shell is about 4 orders of magnitude less probable. From the measured $T_{1/2}$ we deduce log $ft = 7.87 \pm 0.03$. Note also, that the decay of bare ^{187}Re is dominated by the nonunique transition to the first excited state of ^{187}Os, since the decay to the ground state has a much smaller matrix element (logft = 11.0, from the decay of neutral ^{187}Re).

Re ions in a stellar plasma can have average numbers of bound electrons between 1 and more than 20, depending on temperature and density. With the measured ft value the decay rate of ^{187}Re in any charge state, and hence at any temperature, can now be calculated.

Our measurement is very close to log ft = 7.5, which was assumed by Yokoi *et al.* [5] in their study of the ^{187}Re-^{187}Os cosmochronometry.

3. *Cosmochronometric Results*

Recently Takahashi [8] reviewed the progress made towards a reliable evaluation of the age of the Galaxy through the ^{187}Re - ^{187}Os cosmochronometry, the aim of which is to set a lower bound for the age of the Universe. A break through in the problem of transmutations of ^{187}Re and ^{187}Os by weak interaction transitions at high temperatures in stellar environments during „astration“ periods brought our determination of the β–decay of fully-ionized ^{187}Re. This gives an experimental value for the key transition matrix element to the 9.75 keV excited state of ^{187}Os,which allows reliable evaluations for the ^{187}Re β-decay, and ^{187}Os electron capture rates in stellar interiors with the use of the basic formalism and of thermodynamic conditions (temperature, density and composition) given by realistic stellar evolution models.

In a contribution to the Ringberg 98 symposium Takahashi et al. discuss in detail the present status of the ^{187}Re-^{187}Os cosmochronometry.

References

[1] M. Jung et al., Phys. Rev. Lett. 69, 21 64 (1992)

[2] K. Takahashi and K. Yokoi, Nucl. Phys. A404, 578 (1983)

[3] D.D. Clayton, Astrophys. J. 139, 637 (1964)

[4] M. Lindner et al. Geochim. Cosmochim Acta 53, 1597 (1982)

[5] K. Yokoi, K. Takahashi and M. Arnould, Arston. Astrophys. 117, 65 (1983)

[6] Z. Chen, L. Rosenberg and L. Spruch, Phys. Rev. A35 1981 (1987)

[7] W. R. Johnson and G. Soff At. Data Nucl. Data Tables 33, 405 (1985)

[8] K. Takahashi et al. Phys. Rev. C36 1522 (1987)